Timo Lindemann

Droplet Generation
From the Nanoliter to the Femtoliter Range

Dissertation
zur Erlangung des Doktorgrades der Fakultät für Angewandte Wissenschaften der Albert-Ludwigs-Universität Freiburg im Breisgau

Freiburg i. Br., Juli 2006

Dekan
Prof. Dr. Jan G. Korvink

Referenten
Prof. Dr. Roland Zengerle (Freiburg)
Prof. Dr. Jan G. Korvink (Freiburg)

Tag der Prüfung
14. Dezember 2006

Institut für Mikrosystemtechnik (IMTEK)
Lehrstuhl für Anwendungsentwicklung
Fakultät für Angewandte Wissenschaften
Albert-Ludwigs-Universität Freiburg

ERKLÄRUNG

Ich erkläre hiermit, dass ich die vorliegende Arbeit ohne unzulässige Hilfe Dritter und ohne Benutzung anderer als der angegebenen Hilfsmittel angefertigt habe. Die aus anderen Quellen direkt oder indirekt übernommenen Daten und Konzepte sind unter Angabe der Quelle gekennzeichnet. Insbesondere habe ich hierfür nicht die entgeltliche Hilfe von Vermittlungs- oder Beratungsdiensten (Promotionsberaterinnen oder Promotionsberater oder anderer Personen) in Anspruch genommen. Niemand hat von mir unmittelbar oder mittelbar geldwerte Leistungen für Arbeiten erhalten, die im Zusammenhang mit dem Inhalt der vorgelegten Dissertation stehen. Die Arbeit wurde bisher weder im In- noch im Ausland in gleicher oder ähnlicher Form einer anderen Prüfungsbehörde vorgelegt.

Freiburg, den

(Timo Lindemann)

CONTENTS

ABSTRACT

This thesis provides a general description of micro droplet generation at low and medium Weber numbers using analytical, numerical and experimental methods in an engineering manner of contemplation. Based on the presented results guidelines are deduced to support the designing and operating *any* type of micro droplet generator.

In the first chapter the basic differential equations are presented which are relevant for the droplet formation in the micro scale. Based on these fundamentals analytical and numerical descriptions of the droplet formation process will be discussed throughout the thesis. Important dimensionless numbers like the Reynolds, the Weber and the Ohnesorge number are introduced to describe the fluid flow in micro dimensions and the droplet formation qualitatively. Simple analytical expressions are derived for fluidic components like fluidic resistance, fluidic inertance, fluidic capacitance, an outflow model of a nozzle, an inlet resistance and junction effects like a contraction or an expansion of the cross section. Such compact models can be applied to build equivalent fluidic networks for more complicated fluidic systems. In this work some of the considered droplet generators are described by such a network approach.

The main part of the work is engaged with the fundamentals of droplet formation especially with the necessary criteria for a droplet ejection. Therefore the Weber number respectively the critical Weber number is used to derive sufficient critical parameters for the droplet formation like the critical velocity, the critical pressure, the critical time and the critical power. These parameters are introduced using an energetic approach based on the formulations stated in the previous chapter. These critical values are subsequently used to describe the sufficient boundary conditions for a successful droplet generation with a given setup. Moreover these critical values can also be used to depict the influence of the design and geometrical variations or parameter variations of the applied liquid. Since the energetic model is not capable to state the dynamic behavior of a given system it is complemented by a computational fluid dynamics (CFD) study concerning the dependence of the droplet formation process on the actuation dynamics. The role of the critical values is successfully validated using the CFD model. Based on this parameter maps for successful droplet generation in different droplet generation regimes like drop-on-demand, jet-on-demand or a jet ejection with subsequent Rayleigh breakup are presented. Finally a new, unique classification of the various droplet generation mechanisms known today is proposed. This classification is based on the underlying fluid dynamic working principle rather than on obvious design elements of the system or historical reasons.

As a prominent example of a droplet generator a bubble jet printhead design provided by Olivetti I-Jet was studied intensively. This work was carried out within an European project supported by the Federal Ministry of Education and Research

(BMBF), Germany (grant no. 16SV1607) within the EURIMUS program (IDEAL EM 42) applying the previously explained numerical and experimental methods. For a better understanding of the working principle the design and manufacturing of a bubble jet printhead and the characteristic values are presented. A fully three-dimensional CFD simulation model was set up to simulate the ejection process, the capillary filling and the thermal behavior of the printhead. Furthermore, the influence of specific design parameters and the optimization potential are explained in detail. The three-dimensional simulation model of the thermal inkjet printhead developed in this work provides a valuable approach to optimize the printhead regarding droplet volume, droplet velocity, droplet quality and print frequency including 3D sensitive aspects. The correctness of the used pressure boundary condition and the simulation model in the three-dimensional case was verified by comparing simulations with gravimetrical and stroboscopic results. Thus, for the first time a fully 3D simulation of a bubble jet could be presented and validated. For the optimization or the design of a new printhead a variety of model parameters was investigated to study effects on, for example, geometry and ink properties.

The detailed description of the bubble jet printhead is complemented by the examination of seven alternative droplet generators in a more general manner to verify the analytical approach and the criteria to predict the conditions for droplet formation derived in chapter 3. The single droplet generators are studied with respect to dosage technology, experimental results, theoretical description or numerical models. Conclusively the agreement with the considerations presented in chapter 3 is verified. The results presented in this chapter are partially based on work by other persons and are cited where appropriate to complete this thesis. The obtained findings confirm the analytic model approach in general. The derived critical parameters for droplet ejection are in good agreement for most of the systems. The critical parameters provide a sufficient condition to predict droplet breakup in general. In one special case (TopSpot dispenser) droplet breakup is even observed below the critical parameters. This observation is explained by the fact, that the necessary condition for droplet breakup in fact is different from the conditions given by the critical parameters of the model.

To complete the thesis, guidelines for the systematic design of droplet generators are provided based on the presented results. Because the quest for a suitable droplet generator strongly depends on the main requirements and specifications of the system, it is distinguished therein between important main requirements along which the guidelines are developed. After the definition of these main requirements and the presentation of general design rules, specific design rules are recommended for typical applications. Using these recommendations an appropriate droplet generator can be designed from scratch or an existing droplet generator can be optimized.

ZUSAMMENFASSUNG

Diese Arbeit vermittelt ein allgemeines ingenieurmäßiges Verständnis für die Tropfenentstehung bei niedrigen und mittleren Weber Zahlen basierend auf analytischen, numerischen und experimentellen Untersuchungen. Aufbauend auf dieses Verständnis werden Richtlinien präsentiert, die den Entwurf und die Handhabung verschiedenster Mikrotropfenerzeuger unterstützen sollen.

Im ersten Kapitel werden die grundlegenden Differentialgleichungen dargestellt, welche für die Erzeugung mikroskopischer Tropfen relevant sind. Basierend auf diesen Grundlagen werden analytische und numerische Methoden diskutiert, die einen Tropfenentstehungsprozess beschreiben. Um den Fluss in mikroskopischen Dimensionen und die Erzeugung von mikroskopischen Tropfen qualitativ zu beschreiben, werden wichtige dimensionslose Zahlen wie die Reynolds, die Weber und die Ohnesorge Zahl eingeführt. Darüber hinaus werden für fluidische Bauelemente wie ein fluidischer Widerstand, eine fluidische Induktivität, eine fluidische Kapazität, ein Düsenausfluss, ein Einlaufwiderstand und Übergangseffekte wie eine plötzliche Querschnittserweiterung oder -verengung einfache analytische Ausdrücke hergeleitet. Solche so genannten Kompaktmodelle werden verwendet, um äquivalente fluidische Netzwerke komplexerer fluidischer Systeme aufzubauen. Einige der in dieser Arbeit untersuchten Tropfenerzeuger werden mit Hilfe eines solchen Netzwerkansatzes beschrieben.

Der hauptsächliche Teil der Arbeit befasst sich mit den Grundlagen der Tropfenerzeugung und besonders mit den notwendigen Kriterien einer Tropfenerzeugung. Unter Verwendung der Weber Zahl bzw. der kritischen Weber Zahl werden hinreichende kritische Parameter für die Tropfenerzeugung wie die kritische Geschwindigkeit, der kritischen Druck, die kritische Zeit und die kritische Leistung hergeleitet. Basierend auf den zuvor dargelegten Grundlagen werden diese Parameter mit Hilfe eines energetischen Ansatzes hergeleitet. Die resultierenden kritischen Werte werden nachfolgend benutzt, um die hinreichenden Randbedingungen eines Systems für einen erfolgreichen Tropfenausstoß zu beschreiben. Darüber hinaus können diese kritischen Werte auch noch ausgenutzt werden, um beispielsweise den Einfluß von Design Varianten oder unterschiedlichen Flüssigkeit darzustellen. Da das energetische Modell nicht in der Lage ist, Aussagen über das dynamische Verhalten eines vorgegebenen Systems zu machen, wird es durch transiente fluiddynamische (CFD) Simulationen ergänzt, um die Abhängigkeit des Tropfenerzeugungsprozesses von der Antriebsdynamik zu untersuchen. Die Aussagekraft der, mittels des energetischen Modells berechneten kritischen Werte ist erfolgreich anhand des CFD-Modells validiert worden. Basierend darauf ist es zudem möglich, notwendige Kriterien für eine erfolgreiche Tropfenerzeugung zu definieren, abhängig von den unterschiedlichen

Mechanismen der Tropfenerzeugung wie "drop-on-demand", "jet-on-demand" oder Strahlausstoß mit nachfolgendem "Rayleigh Abriß". Schließlich wird eine neue, einzigartige Klassifizierung von unterschiedlichen Tropfenerzeugungsmechanismen vorgeschlagen. Im Gegensatz zu den üblichen Zuordnungen, bei denen die Unterscheidungsmerkmale meistens aus offensichtlichen "Designelementen" des Systems bestehen oder aufgrund historischer "Gründe" unterschieden wird, basiert diese Klassifizierung auf dem eigentlichen Arbeitsprinzip des Systems.

Ein bedeutender Vertreter eines Tropfenerzeugers, ein thermischer Tintendruckkopf der Firma Olivetti I-Jet, wurde intensiv unter Verwendung der zuvor erklärten numerischen und experimentellen Methoden untersucht. Diese Arbeit wurde im Rahmen eines europäischen Projektes durchgeführt, welches vom deutschen Ministerium für Bildung und Forschung (BMBF), (Fördernummer: 16SV1607) innerhalb des EURIMUS Programms (IDEAL EM 42) unterstützt wurde. Zum besseren Verständnis des Arbeitsprinzips wird der Aufbau und die Herstellung sowie die charakteristischen Größen eines thermischen Tintendruckkopfes präsentiert. Ein dreidimensionales CFD Simulationsmodell wurde aufgesetzt, um den Tropfenausstoß, die kapillare Befüllung und das thermische Verhalten des Druckkopfes zu simulieren. Darüber hinaus wird der Einfluß bestimmter Designparameter und das Optimierungspotential ausführlich erklärt. Das dreidimensionale Simulationsmodell stellt einen nützlichen Ansatz zur Verfügung, einen thermischen Tintendruckkopf hinsichtlich Tropfenvolumen, Tropfengeschwindigkeit, Tropfenqualität und Druckfrequenz zu optimieren, auch unter Berücksichtigung dreidimensionaler Aspekte. Die Anwendbarkeit der verwendeten Druckrandbedingung und des dreidimensionalen Simulationsmodells wird nachgewiesen, indem die Simulationen mit gravimetrischen und stroboskopischen Ergebnissen verglichen werden. Demzufolge konnte zum ersten Mal eine vollständig dreidimensionale Simulation eines thermischen Tintendruckkopfes gezeigt und validiert werden. Eine Vielfalt an Modellparametern wurde untersucht, um beispielsweise die Effekte von Geometrie-Variationen oder variierenden Tinteneigenschaften zu ermitteln. Mit Hilfe dieser Ergebnisse kann die Optimierung eines vorhandenen Druckkopfes oder die Konstruktion eines neuen unterstützt werden.

Zur Verifikation des analytischen Modells wird diese ausführliche Beschreibung eines thermischen Tintendruckkopfes ergänzt durch die allgemeinere Untersuchung von sieben weiteren Tropfenerzeugern. Auch hier werden jeweils die kritischen Parameter analysiert, die zu einem erfolgreichen Tropfenausstoß führen und mit den Abschätzungen, die in Kapitel 3 gezeigt werden, verglichen. Darüber hinaus werden die einzelnen Tropfenerzeuger jeweils anhand der Dosiertechnologie, der experimentellen Ergebnissen, der theoretischen Beschreibung oder numerischer Modelle beschrieben. Die in diesem Kapitel präsentierten Ergebnisse basieren teilweise auf der Arbeit von Kollegen. Sie vervollständigen diese Arbeit und wurden entsprechend gekennzeichnet. Die beobachteten Ergebnisse bestätigen den analytischen Ansatz basierend auf der energetischen Betrachtung. Die hergeleiteten

kritischen Parameter für die Tropfenerzeugung stimmen ebenfalls für die meisten Systeme überein. Die kritischen Parameter stellen hinreichende Bedingungen dar, um allgemein einen Tropfenausstoß vorauszusagen. Allerdings kann in einem besonderen Fall, dem TopSpot Dispenser, sogar ein Tropfenabriss unterhalb der kritischen Parameter beobachtet werden. Das kann dadurch erklärt werden, dass sich die notwendige Bedingung für einen Tropfenabriss in Wahrheit von den kritischen Parametern des Modells unterscheiden.

Zur Vervollständigung der Arbeit werden Richtlinien für die systematische Konstruktion von Tropfenerzeugern erläutert, basierend auf den gezeigten Ergebnissen und den erreichten Erkenntnissen. Da die Suche nach einem passenden Tropfenerzeuger stark von den Hauptanforderungen des Systems abhängen, werden Richtlinien verschiedener Hauptanforderungen unterschieden. Nach der Definition dieser Hauptanforderungen und der Aufführung von allgemeingültigen Designregeln, werden spezielle Designregeln für typische Anwendungen empfohlen. Durch Verwendung dieser Empfehlungen kann ein geeigneter Tropfenerzeuger von Grund auf entworfen werden oder ein existierender Tropfenerzeuger optimiert werden.

PUBLICATIONS

Parts of this work have been published at the following journals or conferences:

JOURNALS

1. W. Streule, **T. Lindemann**, G. Birkle, R. Zengerle and P. Koltay, "PipeJet™ - A simple disposable dispenser for the nano- and microliter range", *The Journal of the Association for Laboratory Automation*, vol. 9, pp. 300-306, 2004.
2. **T. Lindemann**, H. Ashauer, Y. Yu, D. Sassano, R. Zengerle and P. Koltay, "One Inch Thermal Bubble Jet Printhead with Laser Structured Integrated Polyimide Nozzle Plate", *Journal of Microelectromechanical Systems*, accepted.
3. M. Hu, **T. Lindemann**, T. Goettsche, J. Kohnle, R. Zengerle and P. Koltay, "A Microfluidic Chip for Discrete Biochemical Release", *Journal of Microelectromechanical Systems*, accepted.
4. C. Cupelli, T. Glatzel, **T. Lindemann**, C. Litterst, C. Moosmann, R. Niekrawietz, W. Streule, R. Zengerle and P. Koltay, "Computational fluid dynamics (CFD) software tools for microfluidic applications - a case and benchmark study", *Computers and Fluids*, submitted.
5. T. Goettsche, C. Ruddy, U. Heller, M. Stehr, H. Ashauer, **T. Lindemann**, P. Koltay, Y. Yu, R.-P. Peters, A. Bellone and P. Soriani, "Comparison of bonding procedures for 3D-structured polyimide films on silicon substrates applied to ink-jet cartridges", *International Journal of Advanced Manufacturing Technology*, accepted.

CONFERENCE PROCEEDINGS

1. **T. Lindemann**, D. Sassano, A. Bellone, R. Zengerle and P. Koltay, "Three-Dimensional CFD-Simulation of a Thermal Bubble Jet Printhead", *Technical Proceedings of the 2004 NSTI Nanotechnology Conference and Trade Show*, Boston, 2004, vol. 2, pp. 227-230.
2. **T. Lindemann**, W. Streule, G. Birkle, R. Zengerle and P. Koltay, "PipeJet™ - A Simple Disposable Dispenser for the Nanoliter Range", *Proceedings of Actuator*, Bremen, 2004, pp. 224-227.

3. **T. Lindemann**, H. Ashauer, T. Goettsche, H. Sandmaier, Y. Yu, R.-P. Peters, D. Sassano, A. Bellone, A. Scardovi, R. Zengerle and P. Koltay, "Thermal Bubble Jet Printhead with Integrated Nozzle Plate", *Proceedings of NIP20, International Conference on Digital Printing Technologies*, Salt Lake City, 2004, pp. 834-839.
4. **T. Lindemann**, H. Ashauer, T. Goettsche, H. Sandmaier, Y. Yu, R.-P. Peters, D. Sassano, A. Bellone, R. Zengerle and P. Koltay, "Bubble Jet Printhead with Integrated Polyimide Nozzle Plate", *Proceedings of 18th IEEE International Conference on Micro Electro Mechanical Systems, MEMS*, Miami Beach, 2005, pp. 560-563.
5. T. Goettsche, C. Ruddy, U. Heller, M. Stehr, H. Ashauer, **T. Lindemann**, P. Koltay, Y. Yu, R.-P. Peters, P. Soriani and A. Bellone, "Development of highly precise bonding procedures for structured polyimide films on silicon substrates", *International Conference on Multi-Material Micro Manufacture (4M)*, Karlsruhe, 2005.
6. M. Hu, **T. Lindemann**, T. Goettsche, J. Kohnle, R. Zengerle and P. Koltay, "Discrete Chemical Release From A Microfluidic Chip", *Proceedings of 19th IEEE International Conference on Micro Electro Mechanical Systems, MEMS*, Istanbul, 2006, pp. 28-31.
7. S. Zibek, W. Nisch, D. Martin, A. Stett, M. Stelzle, M. Hu, P. Koltay, **T. Lindemann**, R. Zengerle, T. Göttsche, J. Kohnle and S. Messner, "Artificial Synapse - Nanofluidiksystem zur lokalen Substanzapplikation mittels nanoporöser Membran mit schaltbarer Permeabilität", *Mikrosystemtechnik-Kongress*, Freiburg, 2005.

1 INTRODUCTION

Liquid droplets of different volumes are used in many applications in various areas of interest. This is the reason why much research work has been dedicated to understand and to describe the numerous existing droplet generation mechanisms. In the following some applications for droplets in the volume range from nanoliters to femtoliters are presented, divided into the segments printing and coating, life science, electronics manufacture, optics and others. Furthermore, the state of the art in understanding and describing droplet formation processes is briefly reviewed. Mainly two approaches to describe the droplet generation can be distinguished: On the one hand the continuum mechanic or fluid dynamic method including analytical descriptions, network approaches or computational fluid dynamics (CFD) methods. On the other hand the particle based approaches like molecular dynamics or dissipative particle dynamics. Finally, in the last section of this chapter the aim and the structure of the present work is pointed out elaborately.

1.1 APPLICATIONS FOR DROPLETS IN THE VOLUME RANGE FROM NANOLITERS TO FEMTOLITERS

There are numerous applications exploiting droplet generating devices and applications with increasing market potential [1]. Due to the huge amount of available techniques, only some of them are selected as example and are presented in the following. It is distinguished between printing and coating, life science, electronics manufacture, optics and other main applications.

1.1.1 PRINTING AND COATING

Printing and coating certainly is the biggest industrial market using single droplets or sprays. Starting with the huge market of well known home and office printers based either on the bubble jet or the piezo principle. Followed by many industrial large format printers for the packaging of materials and direct labeling. High quality color image, low machine cost and low printing noise are basically the main advantages of such inkjet printers producing droplets in the 1 - 100 picoliter range. The two competing technologies in this field are the thermally actuated bubble jet commercially available from Hewlett Packard, Canon, Olivetti I-Jet and others [2-5] and the piezoelectric driven printheads commercially available from Epson, Xaar, Spectra and others [6-10]. Both methods made remarkable progress in the last two decades. Furthermore, there are thousands of applications of spray units used for spraying of colors [11], adhesives [12,13], oils [14,15] and many more.

1.1.2 LIFE SCIENCE

Examples for the use of droplets in the life science are lab on a chip systems, microarrays, DNA synthesis, drug discovery, cell sorting, medical therapeutics, combinatorial chemistry and many more.

Lab on a chip systems [16,17] or microreactors [18-20] rely on micromachined structures, actuators and sensors to rebuild chemical synthesis and analysis processes on a miniaturized level. Advantages of these chips are the reduction of the needed reactants volume and a possible point-of-care use. Droplets can be used in such applications to load reagents, for dispensing of the final product or even without any channel or chamber structures as chemical "micro containers". This is possible due to actuation principles like electrowetting on dielectrics (EWOD) [21-23] or surface acoustic waves (SAWs) [24,25] to move, join and split single droplets on a plain surface.

Besides the mainly supporting use of droplet generators in lab on a chip systems, droplet generators can directly be used to fabricate microarrays. A microarray is a two-dimensional grid of tagged DNA fragments or proteins that is used as an analytic detection method to rapidly detect genetic patterns, such as a diability causing genetic defects or a presence of disease-causing microorganisms [26-28]. The microarray technology has revolutionized the fields of biotechnology and life sciences. It has opened new perspectives for decoding the human genome, for molecular gene and DNA diagnostics, proteomics as well as for new ways in pharmacogenetics. Due to high complexity and diversity of proteins, production of protein microarrays is a big technological challenge and requires very flexible printer systems.

In modern drug discovery, potential drug candidates have to be identified from a huge number of different chemical compounds. This process is called high throughput screening (HTS). It allows the testing of several 100,000 chemicals per day. In HTS, biochemical assays are performed in standardized containments termed micro-well plates. Due to the ongoing miniaturization smaller amounts of liquid have to be handled. Therefore, non-contact dispensing becomes more and more important because of the increasing surface tension effects of small liquid droplets. Thus micro droplet generators are an appropriate solution for non-contact liquid handling. They can decrease the necessary amount of liquid and the processing time for drug discovery experiments where typically thousands to hundreds of thousands of tests involving novel biologically active reagents are required [29-33].

Another interesting field of research is the cell sorting. Cell sorting can be used either to deposit single cells (cloning mode) or to collect large numbers of cells with similar properties (enrichment mode). A small droplet of several micrometers in diameter can contain a single cell. Due to this, such small droplets can be used to handle and sort cells. Cell sorting is a technique that typically includes a droplet generator, a droplet charging and deflecting system and sensors for measuring cell properties by fluorescence and light scatter [34].

Thus far only in vitro applications of droplet generators are presented. Nevertheless there are also in vivo applications like aerosol atomizers for drug delivery, which represent an important application in the medical field. Aerosolized droplets in the range of a few micrometers in diameter containing therapeutic reagents can be used to deliver drugs to the lungs to cure various diseases [35-37].

1.1.3 ELECTRONICS MANUFACTURE

Main application in electronics manufacture using droplets is the deposition of molten solder on circuit boards. This technology can be used to make direct solder connections of components, vertical and horizontal conductive lines and solder bumps for flip chip bonding [38-41]. Due to this, manufacturing technologies can be driven toward further automation, miniaturization and reductions in costs and cycle times. As a non-contact deposition method, this technology may also be applied to print on non-planar and curved surfaces.

A further application for the assembling is the printing of adhesives for sealing and bonding of devices. This could be accomplished quite efficiently by drop-on-demand as well as continuous droplet generators [42].

1.1.4 OPTICS

Small droplets can be used to fabricate lenses and lens arrays suitable for use in new optical components like fiber optics, laser diodes, imaging arrays, displays and optical switches. Cured optical plastics are used instead of glass to produce lenses where the curvature of the lens can be adjusted by control of surface tension and contact angle of droplet deposited on flat substrates.

Large area displays like LCDs or TFTs can also be fabricated by precise deposition of small droplets. The liquid crystals are usually fabricated using screen printing or lithographic techniques. However, with increasing display resolution the liquid crystals have to be smaller and smaller. Due to this the non-contact droplet deposition of the colors is a promising alternative [43].

Moreover also polymer based displays can be manufactured using droplet dispensing systems. Thus far organic polymers are usually used because of their potential low cost and they are typically deposited by spin coating or evaporation. The patterning of the necessary multiple organic layers for red, green and blue is difficult. A direct deposition of patterned luminescent doped polymers by droplet generators like inkjets provides a more simple manufacturing method. A further advantage using droplet generators is the reduction of the used amount of material. The polymer solutions of the three colors are printed directly in the provided positions [44-46].

1.1.5 OTHERS

Another important application using droplet generators are fuel injection systems which are the heart of modern combustion engines. The fuel is atomized into a spray of small droplets provided by a fuel injector [47-50]. For the combustion the droplet size distribution as well as the fuel-air ratio are crucial for an optimum combustion.

A further application using microdroplets is the rapid prototyping of three-dimensional industrial objects making use of the ejection of high-temperature liquid metals, ceramic suspensions, or hardenable polymers [51-54].

Besides these high throughput applications droplet generators can also be used in the drop-on-demand mode. They can be used to deposit lubricants, where needed during manufacture, assembling, or operating. For example special oils can serve as lubrication in small spindle motors without ball bearings. Therefore, the lubricant has to be provided with precise control of quantity and position [55].

1.2 STATE OF THE ART IN UNDERSTANDING AND DESCRIBING DROPLET FORMATION PROCESSES

The state of the art in understanding and describing droplet formation processes is divided into two different perspectives, the continuum mechanics or fluid dynamics approach and the particle based approach. Whilst the continuum mechanics approach bases usually on the Navier-Stokes equation, the continuum equation and the energy equation, the particle based approach bases on the interconnecting forces between neighboring particles like molecules or pseudo particles. Due to the fact that the fluid dynamics methods are mainly used in this work, and therefore are explained in more detail later on, they are only mentioned briefly here.

1.2.1 CONTINUUM MECHANICS / FLUID DYNAMICS

ANALYTICAL DESCRIPTIONS

Lord Rayleigh was the first who derived an analytical description of the droplet generation caused by jet instabilities already in the late 19^{th} century [56]. After that in the beginning of the 20^{th} century, the experimental study of the droplet generation became more and more important. However, even today analytical descriptions for the droplet formation process are still refined and improved [57-62]. These studies are mostly using simplifications of the Navier-Stokes equations like axisymmetric, steady flows with a free surface to describe simple examples of droplet formation. A general analytical description of droplet generation, however, is inhibited by the complexity of the underlying differential equations like Navier-Stokes equation and others (cf. chapter 2).

NETWORK DESCRIPTIONS

The purpose of network simulations, based on lumped-elements or compact models is to describe a fluidic system by an equivalent circuit model. While the full three-dimensional CFD simulation specifies a transient solution on a grid, the network simulation considers a few selected locations ("nodes") only. Furthermore, the integrating or averaging of involved quantities over the cross section of fluidic channels simplifies the mathematical description to a one-dimensional problem. The network simulation thus deals with scalar quantities evaluated at few selected locations.

Lumped-element models can be used to describe fluidic systems with and without free surfaces [63,64] and they are also capable to simulate an entire jet ejection with free surface [65]. A further advantage of network based simulation models is the possible bridging of physical domains like fluid-structure interaction or similar [66-68]. Commercially available tools for network simulation are for example Saber [69] or PSpice [70].

COMPUTATIONAL FLUID DYNAMIC (CFD) DESCRIPTIONS

Due to the complexity of the physics of liquid flow more and more numerical methods are applied to obtain more accurate and realistic solutions. Today CFD tools, as described in section 2.6, are routinely used in engineering applications. The main objective of CFD is to solve a given fluid dynamics problem using the full three-dimensional Navier-Stokes equation. All of the available CFD methods (cf. section 2.6) are using numerical approximation procedures based on the discretization of the problem on a computational grid. CFD simulations are capable to accomplish atomization problems [11,49,50] as well as drop-on-demand droplet formation processes like in inkjet applications [71-73]. Commercially available tools for CFD simulations are CFD-ACE+ [74], Flow3D [75], Fluent [76], CFX [77], Comet [78] or STAR-CD [79].

1.2.2 PARTICLE BASED APPROACHES

The Molecular Dynamics (MD) method is a meshfree particle based approach to model an ensemble of molecules. The principle approach is a straightforward application of Newton's second law, in which the product of mass and acceleration for each molecule constituting the liquid is equated to the forces on the molecule. These are computed according to a model potential - quite often the Lennard-Jones potential. The technique begins with an ensemble of molecules distributed in space. Each molecule has a velocity depending on the thermostat assigned to it such that the distribution of velocities obeys a Boltzmann distribution corresponding to the temperature of the distribution. The molecular velocities are integrated forward in time to arrive at new molecular positions. The intermolecular forces at the new time step are computed and used to evolve the particles forward in time again. As the user desires, the molecular

positions and velocities can be sampled, averaged and used to compute flow quantities such as velocity, density and viscosity. Although the algorithm is relatively simple to explain, it is computational intensive to implement because of the very short time steps needed for the integration and the extremely large number of molecules in even modest volumes of space [80,81]. Using this or similar methods the ejection and breakup of nanojets or droplets has been studied [82,83].

The Dissipative Particle Dynamics (DPD) method relies on "pseudo" particles which correspond to coarse-grained entities, thus representing molecular clusters rather than individual atoms. The particles move off-lattice interacting with each other through a set of prescribed and velocity dependent forces. Particularly there are three types of forces for simple fluids acting on each dissipative particle: a conservative force, a dissipative force that reduces velocity differences between the particles and a stochastic force directed along the line connecting the center of the particles [84]. Since the DPD particles are pictured as having internal degrees of freedom, the forces between them have both a fluctuating and a dissipative component in addition to the conservative forces that are present already at the MD level. Nevertheless, momentum conservation along with mass conservation produce hydrodynamic behavior at the macroscopic level [85]. The advantage of the DPD method is that a larger time scale as well as a larger dimensional scale compared to the MD method can be addressed. Therefore, the method can be considered as an approach to bridge the gap between continuum models and atomistic models.

1.3 Aim and Structure of this Work

Aim of the present work is to provide a general understanding of the droplet generation process using analytical, numerical and experimental methods. Compared to previous publications focused either on purely theoretical or purely experimental study of one specific case, this composition combines various approaches and techniques to the topic of the droplet generation. However, the focus of this work is put on engineering solutions to provide a common general understanding of dispensing technologies rather than the details of a specific device or the physics of the droplet formation process. Hence, the droplet ejection is studied using relatively simple energy estimations based on simplifications of the Navier-Stokes equation and the examination of concrete droplet ejectors. The influence of specific design parameters like the geometry, the used media, the surfaces and the dynamics was studied in general as well as specifically for the single systems to provide a common understanding of the resulting effects. Moreover, a new classification of droplet generators is proposed based on an association to boundary conditions established for CFD simulations. The verification of a newly proposed hypotheses concering the required parameters for a droplet formation was accomplished by investigation of a bubble jet printhead

particularly and alternative droplet generators in general. Based on the presented results the thesis finally provides guidelines and support for designing and operating micro droplet generators in general.

The present work is structured in the following manner: First the fundamentals of fluid dynamics are presented to provide the essential basis to the reader including the underlying differential equations. These include all effects which are relevant for the droplet formation on the micro scale. Important dimensionless numbers like the Reynolds number, the Weber number and the Ohnesorge number are introduced to describe the fluid flow in micro dimensions and the droplet formation qualitatively. By the use of these dimensionless numbers the physical behavior can be easily described qualitatively. Subsequently some analytical solutions of the governing differential equations for selected boundary conditions and simplifying assumptions are presented which can be applied to describe simple fluidic components. These components are a fluidic resistance, a fluidic inertance, a fluidic capacitance, an outflow out of a nozzle, an inlet resistance and a sudden contraction. Such components are required to build equivalent fluidic networks for more complicated fluidic systems. Finalizing the first chapter both simulation methods used within this work, the fluidic network approach and the computational fluid dynamics approach are presented in detail in the third chapter.

The fundamentals of droplet formation are described to provide a general estimation which boundary conditions are necessary to eject a droplet. Since the boundary condition representing the actuation in a model is the most important one, the focus of this chapter is directed to the different kinds of actuation that can be used to generate a droplet. Furthermore, the influences of different parameters like geometry variations, different surfaces, media properties and the actuation dynamics on the droplet formation are presented. Finally a new classification of droplet generators is proposed along the line of the applicable boundary conditions. This leads to a classification which is based on the underlying working principle rather than on obvious construction elements of the system or historical reasons.

Thereafter, the experimental measurement methods used for this work like gravimtrical or optical measurements for the droplet characterization are described.

In the fifth chapter a bubble jet printhead is studied being an eminent droplet generator by applying the previously explained numerical and experimental methods. Therefore the design and manufacturing of a bubble jet printhead, the characteristic values, the simulation of the ejection process by CFD, the influence of specific design parameters and the optimization potential are explained in detail.

After the detailed description of the bubble jet printhead seven alternative droplet generators are considered in a more general manner to verify the approach and classification presented in chapter 3. The single droplet generators were studied concerning dosage technology, experimental results, theoretical or numerical

description. Conclusively the agreement with own considerations is assessed. The examined droplet generators are the dispensing well plate (DWP), fast switching valve systems, the NanoJet system, the PipeJet system, the TopSpot system, the TopSpot Vario system and finally an aerosol atomizer.

To complete the thesis, guidelines for the systematic design of droplet generators are provided based on the presented results. Because the quest for a suitable droplet generator strongly depends on the main requirement of the system, it is distinguished therein between important main requirements along which the guidelines are developed. After the definition of these main requirements and the presentation of general design rules, specific design rules and suitable applications are recommended for certain dispensing technologies.

1.4 Droplet Breakup Regimes

In this section some terms concerning the droplet ejection are defined for the later use in this work. These are expressions of four different breakup mechanisms observed in this work.

Drop-on-Demand Breakup

This droplet breakup regime is characterized by an ejection of a single droplet with a diameter equal or slightly bigger than the nozzle diameter. The ejected droplet can be followed by smaller satellite droplets or a tail which could also disperse into single satellite droplets after a while. In such a system the droplet can be ejected on demand which means that every actuation pulse produces one single droplet. The required actuation for such a droplet breakup should provide a fast actuation, if possible with a counter movement to enforce the droplet breakup. The actuation force should be strong enough to overcome the capillary forces substantially.

Jet-on-Demand Breakup

The jet-on-demand regime is similar to the drop-on-demand regime with the main difference that a jet is ejected rather than a single droplet. However, this jet could possibly also disperse into single droplets after the jet tear off. Nevertheless, the ejected volume is much bigger compared to single droplets produced in drop-on-demand mode. But the ejected jet is still on demand which means that also in this case every actuation pulse produces one single jet. Compared to the drop-on-demand breakup the actuation takes a bit longer which leads to the jet.

Rayleigh Breakup

The Rayleigh breakup is rather a continuous mode than an on-demand mode which means that a liquid jet is ejected out of a nozzle continuously. This jet disperses into single droplets due to the so called Rayleigh instability after a certain distance from the nozzle. This Rayleigh instability is either caused by naturally occurring disturbances

on the jet or by additionally applied external disturbances. In this case the droplet volume almost only depends on the nozzle diameter. The actuation has to be applied much longer compared to the on-demand modes and can be relatively small.

ATOMIZATION BREAKUP

The atomization breakup is mainly characterized by a liquid high speed jet which disperses into a fine spray of many single droplets directly behind the nozzle exit. Further characteristic is the arising spray cone so that the droplet trajectory is not inevitably in line with the nozzle. The ejected droplets usually exhibit a droplet size distribution rather than a constant droplet volume. The actuation is continuously and very strong which leads to very high velocities inside the nozzle.

2 FUNDAMENTALS OF FLUID DYNAMICS

In this chapter some of the fundamental equations of fluid dynamics theory are presented. First of all, the main equations for the fluid flow, the Navier-Stokes equation, the continuity equation and the energy equation are named. Furthermore, the Young-Laplace equation is discussed describing the capillary pressure due to surface forces. This is important for the calculation of free surfaces like for capillary filling or droplet ejection problems. This set of differential equations is sufficient to completely describe the fluid dynamics of a droplet ejection process. Hence, these equations are the basis of an analytical description of any kind of droplet formation. Based on these essential expressions like the fluidic resistance, inertance, capacitance, the outflow out of a nozzle, the inlet resistance and junction effects are derived using analytical solutions for selected boundary conditions. Finally, two approaches for fluidic simulations are presented, equivalent electrical network models and computational fluid dynamic (CFD) simulations. Additionally, three important characteristic numbers for the fluid flow in micro dimensions and the droplet formation are introduced: the Reynolds number, the Weber number and the Ohnesorge number. These dimensionless numbers represent relationships of two different kinds of energy, respectively. The numbers quantifies which of the energies is dominating the flow situation.

2.1 NAVIER-STOKES, CONTINUITY AND ENERGY CONSERVATION EQUATIONS

The governing equations of fluid flow represent mathematical statements of the conservation laws of physics, which are the momentum conservation, the mass conservation and the energy conservation. These three laws are represented by the Navier-Stokes equation, the continuity equation and the energy conservation equation, respectively. These equations are nonlinear partial differential equations like described in the next section.

2.1.1 NAVIER-STOKES EQUATION

The Navier-Stokes equation is the momentum equation for an infinitesimal continuum element *dV* according to Newton's second law. It accounts for surface forces, viscous forces and body forces like gravity, centrifugal, Coriolis or electromagnetic forces. These forces are balanced for the continuum element *dV*. Thus the Navier-Stokes equation can be considered as an extension of the Euler equation by adding the viscous forces due to internal friction [86]. It is valid for stationary as well as for transient

problems. For a Newtonian fluid with constant viscosity η and constant density ρ under isothermal conditions (T = constant) the three vector components of the Navier-Stokes equation can be written in a cartesian coordinate (x, y, z) system:

x component

$$\rho\left(\frac{\partial v_x}{\partial t} + v_x \frac{\partial v_x}{\partial x} + v_y \frac{\partial v_x}{\partial y} + v_z \frac{\partial v_x}{\partial z}\right) = -\frac{\partial p}{\partial x} + \eta\left(\frac{\partial^2 v_x}{\partial x^2} + \frac{\partial^2 v_x}{\partial y^2} + \frac{\partial^2 v_x}{\partial z^2}\right) + \rho f_{\text{body,x}}, \quad (2.1)$$

y component

$$\rho\left(\frac{\partial v_y}{\partial t} + v_x \frac{\partial v_y}{\partial x} + v_y \frac{\partial v_y}{\partial y} + v_z \frac{\partial v_y}{\partial z}\right) = -\frac{\partial p}{\partial y} + \eta\left(\frac{\partial^2 v_y}{\partial x^2} + \frac{\partial^2 v_y}{\partial y^2} + \frac{\partial^2 v_y}{\partial z^2}\right) + \rho f_{\text{body,y}}, \quad (2.2)$$

z component

$$\rho\left(\frac{\partial v_z}{\partial t} + v_x \frac{\partial v_z}{\partial x} + v_y \frac{\partial v_z}{\partial y} + v_z \frac{\partial v_z}{\partial z}\right) = -\frac{\partial p}{\partial z} + \eta\left(\frac{\partial^2 v_z}{\partial x^2} + \frac{\partial^2 v_z}{\partial y^2} + \frac{\partial^2 v_z}{\partial z^2}\right) + \rho f_{\text{body,z}}, \quad (2.3)$$

which can also be written in vector notation:

$$\rho \cdot \left[\frac{\partial \vec{v}}{\partial t} + (\vec{v} \cdot \nabla)\vec{v}\right] = -\nabla p + \eta \nabla^2 \vec{v} + \rho \overrightarrow{f_{\text{body}}}. \quad (2.4)$$

This consists of five terms:

- $\partial \vec{v} / \partial t$ is the transient term.
  The partial time derivative considers the momentum change due to the change in velocity of a continuum element observed at a fixed position.
- $(\vec{v} \cdot \nabla)\vec{v}$ is the convective term.
  It embodies the acceleration of a fluid element experienced while moving to a region of deviating velocity during the time *dt*. If this part is missing, the remaining equation is called the "diffusion equation".
- $\eta \nabla^2 \vec{v}$ is the viscosity term.
  It reflects the inner friction of the fluid. In this form it is only valid for Newtonian fluids where the viscosity is proportional to the shear rate. If this part is missing, the remaining equation is called "equation of convection" or "Euler equation".
- $\rho \overrightarrow{f_{\text{body}}}$ describes the body force term.
  It represents the forces acting on a fluid element, for example gravity, centrifugal, Coriolis, or electromagnetic forces. If the body force is caused only by gravity it is neglectible in systems with dimensions in the micro scale.

- $-\nabla p$ is the pressure gradient.
  It represents the pressure force density in anti parallel direction to the pressure gradient ∇p in the direction of declining pressure.
- Both terms $\rho \overrightarrow{f_{\text{body}}}$ and $-\nabla p$ together are called source terms, resulting from force impact.

The convection term $(\vec{v} \cdot \nabla)\vec{v}$ makes the Navier-Stokes equation a nonlinear second order differential equation that can only be solved for simple cases analytically.

For the analytical consideration of droplet ejection the notation of the Navier-Stokes equation in a cylindrical coordinate system (r, z, θ) is generally more appropriate. For Newtonian fluids under isothermal conditions it yields [87]:

radial component r

$$\rho\left(\frac{\partial v_r}{\partial t} + v_r \frac{\partial v_r}{\partial r} - \frac{v_\theta^2}{r} + v_z \frac{\partial v_r}{\partial z}\right) = -\frac{\partial p}{\partial r} + \eta\left(\frac{\partial}{\partial r}\left[\frac{1}{r}\frac{\partial}{\partial r}(r\, v_r)\right] + \frac{\partial^2 v_r}{\partial z^2}\right), \quad (2.5)$$

height component z

$$\rho\left(\frac{\partial v_z}{\partial t} + v_r \frac{\partial v_z}{\partial r} + v_z \frac{\partial v_z}{\partial z}\right) = -\frac{\partial p}{\partial z} + \eta\left(\frac{1}{r}\frac{\partial}{\partial r}\left[r\frac{\partial v_z}{\partial r}\right] + \frac{\partial^2 v_z}{\partial z^2}\right) + \rho f_{\text{body,z}}\,, \quad (2.6)$$

azimuthal component θ

$$\rho\left(\frac{\partial v_\theta}{\partial t} + u_r \frac{\partial v_\theta}{\partial r} + \frac{v_r v_\theta}{r} + v_z \frac{\partial v_\theta}{\partial z}\right) = \eta\left(\frac{\partial}{\partial r}\left[\frac{1}{r}\frac{\partial}{\partial r}(r\, v_\theta)\right] + \frac{\partial^2 v_\theta}{\partial z^2}\right) \quad . \quad (2.7)$$

If additionally an axisymmetric behavior along the z axis can be assumed - which is justified in most considered cases - the azimuthal component θ can be neglected. This simplifies the above presented Navier-Stokes equation in a cylindrical coordinate system (r, z, θ) for Newtonian fluids under isothermal conditions to [57-61]:

radial component r

$$\rho\left(\frac{\partial v_r}{\partial t} + v_r \frac{\partial v_r}{\partial r} + v_z \frac{\partial v_r}{\partial z}\right) = -\frac{\partial p}{\partial r} + \eta\left(\frac{\partial}{\partial r}\left[\frac{1}{r}\frac{\partial}{\partial r}(r\, v_r)\right] + \frac{\partial^2 v_r}{\partial z^2}\right), \quad (2.8)$$

height component z

$$\rho\left(\frac{\partial v_z}{\partial t} + v_r \frac{\partial v_z}{\partial r} + v_z \frac{\partial v_z}{\partial z}\right) = -\frac{\partial p}{\partial z} + \eta\left(\frac{1}{r}\frac{\partial}{\partial r}\left[r\frac{\partial v_z}{\partial r}\right] + \frac{\partial^2 v_z}{\partial z^2}\right) + \rho f_{\text{body,z}}\,. \quad (2.9)$$

SIMPLIFICATIONS FOR MICROFLUIDIC SYSTEMS

For incompressible fluids in microfluidic systems some approximations are justified to simplify the Navier-Stokes equation.

- The inertia term $\rho(\vec{v} \cdot \nabla)\vec{v}$ and the transient term $\partial\vec{v}/\partial t$ can be neglected assuming stationary and fully developed flow conditions.
- If the body forces $\rho \overrightarrow{f_{\text{body}}}$ only consist of the gravity force, it can be neglected in microfluidic systems [88].

If these assumptions can be applied, this leads to the simplified Navier-Stokes equation, the so called Poisson equation:

$$\frac{\nabla p}{\eta} = \nabla^2 \vec{v}. \tag{2.10}$$

Another possibility to simplify the Navier-Stokes equation is given if the following assumptions are valid:

- If, in contrast to the previous simplification, the inertia term $\rho(\vec{v} \cdot \nabla)\vec{v}$ can not be neglected.
- But, instead of that, the viscosity term $\eta\nabla^2\vec{v}$ can be neglected assuming a frictionless flow ($\eta = 0$).
- And again, a stationary flow ($\partial\vec{v}/\partial t = 0$) is assumed.
- And also the volume forces $\rho \overrightarrow{f_{\text{body}}}$ are neglected.

If these assumptions hold the Bernoulli equation can be deduced from the Navier-Stokes equation [88]:

$$p + \frac{\rho}{2} v^2 = \text{const.}. \tag{2.11}$$

However, both the Poisson as well as the Bernoulli equation assume a stationary flow which is not the case for a dynamic droplet ejection. Hence, these simplifications can be applied for simple stationary flows like for example in channels but not for an unsteady droplet ejection process.

2.1.2 CONTINUITY EQUATION

The continuity equation describes the mass conservation inside a volume element. The in streaming mass and the out streaming mass are balanced [89]:

$$\frac{\partial\rho}{\partial t} + \frac{\partial(\rho v_x)}{\partial x} + \frac{\partial(\rho v_y)}{\partial y} + \frac{\partial(\rho v_z)}{\partial z} = 0, \tag{2.12}$$

or in more compact vector notation:

$$\frac{\partial \rho}{\partial t} + \mathrm{div}(\rho \vec{v}) = 0 . \tag{2.13}$$

For an incompressible fluid the density ρ is constant and equation (2.12) becomes:

$$\frac{\partial v_x}{\partial x} + \frac{\partial v_y}{\partial y} + \frac{\partial v_z}{\partial z} = 0 , \tag{2.14}$$

or in vector notation:

$$\mathrm{div}\ \vec{v} = 0 . \tag{2.15}$$

This can also be written in a cylindrical coordinate system (r, z, θ) for Newtonian fluids under isothermal conditions which is again the more important notation if a axisymmetric behavior of a droplet ejection is considered [87]:

$$\frac{\partial v_z}{\partial z} + \frac{1}{r} \frac{\partial (r\ v_r)}{\partial r} = 0 . \tag{2.16}$$

2.1.3 Energy Conservation Equation

For non isothermal conditions one has to add the energy conservation equation resulting from the thermodynamics. Because only isothermal calculations will be done in this work, the energy equation is only presented for completeness. The energy equation provides a differential equation for the temperature distribution consisting of a balance of heat and mechanical energy [90]:

$$\rho \frac{\partial e}{\partial t} + p \cdot \nabla \vec{v} = \nabla (k\ \nabla T) + \phi , \tag{2.17}$$

where the single expressions have the following definition:

- $\frac{\partial e}{\partial t}$ is the change of the inner energy.
- $p \cdot \nabla \vec{v}$ is the work due to expansion or compression.
- $\nabla (k\ \nabla T)$ is the heat input due to thermal conductivity.
- ϕ is the source term.

2.2 YOUNG-LAPLACE EQUATION

The Young-Laplace equation describes the capillary pressure generated by a curved surface. This pressure is of increasing importance when scaling down the system into micro dimensions like in microfluidic systems. On a plain interface no vertical pressure relative to the surface occurs since all surface tension forces only act in plane and do not have orthogonal components. At curved interfaces like at menisci or droplets on a surface, a normal force vertical to the curved interface occurs. This force causes an interfacial pressure, so called capillary pressure [91-94].

Considering a curved interface element with the length of the edges ds_1 and ds_2, the curvature angles ϑ_1 and ϑ_2 and with the both curvature radii R_1 and R_2 like displayed in figure 2.1 where R_1 and R_2 are the mean curvature radii, i.e. the minimum and maximum radius of the curved interface element [95]. Usually the minimum and maximum radius of the curved interface element are perpendicular. In the special case of an ejected jet the maximum radius is the curvature of the jet along its trajectory whereas the minimum radius is the radius of the jet cross section itself. Using this the following equilibrium approach between the capillary pressure Δp_{cap} and the surface tension σ with the normal force to the surface dF_n can be derived:

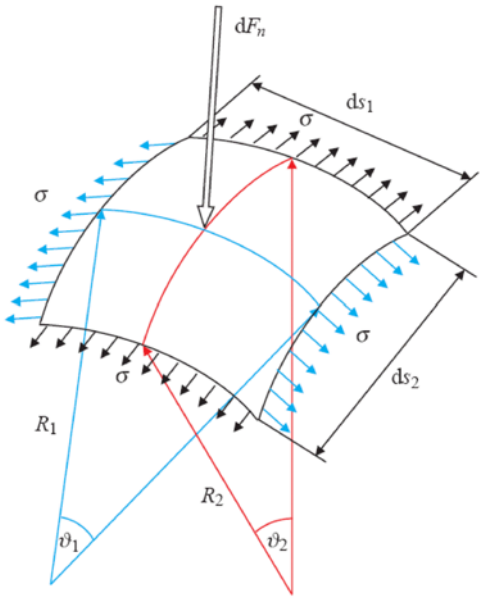

Figure 2.1: *Sketch for the derivation of the capillary pressure. With the normal force to the surface dF_n, the surface tension σ, the curvature angles ϑ_1 and ϑ_2, the curvature radii R_1 and R_2, and the side lengths ds_1 and ds_2 [96].*

$$dF_n = \Delta p_{cap} \cdot ds_1 \cdot ds_2 = \sigma \cdot ds_2 \cdot \vartheta_1 + \sigma \cdot ds_1 \cdot \vartheta_2, \tag{2.18}$$

and with the both curvature angles $\vartheta_1 = \frac{ds_1}{R_1}$ and $\vartheta_2 = \frac{ds_2}{R_2}$:

$$\Delta p_{cap} \cdot ds_1 \cdot ds_2 = \sigma \cdot ds_2 \cdot \frac{ds_1}{R_1} + \sigma \cdot ds_1 \cdot \frac{ds_2}{R_2} \tag{2.19}$$

$$\Rightarrow \quad \Delta p_{cap} = \sigma \cdot \left(\frac{1}{R_1} + \frac{1}{R_2} \right). \tag{2.20}$$

According to this the capillary pressure Δp_{cap} of a spherical droplet with radius R is:

$$\Delta p_{cap} = \frac{2 \cdot \sigma}{R}. \tag{2.21}$$

Considering a liquid droplet on a solid surface surrounded by gas three surface tensions are dominating. σ_{gs} is the surface tension between gas and solid phase, σ_{ls} is the surface tension between liquid and solid phase and σ_{lg} is the surface tension between liquid and gas phase. The liquid surface forms a contact angle Θ with the solid. The surface tensions indicate an equilibrium at the contact point of the three phases which can be expressed [91]:

$$\sigma_{gs} - \sigma_{ls} = \sigma_{lg} \cdot \cos \Theta \tag{2.22}$$

$$\Rightarrow \quad \cos \Theta = \frac{\sigma_{gs} - \sigma_{ls}}{\sigma_{lg}}. \tag{2.23}$$

Therewith two different domains can be distinguished:

- $\sigma_{gs} > \sigma_{ls}$, wetting (hydrophilic) surface, contact angle $\Theta < 90°$.
- $\sigma_{gs} < \sigma_{ls}$, non-wetting (hydrophobic) surface, contact angle $\Theta > 90°$.

Considering this the determination of the capillary pressure in a fluidic channel with radius R and contact angle $\Theta > 0°$, Δp_{cap} has to be adapted to [91]:

$$\Delta p_{cap} = \frac{2 \cdot \sigma}{R} \cdot \cos \Theta. \tag{2.24}$$

Conclusively of section 2.1 and 2.2 the set of differential equations which are relevant for the droplet formation in the micro scale are summarized in the following. Furthermore, following approximations are applied to simplify the set of differential equations as far as possible: The density ρ as well as the viscosity η are assumed to be constant. For the Navier-Stokes equation an axisymmetric behavior is assumed so that the azimuthal component θ can be neglected. Additionally, the volume forces $\rho \overrightarrow{f_{body}}$ are neglected because no gravity or other body forces occur in the considered devices. The energy equation can be neglected completely because only isothermal calculations will be done in this work. Finally, this leads to the relevant set of differential equations:

NAVIER-STOKES EQUATION

radial component r

$$\rho\left(\frac{\partial v_r}{\partial t} + v_r \frac{\partial v_r}{\partial r} + v_z \frac{\partial v_r}{\partial z}\right) = -\frac{\partial p}{\partial r} + \eta\left(\frac{\partial}{\partial r}\left[\frac{1}{r}\frac{\partial}{\partial r}(r\, v_r)\right] + \frac{\partial^2 v_r}{\partial z^2}\right), \tag{2.25}$$

height component z

$$\rho\left(\frac{\partial v_z}{\partial t} + v_r \frac{\partial v_z}{\partial r} + v_z \frac{\partial v_z}{\partial z}\right) = -\frac{\partial p}{\partial z} + \eta\left(\frac{1}{r}\frac{\partial}{\partial r}\left[r\frac{\partial v_z}{\partial r}\right] + \frac{\partial^2 v_z}{\partial z^2}\right) + \rho f_{\text{body,z}} \,. \tag{2.26}$$

CONTINUITY EQUATION

$$\frac{\partial v_z}{\partial z} + \frac{1}{r}\frac{\partial (r\, v_r)}{\partial r} = 0 \,. \tag{2.27}$$

YOUNG-LAPLACE EQUATION

$$\Delta p_{\text{cap}} = \frac{2 \cdot \sigma}{R} \cdot \cos\,\Theta \,. \tag{2.28}$$

This set of differential equations is typically sufficient to completely describe the fluid dynamics of a droplet ejection from a circular nozzle.

2.3 CHARACTERISTIC NUMBERS FOR DROPLET FORMATION

Apart from the governing equations of fluid flow also characteristic dimensionless numbers are used to describe the fluid flow in micro dimensions and the droplet formation qualitatively. Dimensionless numbers are based either on a given geometrical or physical affinity. A geometrical affinity is present through equal proportionality between spatial dimensions like lengths, areas or volumes, or surface roughnesses. A physical affinity is present through equal proportionality between mechanical quantities like time, distance, velocity, force, energy, etc., or material properties like density, viscosity, surface tension, etc. [86]. Dimensionless numbers can be deduced either by a dimensional analysis mainly based on the Π-theorem [86,97,98] or by a comparison of similar quantities. The Π-theorem makes use of the condition that characteristic numbers are the dimensionless product of various dimensional quantities. When comparing two different quantities the unities are vanishing. Hence, the relationship of both quantities can be described in a dimensionless manner. The advantage of dimensionless numbers is that a physical behavior can easily be expressed by a simple number. In our case the characteristic numbers represent the relationship of two different energies, respectively. Hence, the numbers quantifies

which of the energies is the dominant one. The Weber number for example indicates whether the kinetic or the surface tension energy is dominant during a droplet formation, whereas the Ohnesorge number represents the ratio of internal viscosity dissipation to the surface tension force. Furthermore, the Reynolds number will be introduced which is important to distinguish between the mostly occurring laminar flow in microfluidic systems and turbulent flow. Since laminar flow is a requirement for the fluidic network elements to be used, the Reynolds number is also introduced.

2.3.1 REYNOLDS NUMBER

The Reynolds number describes the relation between the dynamic pressure force and the viscous force. It can also be derived by the geometrical affinity of the relations of the inertial energy E_{kinetic} and the viscous dissipation E_{viscous} [80,86,99,100]:

$$Re \sim \frac{E_{\text{kinetic}}}{E_{\text{viscous}}} = \frac{1/2 \cdot m \cdot v^2}{2 \cdot \eta \cdot v \cdot V/l} = \frac{1}{4} \cdot \frac{\rho \cdot v \cdot l}{\eta} \tag{2.29}$$

$$\Rightarrow \quad Re = \frac{\rho \cdot v \cdot l}{\eta}. \tag{2.30}$$

In general, three flow regimes can be distinguished which lead to characteristic flow conditions.

- Creeping flow regime: For $Re < 1$, the nonlinear term $\rho(\vec{v} \cdot \nabla)\vec{v}$ of the Navier-Stokes equation can be neglected. This case is usually referred to as creeping flow. The flow characteristics are determined by viscous forces and the pressure gradient $-\nabla p$ in the Navier-Stokes equation.
- Intermediate flow regime: For $1 < Re < 2300$, the nonlinear term of the Navier-Stokes equation becomes increasingly important. The flow structure can be considered as creeping flow superimposed with the so called secondary flow.
- Turbulent flow regime: For $Re > 2300$, the velocity fluctuates in magnitude and direction over time. The flow is instationary and chaotic.

The creeping flow regime and the intermediate flow regime are generally called laminar flow regime. In microfluidics typically small channel dimensions and low velocities are present leading to flow conditions in the laminar flow regime. Rewriting the Navier-Stokes equation in a dimensionless manner indicates that the Reynolds number determines the dynamics of momentum equation if the Reynolds number is small and the gravity can be neglected [86].

2.3.2 WEBER NUMBER

The dimensionless Weber number represents the ratio of disruptive hydrodynamic forces to the stabilizing surface tension force. Hence, the Weber number indicates whether the kinetic or the surface tension energy is dominant [99-107]. For a spherical droplet the Weber number can be derived using the kinetic energy E_{kinetic} compared to the surface energy E_{surface}:

$$We \sim \frac{E_{\text{kinetic}}}{E_{\text{surface}}} = \frac{1/2 \cdot m \cdot v^2}{A_{\text{droplet}} \cdot \sigma} = \frac{1/12 \cdot \rho \cdot D^3 \cdot \pi \cdot v^2}{D^2 \cdot \pi \cdot \sigma} = \frac{1}{12} \cdot \frac{\rho \cdot D \cdot v^2}{\sigma} \quad (2.31)$$

$$\Rightarrow \quad We = \frac{\rho \cdot D \cdot v^2}{\sigma}. \quad (2.32)$$

Where v is the velocity of the liquid and D is a characteristic length. For droplet ejection processes they correspond to the velocity at the nozzle outlet and the nozzle diameter, respectively.

The Weber number can be used for two different declarations. On the one hand it describes whether a droplet can leave a nozzle at all due to higher kinetic energy compared to surface energy. On the other hand it can describe whether a droplet has the tendency for splashing when the kinetic energy is released at the impact on a surface.

The higher the Weber number the more dominant is the kinetic energy. This means that most of the inserted energy converts into kinetic energy, i.e. an ejected droplet is faster with higher Weber number. The lower the Weber number the more dominant is the surface tension energy. This means that most of the inserted energy converts into surface tension energy, i.e. a droplet formation is critical or even impossible. In figure 2.2 two examples for a high and a low Weber number are displayed, respectively. The high Weber number of 17.4 leads to a fast droplet ejection whereas a low Weber number of 7.9 leads to a pending droplet not overcoming the surface tension. The used contact angle for both simulations was $\Theta = 40°$ (as of silicon). The slow increase of the pending droplet in the second case leads to an increasing wetting of the surface surrounding the nozzle.

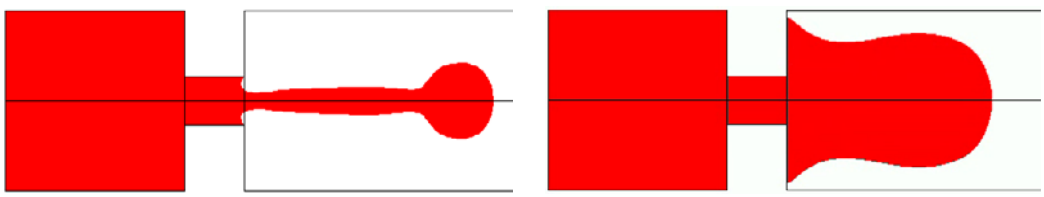

Figure 2.2: *Simulated droplet ejection with a) a high Weber number of 17.4 and b) a low Weber number of 7.9.*

2.3.3 OHNESORGE NUMBER

The shortcoming of the Weber number is its independence of the viscosity of the fluid. Therefore the Weber number is not adequate to distinguish between low or high viscous fluids. But it is well known that viscosity has a considerable effect on the droplet formation process (see chapter 3 for details). For example increasing the liquid viscosity delays the onset of a droplet breakup [106]. To account for the liquid viscosity in droplet formation, the appropriate nondimensional number is the Ohnesorge number which represents the ratio of internal viscosity dissipation to the surface tension energy [87,99,105-108]. The Ohnesorge number may be written in terms of the Reynolds and Weber number:

$$On = \frac{\sqrt{We}}{Re} = \frac{\eta}{\sqrt{\rho \cdot D \cdot \sigma}}. \tag{2.33}$$

The Ohnesorge number is sometimes also referred to as stability number, viscosity number, Laplace number, or Z number [87,99]. It is independent on the velocity and therefore only adequate to describe droplet ejection in conjunction with the Weber number.

The lower the Ohnesorge number the weaker are the friction losses due to viscous forces. This means that most of the inserted energy converts into surface tension energy, i.e. a droplet can be formed. The higher the Ohnesorge number the more dominant is the internal viscous dissipation. This means that most of the inserted energy converts into internal viscous dissipation, i.e. that a droplet formation is critical or even impossible. In figure 2.3 four examples of simulated droplet breakup with increasing Ohnesorge number are displayed. The pictures are taken at the same time. The low Ohnesorge number of 0.066 leads to an ejection of single droplets, an Ohnesorge number of 0.656 leads to single droplets with small tails and higher Ohnesorge numbers of 1.312 and 1.967 lead to connected droplets with increasing thickness of the tail segments in between. The corresponding Weber number is 17.4 for all four cases.

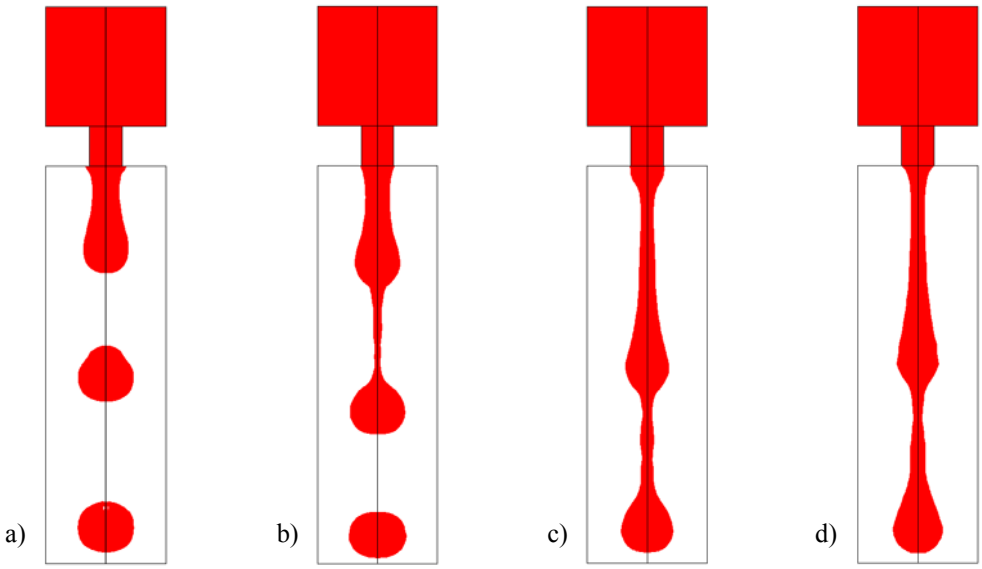

Figure 2.3: *Simulated droplet ejection with a) a low Ohnesorge number of 0.066, b) an Ohnesorge number of 0.656, c) an Ohnesorge number of 1.312 and d) a high Ohnesorge number of 1.967.*

2.4 Analytical Solutions for Selected Boundary Conditions

In the following section some analytical solutions of the Navier-Stokes equation for selected boundary conditions and simplifying assumptions are presented. The approximative solutions can be applied to describe simple fluidic components like fluidic resistance, fluidic inertance, fluidic capacitance, outflow out of a nozzle, inlet resistance, or junction effects. Such components are required to built equivalent fluidic networks for more complicated fluidic systems.

2.4.1 Fluidic Resistance

A pressure driven stationary flow of a Newtonian fluid under isothermal conditions through a cylindrical tube with radius R leads to a parabolic flow profile depending on the radius r. This cylindrical symmetric velocity profile $v(r)$ can be obtained by equating the pressure force with the viscous force [109]:

$$v(r) = \frac{\Delta p}{4 \cdot l \cdot \eta} \cdot (R^2 - r^2), \tag{2.34}$$

The volume flow Φ_V through this tube with parabolic velocity profile can be obtained by integration of $v(r)$ over the radius of the tube R. The result is known as the Hagen-Poiseuille law.

$$\Phi_v = \frac{dV}{dt} = \int_0^R v(r)\, 2\pi r\, dt = \frac{\pi \cdot \Delta p}{2 \cdot \eta \cdot l} \left(\int_0^R R^2 r\, dr - \int_0^R r^3\, dr \right) \tag{2.35}$$

$$\Rightarrow \qquad \Phi_v = \frac{\pi}{8\eta} \cdot \frac{\Delta p}{l} \cdot R^4 . \tag{2.36}$$

In analogy to the electrical resistance $R_{el} = U_{el}/I_{el}$, the fluidic resistance R_{hd} can be motivated by using the following substitutions:

- $R_{el} \Leftrightarrow R_{hd}$
- voltage $U_{el} \Leftrightarrow$ pressure gradient Δp
- current $I_{el} \Leftrightarrow$ volume flow Φ_v

Thus a fluidic equivalent to Ohm's law can be deduced from equation (2.36):

$$R_{hd} = \frac{\Delta p}{\Phi_v} = \frac{8 \cdot \eta \cdot l}{\pi \cdot R^4} . \tag{2.37}$$

As this formula is only valid for cylindrical tubes, a transformation must be performed to describe arbitrary cross sections. This transformation maps any given geometry into an equivalent cylindrical cross section. The general equation for the fluidic resistance can be written as:

$$R_{hd} = C_{geometry} \cdot \frac{\eta \cdot l}{A^2} , \tag{2.38}$$

where $C_{geometry}$ is a constant depending on the shape of the cross section and A is the area of the cross section. For example $C_{geometry}$ is 8π for a circular cross section and $8(1+\alpha)^2/\alpha$ for a rectangular cross section, where α is the ratio of the both edges of the rectangle [86].

2.4.2 Fluidic Inertance

So far only steady flows have been considered. However, many microfluidic devices are actuated by a periodic driving force, e.g. a microdisplacement pump. While studying these devices, often the question arises how fast the fluid adjusts to a pressure change. The physical background of a possible phase shift between the force and the system response roots in the inertial mass of the liquid.

Again making the assumptions of a laminar Hagen-Poiseuille velocity profile $v(r)$ in a circular tube with radius R, length l and cross section A, driven by a pressure gradient Δp, the acceleration $a(r)$ can be determined to be [88]:

$$a(r) = \frac{dv(r)}{dt} = \frac{dF}{dm} = \frac{\Delta p\, dA}{\rho \cdot l\, dA} = \frac{\Delta p}{\rho \cdot l} = \text{const.} . \tag{2.39}$$

The acceleration a is independent of the radius r, i.e. a is constant across the whole channel. Thus the force F on an infinitesimal element of mass dm can be calculated:

$$F = A\,\Delta p = \frac{d(mv)}{dt} = \frac{d(\rho l A v)}{dt} = \rho l \cdot \frac{d(Av)}{dt} = \rho l \cdot \frac{d\Phi_v}{dt}. \tag{2.40}$$

The fluidic law of inertance is obtained from equation (2.40):

$$L_{hd} = \rho \cdot \frac{l}{A}. \tag{2.41}$$

Using again the electrical analogy the fluidic inertance can be defined as:

$$\Delta p = L_{hd} \cdot \frac{d\Phi_v}{dt}. \tag{2.42}$$

2.4.3 Fluidic Capacitance

Like in electric circuits the capacitance also decisively determines the dynamic behavior of a fluidic system. Fluidic capacitances in a microfluidic system can be caused by intentionally inserted elastic components like membranes or tubes, but also non desired effects like compressible fluids or a gas bubble trapped in a fluidic channel can yield fluidic capacitances. Upon application of a pressure they can intermediately store a liquid volume which is later released when the pressure is released. Fluidic capacitances thus convert kinetic flow energy into potential energy.

For a maintained fixed volume V_0 the mass storage or mass flow Φ_v by compression of fluid can be induced by a finite compressibility κ [88]:

$$\Phi_v = \frac{dV}{dt} = \frac{dV}{dp}\frac{dp}{dt} = V_0 \kappa \frac{dp}{dt} = C_{hd} \cdot \frac{dp}{dt}, \tag{2.43}$$

with the fluidic capacitance C_{hd} again being defined analog to the electrical capacitance:

$$C_{hd} = V_0 \cdot \kappa. \tag{2.44}$$

For elastic components like membranes the volume cannot be kept constant. The amount of liquid volume stored in the elastic component ΔV certainly depends on Δp. In a linear system or for small deformations it can be estimated by [88]:

$$\Delta V \overset{\text{def}}{=} C_{hd} \cdot \Delta p \ . \tag{2.45}$$

In this case the volume flow rate can be calculated:

$$\Phi_v = \frac{dV}{dt} = C_{hd} \cdot \frac{dp}{dt}. \tag{2.46}$$

2.4.4 OUTFLOW OUT OF A NOZZLE

The outflow out of a vessel or tube with cross section area A_{in} via a nozzle with cross section area A_{out} and an infinitely short length due to an over pressure in the vessel like it is displayed in figure 2.4 can be derived similar to the equation of Torricelli which is valid for the outflow due to an altitude difference.

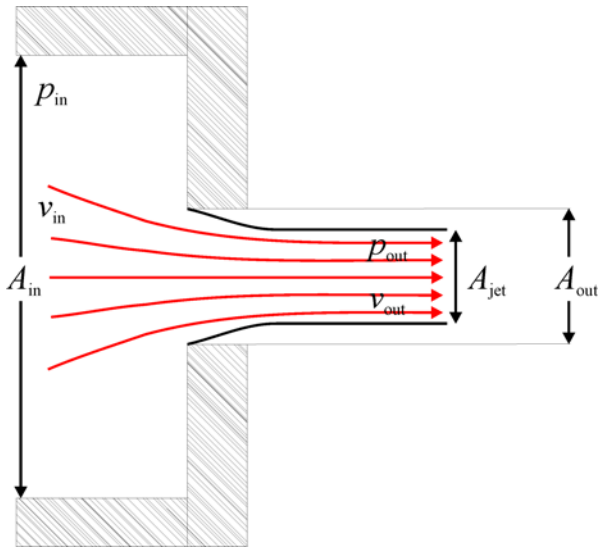

Figure 2.4: *Schematic drawing of the outflow out of a vessel or tube with cross section area A_{in}, pressure p_{in} and velocity v_{in} via a nozzle with cross section area A_{out}, pressure p_{out} and velocity v_{out}.*

The formula for the outflow out of a nozzle can also be applied for approximating the droplet ejection. The resulting resistance due to the outflow out of a nozzle has to be taken into account for every analytical approach describing a droplet formation. The Bernoulli equation (2.11) yields [91]:

$$\frac{p_{in}}{\rho \cdot g} + \frac{v_{in}^2}{2 \cdot g} = \frac{p_{out}}{\rho \cdot g} + \frac{v_{out}^2}{2 \cdot g}, \tag{2.47}$$

where p is the pressure, v is the velocity and g is the normal earth acceleration. The index "in" means the inside of the system, hence, the parameters inside the vessel or tube, whereas "out" means the outside of the system, hence, the parameters at the nozzle or inside the jet. Using the continuity equation:

$$A_{in} \cdot v_{in} = A_{out} \cdot v_{out}, \tag{2.48}$$

leads to the outflow velocity:

$$\frac{p_{in} - p_{out}}{\rho \cdot g} = \frac{v_{out}^2}{2 \cdot g} \cdot \left(1 - \frac{A_{out}^2}{A_{in}^2}\right), \tag{2.49}$$

$$v_{out} = \sqrt{\frac{2 \cdot \Delta p / \rho}{1 - A_{out}^2 / A_{in}^2}}. \tag{2.50}$$

This expression is only valid for large Weber numbers respectively large velocities because the jet has to be fully developed to get an outflow velocity. Nevertheless it can also be used for droplet ejection approximately.

Experimentally determined outflow velocities are generally lower due to friction losses at the nozzle. These losses lead to a reduction of the outflow velocity. An empirically determined velocity coefficient $0 \le \varphi \le 1$ which only depends on the shape of the nozzle can be introduced in equation (2.50) to compensate for this [91]:

$$v_{out,r} = \varphi \cdot v_{out} = \varphi \cdot \sqrt{\frac{2 \cdot \Delta p / \rho}{1 - A_{out}^2 / A_{in}^2}}. \tag{2.51}$$

The theoretical out streaming volume flow $\Phi_{v,th}$ can be calculated with $\Phi_{v,th} = v_{out,r} \cdot A_{out}$. However, the real out streaming volume flow Φ_v is smaller because of the contraction of the jet at the nozzle outlet as a result of the deflection of the stream lines inside the nozzle. The size of the contraction can be described by the empirically determined contraction number $0 \le \alpha \le 1$ which is also depending on the shape of the nozzle [91]:

$$\alpha = \frac{\text{jet cross section}}{\text{nozzle cross section}} = \frac{A_{jet}}{A_{out}}. \tag{2.52}$$

By introducing the outflow number μ which is the product of the velocity coefficient φ and the contraction number α, leads to the empirical volume flow:

$$\Phi_v = \varphi \cdot \alpha \cdot A_{out} \cdot v_{out} = \mu \cdot A_{out} \cdot \sqrt{\frac{2 \cdot \Delta p / \rho}{1 - A_{out}^2 / A_{in}^2}}. \tag{2.53}$$

Hence, the resistance $R_{outflow}$ due to the outflow out of a nozzle can be derived:

$$R_{outflow} = \frac{\Delta p}{\Phi_v} = \frac{\rho \cdot (1 - A_{out}^2 / A_{in}^2)}{2 \cdot \mu^2 \cdot A_{out}^2} \cdot \Phi_v. \tag{2.54}$$

2.4.5 Inlet Resistance

The development of the full parabolic flow profile from an ideal flow source takes a certain distance L_{inlet} like it is displayed in figure 2.5. For this distance an additional pressure loss has to be taken into account when L_{inlet} is not much smaller than the total tube length. The entering length L_{inlet} compared to the channel diameter D for a laminar flow only depends on the Reynolds number [86]:

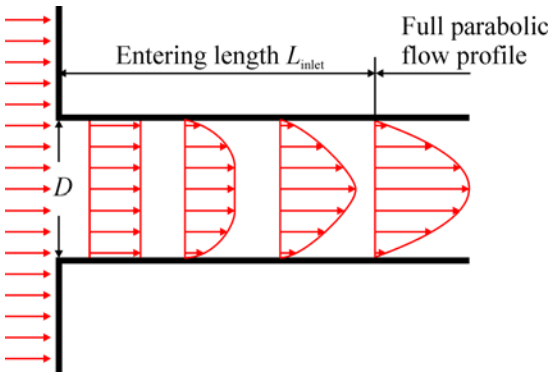

Figure 2.5: *Schematic drawing of the development of the full parabolic flow profile from an ideal flow source which takes a certain distance* L_{inlet}.

$$\frac{L_{inlet}}{D} \approx 0.06 \cdot Re \ . \tag{2.55}$$

The total modified resistance $R_{hd,\,mod}$ which accounts for the entering effect consists of the regular fluidic resistance R_{hd} and an additional nonlinear component depending on the volume flow [90]:

$$R_{hd,\,mod} = R_{hd} + K \cdot \frac{\Phi_v \cdot \rho}{2 \cdot A^2} . \tag{2.56}$$

For fluid channels longer than the entering length $l > L_{inlet}$, K is a constant. For channels with circular cross section $K = 4/3$, for rectangular cross sections K can take on values $0.7 < K < 1.6$, depending on the aspect ratio of the edges of the rectangle [90]. If L_{inlet} is relatively short compared to the length of the entire channel $K \approx 0$.

For channels with a length $l < L_{inlet}$, not allowing for a fully development of the flow profile, the nonlinear resistance can be approximately derived for circular cross sections [90]:

$$R_{hd,\,mod} = 12.2 \cdot \frac{\sqrt{\Phi_v \cdot l \cdot \eta}}{2 \cdot A^2} . \tag{2.57}$$

For rectangular cross sections, where a is the aspect ratio of the both edges of the rectangle, an approximation yields:

$$R_{hd,\,mod} = 7.6 \cdot \frac{a+1}{\sqrt{a}} \cdot \frac{\sqrt{\Phi_v \cdot l \cdot \eta}}{2 \cdot A^2} . \tag{2.58}$$

2.4.6 JUNCTION EFFECTS

In principle there are two different possible junction appearances, the contraction and the expansion of a fluidic flow like it is displayed in figure 2.6. Both contraction as well as expansion lead to an additional pressure loss. However, both pressure losses are not equal which is the reason why such a component can be used as a kind of fluidic diode or flow directing element.

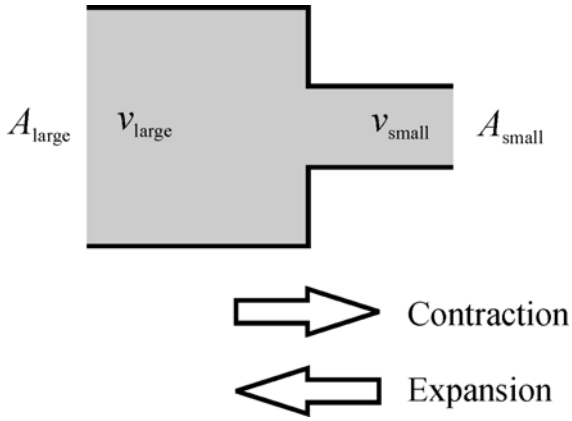

Figure 2.6: *Schematic drawing of the contraction and expansion of a circular channel with cross section areas A_{large} and A_{small}, and velocities v_{large} and v_{small}, respectively.*

CONTRACTION OF THE CROSS SECTION

The resistance of a contraction of the cross section can be derived using the Bernoulli equation (2.11) [90]. The total pressure of the left hand side of the constriction is equal to the total pressure on the right hand side of the constriction. Due to the mass conservation the resistance can be written as [90]:

$$R_{contraction} = \frac{\Phi_v \cdot \rho}{2 \cdot A_{small}^2} \cdot \left(1 + \zeta - \frac{A_{small}^2}{A_{large}^2}\right), \tag{2.59}$$

with the resistance number ζ, depending on the shape of the junction going from $\zeta = 0$ for a smoothly rounded junction to $\zeta = 0.5$ for an angular junction. The resistance is infinite for $A_{small} = 0$ and zero for $A_{small} = A_{large}$.

EXPANSION OF THE CROSS SECTION

The abrupt expansion of the cross section is also known as Borda- or Carnot-push. The resulting flow loss due to the flow release at the junction can be derived using momentum and energy conservation [86]. The resistance can be calculated to [90]:

$$R_{expansion} = \frac{\Phi_v \cdot \rho}{2 \cdot A_{small}^2} \cdot \left(1 - \frac{A_{small}}{A_{large}}\right)^2. \tag{2.60}$$

For example a contraction/expansion component with a two times bigger A_{large} compared to A_{small}, and $\zeta = 0.5$, leads to a contraction resistance which is five times bigger than the corresponding expansion resistance. This means that the flow direction towards the expansion direction experiences a five times smaller fluidic resistance than in the reverse direction. However, the higher the difference between A_{large} and A_{small}, the smaller is the difference of the resistances.

2.5 NETWORK MODELS

Purpose of network models also known as lumped-element models is to describe a fluidic system by an equivalent circuit model. While the full three-dimensional CFD simulation specifies a transient solution on a grid, the network simulation considers a few selected locations ("nodes") only. The intermediate structures are condensed to lumped elements which can be described by distinct transfer functions. Further simplification to a one-dimensional problem results from integrating or averaging involved quantities over the cross section. The network simulation thus deals with scalar quantities evaluated at few selected locations. In electric network simulations these quantities are the potential U and the current I which are preserved according to the relations [88]:

$$\sum_i I_i = 0 \quad \text{at each node}, \tag{2.61}$$

$$\sum_i U_i = 0 \quad \text{along any closed loop}, \tag{2.62}$$

known as Kirchhoff's laws.

A fluidic network can be built from the fluidic components presented in the previous sections and then enforce fluidic equivalents of Kirchhoff's laws to implement the conservation of energy (mesh rule) and mass (nodal equation). The relevant field variables in the Navier-Stokes equation are the pressure and the velocity field.

An essential part of electric as well as fluidic networks is Ohm's law which relates the voltage drop U or pressure drop p across a component to the current I or volume flow Φ_V. The proportionality factor is a complex resistance to evaluate the amplitude and phase shift of the current/flow for a given voltage/pressure. An Ohmic resistance is represented by a real number while an inertance and a capacitance exhibits a 90° phase shift and therefore requires a complex number for representation.

Numerical procedures as implemented in commercial simulation tools like Saber [69] or PSpice [70] to solve the resulting differential equations for the lumped-element network at discrete locations, e.g. via linearization or matrix inversion methods [88]. For more complicated networks containing several single elements, a report, called net

list, of the alignment and the coupling of the network is stored using the Kirchhoff's laws. Therewith, the transfer functions and, hence, the differential equations describing the dynamics of the system are composed.

However, there are still some limits concerning the analogy between fluidic and electric network simulations. While the electrical voltage can have an arbitrary value, there exists no absolute negative fluidic pressure. Another difference is the spreading velocity. The velocity of electrical signals is the speed of light whereas the velocity in fluidic networks is the six order of magnitude lower speed of sound [81,90].

2.6 CFD SIMULATION

Since the Navier-Stokes equation cannot be solved for the majority of problems analytically, numerical methods also known as Computational Fluid Dynamics (CFD) have been developed. This process has been supported by the availability of faster computers, allowing for extensive simulations of fluid dynamics, making the use of CFD common not only for research but also for industrial applications [89,110,111]. Among others the objective of CFD is to solve a given fluid dynamics problem using the full three-dimensional Navier-Stokes equation. Known solution methods are [112]:

- the Finite Volume Method (FVM)
- the Finite Difference Method (FDM)
- the Finite Element Method (FEM)
- the Spectral Element Method (SEM)
- the Lattice-Boltzmann Method (LBM)
- and the Boundary Element Method (BEM)

All of these methods are using numerical approximation procedures based on the discretization of the problem on a computational grid. However, the mainly used method for fluidic problems is the FVM which is also used for all CFD simulations in this work. It is implemented in the commercially available solver CFD-ACE+ from ESI CFD [74] which was used throughout this thesis. Due to this the FVM will be described in more detail in the following.

2.6.1 FINITE VOLUME METHOD

At the beginning of the numerical solution process the solution domain is divided into a number of cells. In each of these cells the momentum, mass and energy conservation, i.e. equations (2.4), (2.15) and (2.17) for the incompressible case, have to be valid. The

discretization of the studied geometry is of essential importance to the whole simulation. It determines the calculation time and the accuracy of the solution. Important attributes of the discretization and the solution algorithm are [89]:

- Consistency: The smaller the grid, the better the approximation.
- Convergence: The solution of the discrete equations leads to an exact solution, if the discretization gets infinitely small.
- Stability: with an appropriate mesh, errors which could cause a wild oscillation or divergence can be damped.
- Conservation: No violation of the conservation equations.
- Constriction: Numerical solutions must be of physical sense (e.g. no negative volumes).

The governing equations (the Navier-Stokes equation, the continuity equation and the energy equation) are numerically integrated over each of the control volumes. As the volume elements fill out the complete solution domain, the conservative attribute is ensured. Every flow coming out of a surface of one finite volume, enters into the adjacent cell. If a general variable ϕ is introduced which can represent scalar quantities like the three velocity components v_x, v_y, v_z, a concentration, a momentum, or a temperature, respectively, the transport equation for the quantity ϕ can be written in a generalized form. Integrating ϕ over a three-dimensional control volume *CV*, which is the key step of the finite volume method, yields the integral form of the general transport equation for property ϕ [89]:

$$\int_{CV} \frac{\partial(\rho\phi)}{\partial t}\, dV + \int_{CV} \mathrm{div}(\rho\phi\vec{v})\, dV = \int_{CV} \mathrm{div}(\Gamma\ \mathrm{grad}\ \phi)\, dV + \int_{CV} S_\phi\, dV\ , \qquad (2.63)$$

where Γ is the diffusion coefficient and S_ϕ is the source term of ϕ. By setting ϕ equal to v_x, v_y, v_z, 1 and inner energy e (or temperature T) and selecting appropriate values for the diffusion coefficient Γ and source terms, special forms for each of the partial differential equations for momentum, mass and energy conservation can be obtained [89]. Hence, this general transport equation has to be solved separately for any required quantity, respectively. The meaning of the four terms in the occurrent succession are [89]:

- The rate of increase of ϕ in the control volume.
- The net rate of flow of ϕ out off the control volume.
- The rate of increase of ϕ due to diffusion inside the control volume.
- The rate of increase of ϕ due to sources inside the control volume.

FINITE DIFFERENCE EQUATIONS

After numerically integrating the terms of equation (2.4), transient term, convection, diffusion and source terms, the discretized equation for the velocity v_x in x-direction at the location P as depicted in figure 2.7 is given by the following linear equation [89]:

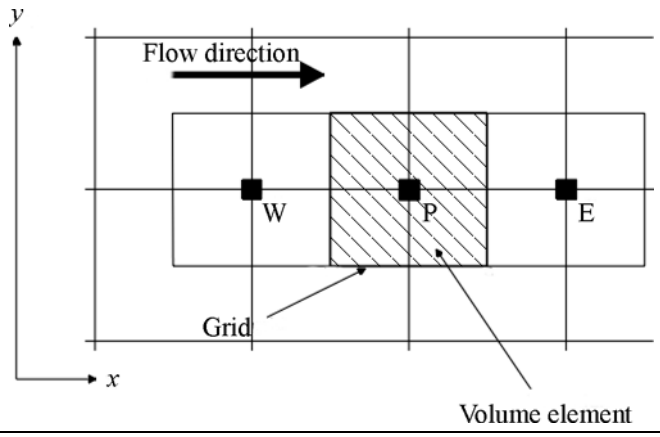

Figure 2.7: *Two-dimensional grid with volume elements and three exemplary center points, W, P and E [113].*

$$\alpha_P \cdot v_{x,P} = \sum_{nb} \alpha_{nb} v_{x,nb} + SV_P + (p_w - p_p)A_p, \tag{2.64}$$

where the subscripts "nb" denote the value at neighboring cells and subscripts "p" and "w" denote the values at the cell with the centre P and W, respectively. V is the volume of a cell, p the pressure, α is known as the link factor, S is part of the momentum source term and A the boundary line, respectively surface at three-dimensional grids, of the considered control volume.

This finite difference equation is the discrete equivalent of the continuous flow transport equation we started with. By formulating these equations for each cell, we get a set of coupled linear equations. To solve the set of discrete solution equations, CFD-ACE+ provides an iterative solution method, applied to each variable, until a convergent solution is found.

As the solutions of the three momentum equations only provide the three velocity components in x, y *and* z-direction, the pressure calculation in CFD-ACE+ is performed by the so called SIMPLEC, semi-implicit method for pressure-linked equations, algorithm [89,110]. The overall flowchart is shown in figure 2.8, where v_x, v_y, v_z are the velocities in x, y, z-direction, p is the pressure and t is the time.

The solution process results in a system of linear algebraic equations which needs to be solved. The complexity and size of the set of equations depends on the number of degrees of freedom of the problem and the number of grid nodes. CFD-ACE+ provides different solution techniques like a direct solver for calculation of additional variables e.g. stress and iterative solvers. From these a conjugate gradient squared (CGS) + preconditioning solver as well as an algebraic multi grid (AMG) solver are available [113-115].

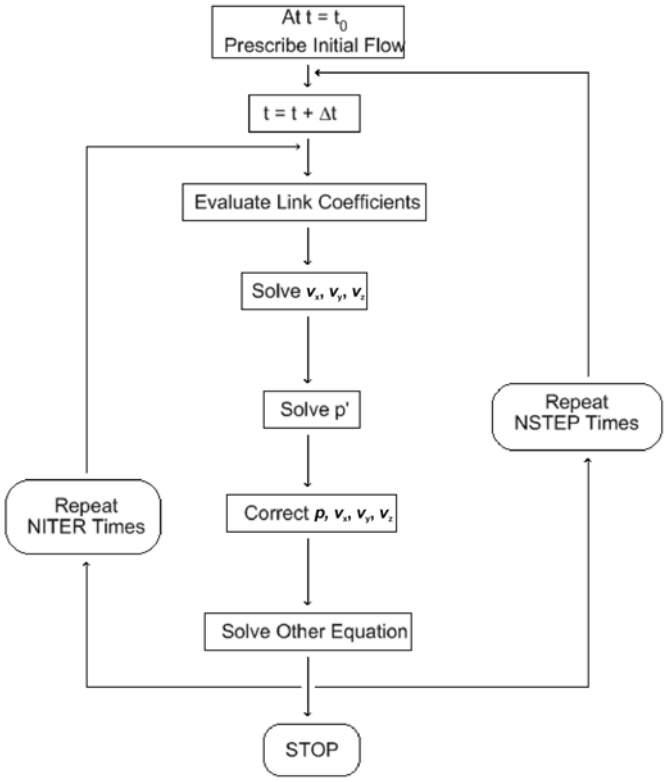

Figure 2.8: *Overall solution flowchart for the SIMPLEC algorithm applied in CFD-ACE+ [113].*

2.6.2 VOLUME OF FLUID METHOD

The Volume of Fluid (VOF) method allows for the simulation of fluid dynamics of two immiscible fluids with arbitrary fluid-fluid interfaces, including fluids with very high density ratios. The effects of surface tensions can also be taken into account. This method is absolutely essential to simulate droplet ejection devices because it provides a way to implement surface tension effects at walls or during the droplet constriction. These effects are fundamental to form a spherical droplet out of a nozzle. This way the droplet shape as well as phenomena during droplet breakup due to the surface tension can be simulated and examined. Hence, the VOF method is the outstanding advantage of CFD simulations compared to analytical or network descriptions of a droplet formation. Furthermore, also capillary filling problems can be simulated using the VOF method. Therein the surface tension represents the only present actuation driving the liquid. Therefore it is important that the surface tension forces are implemented correctly to lead to an active progression of the liquid.

SCALAR FIELD VARIABLE

The central feature of the VOF methodology [116-121] is the scalar field variable F which stands for the distribution of the second fluid in the computational grid. F specifies the fraction of the volume of each computational cell in the grid occupied by

fluid two. The use of the single scalar variable F to describe the liquid distribution and volume evolution leads to the classification of the VOF method as a volume tracking method.

A cell containing only fluid two, will take the value $F = 1$, and $F = 0$ in cells completely filled with fluid one. A cell that contains an interface between fluid one and fluid two would have a value of F between 0 and 1.

For a given flow field with the velocity vector $\vec{v}$ and an initial distribution of F on a grid, the volume fraction distribution F (and hence the distribution of fluid two) is determined by the passive transport equation [118]:

$$\frac{\partial F}{\partial t} + \nabla \vec{v} F = 0 . \tag{2.65}$$

This equation must be solved together with the fundamental equations of conservation of momentum, mass and energy to achieve computational coupling between the velocity field solution and the liquid distribution.

Any volume-specific quantity ϕ in a computational cell is computed from the value of F in accordance to:

$$\phi = F\phi_2 + (1 - F)\phi_1 , \tag{2.66}$$

or respectively for intensive quantities where the effect of density must be included:

$$\phi = \frac{F\rho_2\phi_2 + (1 - F)\rho_1\phi_1}{\rho_{mixture}} , \tag{2.67}$$

where ϕ_2 is the value of the property for fluid two and ϕ_1 is the value of the quantity for fluid one, ρ_2 and ρ_1 are the density of fluid two and fluid one, respectively, and $\rho_{mixture}$ is the density of the mixed phase.

SURFACE RECONSTRUCTION

The presented purely volumetric description of the phase distribution provides no unique definition of the interface between the two phases. Thus, it must be dynamically reconstructed. Three methods of reconstruction of the surface are generally available [122]:

- A "0^{th} order" upwind scheme [122].
- An upwind scheme with the single line interface construction (SLIC) method [123-126].
- An upwind scheme with the piecewise linear interface construction (PLIC) method [124-126].

Because surface tension forces are only supported by the (PLIC) scheme in CFD-ACE+, the "0^{th} order" and the SLIC scheme are not further discussed.

The PLIC method is the most accurate one of the three available schemes. The liquid-gas or liquid-liquid interface is assumed to be planar and is allowed to take any orientation within the cell, in this way it can attain the shape of a polygonal facet which is fully defined by [122]:

- The spatial orientation of the infinite plane containing the facet.
  The orientation is defined by the outward-pointing unit normal of the infinite plane, with the normal always pointing out of the liquid phase towards the gas phase (or the second liquid phase), parallel to the gradient vector of F which is determined by the local distribution of F in a set of cells which includes the target cell and all its immediate neighbors.
- The location of a point within the cell and the infinite plane.
  The location of this anchor point is determined by finding the infinite cutting plane perpendicular to the unit normal of the infinite plane that truncates the correct liquid volume V_{cut} from the cell with the volume V_{c}, following:

$$V_{\mathrm{cut}} = F \cdot V_{\mathrm{c}} . \tag{2.68}$$

COURANT-FRIEDRICHS-LEVI CONDITION (CFL)

In CFD-ACE+ the so-called CFL number provides the possibility to use an auto time step function when using the VOF method. This auto time step function has the advantage that the solver itself determines the optimum time step for the simulation to guaranty convergence and consistency. Due to this it is recommended to use it although the calculation time might increase. This could be because the solver decelerates at "difficult" locations for free surfaces calculated by the VOF method. The CFL number itself provides a control mechanism for the calculation of the auto time steps. Within each computational cell, the stability limit is given by the so-called Courant condition [122]:

$$\Delta t_{\mathrm{c}} = \frac{d_{\mathrm{c}}}{\left|\vec{v}_{\mathrm{c}}\right|}, \tag{2.69}$$

where Δt_{c} is the maximum time step that can be taken in cell c, and $\vec{v}_{\mathrm{c}}$ and d_{c} are the local velocity vector and the local cell "dimension" (or length scale), respectively. The CFL number is defined by [122]:

$$\mathrm{CFL} = \frac{\left|\vec{v}_{\mathrm{c}}\right| \cdot \Delta t_{\mathrm{c}}}{d_{\mathrm{c}}} . \tag{2.70}$$

It specifies the distance crossed by the fluid travelling at the velocity $\vec{v}_c$ as a fraction of the of the local length scale of the cell. Hence, a CFL number of 0.2 for example allows the interface of the fluid to cross 20 % of the cell width during each time step. The CFL number is restricted to CFL < 1 so that the time step is small enough to ensure that the free surface crosses less than one cell during that time step.

SURFACE TENSION

The surface forces are usually computed based on the equilibrium of a curved surface under a surface tension force. The net normal force $\vec{n}$ acting on the surface is equal to the summation of all the tangential forces τ due to surface tension [122]:

$$\int \Delta p \; ds \; = \; \int \tau \; |dx| \, . \tag{2.71}$$

Since the tangential force is equal to:

$$\tau \; = \; \sigma \vec{n} \times \frac{d\vec{x}}{|d\vec{x}|} \, , \tag{2.72}$$

this leads to:

$$\int \Delta p \; ds \; = \; \int \sigma \vec{n} \times d\vec{x} \, , \qquad \vec{n} \; = \; \nabla F \, . \tag{2.73}$$

This formulation requires no information about the global interface shape. When applied at the discrete level, the computation is conservative, in that when the interface is broken into many small pieces, the total force is equal to summation of the forces over all the constitutive pieces. The surface tension simulation is performed in CFD-ACE+ as follows [122]:

- Find the fluid-fluid interface at each cell face,
- Find the unit normal of the interface,
- Apply the above integral to determine an effective cell volume force.
- Apply the determined volume force as source term in the Navier-Stokes equation for the current time step.

3 FUNDAMENTALS OF DROPLET FORMATION

Nowadays there are many applications using droplets in the volume range below several microliters with increasing market potential [1]. However, the first analytical treatment of droplet generation dates back already in the late 19th century. Lord Rayleigh was the first to describe the droplet generation caused by jet instabilities analytically [56]. Starting in the early 20th century, the experimental study of the droplet generation became more and more important [102,103]. But even today the demand for analytical solutions for droplet ejection is still present [57-61]. These studies were mostly using simplifications of the Navier-Stokes equations like axisymmetric, steady flows with a free surface to describe simple examples of droplet formation. However, due to the increasing complexity of the used fluidic systems more and more numerical methods are applied to obtain more accurate and realistic solutions [104]. Today the CFD tools, as described in section 2.6, are mainly used for numerical calculations of more complicated droplet ejection devices as discussed in chapter 5 and chapter 6.

The purpose of this chapter is to provide a general estimation what boundary conditions are necessary to eject a droplet. The most important boundary condition is the actuating boundary condition because it is the driving force for the droplet formation. Hence, the focus of the next section is which kind of actuation is required to obtain a droplet formation. Furthermore, the influences of different parameters like geometry variations, different surfaces, various media and the actuation dynamics on the droplet formation are discussed. Finally a new classification of known droplet generators is proposed based on the underlying working principle rather than on obvious construction elements of the system or historical reasons. In this context the main actuation principles like pressure boundary conditions, flow boundary conditions, combined pressure and flow boundary conditions and acoustic actuation are distinguished. The reason for this new kind of classification is the possibility to assign typical features to the single actuation principles which are presented in chapter 7.

3.1 CRITERIA FOR DROPLET EJECTION

"The process of drop ejection is not as simple as taking a fluid chamber with a small hole and pressurizing it enough for fluid to start emerging from the ejection nozzle hole" [100]. To accomplish monodisperse droplets ejected out of a nozzle, one needs the ability to produce high-speed fluid jets of approximately the diameter of the desired

droplets. Additionally, the behavior of the jets has to be controlled precisely enough to cause them to consistently disperse into uniformly sized droplets. In general there are two different methods to eject monodisperse droplets. The first method, the so called continuous jet method, is to break up a continuously flowing fluid jet. Either by driving the fluid with a source of acoustic energy in order to form standing wave nodes along its length, or by always existing natural disturbances. The ejected jet finally disperses into discrete droplets. The second method, the drop-on-demand method, there against is to generate single droplets instead of breaking up a continuous jet. This is mainly done by short pressure pulses, small volume displacements or acoustic actuation of single or multiple nozzles to eject a droplet on demand. These actuation principles are capable to produce droplets in the kilohertz range with random accessibility.

Main differences of the two methods are the maximum possible frequencies, the necessary amount of liquid, the random accessibility of droplets and the complexity of the system setup. While the continuous jet dispenser is capable of producing droplets in the MHz range, the drop-on-demand method produces droplets with a frequency of several kHz. The advantage in terms of throughput of the continuous jet method is faced with the disadvantages of the necessary amount of liquid which is needed and the relatively high complexity of the system setup compared to the drop-on-demand technique. However, the random accessibility of droplets, the less required amount of liquid and the simpler system setup are reasons why the drop-on-demand method is the more common method nowadays in most printing as well as in medical or biological dispensing applications. But nevertheless also the continuous jet method is still in use for some applications.

3.1.1 Critical Weber Number

The creation of spherical droplets has been the focus of numerous studies over the years [56-61,99-104,108,141]. These show conclusively that for both steady and transient flows the onset and mechanisms of droplets breakup can be correlated with the non-dimensional Weber number as defined in section 2.3.2. The main focus of these studies is the aerodynamic breakup of liquid fuel jets into high-speed flows preferably used for combustion. However, the results can also be applied for drop-on-demand dispensers because the Weber number utilizes the relative velocity between liquid and ambient air. Hence, the Weber number is the most important dimensionless number characterizing the droplet formation. Therefore, the Weber number can be used to distinguish between occurring droplet formation regimes as it is explained in the following. Additionally the Weber number can be applied to determine the threshold of droplet formation. However, the critical Weber number is only a sufficient condition for a droplet breakup and not necessary. This means that if the critical Weber number is surpassed certainly a droplet breakup will occur. But moreover a droplet ejection is also possible at lower Weber numbers. The only necessary condition for a droplet

formation is that the supplied energy is sufficient to overcome friction losses and the surface energy of an ejected droplet. An example of such a droplet ejection is demonstrated by the TopSpot system presented in section 6.5.

Returning to the derivation of the Weber number in section 2.3.2, the Weber number has to be 12 to equilibrate kinetic and surface energy:

$$\frac{E_{\text{kinetic}}}{E_{\text{surface}}} = \frac{1}{12} \cdot We\,. \tag{3.1}$$

According to this, a Weber number larger than 12 signifies that the disruptive hydrodynamic forces are larger than the stabilizing surface tension forces. Additionally this crucial Weber number, at which a droplet breakup first can occur, can also be determined empirically. This empirical crucial Weber number is also around $We = 12$ [49,50,105,106,127]. However, a constant crucial Weber number is only valid for liquids with low viscosity such that the Ohnesorge number is small, $On < 0.1$ (cf. section 2.3.3). This is the case for viscosities $\eta < 10$ mPas for appropriate spatial dimensions in the micro scale. For higher viscous fluids a viscosity dependent expression has to be added to this crucial Weber number known as critical Weber number We_{critical}. A useful empirical correlation for the critical Weber number with increasing viscosity is [105,106]:

$$We_{\text{critical}} = 12 \cdot (1 + 1.077\ On^{1.6}) \tag{3.2}$$

The dependency of the critical Weber number on the Ohnesorge number is displayed in figure 3.1.

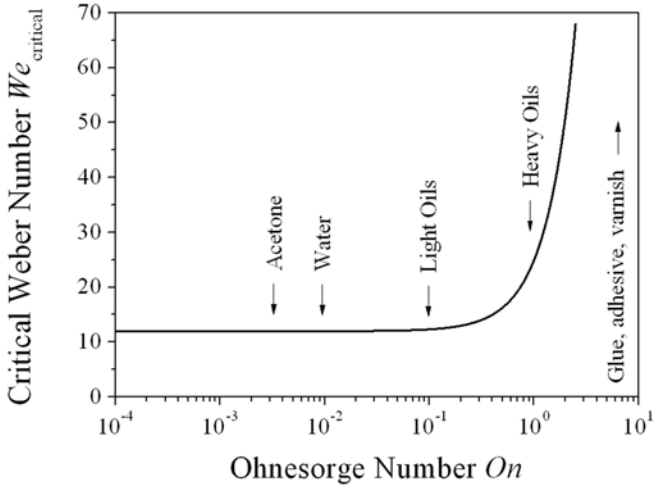

Figure 3.1: *Critical Weber number We_{critical} depending on the Ohnesorge number On and typical Ohnesorge regimes for different media.*

Besides the critical Weber number for a drop-on-demand breakup also the criterion of $We > 8$ for a Rayleigh breakup is reported [128]. The Rayleigh breakup mechanism is explained in more detail in section 3.1.3. This limit can also be motivated by the lower limit of a jet formation in the case of dripping out of a vertical capillary with diameter D_{nozzle} under the action of gravity [129]. The static pressure p_{stat} inside a hanging droplet is:

$$p_{\text{stat}} = \frac{4 \cdot \sigma}{D_{\text{droplet}}}. \tag{3.3}$$

The dynamic pressure p_{dyn} due to a velocity v yields:

$$p_{\text{dyn}} = \frac{\rho}{2} \cdot v^2. \tag{3.4}$$

Considering both pressures to be equal also leads to a correlation with the Weber number [129]:

$$\frac{p_{\text{dyn}}}{p_{\text{stat}}} = \frac{1}{8} \cdot \frac{\rho \cdot D_{\text{droplet}} \cdot v^2}{\sigma} = \frac{1}{8} \cdot We. \tag{3.5}$$

Hence, a Weber number of 8 arises from the equilibrium of dynamic and static pressure.

Furthermore, an additional criterion $We > 40$ to predict the onset of the atomization regime is suggested [99,128]. In contrast to the Rayleigh breakup regime and the drop-on-demand regime, during atomization the ejected jet breaks up completely within a short distance from the discharge nozzle exit in a chaotic and irregular manner forming a conical spray [99]. The aerodynamic interaction, i.e. the very fast relative motion combined with air friction, causes irregularities in the originally smooth liquid jet surface. This leads to unstable wave growth on the jet surface producing unstable ligaments. The average droplet diameter generated by atomization is much smaller than the jet diameter.

In conclusion it is possible to distinguish between different mechanisms of droplet breakup for low viscous media. These breakup mechanisms are [128]:

- $8 < We \leq 12$ — Rayleigh breakup regime
- $12 < We \leq 40$ — "Wind-induced" regime [128] or drop-on-demand regime
- $We > 40$ — Atomization regime

However, this classification originally was introduced for jet breakups and not for drop-on-demand breakups with short pressure pulses. Since the Weber number can be written using the Reynolds number and the Ohnesorge number (cf. equation (2.33)) the different breakup regimes for low viscous media can be illustrated in a diagram of Ohnesorge number versus Reynolds number like it is displayed in figure 3.2. Due to

the hyperbolic dependency of the Ohnesorge number on the Reynolds number, the critical values are represented by lines in the logarithmic plot. Furthermore, in figure 3.3 the different breakup regimes are displayed depending on the velocity v and the droplet diameter D for water as ejected liquid (ρ = 1 g/cm^3, σ = 72.5 mN/m and η =1 mPas).

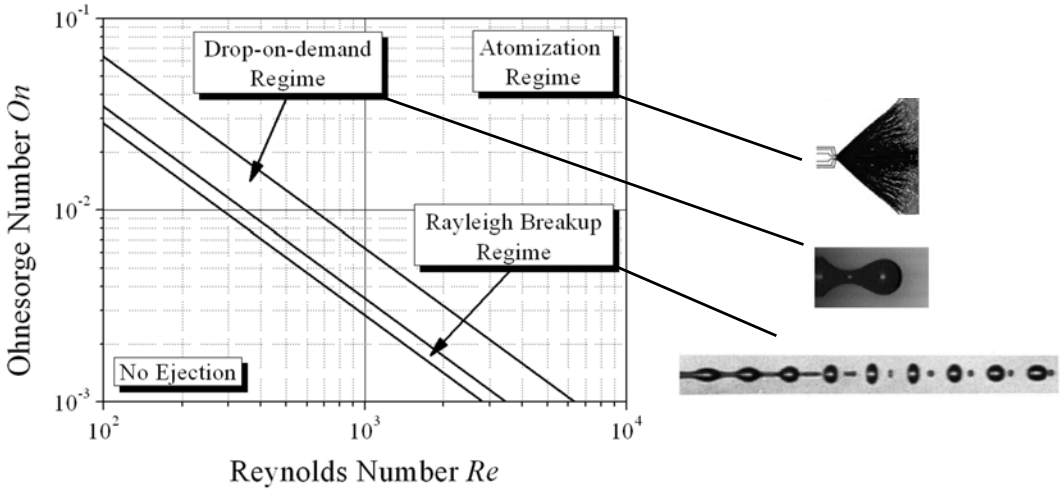

Figure 3.2: *Different breakup regimes for low viscous media represented by the relationship of the Ohnesorge number versus the Reynolds number.*

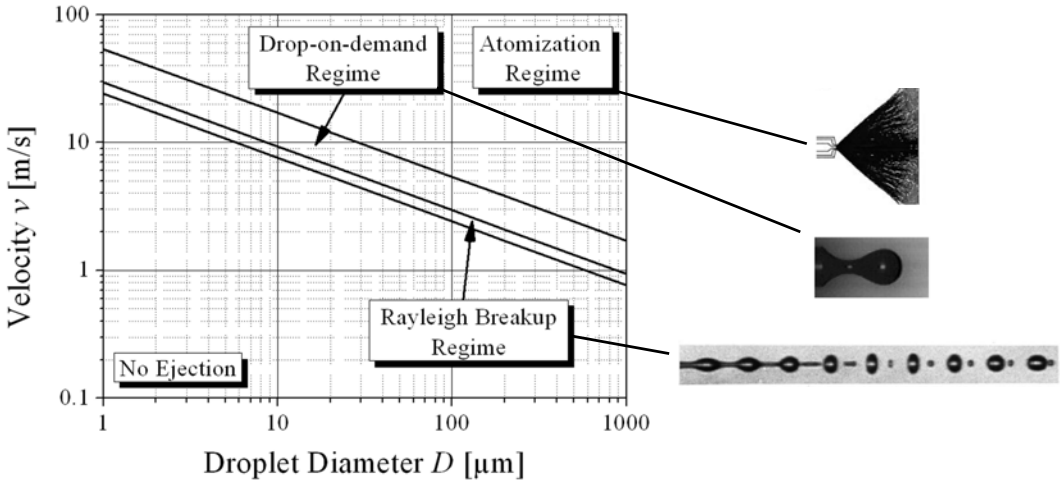

Figure 3.3: *Different breakup regimes represented by the relationship of the velocity v versus the droplet diameter D for water as ejected liquid.*

3.1.2 Critical Parameters for Droplet Formation

In the previous section, the critical Weber number was introduced as sufficient criterion for droplet formation. But what does this indicate for an existing system or the design of a new system? For this purpose, it is essential to know, how much

pressure is sufficient to eject a single liquid droplet out of a nozzle. To address this question an energetic estimation of the conditions in a simplified model with a circular inlet channel and nozzle as depicted in figure 3.4 is derived in the following.

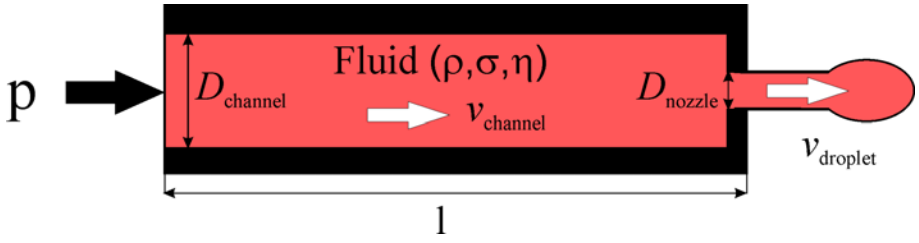

Figure 3.4: *Schematic drawing visualizing the assumption for the necessary pressure for a droplet breakup using the critical Weber number.*

The mechanical work W_{pressure} generated by an external pressure which is necessary to eject a droplet of the volume V_{droplet} with a pressure loss p over the simplified model consists of three single expressions. These are the energy loss due to friction E_{friction} in the channel, representing all viscous and geometrical pressure losses, the energy required to create the surface of a spherical droplet E_{surface} and the kinetic energy of the resulting free flying droplet E_{kinetic}:

$$W_{\text{pressure}} = E_{\text{friction}} + E_{\text{surface}} + E_{\text{kinetic}} \,. \tag{3.6}$$

Assuming an incompressible liquid and using the fact that the work and the energies can be normalized to the pressure p in a fixed volume element ΔV, which can be considered to be equal to the ejected droplet volume V_{droplet}, leads to:

$$E = p \cdot \Delta V = p \cdot V_{\text{droplet}} \,. \tag{3.7}$$

Using the definitions deduced in section 2.4 for the fluidic resistance, the entire system can be constructed by the fluidic resistance of the circular channel $R_{\text{hd, channel}}$ and the circular nozzle $R_{\text{hd, nozzle}}$ (equation (2.37)), the resistance due to the outflow out of the nozzle R_{outflow} (equation (2.54)) and the resistance due to the contraction of the cross section $R_{\text{contraction}}$ (equation (2.59)). Fluidic inertance and fluidic capacitance are neglected in this energetic estimation. The volume flow Φ_{v} can be replaced by the mean velocity $\bar{v}_{\text{channel}}$ through the cross section area A_{channel} of the channel. Hence, E_{friction} can be written as:

$$E_{\text{friction}} = (R_{\text{hd, channel}} + R_{\text{hd, nozzle}} + R_{\text{outflow}} + R_{\text{contraction}}) \cdot V_{\text{droplet}} \cdot \Phi_{\text{v}} \tag{3.8}$$

$$= (R_{\text{hd, channel}} + R_{\text{hd, nozzle}} + R_{\text{outflow}} + R_{\text{contraction}}) \cdot V_{\text{droplet}} \cdot A_{\text{channel}} \cdot \bar{v}_{\text{channel}} \tag{3.9}$$

In the following the nozzle length is assumed to be infinite small so that the fluidic resistance $R_{\text{hd, nozzle}} = 0$. Furthermore, the resistances due to the outflow out of the nozzle R_{outflow} and due to the contraction of the cross section $R_{\text{contraction}}$ are neglected. This is done to have an estimation as simple as possible. Consideration of these terms would lead only to a linear offset. According to this E_{friction} can be simplified to:

$$E_{\text{friction}} \approx V_{\text{droplet}} \cdot R_{\text{hd, channel}} \cdot \Phi_{\text{v}} \tag{3.10}$$

$$\Rightarrow \qquad E_{\text{friction}} \approx V_{\text{droplet}} \cdot \frac{8 \cdot \eta \cdot l}{\pi \cdot \left(\frac{D_{\text{channel}}}{2}\right)^4} \cdot A_{\text{channel}} \cdot \bar{v}_{\text{channel}} \tag{3.11}$$

$$\Rightarrow \qquad E_{\text{friction}} \approx V_{\text{droplet}} \cdot \frac{32 \cdot \eta \cdot l}{D_{\text{channel}}^2} \cdot \bar{v}_{\text{channel}} \,. \tag{3.12}$$

The surface energy E_{surface} of a spherical droplet is defined by the surface tension σ and the surface area of the droplet A_{droplet}. If the droplet diameter is supposed to be equal to the nozzle diameter D_{nozzle} the surface energy E_{surface} can be equated to:

$$E_{\text{surface}} = A_{\text{droplet}} \cdot \sigma = \pi \cdot D_{\text{nozzle}}^2 \cdot \sigma = V_{\text{droplet}} \cdot \frac{6 \cdot \sigma}{D_{\text{nozzle}}} \,. \tag{3.13}$$

Finally, the kinetic energy E_{kinetic} of the flying droplet with the droplet velocity v_{droplet} directly at the nozzle outlet, can be written as:

$$E_{\text{kinetic}} = \frac{1}{2} \cdot m \cdot v_{\text{droplet}}^2 = \frac{1}{2} \cdot V_{\text{droplet}} \cdot \rho \cdot v_{\text{droplet}}^2 \,. \tag{3.14}$$

Using the continuity equation both considered velocities can be linked to each other:

$$\bar{v}_{\text{channel}} = v_{droplet} \cdot \frac{D_{\text{nozzle}}^2}{D_{\text{channel}}^2} \,. \tag{3.15}$$

Conclusively the mechanical work due to an external pressure can be equated to:

$$W_{\text{pressure}} = V_{\text{droplet}} \cdot \left[\frac{32 \cdot \eta \cdot l \cdot D_{\text{nozzle}}^2}{D_{\text{channel}}^4} \cdot v_{\text{droplet}} + \frac{6 \cdot \sigma}{D_{\text{nozzle}}} + \frac{1}{2} \cdot \rho \cdot v_{\text{droplet}}^2 \right], \tag{3.16}$$

and the required pressure p yields:

$$p = \frac{32 \cdot \eta \cdot l \cdot D_{\text{nozzle}}^2}{D_{\text{channel}}^4} \cdot v_{\text{droplet}} + \frac{6 \cdot \sigma}{D_{\text{nozzle}}} + \frac{1}{2} \cdot \rho \cdot v_{\text{droplet}}^2 \,. \tag{3.17}$$

Taking advantage of this formula, the sufficient pressure for a droplet ejection with known droplet velocity can be estimated, or the resulting droplet velocity with known pressure can be estimated. However, this formula is valid only if a droplet is issued at all.

Returning to the critical Weber number given by equation (3.2), and remembering the definition of the Weber number (equation (2.32)), the critical Weber number can be transformed into a critical velocity v_{critical} which is at least necessary to force a droplet breakup:

$$v_{\text{critical}} = \sqrt{\frac{We_{\text{critical}} \cdot \sigma}{D_{\text{nozzle}} \cdot \rho}}. \tag{3.18}$$

This minimum velocity is required for equation (3.17) to hold. Inserting this critical velocity as droplet velocity into equation (3.17), a critical pressure p_{critical} can be estimated depending only on media parameters, geometry parameters and the critical Weber number:

$$p_{\text{critical}} = \frac{32 \cdot \eta \cdot l \cdot D_{\text{nozzle}}^2}{D_{\text{channel}}^4} \cdot \sqrt{\frac{We_{\text{critical}} \cdot \sigma}{D_{\text{nozzle}} \cdot \rho}} + \frac{6 \cdot \sigma}{D_{\text{nozzle}}} + \frac{1}{2} \cdot \rho \cdot \left(\frac{We_{\text{critical}} \cdot \sigma}{D_{\text{nozzle}} \cdot \rho}\right) \tag{3.19}$$

$$\Rightarrow \quad p_{\text{critical}} = \frac{32 \cdot \eta \cdot l \cdot \sqrt{We_{\text{critical}} \cdot \sigma \cdot D_{\text{nozzle}}^3}}{D_{\text{channel}}^4 \cdot \sqrt{\rho}} + \frac{6 \cdot \sigma}{D_{\text{nozzle}}} + \frac{We_{\text{critical}} \cdot \sigma}{2 \cdot D_{\text{nozzle}}}. \tag{3.20}$$

This critical pressure is the minimum pressure required for ejecting a droplet in the given configuration. The critical velocity at the nozzle outlet can also be used to calculate a critical volume flow $\Phi_{\text{v, critical}}$ which has to be surpassed to get a droplet ejection:

$$\Phi_{\text{v, critical}} = v_{\text{critical}} \cdot \left(\frac{D_{\text{nozzle}}}{2}\right)^2 \cdot \pi = \sqrt{\frac{We_{\text{critical}} \cdot \sigma}{D_{\text{nozzle}} \cdot \rho}} \cdot \left(\frac{D_{\text{nozzle}}}{2}\right)^2 \cdot \pi \tag{3.21}$$

$$\Rightarrow \quad \Phi_{\text{v, critical}} = \frac{\pi}{4} \cdot \sqrt{\frac{We_{\text{critical}} \cdot \sigma \cdot D_{\text{nozzle}}^3}{\rho}}. \tag{3.22}$$

In order to estimate the maximum time available for the ejection of an arbitrary volume, the droplet volume V_{droplet} can be fixed assuming a droplet diameter equal to the nozzle diameter D_{nozzle}. Hence, a critical time t_{critical} can be calculated that might not be surpassed to deliver a fixed droplet volume through the nozzle with a given flow. Using the critical volume flow $\Phi_{\text{v, critical}}$ as minimum flow condition t_{critical} yields:

$$t_{\text{critical}} = \frac{V_{\text{droplet}}}{\Phi_{\text{v, critical}}} = \frac{1/6 \cdot D_{\text{nozzle}}^3 \cdot \pi}{v_{\text{critical}} \cdot \left(\frac{D_{\text{nozzle}}}{2}\right)^2 \cdot \pi} = \frac{2}{3} \cdot \frac{D_{\text{nozzle}}}{v_{\text{critical}}} \tag{3.23}$$

$$\Rightarrow \quad t_{\text{critical}} = \frac{2}{3} \cdot \frac{D_{\text{nozzle}}}{\sqrt{\frac{We_{\text{critical}} \cdot \sigma}{D_{\text{nozzle}} \cdot \rho}}} = \frac{2}{3} \cdot \sqrt{\frac{D_{\text{nozzle}}^3 \cdot \rho}{We_{\text{critical}} \cdot \sigma}}. \tag{3.24}$$

However, the critical time is only valid for the ejection of a droplet with a diameter equal to the nozzle diameter. Of course, the critical time increases if the droplet volume is assumed to be larger.

Furthermore, the critical time is an important number to determine the maximum theoretical dosage frequency:

$$f_{\max} = \frac{1}{t_{\text{critical}}}. \tag{3.25}$$

In practice however, the dosage frequency can be much lower due to starving effects caused by low surface tension and high fluidic resistance [131,132]. Combining the both criteria for a successful droplet formation (3.20) and (3.24) directly leads to the minimum or critical power P_{critical} sufficient to eject the droplet:

$$P_{\text{critical}} := \frac{p_{\text{critical}} \cdot V_{\text{droplet}}}{t_{\text{critical}}}. \tag{3.26}$$

From the before said two necessary conditions can be deduced which are sufficient for a droplet ejection of one single droplet with the diameter of the nozzle D_{nozzle} to take place. The critical pressure p_{critical} has to be exceeded for a duration of maximally the critical time t_{critical} to enforce a single droplet formation. If the critical time is exceeded by far a jet rather than a single droplet is ejected. These both criteria can also be expressed in the form that the critical power has to be surpassed to enforce a single droplet formation:

- $p \geq p_{\text{critical}}$
- $t \leq t_{\text{critical}}$

$\Bigg\}$ $P \geq P_{\text{critical}}$

Despite the simple approach many useful informations about the critical pressure, the critical time and the critical power can be obtained by the presented model. However, there are also limitations of the model summarized in the following:

- Only a static reflection is performed. No time dependent behavior description is included.
- No statement on the shape or quality of the ejected droplet is carried out.
- No influence of surfaces respectively contact angles is implemented.
- Only Newtonian fluids are considered.

3.1.3 Jet Ejection with Subsequent Rayleigh Droplet Breakup

The simplest way to produce droplets is to pressurize a fluidic reservoir by pneumatic or also hydraulic pressure to generate a continuous jet out of a nozzle. As described for continuous jet ejectors, this jet with approximately the diameter of the nozzle disperses into several single droplets due to always existing surface disturbances on the jet [57]. These disturbances can be caused by intentional or unintentional perturbations of the system. Intentional perturbations can be induced for example by a vibrating

piezoelectric transducer or an acoustic vibrator. Droplet volume, droplet velocity and quality of ejected droplets depend on the design of the used ejection system as well as on the liquid properties.

The condition for best performance of such a device was derived by Rayleigh and can be realized by an optimum perturbation wave length λ_{opt} depending only on the nozzle diameter D_{nozzle} [56,99,133-137]. The corresponding frequency f_{opt} can be calculated by dividing the speed of sound c in the used media ($c \approx 1500$ m/s in water) and λ_{opt}:

$$\lambda_{opt} = 4.508 \cdot D_{nozzle}, \tag{3.27}$$

$$f_{opt} = \frac{c}{\lambda_{opt}}. \tag{3.28}$$

The liquid jet collapses, forming droplets of uniform size at uniform spacing. After breakup, the separated liquid jet of length $4.508\, D_{nozzle}$ converts into a spherical droplet. Hence, the droplet diameter $D_{droplet}$ can be determined [99]:

$$D_{droplet} = 1.89 \cdot D_{nozzle}. \tag{3.29}$$

In the case of a non intentionally disturbed jet, only the breakup length $L_{breakup}$, being the distance from the nozzle where the droplet breakup occurs, can be determined [83,87,138]:

$$\frac{L_{breakup}}{D_{nozzle}} = 19.5 \cdot \left(\sqrt{We} + 3 \cdot \frac{We}{Re}\right)^{0.85}. \tag{3.30}$$

Overall, the Rayleigh breakup was studied intensively [56,57,87,99,133-138], but since it is further not used in this thesis it will not be discussed in more detail. A typical jet ejection with subsequent Rayleigh droplet breakup is displayed in figure 3.5.

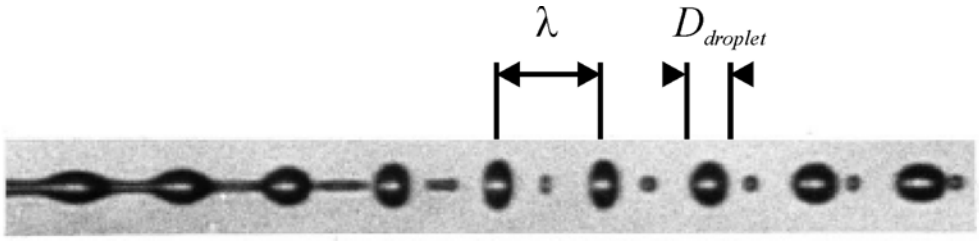

Figure 3.5: *Typical jet ejection with subsequent Rayleigh droplet breakup.*

3.2 Influence of Parameters on Droplet Ejection

As it could be seen in the previous section, there are several parameters within the formulas influencing the critical pressure, the critical time, the critical power and thereby the droplet ejection. All these parameters are discussed in more detail in this section in a general way. More specific correlations between parameters and

performance are presented in chapter 5 and chapter 6 for concrete devices. The influences of parameters are mainly studied in the framework of the model presented in section 3.1.2. In the following sections the effect of spatial dimensions, liquid properties, surface attributes and actuation dynamics are examined in detail.

3.2.1 GEOMETRY

The influence of geometry parameters like channel lengths, nozzle length, nozzle diameter, chamber height, or shape and size of cross sections can be explained regarding the fluidic elements derived in section 2.4.

For example the fluidic resistance (cf. equation (2.37)) depends linearly on the channel length but it is reversely proportional to R^4, the channel radius. The fluidic inertance (cf. equation (2.41)) depends linearly on the channel length and inversely proportional on the cross section area, whereas the junction effects like contraction or expansion only depends on the both involved cross section areas (cf. equation (2.59) and (2.60)). Taking all these dependencies, the influence of resistance, inertance and geometry on the critical pressure, the critical time and the critical power, as calculated in the previous section, can be estimated straight forward.

Considering the simple model of the previous section (cf. figure 3.4), the critical pressure, the critical time and the critical power can be estimated quantitatively if the geometrical dimensions and the used medium is fixed. In the following the channel diameter and the nozzle diameter are supposed to be equal ($D_{\text{nozzle}} = D_{\text{channel}}$) and water is assumed as dosage liquid. In figure 3.6 critical values are displayed for a fixed channel length of 500 µm and a varying channel and nozzle diameter. By varying the diameter from 12.5 µm to 500 µm, the critical pressure decreases from 930 kPa to 2 kPa, whereas the critical time increases from 1 µs to 250 µs and the critical power decreases from 1 mW to 0.5 mW. It can be seen that it is very difficult to eject a single droplet out of a 12.5 µm diameter nozzle where a pressure of about 10 bar has to be applied for less than 1 µs resulting in a power of 1 mW.

In figure 3.7 the critical pressure, the critical time and the critical power are displayed for a fixed nozzle diameter of 100 µm and a varying channel length. Increasing the channel length from 100 µm to 5 mm leads to an increase of the critical pressure from 10 kPa to 56 kPa which has to be supplied at the distant end of the channel. Whereas the critical time is independent on the channel length and stays on 23 µs, and the critical power increases from 0.2 mW to 1.4 mW. The shaded area indicates the area below the critical power. Thus, the shaded area corresponds to the parameter range where the power is below the critical power, i.e. no droplet breakup occur. There against the non shaded area corresponds to the parameter range where the power is above the critical power, i.e. a droplet breakup occurs. It follows from this characteristics that first, friction losses in the supply line can be considerable. Second the supply lines should be adequately short to avoid power losses by friction in a well designed device.

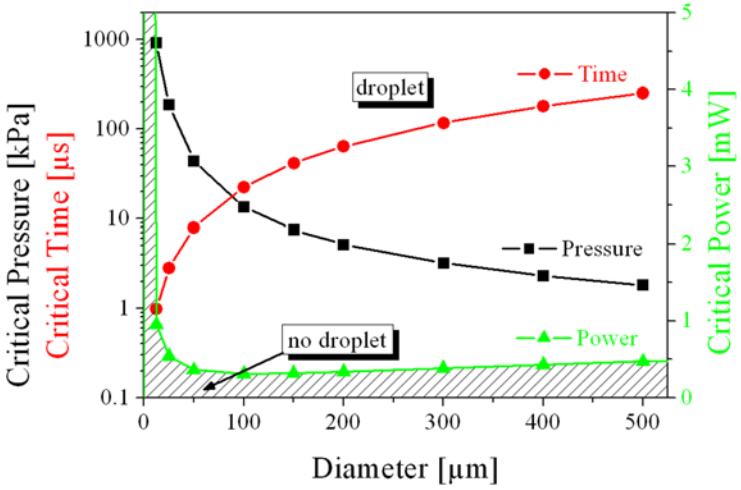

Figure 3.6: *Dependency of the critical pressure, the critical time and the critical power on the nozzle diameter (Medium = water, channel length = 500 µm). The shaded area indicates the area below the critical power where no droplet breakup occurs.*

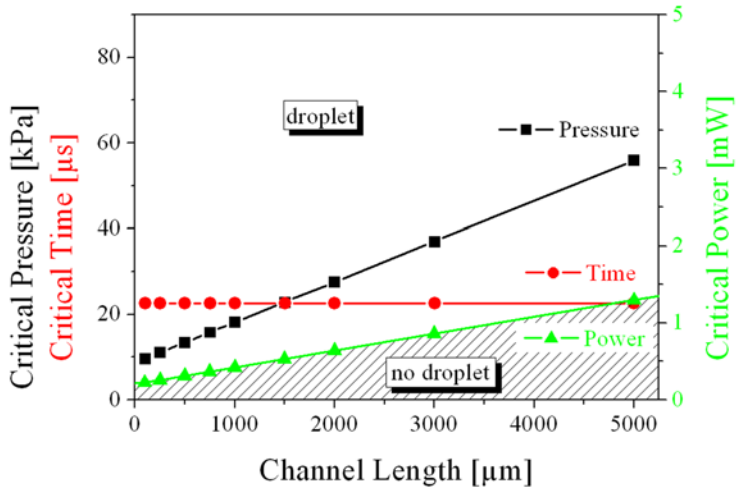

Figure 3.7: *Dependency of the critical pressure, the critical time and the critical power on the channel length (Medium = water, nozzle diameter = channel diameter = 100 µm). The shaded area indicates the area below the critical power where no droplet breakup occurs.*

3.2.2 MEDIA

The dependency of droplet generation on the media properties like density, surface tension or viscosity can also be inferred from the formulas given in section 2.3 and 2.4. However, the well known fact that with decreasing surface tension it is very hard to eject single droplets without any tail or satellite droplets can not be quantified by formulas. In this case the surface tension forces are not strong enough to build a spherical droplet and the concrete shape of the ejected liquid column can only be assessed by a full CFD treatment.

Furthermore, it becomes more and more difficult to eject a droplet with increasing viscosity because high viscous liquids like oils or adhesives cause high fluidic resistances and also increase the required critical Weber number due to high Ohnesorge numbers (cf. section 2.3). Some of these liquids can have the additional disadvantage of a non-Newtonian behavior which makes the simple estimations applied here invalid and which can cause additional practical problems.

Keeping this limitations in mind and returning to the analytical model, the dependency of the critical pressure, the critical time and the critical power can be calculated for a fixed geometry. Assuming the above presented model with a nozzle diameter of 100 µm and a channel length of 500 µm, the influence of varying density, surface tension and viscosity can be quantified.

Figure 3.8 shows the dependency of the critical pressure, the critical time and the critical power on the liquid's density with fixed viscosity and surface tension. Increasing the density from 0.25 g/cm^3 to 15 g/cm^3 leads to a change of the critical pressure from 18 kPa to 10 kPa, to a change of the critical time from 11 µs to 88 µs and to a change of the critical power from 0.8 mW to 0.06 mW. Concluding it can be stated that a higher density is preferable for an easier droplet ejection concerning required pressure, available time and required power.

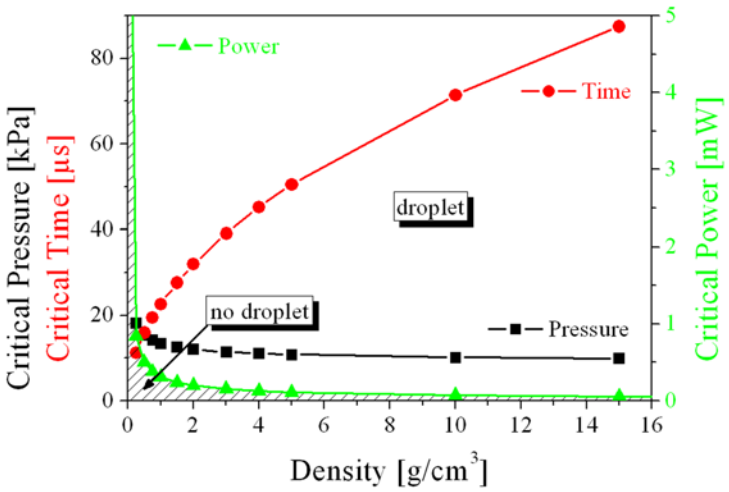

Figure 3.8: *Dependency of the critical pressure, the critical time and the critical power on the density of the used liquid (Nozzle diameter = 100 µm, channel length = 500 µm, η = 1mPas, σ = 72.5 mN/m). The shaded area indicates the area below the critical power where no droplet breakup occurs.*

By varying the surface tension from 10 mN/m to 500 mN/m with fixed density and viscosity, the critical pressure increases from 3 kPa to 72 kPa for a capillary with 100 µm diameter and 500 µm length like considered before. Whereas the critical time decreases from 61 µs to 9 µs and the critical power increases from 0.03 mW to 4.4 mW as depicted in figure 3.9. The influence of the surface tension on the critical pressure and on the critical power is higher compared to the influence of the density, but the

effect on the critical time is located in the same range. In this figure a low surface tension seems to be the best solution for a satisfactorily droplet ejection regarding critical pressure, time and power, but it has to be considered that a higher surface tension is favorable concerning jet contraction, droplet breakup and the quality of the droplet.

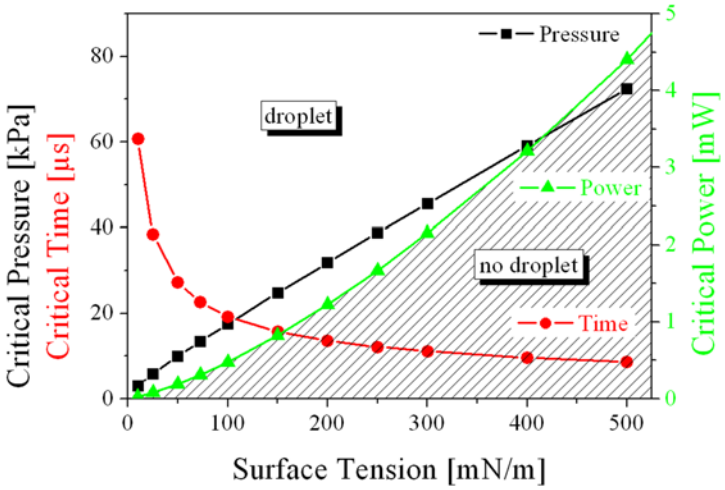

Figure 3.9: *Dependency of the critical pressure, the critical time and the critical power on the surface tension of the used liquid (Nozzle diameter = 100 µm, channel length = 500 µm, ρ = 1 g/cm³, η = 1mPas). The shaded area indicates the area below the critical power where no droplet breakup occurs.*

In figure 3.10 the critical pressure, the critical time and the critical power are displayed for a varying dynamic viscosity from 0.25 mPas to 1000 mPas with fixed density and surface tension. Increasing the viscosity leads to an increase of the critical pressure from 10 kPa to 35.6 MPa, whereas the critical time is decreasing from 22.6 µs to 3 µs, and the critical power is increasing from 0.2 mW to 6 W. Thus, low viscous fluids should definitely be preferred to enable easy droplet generation. The reason for the considerable effect of viscosity on the critical parameters is the big influence of the viscosity respectively Ohnesorge number in the empirical definition of the viscosity dependent critical Weber number in equation (3.2).

3.2.3 SURFACES

The natural way to quantify the influence of different surfaces, which can be realized by different materials or coatings on the droplet ejection process, is the contact angle depending on the combination of fluid and surface. On the one hand the contact angle influences the strength of a possibly present capillary pressure. On the other hand it regulates also the direction of the capillary forces. In a hydrophilic capillary the liquid tends to fill the capillary whereas in a hydrophobic capillary the liquid is held back. Hence, the capillary pressure either directs towards the unfilled domain or towards the already filled domain for the hydrophilic and hydrophobic capillary, respectively. Both

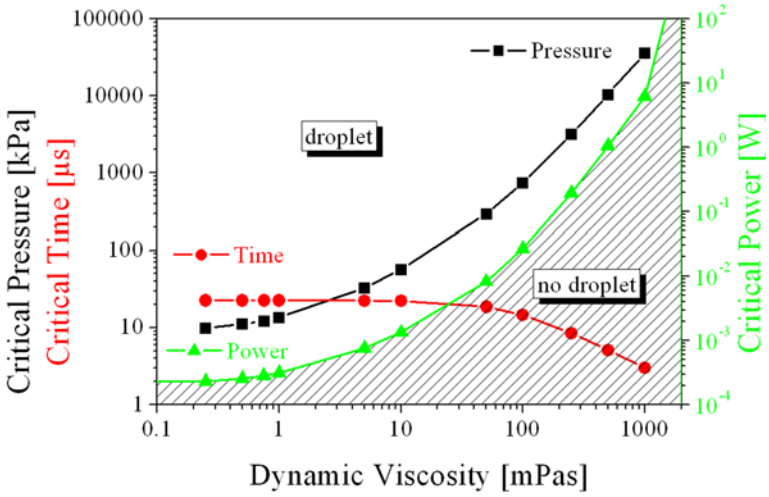

Figure 3.10: *Dependency of the critical pressure, the critical time and the critical power on the viscosity of the used liquid (Nozzle diameter = 100 µm, channel length = 500 µm, ρ = 1 g/cm³, σ = 72.5 mN/m). The shaded area indicates the area below the critical power where no droplet breakup occurs.*

effects can be gathered from the definition of the capillary pressure in equation (2.24). A hydrophilic material has a contact angle of $\Theta < 90°$ supporting the spreading of a droplet and with that a wetting of the surface by the liquid, whereas a hydrophobic material has a contact angle of $\Theta > 90°$ supporting the dewetting of a droplet.

The best performance can be achieved with a droplet generator, which has a contact angle as low as possible inside the system to guaranty a reproducible and fast capillary filling. A contact angle as high as possible outside the system is beneficial to avoid a wetting of the surface surrounding the nozzle. Such a good performance of a device can be attained by appropriate selection of the used materials as well as with a subsequent chemical modification of the corresponding surfaces [139,140]. A non-wetting of the surface surrounding the nozzle is absolutely necessary to avoid any non-reproducible unfavorable effects during the droplet formation at the outer surface. These effects could either be a deflection or disruption of the droplet trajectory or even a complete malfunction of the device. This could take place if the amount of liquid is too much to eject a droplet through this additional liquid layer. To illustrate the effect of a hydrophobic respectively hydrophilic surface surrounding the nozzle two corresponding results of a CFD simulation are depicted in figure 3.11. The droplet generation out of a nozzle with diameter D_1 with hydrophobic surface surrounding the nozzle (cf. figure 3.11 a)) works well. There against the droplet generation out of a nozzle with diameter D_1 with hydrophilic surface surrounding the nozzle (cf. figure 3.11 b)) leads to an enlarged effective diameter $D_2 > D_1$. This enlarged effective diameter leads to a higher power required for a proper droplet ejection (cf. figure 3.6). Hence, if the enlarged diameter D_2 is too large, the droplet ejection even could fail.

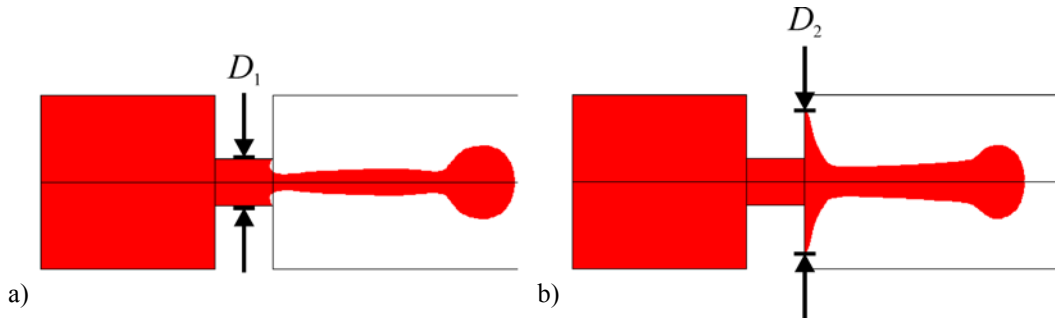

Figure 3.11: *Simulated droplet ejection with a) a perfect hydrophobic (Θ = 0°) and b) a perfect hydrophilic (Θ = 180°) surface surrounding the nozzle.*

3.2.4 Actuation Dynamics

So far only static reflections of the droplet ejection were discussed. The energy approach in section 3.1 provides no results regarding time evolution except the estimation of the critical time. But considering a time dependent pressure pulse makes the problem more complicated because time dependent properties like inertances or capacitances have to be implemented. However, the actuation dynamics are affecting the droplet formation considerably concerning droplet volume, velocity and shape. With an appropriate actuation dynamic it is even possible to reduce the ejected droplet volume an order of magnitude, so that the droplet diameter is even smaller than the nozzle diameter [141]. Thus it is important to consider the time dependence of the actuation if variations are in the order of the critical time or the inertance of the system is high.

In the following the influence of the dynamics of the driving pressure on the droplet ejection are discussed. Therefore, a simple nozzle geometry containing a nozzle and a nozzle chamber like it is shown in figure 3.12 is considered as example. The circular nozzle and nozzle chamber have a diameter of 4 µm and 15 µm, and a length of 5 µm and 15 µm, respectively. Regarding a fluid with $\rho = 1$ g/cm^3, $\sigma = 37.2$ mN/m and $\eta = 0.8$ mPas, results in a critical pressure of $p_{critical} = 197$ kPa using equation (3.20), a critical time of $t_{critical} = 0.3$ µs using equation (3.24) and a critical power $P_{critical} = 26$ µW using equation (3.26).

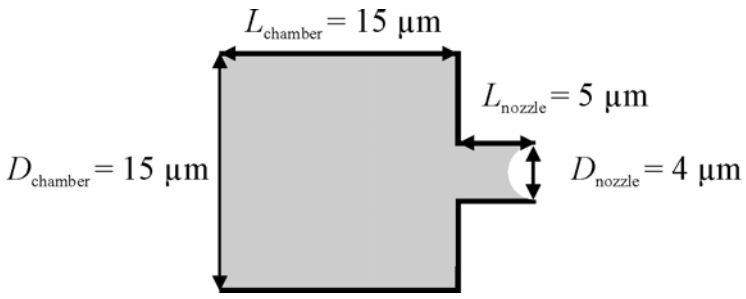

Figure 3.12: *Schematic drawing of a nozzle geometry containing a nozzle and a nozzle chamber considered as example.*

CFD Simulation

To study the influence of different applied time dependent pressure pulses the above presented geometry was implemented as CFD model. The two-dimensional axisymmetric model consists of a structured computational grid of about 4,500 cuboid cells where the smallest one has an area of 3.9 x 10^{-21} m^2 and the largest one has an area of 1.3 x 10^{-18} m^2 as it is displayed in figure 3.13. The VOF method including surface tension and the auto time step function was used with a CFL number of 0.2 (cf. section 2.6.2). The time steps varied in the range of 1 ns - 10 ns. The CGS solver and the PLIC surface reconstruction were chosen and the removal of "Flotsam and Jetsam" was turned on. This option restrains the generation of tiny isolated droplets of liquid in the gas phase or tiny isolated bubbles in the liquid phase, the so-called "flotsam and jetsam". The volume at the nozzle outlet is called control volume and it is necessary to simulate and visualize the trajectory of the ejected droplet. Figure 3.13 shows also the applied boundary conditions. At the pressure inlet the liquid (fluid 1) is pushed inside the model. The inner wall of the nozzle and the nozzle chamber is assumed to be full-wetting. The wall surrounding the outside of the nozzle is assumed to have a contact angle of $\Theta = 40°$ (as of silicon). The outlet to the surrounding environment filled with air (fluid 0) has a constant pressure of 0 Pa which means atmospheric pressure. Finally the model exhibits a rotational symmetry around the axis of symmetry. Typically, one complete simulation (30 µs simulation time) takes about 10 to 15 hours on a state of the art PC (Pentium P4, 1.8 GHz, 512 MB RAM).

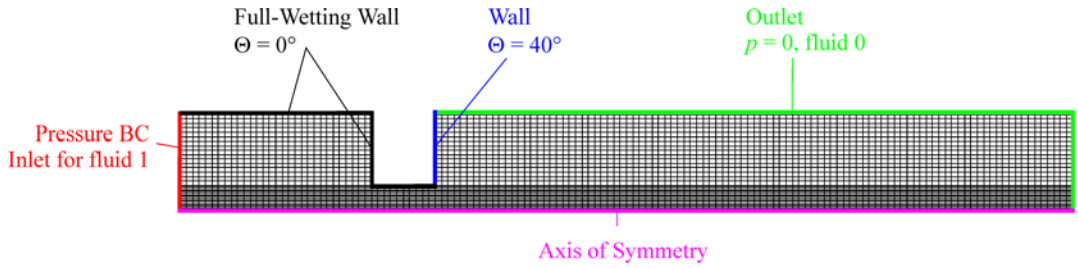

Figure 3.13: *Structured grid of the used nozzle model depicted in figure 3.12 and applied boundary conditions.*

Based on the presented model a set of simulations was performed with varying time dependent pressure boundary conditions at the inlet of the nozzle chamber. First of all a constant pressure below the critical pressure and one slightly above it were applied to verify the energetic model. In figure 3.14 two pictures of the CFD simulations are displayed for the pressures of 150 kPa and 200 kPa, respectively. The lower pressure is not enough to overcome the hindering surface tension forces and the delivered liquid volume leads to a wetting of the surrounding surface. A pending droplet is created. In contrast to that the higher pressure leads to a jet ejection. Using the velocities at the nozzle outlet provided by the CFD simulation and averaged over the cross section, the Weber number can be calculated to compare it with the critical value. The averaged velocities at the nozzle outlet can be obtained by a direct output of the CFD tool for

every time step. The maximum velocity over the time was taken to calculate the corresponding Weber numbers. The Weber numbers for these both cases are $We = 6.7$ and $We = 10.0$ for the low and the high pressure, respectively. Both values are lower than the critical value 12 for the drop-on-demand breakup, but the second one fulfils the criterion $We > 8$ for a Rayleigh breakup. In contrast to this, the calculation of the Weber numbers using the energetic approach in section 3.1.2 leads to $We = 6.7$ and $We = 12.5$, respectively. This example demonstrates, that the analytical model is of qualitative nature only and cannot replace a full CFD treatment where additional pressure losses are taken into account. Nevertheless, it provides a good estimate of the qualitative behavior to be expected.

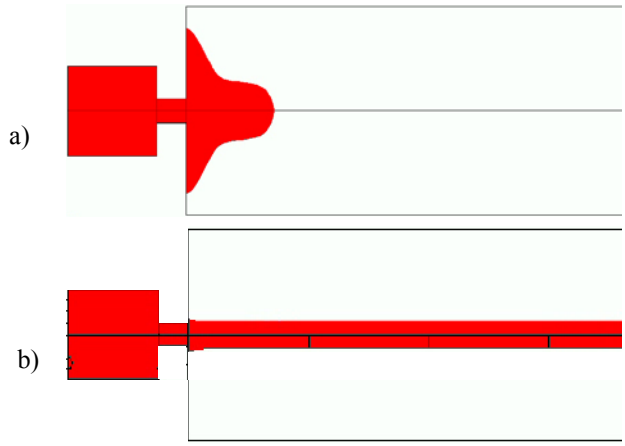

Figure 3.14: *Results of the CFD simulation for a constant pressure of a) 150 kPa and b) 200 kPa. The Weber numbers are a) We = 6.7 and b) We = 10.0.*

The further proceeding was to superimpose a periodic, time dependent disturbance on the constant pressure offset. A sinusoidal disturbance with a frequency of 350 kHz was chosen because of an existing application with this boundary condition. However, this frequency is far away from the optimum disturbance frequency for Rayleigh breakup, which would be about 83 MHz in this case, calculated with equation (3.28). Nevertheless, also with such a smaller frequency, the droplet breakup can be supported to a certain extent. In figure 3.15 and figure 3.16 the results for the simulations with a constant pressure offset of 200 kPa and a pressure amplitude of 20 kPa and 50 kPa are displayed, respectively. The corresponding Weber numbers are $We = 11.1$ and $We = 12.9$ for the lower and the higher pressure amplitude, respectively. The higher pressure amplitude leads to a higher maximum velocity at the nozzle outlet, but also to a shorter distance where the droplet breakup occurs. For comparison with the critical values of pressure, time and power, the obtained values are marked in the figures. The critical pressure is drawn as horizontal line and the time how long the critical pressure is surpassed is written in the box. The time dependent power was calculated by multiplying the applied pressure with the obtained volume flow. The maximum power as well as the mean power were determined over one half period during which the critical pressure was exceeded. The time how long the critical pressure is surpassed is

1.43 µs, respectively, which is about 4.8 times the critical time. The calculated mean power of 3.38 µW, respectively 3.96 µW and the calculated maximum power of 4.18 µW, respectively 5.08 µW are 7.7 to 5.1 times smaller than the critical power.

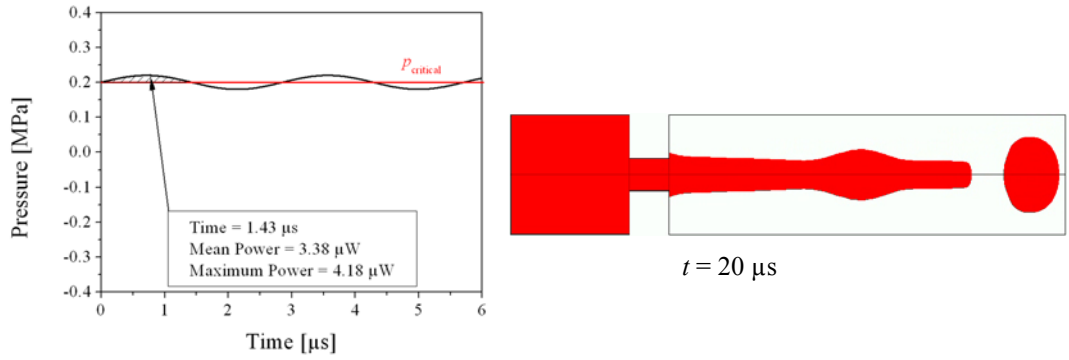

Figure 3.15: *Applied pressure boundary condition for the CFD simulation with a constant pressure offset of 200 kPa and a superimposed pressure amplitude of 20 kPa at a frequency of 350 kHz and the corresponding simulation result. The Weber number is We = 11.1.*

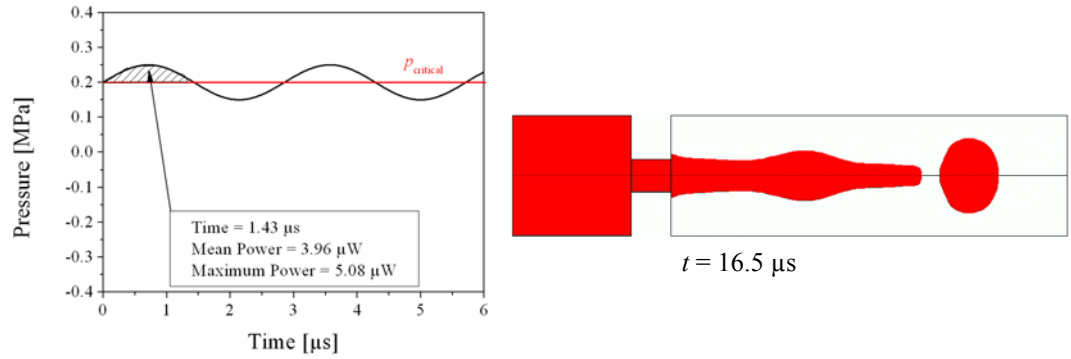

Figure 3.16: *Applied pressure boundary condition for the CFD simulation with a constant pressure offset of 200 kPa and a superimposed pressure amplitude of 50 kPa at a frequency of 350 kHz and the corresponding simulation result. The Weber number is We = 12.9.*

Comparatively, the breakup length for a non-disturbed jet with subsequent Rayleigh breakup can be calculated using equation (3.30), which leads to a breakup length of about 250 µm for both cases, whereas the CFD simulation for the disturbed jet results in a breakup length of about 40 µm and 30 µm. This discrepancy can be explained by the fact that an additional disturbance leads to a faster growth of the natural occurring disturbance, hence, an earlier breakup compared to the non-disturbed case.

For a jet ejection using a constant pressure with a subsequent Rayleigh droplet breakup it is apparently necessary to surpass the critical Weber number of 8 instead of 12. This could be proven by a set of simulations depicted in the figure 3.21. Furthermore, superimposing the constant driving pressure with a more or less pronounced disturbance leads to the possibility to control the droplet breakup concerning breakup length and droplet velocity.

To achieve the intended drop-on-demand droplet ejection the amplitude of the disturbance has to be intensified while the pressure offset can be reduced. Nevertheless, the critical pressure has to maintained at least for the critical time to generate a droplet as it can be seen in figure 3.17 to figure 3.19. In all figures the pressure offset is 100 kPa with increasing pressure amplitude from 150 kPa to 250 kPa. The applied pressure amplitude of 150 kPa in figure 3.17, which corresponds to a Weber number of We = 11.2, does not suffice to eject a droplet. The extracted volume increases with the time but it pulsates at the nozzle outlet not overcoming the attractive surface tension forces and a pending droplet is created. A Weber number of We = 14.2, which can be observed for a pressure amplitude of 200 kPa in figure 3.18, is sufficient to eject single droplets in a drop-on-demand mode or at least with a very short breakup length. A satisfactory performance can be achieved using 250 kPa as pressure amplitude resulting in a Weber number of We = 17.4 as depicted in figure 3.19. This mode is more stable compared to the previous one and the ejected droplets have larger distances in between. The time how long the critical pressure is exceeded is 0.77 µs, 0.96 µs and 1.06 µs, respectively, which is about 2.6, 3.2 and 3.5 times the critical time, respectively. The calculated mean power of 3.93 µW, 4.96 µW and 6.16 µW, respectively and the calculated maximum power of 4.66 µW, 6.39 µW and 8.38 µW, respectively are 6.6 to 3.1 times smaller than the critical power.

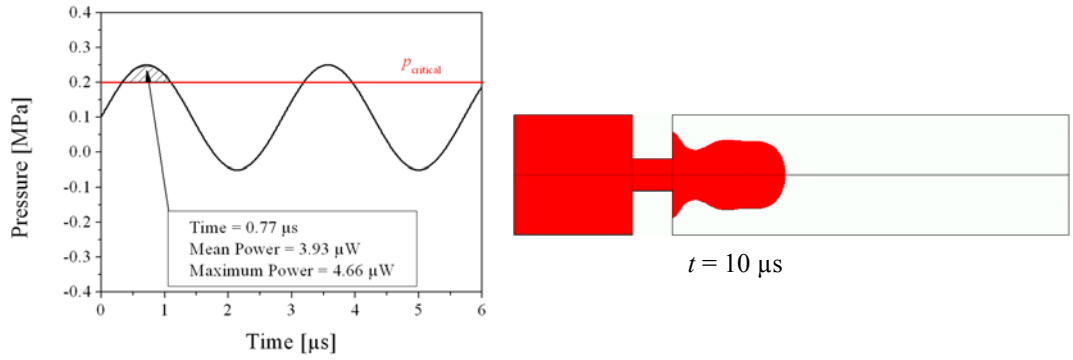

Figure 3.17: *Applied pressure boundary condition for the CFD simulation with a constant pressure offset of 100 kPa and a superimposed pressure amplitude of 150 kPa at a frequency of 350 kHz and the corresponding simulation result. The Weber number is We = 11.2.*

Contrary to the Rayleigh breakup mode, a Weber number surpassing the critical value of 12 is necessary to eject droplets in the drop-on-demand mode. However, the applied pressure amplitude has to be relatively high to insure a stable operation. Otherwise, the distance of subsequent droplets decreases with time and some of them even collide. This can happen repetitively or chaotically. The amplitude can also be used to vary the droplet velocity and the distance between two subsequent droplets. There against, the droplet volume and shape seem to be nearly independent on the applied pressure amplitude as well as offset at a stable operation.

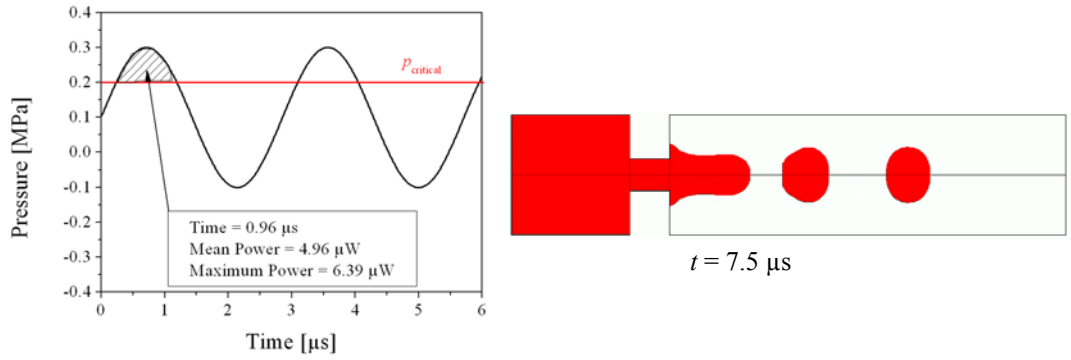

Figure 3.18: *Applied pressure boundary condition for the CFD simulation with a constant pressure offset of 100 kPa and a superimposed pressure amplitude of 200 kPa at a frequency of 350 kHz and the corresponding simulation result. The Weber number is We = 14.2.*

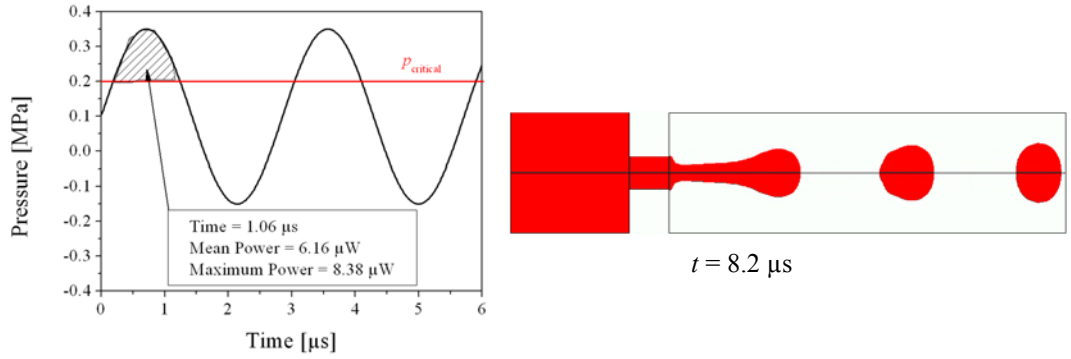

Figure 3.19: *Applied pressure boundary condition for the CFD simulation with a constant pressure offset of 100 kPa and a superimposed pressure amplitude of 250 kPa at a frequency of 350 kHz and the corresponding simulation result. The Weber number is We = 17.4.*

One could assume that a sinusoidal pressure boundary condition without pressure offset, like it is displayed in figure 3.20 for a pressure amplitude of 300 kPa, should yield an optimum droplet ejection. However, a pressure profile where the average pressure is zero leads to a sucking back of air into the nozzle chamber. Furthermore, a bursting of the droplet due to the successional droplet can be observed like displayed in figure 3.20. The same behavior can be observed independently on the pressure amplitude. According to this, a certain pressure offset is necessary for a satisfactory refilling of the nozzle and a homogeneous droplet generation.

The jet or droplet breakup can also be affected by varying the applied disturbance frequency. For a jet ejection with subsequent Rayleigh breakup the disturbance frequency is crucial to achieve either a stable or a chaotic breakup. If a stable jet ejection is present, the jet breakup length can be influenced by the disturbance frequency. Consider the stable jet ejection with Rayleigh breakup with the pressure boundary condition given in figure 3.16. Reducing the disturbance frequency step wise to 150 kHz, leads to an increasing jet breakup length. Below 150 kHz, the stable

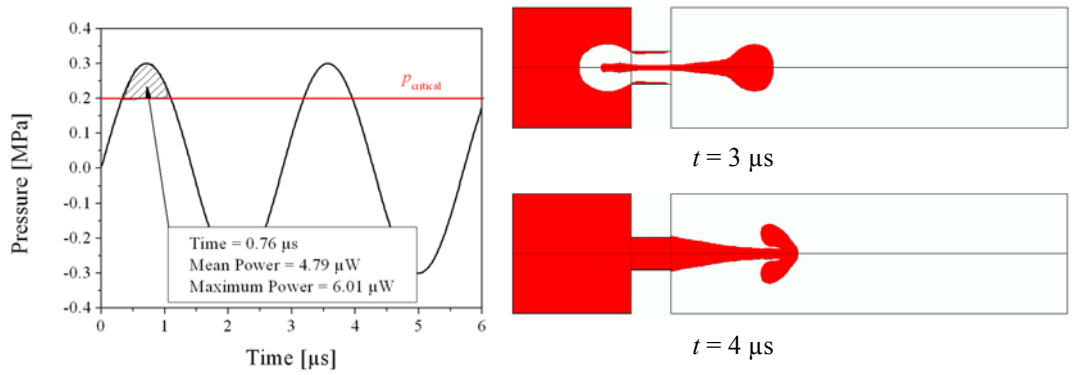

Figure 3.20: *Applied sinusoidal pressure boundary condition for the CFD simulation with a pressure amplitude of 300 kPa at a frequency of 350 kHz and the corresponding simulation result at two different times. The second picture indicates the first ejected droplet bursted by the successional faster droplet.*

Rayleigh breakup with a fixed jet breakup length even changes in a chaotic breakup with no stable jet breakup length. Increasing the frequency up to 500 kHz leads to ever shorter and shorter jet breakup lengths.

Furthermore, also the droplet ejection with drop-on-demand breakup can be affected by the applied disturbance frequency concerning droplet volume, droplet velocity and droplet spacing. Consider the stable droplet ejection with drop-on-demand breakup with the pressure boundary condition given in figure 3.19. Reducing the disturbance frequency to 50 kHz leads to single jets with increasing length rather than single droplets. However, these jets are ejected "jet-on-demand" and are not comparable to the stable jets occurring at a Rayleigh breakup. Increasing the frequency results in smaller droplets with decreasing droplet spacing. Finally, at frequencies over 450 kHz, no more droplet breakup can be observed because the droplets are following to fast that they can not detach anymore.

Summarizing the results presented so far, a jet ejection with subsequent Rayleigh droplet breakup can be achieved by a constant pressure offset with no or a small superimposed disturbance. For a Rayleigh breakup the Weber number should exceed the critical value of 8 but not necessarily has to surpass the critical value of 12. A drop-on-demand breakup can be obtained using a smaller constant pressure offset and a relatively high disturbance to create single droplets. In this case a Weber number higher than the critical Weber number of 12 has to be attained to get a single droplet ejection. However, the critical pressure calculated with equation (3.20) has to be exceeded in both cases. At least for the critical time, to force a droplet breakup, whether Rayleigh or drop-on-demand.

In figure 3.21 the pressure offset and disturbance amplitude for both types of droplet breakup are displayed for the considered specific problem. The approximate division is based on the accomplished simulations indicated by the dots. From a certain pressure offset on (approximately 0.2 MPa), always a jet with a Rayleigh breakup occurs, whereas only a small range exists, where a drop-on-demand breakup occurs.

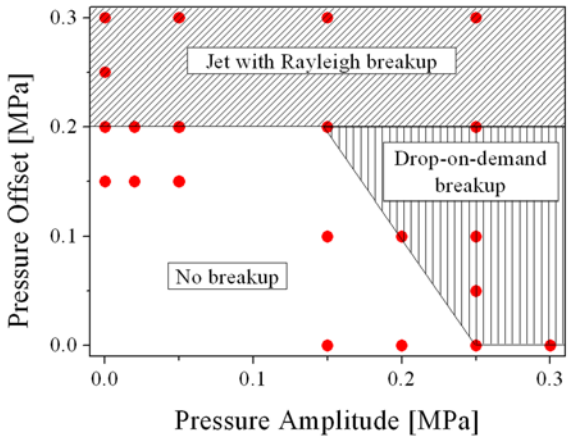

Figure 3.21: *Pressure offset and disturbance amplitude for the both occurring droplet breakup mechanisms, the Rayleigh breakup and the drop-on-demand breakup using a constant pressure offset and an additional superimposed sinusoidal disturbance. The approximate division is based on the accomplished simulations indicated by the dots.*

As alternative to the use of a constant pressure or an additional superimposed sinusoidal disturbance, also a rectangular pressure pulse with variable pressure height and pressure duration can be considered. Such a pulse shape is typical for piezoelectric drop-on-demand inkjet devices. To investigate such an operation mode, the above presented CFD model was used applying a rectangular pressure pulse with pressure head p and pulse duration t_{on} as depicted in figure 3.22. The pressure head was varied from 150 kPa to 350 kPa and the duration was varied from 0.25 µs to 10 µs. The ejected droplet volume and the obtained Weber number serve as appropriate values for comparison.

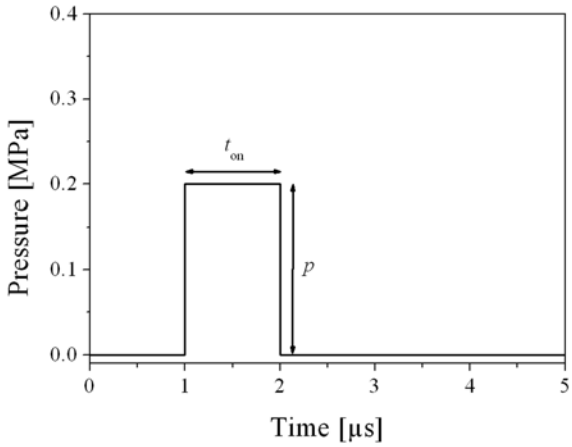

Figure 3.22: *Ejected volume depending on the pressure p and the pressure duration t_{on} using a rectangular pressure pulse with corresponding values.*

In figure 3.23 and figure 3.24 the effect of the pressure p and the pressure duration t_{on} on the ejected volume and on the Weber number are displayed, respectively. The ejected volume depends linearly on the pressure duration as well as on the pressure

head, except of inertial effects which are present for very short pressure durations (< 1 µs). The Weber number, and with it the velocity, also depends linearly on the pressure, but it is nearly independent on the pressure duration after a constant flow is established.

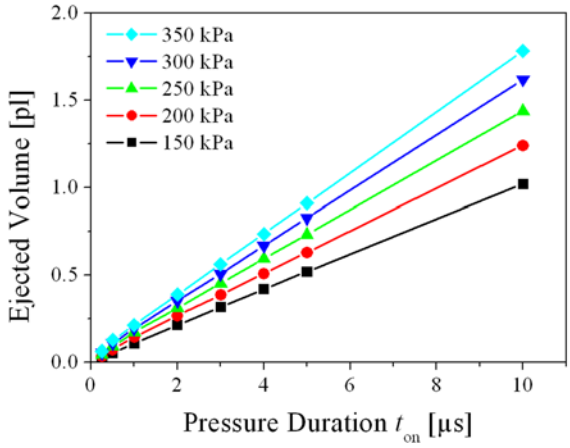

Figure 3.23: *Ejected volume depending on the pressure p and the pressure duration t_{on} using a rectangular pressure pulse with corresponding values.*

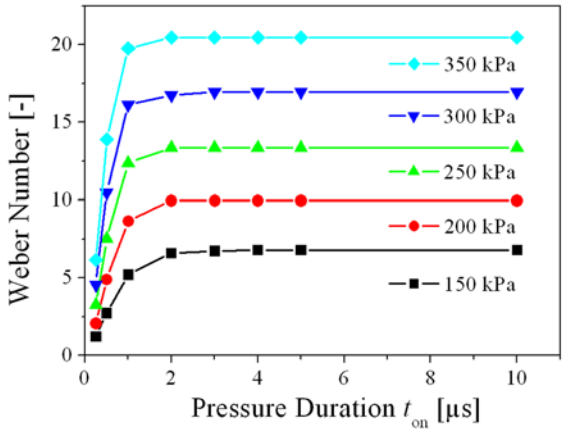

Figure 3.24: *Weber number depending on the pressure p and the pressure duration t_{on} using a rectangular pressure pulse with corresponding values.*

In the case of a rectangular pressure pulse it has to be distinguished between no ejection, a "jet-on-demand" breakup where the jet can separate into several single droplets and a drop-on-demand droplet formation. To generate a jet with subsequent Rayleigh breakup much longer pressure durations would be necessary. Whether one or the other of these possibilities occur can not be deduced by the pressure durations or Weber numbers only. To differentiate between drop-on-demand and jet-on-demand breakup the evaluation of the CFD simulations is necessary. In figure 3.25 the assumed pressure head p and pressure duration t_{on} for the both occurring breakup mechanisms are displayed. The approximate division is based on the accomplished simulations indicated by the dots. Surprisingly, a droplet breakup can be observed at Weber

numbers of 10, which is slightly below the critical value. However, for both breakups the pressure exceeds the critical value of 200 kPa for at least 1.2 µs which is 4 times the critical time.

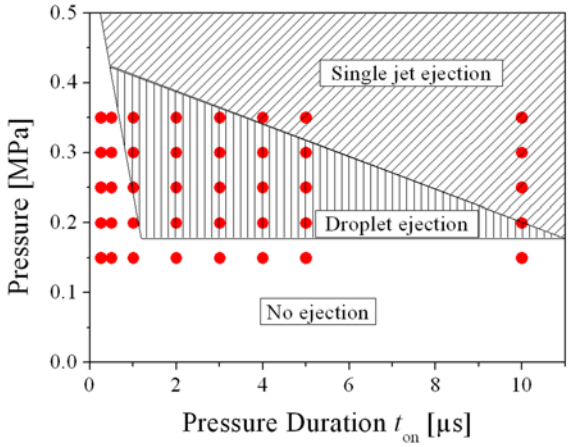

Figure 3.25: *Pressure conditions for the both occurring droplet breakup mechanisms, the "jet-on-demand" and the drop-on-demand breakup using a rectangular pressure pulse with pressure p and pressure duration t_{on}. The approximate division is based on the accomplished simulations indicated by the dots.*

In summary of the above presented results two criteria for the ejection of a jet or a droplet can be fixed. First, if the actuation pressure exceeds the critical pressure $p_{critical}$ for at least a crucial time, or if the mean value of a dynamic pressure pulse achieves or exceeds the critical pressure, a jet is ejected. The at least required time period can be estimated out of the CFD simulations to be about 1.2 µs for the presented case, which corresponds to 4 times the calculated critical time of $t_{critical}$ = 0.3 µs for a single droplet with a diameter equal to the nozzle diameter. If the actuation pressure exceeds the critical value significantly for a period of time longer than 4 x $t_{critical}$ = 1.2 µs a droplet or jet is ejected. The reason for this is that the diameter of the really ejected droplet is not equal to the diameter of the nozzle but somewhat larger. It is about 6.3 µm instead of 4 µm which is the nozzle diameter. Due to this the really ejected volume is about 4 times larger than the assumed volume with a 4 µm droplet. Hence, at a fixed velocity respectively volume flow at the nozzle outlet the time has to be 4 times longer to eject a 4 times larger volume. Due to this the required time of 1.2 µs in the CFD simulations and the 4 times shorter critical time of 0.3 µs, calculated with the energetic approach are equivalent. Thus, the critical time has to be scaled with the really ejected volume compared to the assumed volume in the energetic approach.

NETWORK MODEL

In order to provide a faster method than CFD to describe the dynamic behavior of droplet ejection processes, a network model was set up. It is based on the nozzle geometry depicted in figure 3.12 and relies on the network tool Saber [69]. The used inlet boundary condition was assumed to be the same pressure boundary condition as

used for the CFD simulations presented in the previous section. The system was initially built up using only the formulas for fluidic resistance and inertance introduced in section 2.4. To validate the network model it was compared to the results of the CFD simulation. Initial deviations could be eliminated by considering all supplementary pressure losses as listed in equation (3.8) which could also be observed in the CFD model. In the forward direction of the flow, the additional resistance due to the contraction of the cross section (cf. section 2.4.6) and due to the entering length (cf. section 2.4.5) had to be implemented. The corresponding pressure losses are visualized in figure 3.26 by CFD simulation results. In the backward direction the resistance due to the expansion of the cross section (cf. section 2.4.6) and due to an additional inertance (section 2.4.2) produced by the slowly stretching of the velocity profile had to be implemented into the network model. This slowly stretching of the velocity profile inside the CFD simulations is displayed in figure 3.27. The length of the additional inertance in backward direction depends on the entering length of the nozzle (cf. section 2.4.5). However, comparing the results of the network model with the CFD simulation an inertance with the length of the entering length calculated with equation (2.55) didn't suffice to get the same results. An inertance length of twice the entering length has to be added to get finally the same results as the CFD simulations. The pressure loss due to the outflow of the nozzle (cf. section 2.4.4) is omitted in this case because the droplet formation itself was not considered but only the pressure losses inside the nozzle.

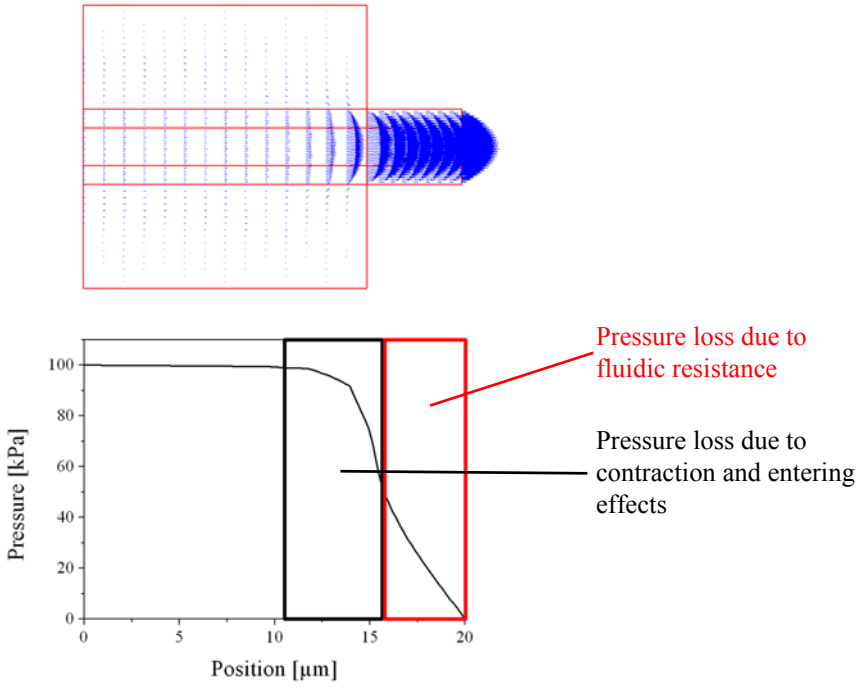

Figure 3.26: *Visualization of the additional pressure loss due to the contraction of the cross section and due to the entering length for the forward direction.*

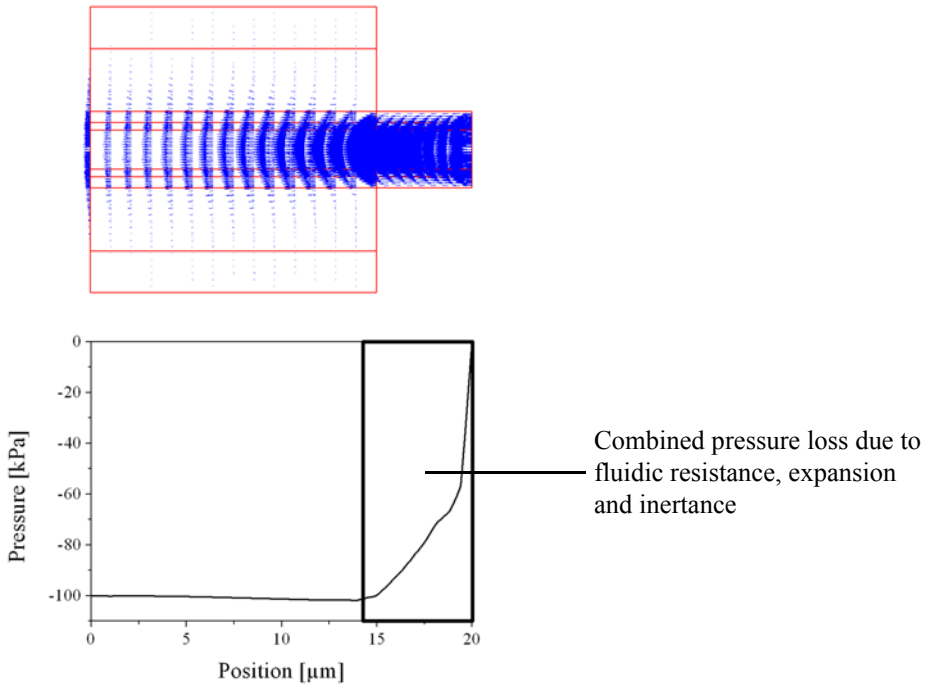

Figure 3.27: *Visualization of the additional pressure loss due to the expansion of the cross section and due to an additional inertance for the backward direction.*

The final network model providing the same results as the corresponding CFD simulations is displayed in figure 3.28. The nozzle is realized by a fluidic resistance, inertance and additional components. These are an additional fluidic resistance representing the pressure losses due to junction effects and an additional fluidic inertance which is produced by the slow stretching of the velocity profile and which is only valid for the backward direction.

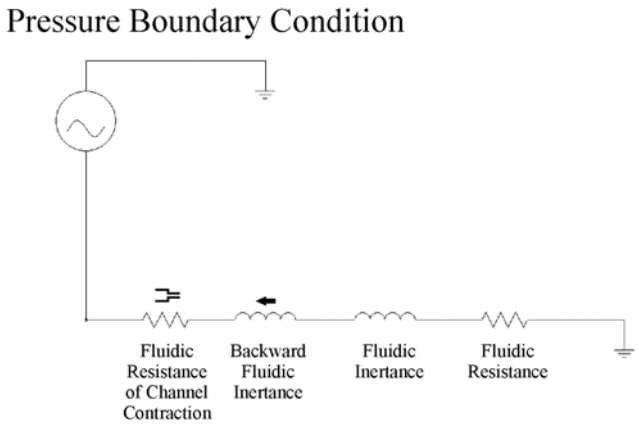

Figure 3.28: *Final network model providing the same results as the corresponding CFD simulations.*

Comparing the results of the CFD simulations with the corresponding network simulations good agreement can be obtained. However, these simulations have been performed without VOF method, i.e. without taking into account the free surface of an ejected droplet. First a stationary simulation has been performed to study the stationary

behavior of the nozzle in forward as well as backward direction. For a constant pressure of 100 kPa which leads to a flow in the forward direction the attained flow rates are 73.0 x 10^{-12} m^3/s for the CFD and 74.3 x 10^{-12} m^3/s for the network simulation, respectively. For a constant pressure of -100 kPa which leads to a flow in the backward direction the attained flow rates are -64.8 x 10^{-12} m^3/s for the CFD and -68.9 x 10^{-12} m^3/s for the network simulation, respectively. The comparison of the dynamic behavior of both models is displayed in figure 3.29. The displayed time dependent pressure was used as input for both methods. The obtained flow rates are very similar for the forward as well as for the backward direction.

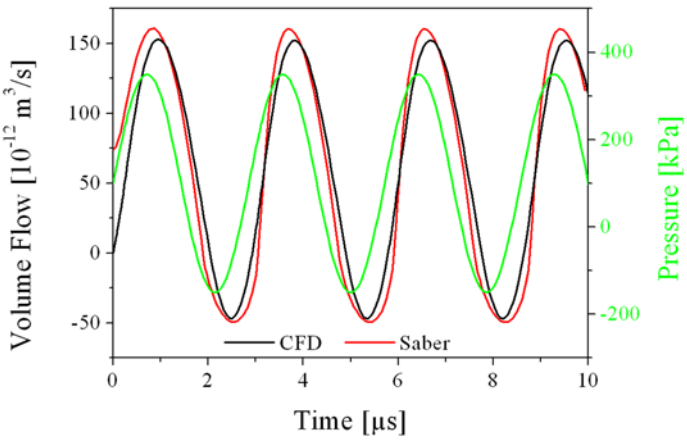

Figure 3.29: *Comparison of the obtained flow rates for the CFD simulation and the network simulation using Saber. The time dependent pressure was used as input for both methods.*

This network model complements the both presented simulation methods, analytical estimations and CFD simulations. The analytical calculations provide a fast estimation of the requirements of a droplet generator, whereas the CFD simulations provide very detailed informations but need much time. There against, the network model provides a fast, robust and reliable method describing a droplet ejector, however, disregarding details of the droplet formation and morphology, and surface tension effects.

3.3 Classification of Droplet Generators

Aim of this section is to derive a clear classification of droplet generating devices based on the applied actuation principle which results in a specific boundary condition. This is different from the majority of publications which consider the obvious construction elements of droplet generators or provide classifications based on historical reasons. Grounded on the concept applied in CFD simulations where either a pressure boundary condition or a flow boundary condition is used, real droplet generators can be distinguished using the type of actuation mechanism. Of course pressure and flow are not independently tunable because they are connected by the

Navier-Stokes equation. Nevertheless, in many droplet generators either the pressure or the flow is controlled externally. On the one hand an external ideal pressure source can be considered to be not influenced by the flow inside the device. On the other hand an external ideal flow source provided by a volume displacement with sufficiently strong actuator should not be influenced by the pressure inside the device. Thus either a pressure boundary condition or a flow boundary condition is appropriate for the description by CFD and thus for classification. However, there exist also droplet generators where a combination of pressure and flow represents the correct boundary condition. In this case neither an ideal pressure source nor an ideal flow source is the correct assumption. The pressure inside the system is influenced by the flow and vice versa. Due to this also a third group of droplet generators with a combined pressure and flow boundary condition has to be established.

Finally, a fourth group is listed containing the acoustic actuation which is a special kind of pressure boundary condition. The reason for the distinction is that the acoustic boundary condition has a totally different physical background compared to the other boundary conditions. Whilst the pressure, the flow and the combined pressure and flow boundary conditions can be completely described by the set of differential equations (2.25) to (2.28) explained in section 2.2, the one-dimensional pressure spreading within an acoustic actuated system follows the so called wave equation [109,142]:

$$\frac{\partial^2 p}{\partial x^2} = \frac{1}{c^2} \cdot \frac{\partial^2 p}{\partial t^2}. \tag{3.31}$$

Where the factor c indicates the properties of the used medium like density, elasticity and similar which is equivalent to the phase velocity. In contrast to the pressure, the flow and the combined pressure and flow boundary conditions for the acoustic actuation the convective term $(\vec{v} \cdot \nabla)\vec{v}$ of the Navier-Stokes equation vanishes because no substantial liquid flow inside the device occurs. Additionally the density of the medium has to be considered for the acoustic actuation to implement the pressure spreading.

The presented classification, however, is not absolutely fixed by the fluidic setup because single droplet generators can even change the group by operating it in different modes. For example a device out of the pressure or flow boundary condition class can convert in the combined pressure and flow boundary condition class or vice versa. This can occur when the actuation behavior changes due to changes in the setup.

3.3.1 Pressure Boundary Condition

Regarding the simple model in figure 3.12, a pressure boundary condition exists when the nozzle chamber is pressurized by some kind of actuation producing a constant or transient pressure. This results - according to the Navier-Stokes equation - in a volume flow depending on the geometry and the fluid properties. However, the arising volume flow does not affect the pressure backwardly. In real devices the way how the pressure

is produced depends on the actual system. This group especially encloses all droplet generators using a constant pressure with subsequent Rayleigh breakup or a constant pressure switched by a fast valve. In these cases the pressure can be considered to be provided from a large pressure reservoir which is not influenced by the small volume change caused by the droplet ejection.

An example for this class of devices discussed within this thesis is the Dispensing Well Plate, which is explained in section 6.1 in more detail. Furthermore, there are some droplet generators like from Vermes [143], Delo Industrieklebstoffe [42], NanoJet from microdrop Technologies [144], or Cartesian Dispensing Systems [145] where the droplet generator itself is a kind of fast switching valve. In some cases, the movement of a piston or a similar component adds an additional momentum to the droplet. If this is the case the classification eventually has to be done according to section 3.3.3. These kind of droplet generators are described in more detail in section 6.2. The TopSpot method, described in section 6.5, is based on a chamber filled with air which is compressed by a fast movement of a piezoelectric stack. Due to this a pressure is generated in this chamber and the technology has to be classified to be based on a pressure boundary condition. Furthermore, all syringe solenoid systems, based on a displacement of liquid creating an overpressure within a tubing system and the droplet ejection through a capillary tip controlled by a electromagnetic valve, are also arranged in this class of boundary condition.

3.3.2 Flow Boundary Condition

In contrast to the pressure boundary condition, in the class of flow boundary condition based devices predominantly the flow is adjusted by the external actuation. Mainly this means that a fixed volume displacement is generated within a certain period of time which leads to a preset volume flow. The pressure inside the system follows from the Navier-Stokes equation and depends on the geometry and the fluid properties. However, the arising pressure can be assumed not to affect the volume flow reversely. Such a volume displacement or flow can be achieved for example by reduction of a chamber volume due to a bending of a membrane by a piston or by squeezing a tube or a capillary.

The NanoJet device, which is described in section 6.3, is one example of a device driven by a flow boundary condition. A fluid chamber covered with a silicon membrane is compressed by bending the membrane using a piezoelectric stack. This leads to a volume displacement inside the chamber. The used piezo stack is much stronger compared to piezo discs or beams usually used in piezo inkjet devices. Due to this the piezo stack is capable to displace the liquid in spite of any back pressure. The PipeJet principle, like explained in section 6.4, is based on a volume displacement inside a polymer tube due to a squeezing of the tube using again a piezoelectric stack. The TopSpot Vario technology, which is a variation of the TopSpot technology, applies an elastomer to create a volume displacement at the backside of the nozzles. This

technology is explained in more detail in section 6.6. The replacement of the air chamber with the elastomer in the TopSpot device leads to a change of the actuation boundary condition. This is due to the fact that the incompressible elastomer transfers the stroke of the actuator into a volume displacement instead of a pressure generation like it is the case for the compressible air chamber. A further example for this class of devices are the micropipettes from TTP Labtech [146] made of high grade polyethylene and stainless steel. The so formed "micro" syringes are actuated by moving the piston with a programmable stepper motor.

3.3.3 Combined Pressure and Flow

Some droplet generators do fit in none of the above presented classes because neither the pressure nor the flow can be controlled independently. In these devices only a combination of the quantities can be influenced. Either the actuator is not strong enough to impose a predefined boundary condition. Or the device is designed in a way to support coupling between liquid flow and pressure. The best example for this class is the thermal bubble jet printhead which is described in detail in chapter 5. In the bubble jet the actuation is created by a heating pulse and the resulting vapor bubble. But the bubble represents a pressure as well as a flow boundary condition. In the first actuation period of the bubble creation a very high pressure is generated due to the explosive vaporization of the ink. In this period a pressure boundary condition is predominating the actuation. After that the growing bubble generates a volume displacement due to its increasing size. In this period a flow boundary condition is dominating the actuation. However, the vapor bubble is compressible and due to this the size of the bubble depends on the pressure inside the nozzle chamber as well as on the volume flow. Hence, the bubble jet experiences definitely a combined pressure and flow boundary condition. Nowadays, bubble jet printheads are manufactured by e.g. Hewlett Packard [2], Canon [3], Olivetti I-Jet [4] and Lexmark [5].

A further example of a combined actuation is the aerosol atomizer, explained in section 6.7, due to the fast movement of the covering membrane at an operation frequency of several hundred kilohertz, a pressure is generated inside the fluid chamber. However, the membrane also produces a volume displacement which also contributes to the droplet ejection. Despite the fast movement acoustic effects can be excluded at least in the actuation direction because the nozzle channel is too short for an acoustic wave length to be established. But a disturbing effect of possible acoustic waves perpendicular to the actuation movement can not be excluded. In consequence of this the aerosol atomizer is a highly complicated droplet generator with a mixed boundary condition with at least pressure and flow components. It is still not clear if also vertical acoustic effects have to be considered.

The droplet generator from GeSim [147] is very similar to the NanoJet system which is described in section 6.3 and arranged in the flow boundary condition class. The reason why the NanoJet system and the GeSim system are classified differently

although both are based on the same functional principle is the different actuators. Due to the strong actuator (damping force ≈ 1000 N) and the high displacement of the actuator in the NanoJet system the resulting volume displacement can be assumed as flow independent. This means that only negligible coupling is present between volume displacement and generated pressure. This is the reason why it is qualified for the flow boundary condition class. The "weak" actuator (damping force ≈ 5 N) and the strong coupling of piezoelectric actuator and membrane in the GeSim system yield that the volume displacement depends on the pressure inside the system. This is the reason why it fits in the combined pressure and flow boundary condition class.

A similar problem can occur with the PipeJet system. If the used polymer tube allows for a squeezing only and not for an elastic deformation of its walls, the system is classified correctly in the flow boundary condition group. However, if the tube shows elastic deformation in itself, a fluidic capacitance has to be considered creating a coupling between the pressure boundary condition and the flow boundary condition. In this case the PipeJet has also to be classified in the group of combined actuated systems because than it has an additional pressure component which can not be neglected.

3.3.4 Acoustic Actuation

In principle, the acoustic actuation is a special kind of the pressure boundary condition because also here a pressure is generated. However, in contrast to a pressure boundary condition creating a convective flow, the acoustic actuation does not lead to a substantial liquid flow inside the device during droplet ejection. The spreading velocity of the induced density fluctuations is approximately the speed of sound in the liquid which is much faster than in the case of a fluid dynamic pressure actuation. In practice the acoustic pressure is mostly generated with a piezoelectric transducer. The created shock wave travels through the liquid where it can be influenced by reflections from the channel walls. In some cases such reflections are intended to make use of constructive interferences by establishing a standing wave for a short period of time. When the shock wave hits the meniscus at the nozzle the pressure is transformed into kinetic energy and a droplet is ejected. This principle is very reproducible if all parameters are kept constant, however, it is very sensitive to the fluid properties. This method is used by most of the inkjet manufacturers using a piezoelectric actuator which are Epson [6], Xaar [7], Spectra [8], Xerox [9] and TallyGenicom [10] in order to mention the most important ones. But there are also manufacturers focused on other applications like the MicroDrop method from microdrop Technologies [144] and a nanopipetting option from Tecan [148] using this technology. In contrast to all others, Xaar uses a piezoelectric transducer in a shear mode and the additional effect that the printhead picks up "swing" using the reflection of the shock wave at the rear end of the channel to intensify the pressure at the nozzle [7,149,150].

A special variant of the acoustic actuation is the focused ultrasound acoustic actuation which was originally invented by Xerox [9] for printing applications at Palo Alto Research Center (PARC) [151-153]. The function principle is the same as the normal acoustic actuation with the main difference that no nozzle is required. The shock wave is focused on the liquid surface by an acoustic Fresnel lens. Due to this it is possible to eject droplets with different size (from picoliter to nanoliter) from the same device which is applied by Labcyte [154]. Advantage of this method is the simple fluidic setup and that the droplet volume is tunable in a certain range by adjusting the focal distance of the acoustic lens [100].

3.3.5 Definitions of Droplet Generation Mechanisms

In order to distinguish between different droplet formation mechanisms in the following, three different kinds of droplet formation mechanisms observed in section 3.2.4 are defined. Additionally typical parameters of these droplet formation mechanisms are demonstrated based on the findings observed in this chapter. Therefore the typical droplet volumes, the typical time scales and the typical Weber numbers are indicated.

- Drop-on-demand breakup:
  The droplet volume is in the range of equal to 5 times the volume of a droplet with a diameter equal to the nozzle diameter V_{nozzle}. The time scale is in the range of $t_{critical}$ to 5 times $t_{critical}$. The Weber number is in the range of 12 to 40.
  ($V_{nozzle} < V < 5 \times V_{nozzle}$, $t_{critical} < t < 5 \times t_{critical}$, $12 < We \leq 40$).
- Jet-on-demand breakup:
  The jet volume is in the range of 10 times to 50 times the volume of a droplet with a diameter equal to the nozzle diameter V_{nozzle}. The time scale is in the range of 5 times $t_{critical}$ to 50 times $t_{critical}$. The Weber number is in the range of 12 to 40.
  ($10 \times V_{nozzle} < V < 50 \times V_{nozzle}$, $5 \times t_{critical} < t < 50 \times t_{critical}$, $12 < We \leq 40$).
- Rayleigh breakup:
  The ejected volume is larger than 50 times the volume of a droplet with a diameter equal to the nozzle diameter V_{nozzle}. The time scale is longer than 50 times $t_{critical}$. The Weber number is in the range of 8 to 12.
  ($V > 50 \times V_{nozzle}$, $t > 50 \times t_{critical}$, $8 < We \leq 12$).

4 EXPERIMENTAL METHODS

Beyond the theoretical description of the droplet formation also the experimental methods characterizing the droplet ejection process are not trivial. Especially when keeping in mind that the considered droplet volumes vary from the nanoliter to the femtoliter range. Furthermore, the droplet velocities vary typically from below 1 m/s to 12 m/s and the ejection frequencies can change from below 1 Hz to several hundreds of kHz. The most commonly applied methods to measure these values, which also have been used for this work, are presented in the following.

4.1 GRAVIMETRICAL MEASUREMENTS

A straightforward approach to define the volume of a dispensed droplet is to weigh it. It is a reliable and easy-to-handle measurement method. Using the density ρ of the liquid, which can be self-measured or obtained from literature and the measured mass m, the volume V is calculated with the simple formula

$$V = \frac{m}{\rho}. \tag{4.1}$$

But measuring droplets in the nanoliter or picoliter range is not that simple at all. In the case of water with a density $\rho = 1000\ \mathrm{kg/m^3}$ the droplets, having a volume of about 10 nl for instance, weigh only about 10 µg. Due to this, several effects make it very difficult to determine the weight of a single droplet.

First of all, the balance is not responding immediately after the bounce of the droplet due to the inertia of the system. It lasts about two seconds until the balance indicates a change of the mass whereas this idle time can be reduced by shooting multiple droplets. But due to this the impact on the balance is higher and the balance requires more time to settle. Furthermore, the evaporation of the droplet eliminates the possibility to read out the measured value directly while the balance equilibrates [155]. A procedure to obtain reproducible and accurate results despite the mentioned difficulties is described in the following.

THE BALANCE

The used balance used for gravimetrical measurements is a "Sartorius SC2" [156]. It is an electronic precision balance with a measurement range up to 2.1 g and a precision of 0.1 µg (last digit). It consists of two parts, the weighing cell and the electronic evaluation unit. The droplets are dispensed onto a weighing scale. To minimize the impact of air turbulences, it is surrounded with a windbreak. The electronic evaluation

unit is used to display the mass and to program the function mode of the balance. A RS 232 connection allows to examine the values using a computer for an advanced evaluation. The maximum sample rate of the balance is 10 Hz.

Experimental Setup

In order to separate the ambient disturbances like slightly air turbulences or vibrations, the balance is placed on a vibration absorbing granite table. The investigated droplet ejector is arranged above the weighing scale also positioned on the granite table. The scale is preloaded with a small reservoir filled with the liquid to be ejected, in order to reduce evaporation effects. If now a droplet is supplemented to the reservoir only the fluid level changes slightly but the free surface area remains unchanged. Surrounding the weighing scale, another container filled with water is placed to establish a saturated humidity in the windbreak which also reduces the evaporation rate. The whole setup is covered with a transparent plastic box to protect the measurement against turbulences like it is displayed in figure 4.1.

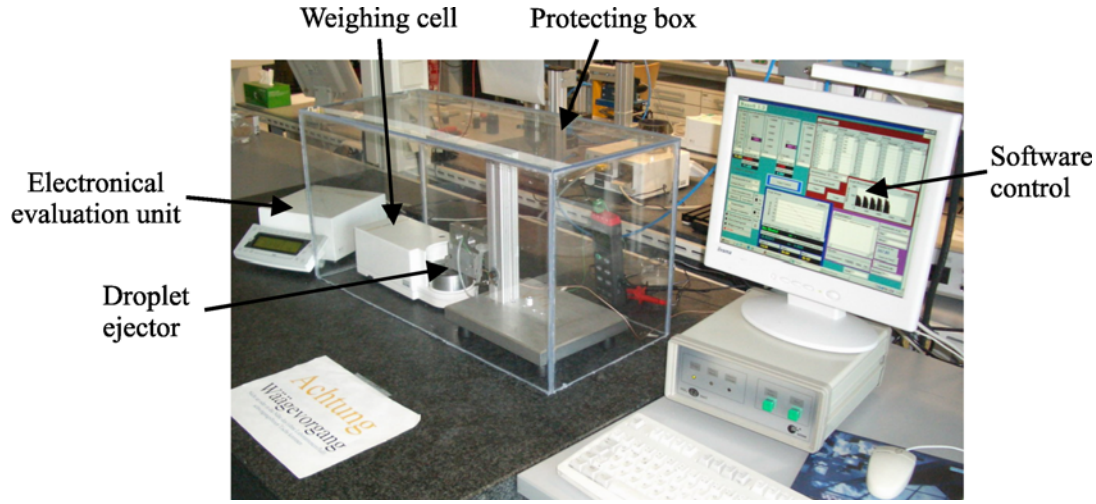

Figure 4.1: *Experimental setup for the weighing procedure.*

Weighing Procedure

To determine the droplet volume, the actual value of the balance is recorded before a droplet is dispensed. Therefore, five values are averaged because the water in the reservoir is evaporating continuously. A time of five seconds are granted to allow the balance to calm. The measured values during this time are not considered for the mass determination. Afterwards the evaporation is recorded using several measured values. The first measurement value can be obtained by extrapolating the linear evaporation line. The difference between these two measurements is equivalent to the dispensed droplet mass from which the volume can be calculated using equation (4.1). A typical measurement curve and the evaluation procedure is displayed in figure 4.2 [157].

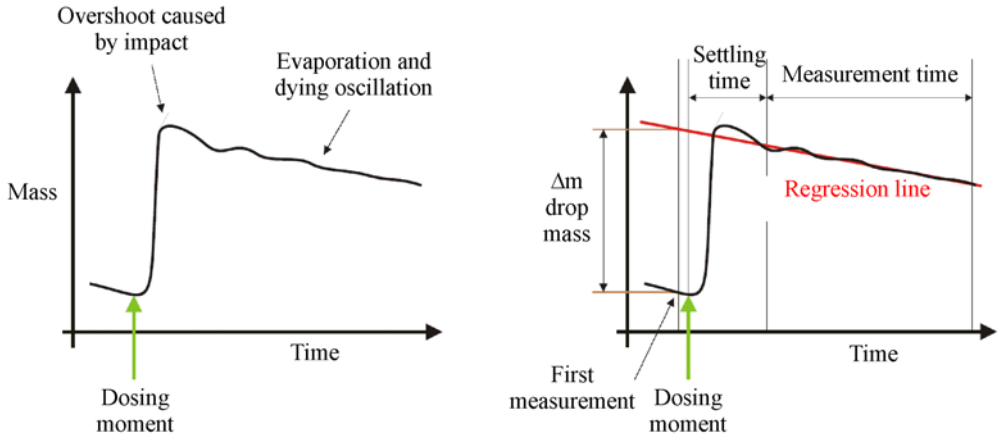

Figure 4.2: *a) Typical measurement curve, b) evaluation procedure for the determination of the dispensed mass [157].*

ERROR CONSIDERATION

Basically every measurement of a physical value is loaded with an error, i.e. the measured value is not correct. Hence, occurring errors have to be considered for the gravimetrical measurements. The absolute error Δx of a measurement results from the measured value x minus the true value x_t:

$$\Delta x = x - x_t . \tag{4.2}$$

Because the true value cannot be determined certainly, a confidence interval is specified rather than stating the measured value:

$$x_t = x \pm \Delta x . \tag{4.3}$$

There are two kinds of errors occurring in experimental examinations. A systematic error and a random error. A systematic error can arise from imperfect measurement equipment, neglected influences (pressure, temperature and others) or equipment affecting the considered device. Usually it leads to a constant offset of the measured value. These kind of errors can normally be minimized using a calibration or correction. Systematic errors which are not ascertainable are estimated and added to the random error. A random error can arise from inaccurate reading of a measurement display or statistical acting influences like vibrations or voltage fluctuations. For single measurements the random error has to be estimated. For numerous measurements the random error and the confidence interval can be calculated using statistical methods.

For the calculation of the confidence interval two values are calculated, the arithmetical mean value and the standard deviation. The mean value $\bar{x}$ of n measurements can be calculated using [95]:

$$\bar{x} = \frac{1}{n} \cdot \sum_{i=1}^{n} x_i , \tag{4.4}$$

The standard deviation s is a quantity for the reliability and can be calculated using [95]:

$$s = \sqrt{\frac{1}{n-1} \sum_{i=1}^{n} (x_i - \bar{x})^2} \quad . \tag{4.5}$$

If several measured values are used for calculating the aimed result, the maximum error has to be calculated using the error propagation rules. For a sum or difference of measured quantities the absolute maximum error is the sum of the absolute errors of the single quantities. For a product or quotient of measured quantities the relative maximum error is the sum of the relative errors of the single quantities [109].

Due to the fact that usually numerous gravimetrical measurements are performed, the random error can be calculated using the mean value and the standard deviation. However, sometimes it is necessary to take every single measurement into account, e.g. for time dependent measurements. In this case a random error has to be added to the measurement result which can arise from possibly vibrations or air turbulences. However, the size of this random error cannot be estimated easily because it depends on the intensity of the disturbance.

The systematic error due to the evaporation of the dispensed liquid was considered as good as possible by the implemented weighing procedure presented above. Nevertheless, a possibly still existing systematic error despite the evaporation correction has to be considered. Due to the absence of an established value the maximum systematic error is assumed to be less than 10 % of the measured value. Additionally, the random error due to the precision of the balance (0.1 µg) has to be added to every measurement. Further systematic errors are not known.

Hence, the total maximum error for numerous repeated gravimetrical measurements can be estimated to 10 % of the measured value plus 0.1 µg measurement inaccuracy. Since the aimed mass mostly exceeds 10 µg, the measurement inaccuracy of the balance can be neglected. However, if single measurements are required a random error has to be added depending on the outer circumstances of the measurement setup. Also in this case the maximum error can not be fixed because of the unpredictability of this error. However, under regular conditions this random error can be assumed to be also maximal 10 % of the measured value. This in addition with the before mentioned maximum systematic error of 10 % leads to a total maximum error of 20 % of the measured value for single measurements.

According to this, for example, a single measurement of 20 µg (= 20 nl for ρ = 1000 kg/m^3) indicates a maximum error of 4.1 µg. Hence, the confidence interval would be 20 µg ± 4.1 µg respectively 20 µg ± 20.5 %. If the value is a result of various measurements the standard deviation has to be taken into account instead of the random error of 10 %.

4.2 OPTICAL MEASUREMENTS

Beyond the gravimetrical measurements the optical measurements are the most important and evident because of the illustrative results. There are several optical methods to examine the droplet ejection process and to evaluate the results concerning droplet volume, velocity and shape. In the next sections some of the most prominent methods are described.

4.2.1 STROBOSCOPIC IMAGING

The probably most acknowledged optical examination method to observe the droplet ejection is to record it with a camera. But the small size and the high velocity of the ejected droplets require a high quality camera as well as a very bright light source. The principle of the stroboscopic procedure is using the reproducibility of an ejection process. The resulting picture sequence is not made of one ejection cycle but it is made of several successive ejection events. Every picture is made after an increasing time delay subsequent to the ejection start. That means that a fluent film of the ejection process can be recorded presupposed the ejection is very reproducible. Nevertheless, all measurement quantities like droplet volume, velocity and also the shape can be extracted out of this data.

The usual method to illuminate the droplet is a kind of bright background illumination either with a lasting cold light source, as in the setup used for this work, or a pulsed flash light or LED flash light, which is the preferable solution. The advantage of a pulsed flash light is a reduced background noise leading to a better sharpness and contrast of the pictures.

To capture the pictures, a microscope with suitable magnification, a camera with a fast, high resolution CCD or CMOS chip and a computer with installed frame grabber card is needed. The microscope should have a magnification to recognize a droplet of a few micrometers with a sufficient yield of light. The camera and the camera chip need a fast enough shutter time of not more than 1/500,000 seconds and have to provide the possibility to store at least one to ten pictures per second to realize a high enough recording frequency. Finally the frame grabber card also has to offer appropriate storing speed and trigger processing of external signals. The used system "Mocon-RT" [158] consists of a stroboscopic camera, a computer with installed frame grabber and control card and an appropriate software as depicted in figure 4.3.

The required exposure time of one microsecond or less, to record a ten micrometer droplet with a velocity of approximately 10 m/s with sufficient sharpness and contrast, has to be realized either with a fast switching light source or with a suitable shutter time of the camera. The optimum is achievable by a combination of both.

To determine the volume of the ejected droplet a picture has to be chosen in which the droplet shows a nearly spherical shape. Taking the known size of the nozzle as reference, the diameter of the droplet can be determined by [157]:

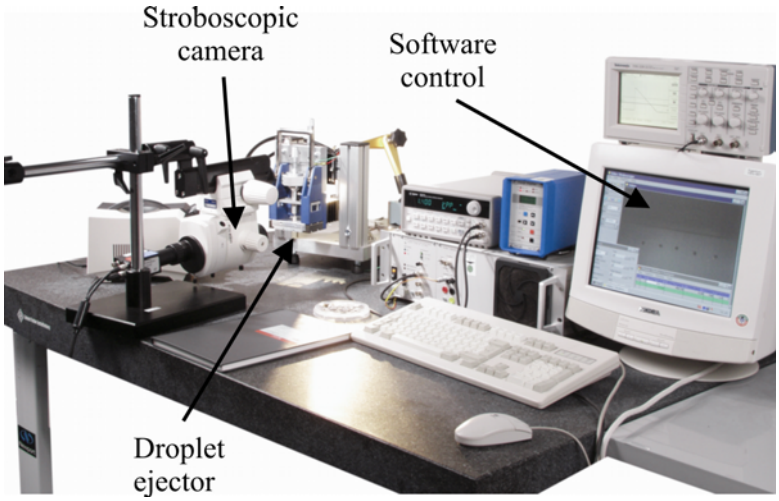

Figure 4.3: *Experimental setup for the recording of the stroboscopic pictures.*

$$D_{\text{droplet}} = \frac{D_{\text{nozzle}}}{P_{\text{nozzle}}} \cdot P_{\text{droplet}} \tag{4.6}$$

Where P is the diameter in pixels and D is the diameter in micrometers. Assuming a perfect sphere, the droplet volume can be calculated using the derived diameter:

$$V_{\text{droplet}} = \frac{1}{6} \cdot \pi \cdot D_{\text{droplet}}^{3} \tag{4.7}$$

Determining the velocity of the droplet can be done in the same manner. Comparing the known nozzle diameter with an arbitrary flight distance of the droplet and the knowledge of the flight time, the average droplet velocity can be calculated. In practice blurred pictures due to high velocity aggravate the determination of the droplet velocity as well as the volume in order that considerable measurement errors have to be accounted for. This is due to the fact that a fast travelling droplet cannot be captured at a fixed position because of the limited shutter time of the camera.

The error consideration for the stroboscopic imaging is basically the same as presented in the previous section for the gravimetrical measurements. A systematic error for the stroboscopic imaging can be found in the time counting of the PC. An insufficient accurate time counting can lead to an error calculating the droplet velocity. Since no corresponding data from the manufacturer is available the maximum error is assumed to be 10 % of the used time delay. For the smallest possible delay time step of 50 ns in the used system this would lead to a maximum systematic error of 5 ns because of the insufficient accurate time counting.

A random error can be found in the read out of the pixels for the determination of the droplet diameter and the travelled distance. This error is based on two problems. First a blurred picture due to high droplet velocities adds an error as mentioned before. Second the number of pixels representing one droplet is limited due to the resolution of the used camera. For the used camera with 640 x 480 pixels one pixel equals a

quadratic region with an edge length of about 0.9 µm for the highest magnification. This can be deduced by counting the pixels of a known spatial dimension in a photograph with described setup. Hence, a spherical droplet with 30 pl respectively about 20 µm diameter is represented by at least 350 pixels like it is displayed in figure 4.4. However, the pixels at the periphery can not be clearly associated to the droplet even if no blur is present. From various measurements it could be deduced that a maximum error of 350 ± 88 respectively 350 pixels ± 25 % is possible. The droplet diameter exhibits a smaller error compared to the area but nevertheless it is still equipped with a random error of at least 10 %. This random error depends on the used magnification as well as on the size of the captured spatial dimension. Due to this a general error can not be estimated. However, the exemplary presented estimation is the worst occurring case. This random error is amplified by additionally occurring blur of the picture due to high droplet velocities because than the periphery of a droplet is not as sharp-edged as in figure 4.4.

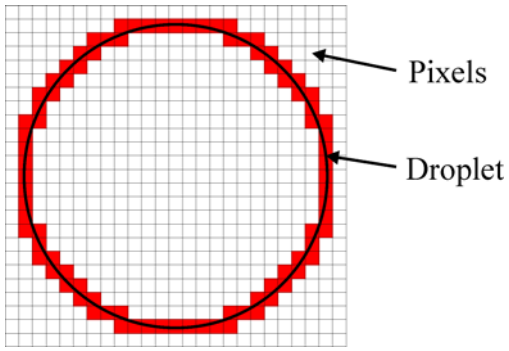

Figure 4.4: *Schematic of a droplet represented by the pixels of a stroboscopic picture. The pixels at the periphery can not be clearly associated.*

Conclusively, the determination of the droplet diameter using equation (4.6) leads to an estimated total maximum error of 20 % because two errors have to be summarized. The pixels of the nozzle diameter as well as the pixels of the droplet diameter have to be counted and thus are equipped with an error. Since the droplet diameter contributes to the droplet volume with the power of three, the total maximum error for the droplet volume calculated by equation (4.7) can be estimated to be 3 x 20 % = 60 %. For the calculation of the droplet velocity the flight distance as well as the flight time have to be considered. The random error of the flight distance can also be estimated to be 20 % because of the same reasons like for the droplet diameter. As mentioned before the systematic error of the flight time can be estimated to 10 % of the used delay time of the stroboscopic system. Hence, the estimated total maximum error of the calculated droplet velocity is 30 %. For example if the droplet flight distance is determined to be 500 µm ± 20 % (100 µm) at a delay time of 50 µs ± 10 % (5 µs), the resulting droplet velocity can be calculated to 10 m/s ± 30 % respectively 10 m/s ± 3 m/s.

4.2.2 High-Speed Pictures

In contrast to stroboscopic cameras high-speed cameras capture pictures in real time which means, that a few pictures can be made of a single ejection event within a time interval of less than one microsecond. As the storing of a high-resolution picture claim the most time in optical measurements, high-speed cameras are equipped with special CCD chips providing an internal cache for two, four or few more pictures. After this internal cache is filled, the data is stored on a local hard disk taking several microseconds. After that the next picture sequence can be recorded. According to this, this method is limited to a few pictures of one ejection event, but therefore the movement of one single droplet can be followed.

Also this method needs a bright light source to provide enough light for these high shutter speeds which is also capable to make two or more pulses with the same frequency as the high-speed camera. For this usually a laser is used with a pulse width of about 20 ns. This method was used only once for this work at an external company offering such a service [159].

4.2.3 Laser and Light Barriers

Another optical method but without direct evaluation of pictures is using laser or light barriers to describe the droplet properties. Due to the difference in absorbed respectively scattered intensity of air and the liquid, a difference in radiation intensity can be detected on the light receiver whether the droplet blocks the light path or not [155]. Micro light barriers capable of detecting objects with a diameter of 125 µm normally consist of laser emitters or use optical fibres to create thin light beams, but there are also light barriers using standard red or infrared light without optical fibres. Usually two light barriers with a given gap are used for the droplet detection to determine the droplet or jet length as well as its mean velocity. Using this, also the droplet volume can be estimated.

Disadvantage of this method is that the resolution of the barriers as well as the used gap have to be adjusted to the examined device because this depends on the inspected droplet volume and velocity. Furthermore, no statement on the shape of the ejected droplet or jet can be done using this method. However, the auspicious price for such a system compared to others is an evident benefit.

4.3 Alternative Methods

The above described methods form only a part of available techniques for the droplet ejection examination. Especially for smaller droplets like in aerosol atomizer applications sometimes other measurement methods are used. Exemplary an additional mechanical as well as an optical method for the statistical evaluation of sprays of very small droplets are explained in the following.

CASCADE IMPACTOR

The Andersen Cascade Impactor (ACI) [160] is an example for a mechanical method to sieve small particles or droplets in several stages. The ACI is an eight stage cascade impactor for measuring the fine particle dose and size of the aerosol cloud generated by Metered Dose Inhalers (MDIs) and Dry Powder Inhalers (DPIs). The eight stages made of stainless steel or aluminium simulate the various parts of the human respiratory system, as follows [160].

- Stage 0: 9.0 - 10.0 µm
- Stage 1: 5.8 - 9.0 µm
- Stage 2: 4.7 - 5.8 µm (pharynx)
- Stage 3: 3.3 - 4.7 µm (trachea & primary bronchi)
- Stage 4: 2.1 - 3.3 µm (secondary bronchi)
- Stage 5: 1.1 - 2.1 µm (terminal bronchi)
- Stage 6: 0.7 - 1.1 µm (alveoli)
- Stage 7: 0.4 - 0.7 µm (alveoli)

The impactor is designed such that as the aerosol stream passes through each stage, droplets having a large enough inertial momentum will impact upon that particular stage plate, whilst smaller droplets will pass to the next impaction stage. A known problem of such impactors is the vaporization on the way through the impactor case. Further drawback is the absence of any velocity information of the droplets.

LASER DIFFRACTION

The Malvern Spraytec system [161] is an example for an optical method for in-situ, real-time measurements of the droplet size distribution of sprays and aerosols using the laser diffraction technique. Using just two lens systems, this method can measure droplet size distributions over an extremely broad dynamic range of 0.1 µm to 2,000 µm with an acquisition rate of up to 10 kHz. This system ensures the complete characterization of both pulsed and continuous spray events, fully capturing the changes in droplet size observed as a function of time.

For laser diffraction droplet sizing an expanded laser beam passing through a spray is used. Each droplet illuminated by this beam contributes to the light intensity recorded by the receiver. From the light intensity distribution captured by the receiver, a droplet size distribution is calculated, as though the droplets were spherical. Disadvantage of this method is also that no velocity of the droplets can be examined.

5 BUBBLE JET – AN EMINENT DROPLET EJECTOR

High quality color image, low machine cost and low printing noise are basically the main advantages of ink jet printers. This has led to a rapid expansion of this technology in the recent years. The two competing actuation principles of these, so-called drop-on-demand printers are the piezoelectric driven printhead as reported in [149,150] and the thermally actuated bubble jet printhead developed in the 1980's [162]. Both methods made remarkable progress in the last years [163]. Currently the bubble jet printer outstands with low manufacturing costs at competitive print quality. The aim of manufacturers and many researchers is the further optimization concerning maximum print frequency, active area of the printhead, resolution and quality of ejected droplets [164-170]. This requires a further miniaturization and optimization of the printhead geometry including fluid channels, heaters and nozzles to achieve an ideal printhead performance. Furthermore the number of nozzles and the printhead size should be increased to gain printing speed. An important tool for the optimization is the simulation of the complete device which is very cost- and time-effective compared to experimental hardware optimization. With CFD simulations a variety of relevant parameters like geometrical dimensions and ink properties can be investigated. Also the use of integrated nozzle plates is beneficial for the optimization of the printhead as will be shown in the following.

5.1 DESIGN AND MANUFACTURING OF A BUBBLE JET PRINTHEAD

In this section first the general working principle of a bubble jet printhead is explained. Subsequently the specific bubble jet printhead design considered in this work and the corresponding fabrication procedure is described. The results presented in the following were accomplished within an European project consortium consisting of Olivetti I-Jet [4], Böhringer Ingelheim microParts [35], HSG IMIT [171] and IMTEK [172]. This work was supported by Federal Ministry of Education and Research (BMBF), Germany (grant no. 16SV1607) within the EURIMUS program (IDEAL EM 42).

5.1.1 WORKING PRINCIPLE

There are two basic principles of thermal bubble jet printheads like it is displayed in figure 5.1. The so-called edge-shooter where the nozzle is arranged perpendicular to the fabrication layer. In this case, the nozzles are often laser drilled. And the so-called side-shooter where the nozzle is arranged parallel to the fabrication layer. In this case, the nozzles are arranged in the same plane like the fluidic channels. But in general both configurations are manufactured in the same way: Typically there are three layers, a silicon substrate containing the electronics and protection layers, the fluidic layer containing the fluidic channels and nozzle chambers, and finally the nozzle layer containing only the circular nozzles [173,174]. Nowadays the objective is often to shift to a two layer design or even to monolithic printheads [169,170,175].

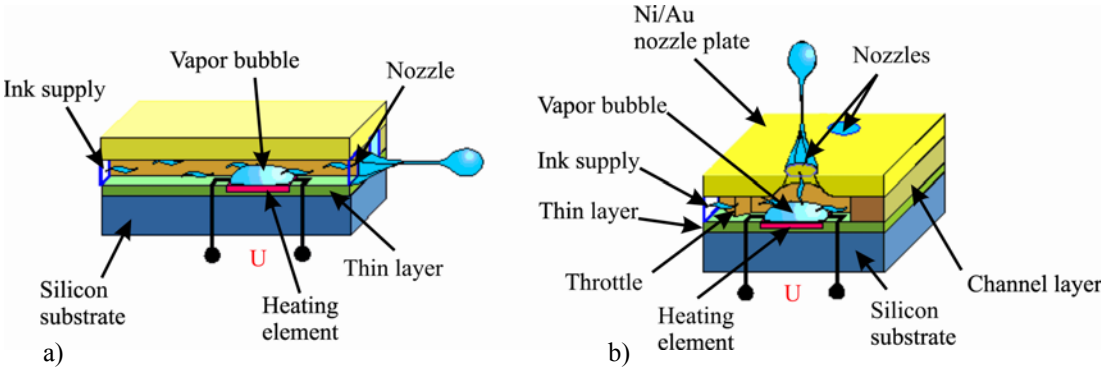

Figure 5.1: *The both known basic principles of thermal bubble jet printheads. a) The so-called edge-shooter, fabricated by Canon and b) the so-called side-shooter, fabricated by HP, Lexmark, Olivetti and Xerox [173,174].*

The functional principle of a thermal bubble jet printhead is based on a current pulse in the range of some microseconds applied to a micro heater of several micrometers spatial dimensions which leads to a very short heating pulse at the solid-liquid interface. This heating pulse lasts about 2 µs to 10 µs and leads to a temperature of up to 500°C at the solid-liquid interface for a short period of time. Due to this, nucleation begins at the surface of the heater forming a small vapor bubble which expands explosively. The increasing vapor bubble leads to a volume displacement of the ink towards the ink supply channel as well as to the nozzle and finally to a droplet ejection out of the nozzle. The detaching of the vapor bubble from the hot surface results in a concurrent cooling down of the bubble which results in condensation and collapse of the bubble. The suction of the collapsing bubble and the capillary forces inside the printhead lead to refilling of the nozzle chamber that it is finished before the next shot after approximately 10 µs. The nucleation, vaporization, expansion and collapsing phenomenon was investigated in many research papers [176-181]. The fast explosion of the bubble leads to a characteristic pressure behavior inside the liquid. Starting instantaneously with a very high pressure of about 7 MPa to 9 MPa right at the

beginning of the vaporization, the pressure decreases exponentially during a few microseconds. During the bubble collapse the pressure is slightly negative compared to the ambient pressure and returns to zero after the final collapse.

Despite the fact that this phenomenon is very complicated, it is also very reproducible and cheap compared to other techniques. And also the manufacturing methods for the actuation part are very simple and can be realized down to very small structures in the tenth of micrometers. Hence a high heater density on the chip and thus a high print resolution of the inkjet printhead can be realized. A normal printhead consists of 200-450 nozzles in several rows connected with one fluidic feeding slot and electrical actuated with a multiplexer on-board in most cases.

Typical values for commercial available bubble jet printheads are a droplet volume of 2 pl to 40 pl, a droplet velocity of 10 m/s to 15 m/s, a print frequency of up to 15 kHz and a physical resolution of up to 1200 dpi.

The utilization of the thermal actuation is not limited to the inkjet topic. In the meantime there are also other applications mostly micro pumps for transporting small amounts of liquid [182-187]. These pumps are mostly used for medical, biological or life-science applications. But the significant disadvantage of relying on liquids which can be easily vaporized prevents this actuation method for multi purpose use.

5.1.2 SUBSTRATE

The substrate of the printheads used in this work provided by Olivetti I-Jet [4] is fabricated using customarily surface micromachining methods in a cleanroom. A schematic cut through the printhead is displayed in figure 5.2. On the one hand it shows the fluidic layer but on the other hand the structure of the substrate is visible consisting of a silicon basis, a silicon oxide, TaAl as heater material, Al as conducting lines and SiC, SiN and Ta as protecting layers. The protecting layers protect the heater mechanically against the back-bounce of the collapsing bubble as well as chemically against the aggressive ink. All of the layers should provide a high thermal conductivity to provide most of the heating energy to the ink except of the SiO_2 which acts as thermal insulator towards the silicon.

A photograph of the top of the used substrate is displayed in figure 5.3. On both long edges the bond pads can be seen. Due to the utilization of a multiplexer on chip, the single heaters are divided in 16 groups, 12 heaters per group. At the same time only one heater per group can be activated. In the middle of the chip the ink feeding slot is located serving for the ink supply. This slot is powder blasted which is the last task in the manufacturing of the substrate before the assembling with the nozzle plate.

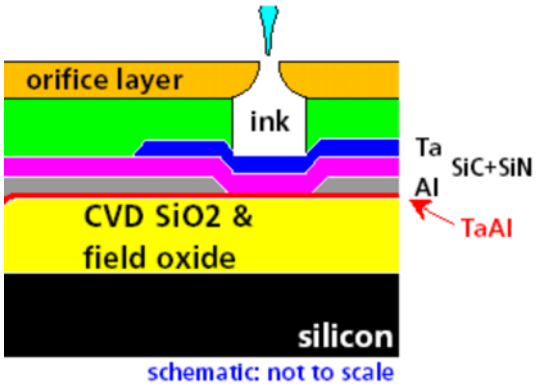

Figure 5.2: *Schematic cut through the Olivetti I-Jet printhead construction.*

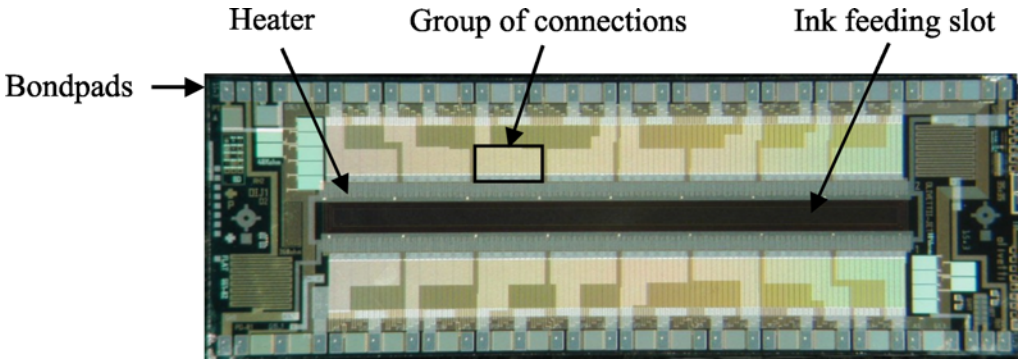

Figure 5.3: *Photograph of the top of the used substrate.*

5.1.3 Nozzle Plate

The integrated nozzle plate with two precisely aligned structural layers is made by an advanced laser ablation process. An adequate design of the fluidic supply is of outstanding importance to achieve high print frequencies [188]. This integrated nozzle plate avoids the generally used three layer design where the first layer includes the electronics and the heaters, the second layer contains the fluidic parts like channels or nozzle chambers and finally the nozzle plate with usually laser drilled nozzles [189]. The main advantage of the two layer design is the reduction of processing steps and the necessity of only one assembling step. Due to less and smaller alignment errors, smaller fluidic structures can be realized leading to a better control of the printhead geometry and to improved optimization opportunities for the ejection process.

One possible approach to meet the demands of high printing speed is to use a much wider printhead in order to address a larger area in the same time. A one inch printhead with integrated nozzle plate provides a realistic and cost effective solution to this problem. To achieve such a large printhead with integrated nozzle plate is however very challenging because of the high requirements concerning the fabrication technology of the nozzle plate, the alignment of nozzle plate and substrate and the

assembly of the printhead. The results reported in the following provide suitable solutions to all of these problems. Therewith, a one inch printhead with integrated nozzle plate was realized for the first time within the IDEAL project.

LASER MACHINING

An excimer laser with a wavelength of 248 nm was used to structure different designs of integrated nozzle plates. A 1/3 inch nozzle plate and finally a one inch nozzle plate with different channel / nozzle dimensions and different foil thickness were fabricated, respectively.

The 1/3 inch nozzle plate has been processed by using a commercial excimer laser system (LPX 305 made by Lambda Physik AG) [190]. But the structured area of a one inch nozzle plate exceeds the exposure area of typical commercial systems for excimer laser ablation. The whole structured area of a one inch nozzle plate must be firstly divided into several parts and then the laser has to step these parts sequentially. This can easily be realized for the nozzle layer. The channel layer however, is a whole area without any break. A stepping process would produce overlaps between the sub-areas. To avoid this, a full-scale scanning process was developed by Böhringer Ingelheim microParts [35] for lasering the channel layer. Also the used laser system was modified to get improved behaviors in order to realize the new process. With this process the nozzle plate was structured by 2-dimensional scanning "on the fly".

The 50 µm and 75 µm thick polyimide foils (for the 1/3 inch and for the one inch nozzle plate respectively) were structured successfully in two precisely aligned structural layers by the 2-dimensional scanning process in combination with the sequential nozzle stepping. The two masks required contain the nozzle chamber with the ink channels and the nozzle, respectively. The misalignment of the two laser processes is less than 1 µm. A SEM picture of one nozzle chamber of the 1/3 inch nozzle plate is depicted in figure 5.4 a) and the corresponding nozzle outlet is displayed in figure 5.4 b). An excellent sharpness of the edges and planar surfaces can be observed. In figure 5.5 a similar picture for the one inch nozzle plate is displayed.

To fulfill the specifications of different nozzle and chamber designs the draft angle of the lasered structures can be varied between 7° and 28° by varying the energy density of the laser pulse in a certain range and in addition by using other techniques such as a wobble plate in the laser optics. The draft angle also depends on the material of the nozzle plate and the ablation depth. In figure 5.6 a vertical cut through the 1/3 inch nozzle plate is displayed. The void was filled with a filler material to avoid damage of the structure during preparation. The nozzle exhibits a typical draft angle of about 8° and the chamber shows clearly the two structural layers with different heights.

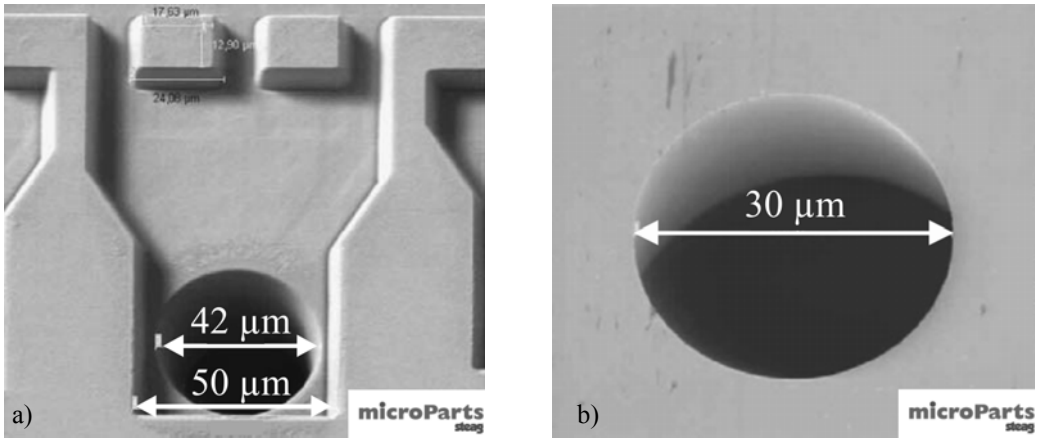

Figure 5.4: *Full-scale lasered 1/3 inch nozzle plate consisting of two precise aligned structural layers. The nozzle chamber, ink channel and the nozzle. View from the inlet a) and outlet b), respectively.*

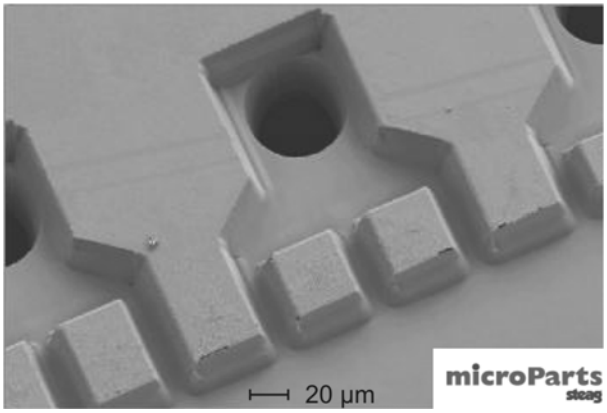

Figure 5.5: *View from the inlet of a full-scale lasered one inch nozzle plate consisting of the two precise aligned structural layers.*

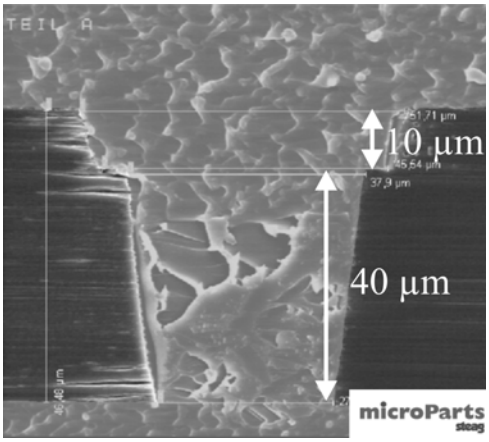

Figure 5.6: *Vertical cut through the two structural layers of the 1/3 inch nozzle plate with a nozzle chamber and nozzle filled with a filler material (light area) to avoid the damage of the structure.*

SURFACE TREATMENT

After the laser machining of the nozzle plates various treatments of the surfaces are required. On the one hand a cleaning of the laser entry side is necessary to remove the remains of the laser process. Therefore different kinds of cleaning processes such as cleaning with organic / inorganic solvent, ultrasonic cleaning and plasma cleaning using oxygen (O_2), oxygen-argon (O_2-Ar) or oxygen-tetrafluoromethane (O_2-CF_4) and combinations of those processes were tested to prove the best purification. It is well known, that for a plasma cleaning process the parameter-set (pressure, temperature, gas flow rate, process duration, field density and frequency) plays an important role. Process optimization for the nozzle plate cleaning has been made successfully with a commercial system by Böhringer Ingelheim microParts [35]. The best result was obtained using the oxygen plasma in combination with a suitable pre-cleaning like it is depicted in figure 5.7 before a) and after the cleaning b), respectively.

On the other hand a surface treatment of the front side of the nozzle plate is necessary to provide an adequate hydrophobicity. Using a chemical treatment leads to an increase of the contact angle of up to 95° and shows a better long-term stability compared to conventional plasma treatments.

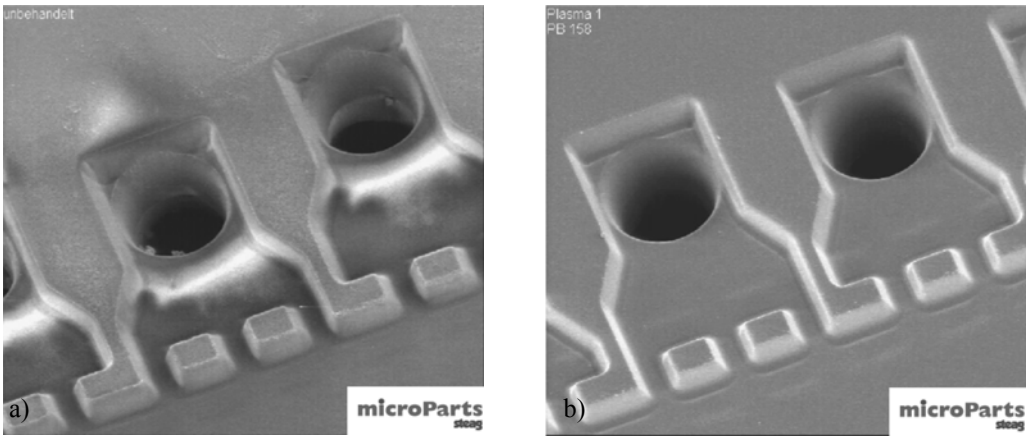

Figure 5.7: *Laser structured 1/3 inch nozzle plate before a) and after b) the cleaning in an oxygen plasma.*

5.1.4 ASSEMBLING

The major challenges for completing the printhead are the assembly of the structured nozzle plate with the silicon chip and the requirement of the minimum height of the adhesive to guaranty the spatial tolerances. Especially when depositing adhesive layers with a thickness of less than 10 µm, one has to face two major challenges. First the depositing process itself because it is not trivial to produce such a thin adhesive layer. Second the properties of the resulting thin layer of adhesive that can significantly differ from the characteristics of the bulk material. Reasons for this behavior can be found in

the dominating surface effects towards structural properties of the bulk material, inhibition of oxygen from the surrounding atmosphere as well as possible evaporation of solvents or hardeners.

Different approaches were analyzed by the HSG-IMIT [171] to coat the provided substrate with a homogenous thin adhesive layer. Applying different well known procedures of coating like spraying, spinning, capillary transport and transfer techniques, different types of epoxy based adhesives were studied. Epoxy was chosen because of the suitable media properties and good adhesion abilities. Main challenges are the prevention of bubble embedding, desiderative bond strength or plugging of the fluid channels.

Finally, the best performance was achieved using a roller transfer technique like illustrated in figure 5.8. To achieve a homogeneous adhesive transfer, the polyimide needs to be cleaned properly. This was achieved by low power ultrasonic cleaning first in acetone and then in isopropanol. A subsequent exposure to an oxygen plasma created free bonds at the surface of the polyimide film, increasing the surface activity and thus its affinity to the adhesive. The adhesive was filled into a 5 µm deep RIE-etched silicon pot and leveled out by a doctor blade. Using a metal roller, the structured polyimide nozzle plate was subsequently coated with adhesive. Once leveled, the adhesive can be used for 15 minutes due to an increase in adhesive viscosity. The reason for this rapid increase in viscosity in thin layers relates to the evaporation of not reacted hardener. A flip-chip-bonder from FineTech GmbH [191], was used to transfer the coated polyimide film onto the printhead substrate with an alignment accuracy of 5 µm without clogging of the fine structures (cf. figure 5.9). The adhesive Epotek 353ND by Polytec [192] showed adequate performance to create a layer thickness of approximately 3 µm. After an adequate curing process of 90 minutes at a temperature of 85°C, satisfactory bond forces were obtained.

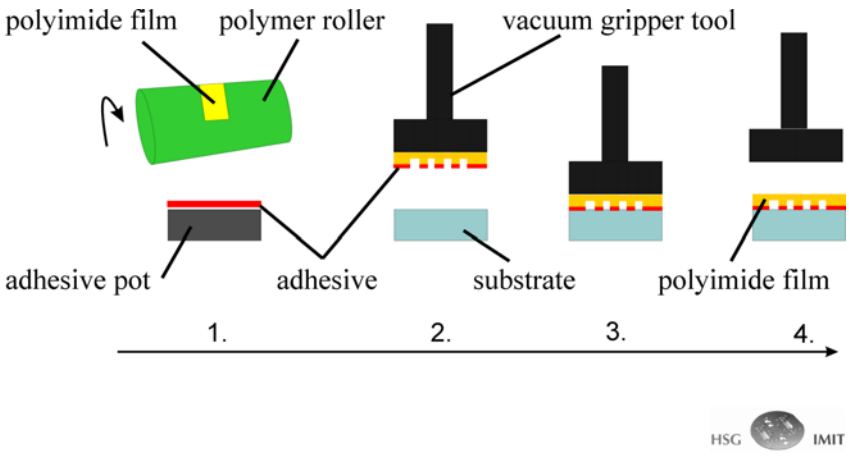

Figure 5.8: *Schematic illustration of the adhesive roller transfer process. 1. Picking up adhesive out of a pot directly on the polyimide film using a polymer roller. 2. Pick the coated polyimide film using a vacuum gripper tool. 3. Alignment on the substrate. 4. Finally removing the gripper tool.*

5.2 Experimental Results

To prove the successful assembling of the integrated nozzle plate different tests have been performed. First the capillary filling of the printhead was studied using an optical observation like it is displayed in figure 5.9.

Furthermore, a cut through the channel structures inside the nozzle plate as it is displayed in figure 5.10 was analyzed. The trapezoid cross section of the channels, the adhesive layer and also a slight capillary wicking by adhesive can be seen.

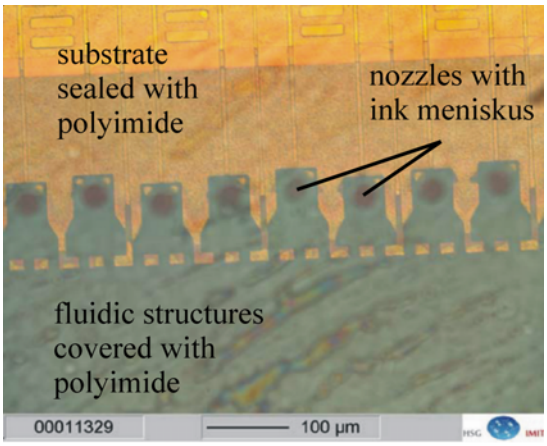

Figure 5.9: *Assembled nozzle plate on printhead substrate. The dark areas are ink filled fluidic structures, whereas the light areas represent leak-proof joined areas. The ink meniscus inside the nozzles can be seen as dark discs.*

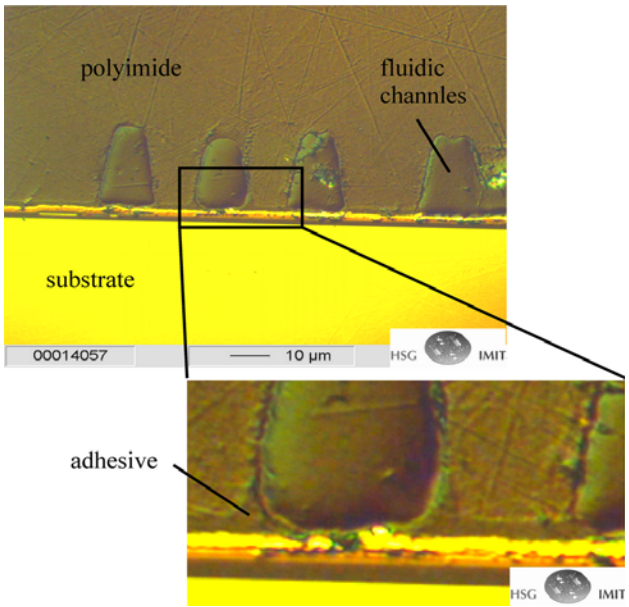

Figure 5.10: *Cut through an assembled printhead showing the polyimide film sealed on the substrate without clogging the fluidic channels.*

The functionality of the printhead was analyzed by operating single nozzles at different frequencies. Due to the fact that it was not possible to implement the printhead in an inkjet cartridge, it was necessary to glue the printhead on a custom made PCB board like it is displayed in figure 5.11. The electrical contacting was done by wire bonding and the fluidic contacting was done by a drilled hole from the backside of the PCB board. The wire bonds were protected by an epoxy based adhesive.

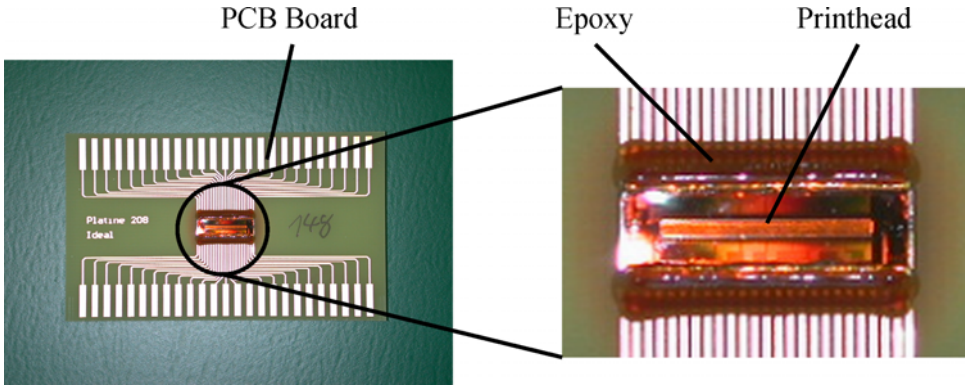

Figure 5.11: *Printhead bonded on a commercial PCB board. The wire bonds are protected with an epoxy based adhesive.*

This setup was used to take stroboscopic pictures which are illustrated in figure 5.12 a) and b) for the 1/3 inch and the one inch printhead, respectively. After operation and cleaning with acetone in an ultrasonic basin the printhead demonstrates a good and reproducible functionality which indicates the robustness of the assembly. Also after standardized temperature, humidity and ink saturated storing the devices worked properly with a deviation of the droplet volume of less than 5 % for the 1/3 inch devices. The performed reliability tests consisted of:

- Temperature alteration test: -20°C < T < +120°C, 53 hours (DIN IEC 68 214).
- Humidity storing test: 85 % relative humidity, 85°C, stationary, 90 hours (DIN IEC 68 256).
- Ink storing test: completely covered by ink, 24 hours.

Finally, also gravimetrical measurements have been performed. Because of the low mass of a single droplet (approximately 20 pl) 10,000 shots were averaged within every weighing procedure. The droplet volume was studied concerning the dependence of the dosage volumes on the shot frequency as depicted in figure 5.13 a). In this case the mean value of four nozzles and the corresponding standard deviation is displayed. The increase of the droplet volume arises from a slightly warming of the ink inside the nozzle chamber during operation and the resulting decrease of the ink viscosity. The final decrease is explained by the lack of time for refilling ("starving"

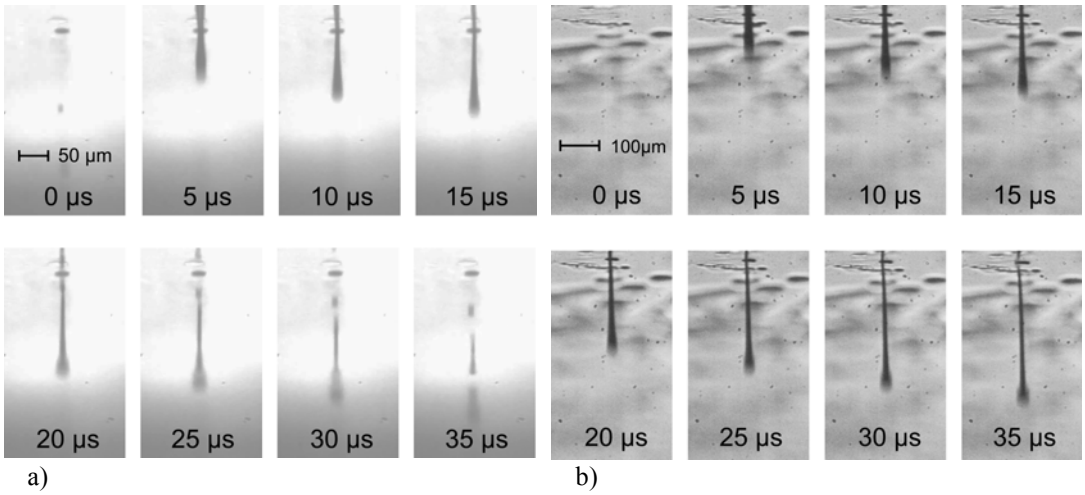

Figure 5.12: *Ejection cycle of the 1/3 inch a) and the 1 inch b) printhead taken by stroboscopic imaging.*

effect). Furthermore, the reproducibility of the droplet volume was investigated by 20 successive measurements as described before at different frequencies as depicted in figure 5.13 b). A CV of less than 4 % was obtained for all frequencies.

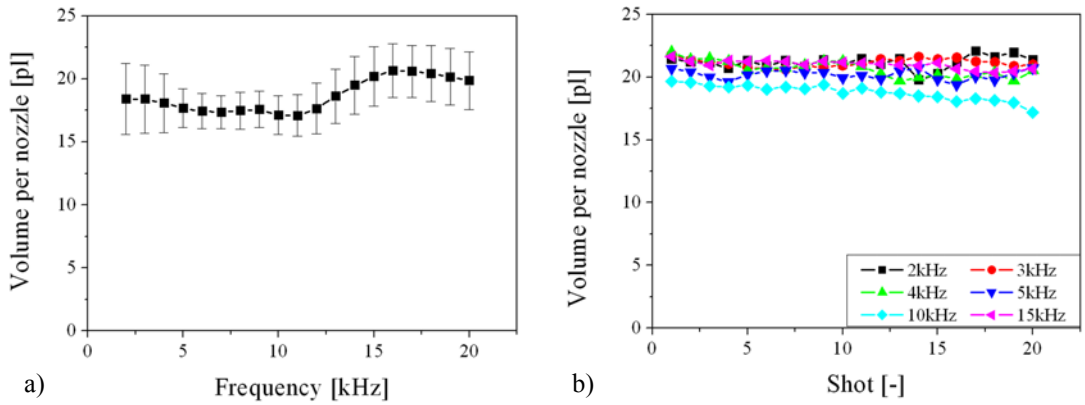

Figure 5.13: *Gravimetrical measurements for the bubble jet. a) Droplet volume depending on the shot frequency. b) Reproducibility of the droplet volume over 20 cycles at different frequencies.*

5.3 Characteristic Values

Describing the performance of an inkjet printhead some characteristic values have to be introduced. In the following the most important values are explained in more detail. The dependency of these values on other parameters like geometric variations or ink properties are presented in section 5.5.

5.3.1 Droplet Volume

The droplet volume of inkjet printheads is nowadays in the range of 1-2 pl (Canon) to 4 pl (HP) for color printheads and about 10-30 pl for black printheads. The smaller droplets guaranty a better resolution and a better sharpness of the pictures, whereas the larger droplets realize a faster and more covered printout. But for large format printers or printers for industrial applications the droplet volume is still about 70-120 pl to have an appropriate short time for the printout.

5.3.2 Droplet Velocity

The droplet velocity is another important value for the printhead performance because besides the maximum print frequency the velocity regulates the maximum speed of the printhead movement. With a general droplet velocity of 10-15 m/s, the usually used distance between printhead and paper of 1 mm, is attained after about 100 µs. With higher droplet velocities the impact position of the droplet can be controlled much easier also at higher movement speed.

5.3.3 Print Frequency

The print frequency of an inkjet printer is probably the most important value because the relatively slow print frequency is the biggest disadvantage of inkjet printers compared to the much faster laser printers. This is the reason why increasing the print frequency is a challenging task for the inkjet manufacturers to compete against the laser printer technology. Currently the typical print frequency of commercial devices is about 12-18 kHz for single nozzles.

5.3.4 Droplet Quality

To realize more and more perfect printouts of digital pictures, not only the maximum resolution and the smallest droplet volume is important, but also the droplet quality. A good droplet quality means that the tail of the ejected droplet, which is characteristic for bubble jet printheads (cf. figure 5.12), is as small as possible. An existing tail mostly separates into several satellite droplets, these can hit the paper at a different position as the main droplet due to the relative movement of the printhead causing a blurring of the printed image. The ideal solution would be, to have a perfect spherical droplet without any tail or satellite droplets like it is claimed by Canon for their newest printhead generation [193,194]. This design totally avoids the formation of satellite droplets due to prevention of the bubble collapse. This is done by an increasing vapor bubble, which is larger than the nozzle chamber. Thus the bubble does not collapse but explodes out of the nozzle.

5.3.5 Resolution

Talking about the print resolution, it has to be distinguished between the maximum physical resolution and the maximum print resolution. The maximum physical resolution is defined by the pitch between two nozzles. This physical resolution is normally improved by using two parallel rows of nozzles, where each nozzle of the first row is located in the center of two nozzles of the second row.

The maximum print resolution usually is better due to some structural refinement. Either the printhead is inclined to the direction of the movement, e.g. 45° leads to the optimum print resolution, or the printhead moves several times over the same area with a slight offset to print inside the empty spaces of the first passage.

The commercial available printheads demonstrate a physical resolution of 600-1200 dpi, which means a pitch of about 21 µm, whereas the maximum print resolution is about 2400-4800 dpi.

5.4 Simulation of the Ejection Process

Due to the complexity of the ejection process of a thermally actuated bubble jet printer including heating of the micro heater, bubble nucleation, collapse of the vapor bubble and the actual droplet ejection [104,181,195-197] no complete physical simulation could be accomplished so far. The simulation task is typically modelled separately for actuation and ejection throughout the literature. To model the actuation in the simulations performed for this work an equivalent pressure boundary condition proposed by Asai et al. [198-202] was applied. Using this pressure pulse as input for the simulation package ACE+ of ESI-Group [74] a CFD simulation has been set up and the droplet ejection process has been studied like follows. The presented model is the first known successfully accomplished three-dimensional CFD simulation of a bubble jet printhead using the pressure boundary substitution proposed by Asai. The results were also published on several conferences [203-205].

5.4.1 CFD Model

Geometry

To examine the influences occurring in the real device a complete three-dimensional model, instead of a simplified two-dimensional nozzle like in section 3.2.4, was set up for the Olivetti bubble jet. Real three-dimensional influences could be the effects of asymmetric ink inlet channels or a non-spherical bubble shape. But also the effects appearing at problematic parts of the printhead geometry, for example problems of the capillary refilling at convex edges or transitions between the angular nozzle chamber

and the round nozzle, can only be examined in full 3D simulations. A further advantage of the three-dimensional model is, that the realistic flight path of the droplet can be studied in dependence of the whole geometry.

The 3D model of an Olivetti I-Jet printhead, like it is displayed schematically in figure 5.14 has been set up to simulate a complete dosage cycle including first priming, printing and refilling. Thus it was possible to simulate the print frequency as well. Additionally, also slight design variants with varying nozzle diameter, nozzle length, nozzle chamber height, draft angle and supply channel geometry were realized, respectively. Furthermore also the first priming and the temperature distribution due to the rapid heating of the vapor bubble were examined.

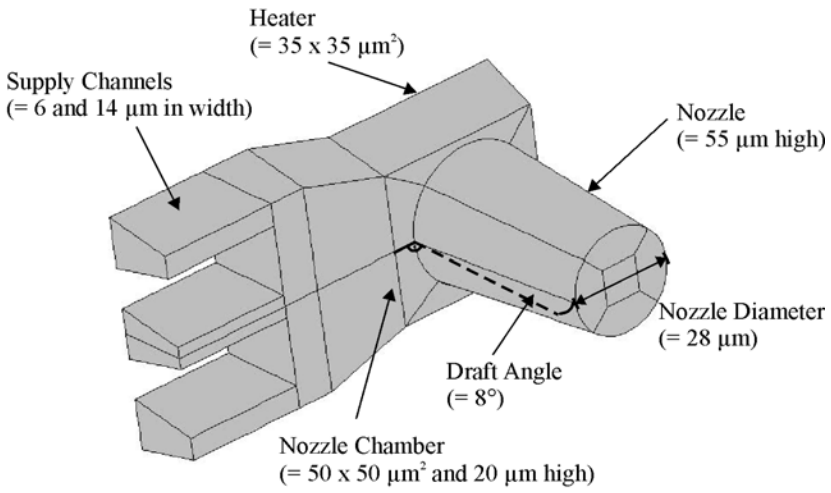

Figure 5.14: *Picture of the 3D model of one nozzle of the 1/3 inch bubble jet printhead showing only the fluidic part.*

For the CFD simulation it was necessary to model the geometry by a three-dimensional structured computational grid consisting of up to 200,000 cuboid cells where the smallest one has a volume of 1.6×10^{-19} m^3 and the largest one has a volume of 2.9×10^{-16} m^3. The gridding was done with an additional tool of the CFD package, CFD-GEOM, the geometry and grid generation system. To reduce the number of required grid elements every symmetry plane of the simulated design was exploited. In the case of the printhead only one half of a single printing element was simulated. In figure 5.15 the used grid is displayed from different point of views. The used number of grid elements was checked to be sufficient concerning consistency, convergence and required computing time. This was done by comparing the results of simulations based on models with different numbers of grid elements. The present grid was chosen as optimum regarding minimum computing time and maximum consistency and convergence compared to high-grid solutions. The volume at the nozzle outlet is called control volume and it is necessary to simulate and visualize the trajectory of the ejected droplet.

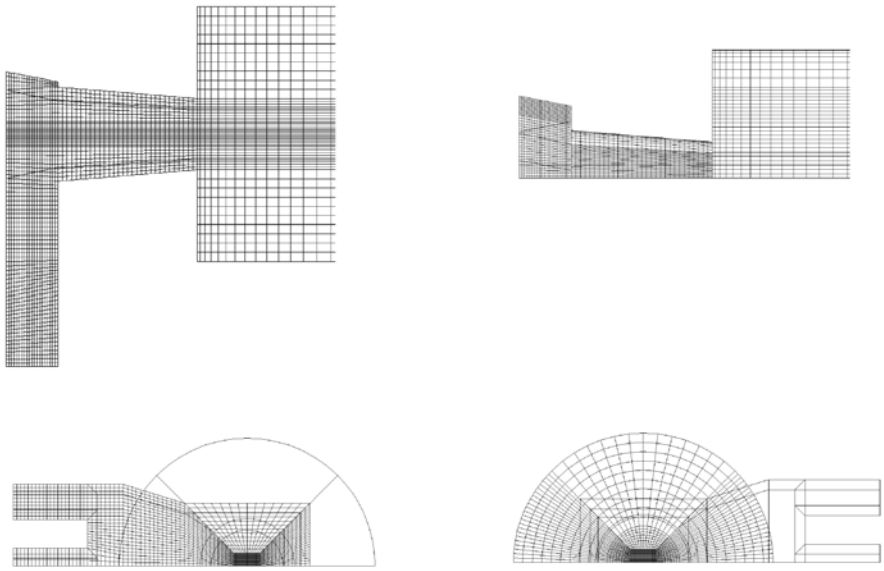

Figure 5.15: *Structured grid from different point of views of the printhead geometry depicted in figure 5.14.*

The VOF method including surface tension and the auto time step function was used with a CFL number of 0.2 (cf. section 2.6.2) to solve the model. The time steps varied in the range of 1 ns - 10 ns. The CGS solver and the PLIC surface reconstruction was chosen and the removal of "Flotsam and Jetsam" was turned on (cf. section 3.2.4). The water based ink has a density of $\rho = 1$ g/cm^3, a surface tension of $\sigma = 42$ mN/m and a dynamic viscosity of $\eta = 1.24$ mPas.

In figure 5.16 the applied boundary conditions are displayed. First of all the pressure inlet represents the heater area where fluid 0 respectively air (vapor) is pressed into the system. The applied pressure pulse is explained in the following. The reservoir inlet represents the fluidic supply from the reservoir. At this boundary fluid 1 respectively ink is applied with no over pressure. The inner wall of the nozzle, the nozzle chamber and the supply channels are assumed to be full-wetting. The wall surrounding the outside of the nozzle is assumed to be non-wetting. Finally at the outlet to the surrounding environment fluid 0 respectively air is present with no over pressure. The non-visible implemented symmetry boundary condition which is located in the paper plane completes the device out of the half model.

PRESSURE BOUNDARY CONDITION

A given current pulse through a micro heater of a bubble jet printhead can be converted into an equivalent exponential decreasing pressure function following the approach of Asai et al. [198-202]. According to this the initial pressure of this pressure pulse can be determined using the Clausius-Clapeyron equation [206,207]:

$$p_{\mathrm{v}}[T_{\mathrm{v}}] = p_{\mathrm{atm}} \cdot \exp\left[\frac{m_{\mathrm{M}} \cdot Q_{\mathrm{vap}}}{\mathrm{R}} \left(\frac{1}{T_{\mathrm{b}}} - \frac{1}{T_{\mathrm{v}}}\right)\right], \tag{5.1}$$

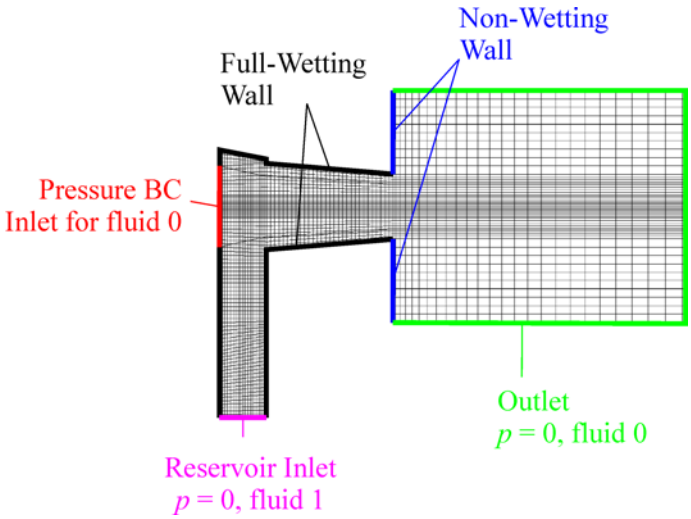

Figure 5.16: *Structured grid used for simulation of the Olivetti bubble jet printhead and the applied boundary conditions.*

where p_v and T_v are the approximately uniform pressure and temperature in the vapor bubble, p_{atm} is the atmospheric pressure (= 100 kPa), R is the gas constant (= 8.3148 J mol^{-1} K^{-1}), T_b is the boiling point of the ink, and m_M and Q_{vap} are molecular weight and heat of vaporization, respectively. Adding a time-dependent heating pulse leads to the following exponentially decreasing pressure function $p_v[t]$ which is displayed in figure 5.17:

$$p_v[t] = p_v(T_t) \cdot \exp\left[-\left(\frac{t}{t_0}\right)^{0.5}\right] + p_s(T_{amb}), \tag{5.2}$$

where $p_v(T_t)$ is the initial bubble pressure depending on the maximum heating temperature T_t (In the case of the Olivetti bubble jet the initial bubble pressure is 9 MPa) and p_s is the bubble pressure in the later stage depending on the ambient temperature T_{amb}. The parameter t_0 is a time constant indicating the speed of the pressure decrease. It depends on the geometry and the thermal properties of the used materials, but it is also affected by the dynamics of the heating pulse. The time constant t_0 has been estimated to be 0.055 µs by calibrating a series of simulations with corresponding experimental results starting from the value of 0.17 µs reported in the literature [199,201]. Therefore a set of simulations was set up with different time constants. Finally the time constant of 0.055 µs was chosen which lead to the most concurring droplet volume compared to the experimental findings. A 10 % change of the time constant leads to a change of the ejected droplet volume of nearly 10 %, whereas the dependency is linear which can be seen in figure 5.18. However, in reality this time constant can not be chosen arbitrarily. It is limited by the nucleation threshold and by the destructive power consumption of the micro heater. This calibration of the model was necessary due to the more complicated three-dimensional geometry compared to the simple assumptions made in [199,201] which leads to a different nucleation and bubble collapse in the present case.

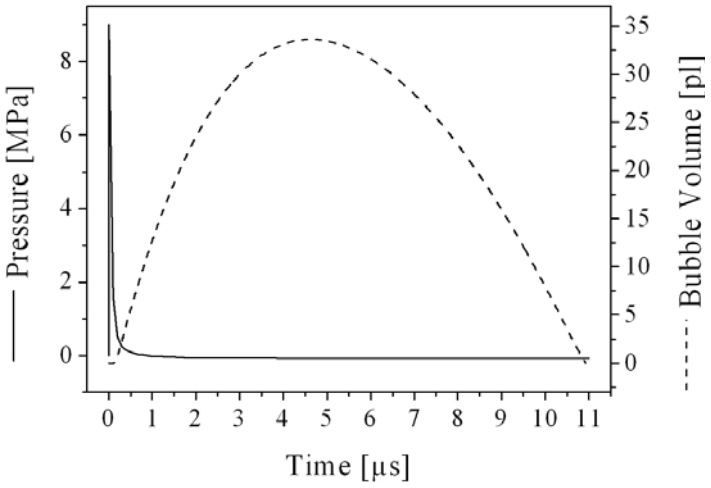

Figure 5.17: *Pressure pulse used as pressure boundary condition following the approach from Asai et al. and the bubble volume resulting from the CFD simulation of the design shown in figure 5.14.*

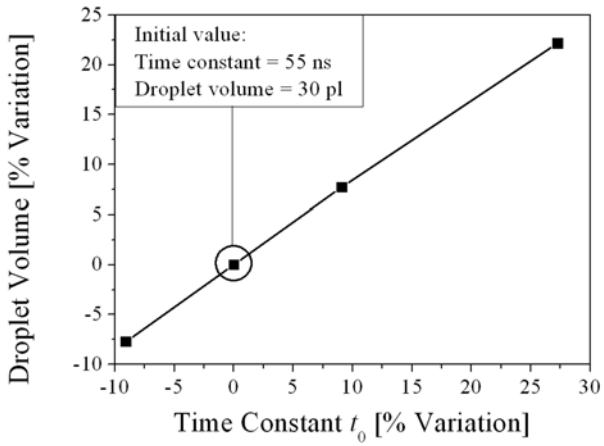

Figure 5.18: *Relative dependency of the ejected droplet volume on the time constant t_0 using the exponential decreasing pressure function occurring in a bubble jet printhead.*

RESULTING BUBBLE VOLUME

The presented pressure boundary has been applied to the model of different printhead designs under study by substituting the heater area of the real design with an inlet pressure boundary in the simulation using air as incoming medium. This simplification of using air instead of vapor is necessary because the CFD solver only can handle two different kinds of fluids, ink and air in this case. However, due to the previously presented calibration this simplification is not critical regarding the droplet volume. The pumped air forms the bubble, displaces the ink and creates a flow through the nozzle as well as back into the reservoir. The exponential decreasing pressure function results in a parabolic time-dependency of the bubble volume as displayed in

figure 5.17. Whereas maximum bubble volume and time characteristics depend essentially on the printhead geometry and ink properties. These are summarized in the empirical parameter t_0 of Asai's model.

Using the described approach for the pressure boundary condition the simulation results of simple 2D devices presented in the literature [164,167,208] could be reproduced easily by using the Volume of Fluid (VOF) method [116-121] including surface tension like implemented in CFD-ACE+. Afterwards the more complicated 3D model of the Olivetti I-Jet printhead, like it is displayed in figure 5.14 has been set up for the simulations. The simulation of a complete ejection process took about two days of computing time on a state of the art PC (Pentium P4, 1.8 GHz, 512 MB RAM).

5.4.2 VALIDATION

Comparing the simulations with experimental results like stroboscopic pictures as displayed in figure 5.19, good qualitative agreement has been obtained. The shape of the droplet and the tail look very similar. However, the experimental observed tail separates into satellite droplets earlier compared to the simulated one. The reason for this discrepancy is not clarified satisfactorily. The experimental behavior, however, is very reproducible which is proven by the fluent flow of the stroboscopic pictures.

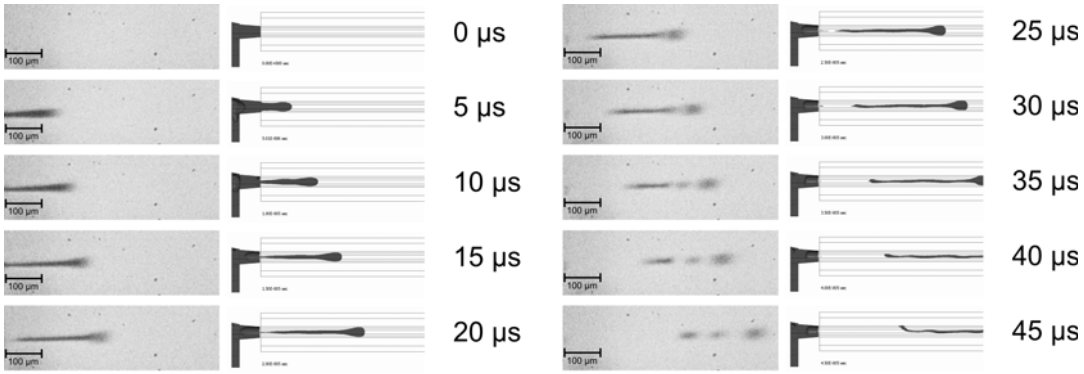

Figure 5.19: *Comparison of the 3D simulations of the droplet ejection of a 1/3 inch printhead (only the fluidic part is shown) and the corresponding stroboscopic pictures.*

For the quantitative comparison between experimental findings and simulations it has to be considered that the CFD simulations have been calibrated to the data of the manufacturer (cf. section 5.4.1). Therefore the time constant t_0 has been estimated in order to reach the droplet volume obtained by the manufacturer (cf. figure 5.18). Due to this the simulated droplet volumes of 30 pl for the nozzle of the 1/3 inch printhead and 73 pl for the nozzle of the one inch printhead agree perfectly to the intended droplet volume of the printhead manufacturer. The determination of the droplet volume out of the CFD simulation is done by integrating the volume flow at the nozzle outlet. The volume flow can be taken out of an ASCII file provided by the simulation tool at any arbitrary interface or inlet/outlet of the model.

Nevertheless the simulated droplet volumes as well as the given values of the manufacturer were intended to be reproduced by own measurements. Therefore the printhead prototypes were characterized gravimetrically (cf. section 5.2) using a custom made setup depicted in figure 5.11. The obtained quantitative agreement between experimental findings and simulations is also acceptable. The indicated errors are the CV of the measurements. The gravimetrically measured droplet volume of 21 ± 5 pl is slightly smaller compared to the intended and simulated volume of 30 pl for the nozzle of the 1/3 inch printhead. This is apparently due to the practical setup depicted in figure 5.11. The fluidic supply through the drilled hole from the backside increases the fluidic resistance considerably compared to the intended packaging in an inkjet cartridge and therefore in the implemented simulation model. There against the printhead inside a cartridge is supplied with ink via a feeding slot over the whole length of the printhead. For the one inch printhead the intended and simulated droplet volume of 73 pl differs more significantly from the measured volume of about 58 ± 11 pl. This is also caused by the experimental setup (cf. figure 5.11) used for the one inch printhead as well. The experimental setup is even worse compared to the setup for the 1/3 inch design because the one inch printhead has no feeding slot due to fabrication problems. Hence, the printhead has to be filled via a hole in the polyimide nozzle plate produced by sticking with a syringe needle. This causes a much higher fluidic resistance from the supply channels.

The simulated velocities are 11 m/s for the 1/3 inch design and 12 m/s for the one inch design. Compared to the own experimental obtained velocities of 12 ± 3 m/s and 11 ± 3 m/s for the 1/3 and one inch design, respectively, the simulated values agree quite good. In this case for the evaluation of the velocity by stroboscopic pictures an error of about 30 % has to be considered instead of an error of 20 % presented in section 4.2.1. The higher random error is explained by the intensively blurring due to the high velocity of the droplet. The determination of the droplet velocity from the CFD simulation is done by measuring the mean velocity of the droplet 100 µm outside the nozzle using the post-processing tool from CFD-ACE+. The intended droplet velocities of the printhead manufacturer are 11 m/s and 10 m/s for the 1/3 and one inch design, respectively. Additionally in figure 5.20 the simulated and measured travelled distance of the droplet is displayed depending on the elapsed time. The distance was also obtained out of the post-processing tool by measuring the distance from the nozzle to the leading end of the droplet. The same way the experimental travelled distance was determined out of the stroboscopic pictures depicted in figure 5.19. Using this the time dependent velocity can be calculated which initially decreases and then stays nearly constant for the CFD simulation whereas the experimental velocity is more fluctuating.

The estimation of the critical values of the inkjet using the energetic model in section 3.1.2 leads to a critical pressure of $p_{critical} = 30$ kPa using equation (3.20), a critical time of $t_{critical} = 4.4$ µs using equation (3.24) and a critical power of $P_{critical} = 78$ µW using equation (3.26). The critical pressure of 30 kPa is surpassed clearly by the high initial value of the dominating pressure pulse (cf. figure 5.17).

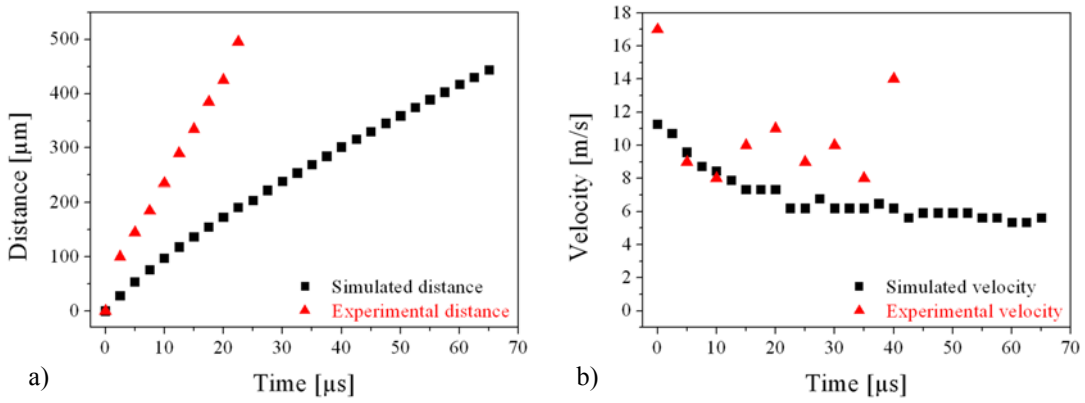

Figure 5.20: *Time dependent travelled distance a) and time dependent velocity b) of the droplet obtained by the CFD simulation as well as experiments.*

However, this is happening only for a fraction of the critical time. Hence, no droplet ejection would be expected. This inconsistency can yet be explained by the fact that the bubble jet printhead has a combined pressure and flow boundary condition (cf. section 3.3.3). Due to this also the time period of the volume displacement of the vapor bubble has to be taken into account. Thus the duration of the driving actuation is about 11 µs instead of below 1 µs (cf. figure 5.17). These 11 µs are 2.5 times the critical time of 4.4 µs. This factor of 2.5 agrees very well with the ejected droplet volume. Considering the volume of a droplet with the diameter of the nozzle of 11.5 pl as it is the basis of the energetic approach, the really ejected droplet volume of 30 pl is also about 2.5 times larger. Thus the occurring actuation time as well as the ejected volume are about 2.5 times larger than the predicted values of the energetic estimation. Comparing the critical power of 78 µW for a droplet ejection with the required electrical power of about 4 W per nozzle exhibits a clear discrepancy. That means that only about 1/50,000 of the inserted power is used for the droplet ejection. The rest is used up by temperature losses.

Calculating the Weber number for the inkjet out of the CFD simulations results in a very high Weber number of $We = 67$ at the highest velocity in time. Considering the classification in section 3.1.1 this would be in the atomization regime. However, due to the fact that this high Weber number is only attained for a time much shorter than the critical time leads to a droplet formation instead of an atomization.

5.4.3 First Priming

Apart from a complete ejection sequence also a reliable first priming of the printhead is important to guaranty a robust functionality of the printhead. Enclosed and trapped gas bubbles would lead to malfunction or erratic behavior. In figure 5.21 a picture sequence of the simulated first priming is displayed from different point of views, respectively. The used grid was the same as for the droplet ejection simulations. The inner walls of the nozzle and nozzle chamber are ideally full wetting. The reservoir

inlets were realized as pressure boundary condition (p = 0 Pa, fluid 1), and the nozzle outlet was also realized as pressure boundary condition (p = 0 Pa, fluid 0). As initial condition a small amount of liquid was placed in the reservoir channels to facilitate the beginning and convergence of the simulation. The filling simulation took about three to four weeks of computing time on a state of the art PC (Pentium P4, 1.8 GHz, 512 MB RAM). The very long computing time compared to the droplet ejection is due to the low dynamics during the capillary filling and the resulting small time steps automatically calculated by the solver using the progressing interface. In the results, there is no stagnancy of the meniscus movement or an enclosed bubble visible. The small amount of liquid which is visible after 90 µs arise from small numerical errors. This could be suppressed by a procedure called "remove flotsam jetsam" implemented in CFD-ACE+ which was not activated in the simulation. Therewith small amount of liquids can be removed depending on their appearance frequency [122]. The first priming takes about 350 µs starting at the big ink feeding slot.

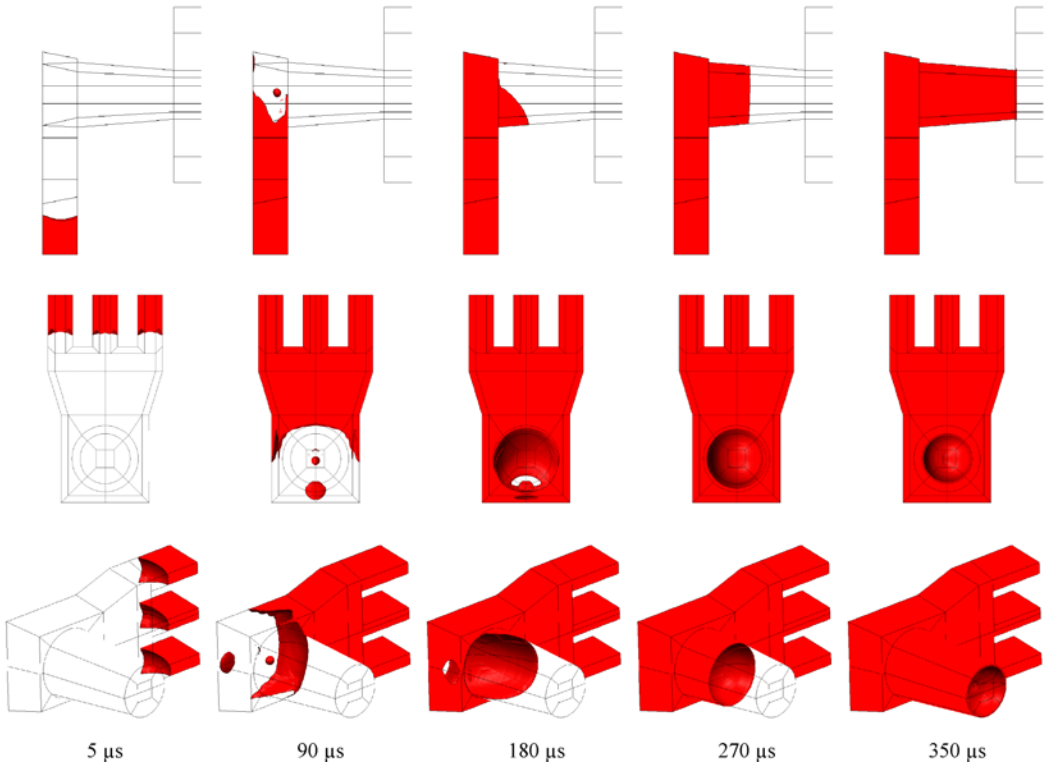

Figure 5.21: *Simulated picture sequence of the first capillary filling of one nozzle from different point of views.*

5.4.4 Temperature Distribution

Another interesting point is the thermal behavior inside the printhead. Due to an increased temperature inside the nozzle chamber the ink would have a reduced viscosity leading to change in the print performance. In figure 5.22 a picture sequence of the temperature distribution inside the printhead with an initial temperature of 400°C or 773 K is shown. The bubble temperature is nearly cooled down after 5 µs and

totally at ambient temperature after completion of the ejection cycle of about 10 µs. Due to this no warming of the ink in the nozzle chamber can be expected. However, during operation of a real printhead in a printer with several kilohertz, the entire printhead warms up to about 50°C, which is the experience of the printhead manufacturer and could also be observed in experiments. This contradiction can be explained by two facts not implemented in the CFD simulation. First the real device warms up completely due to the heat generation of several hundreds of heaters and the thermal conductivity of the used materials, which is not considered in the CFD model. Second the real device indicates a warming after thousands of thousands of droplet ejections which can also not be realized by the CFD simulation due to the lack of computing time. Hence, the temperature behavior during one ejection cycle could be observed using the CFD simulation but the long term temperature behavior occurring in the real device cannot be reflected by this method.

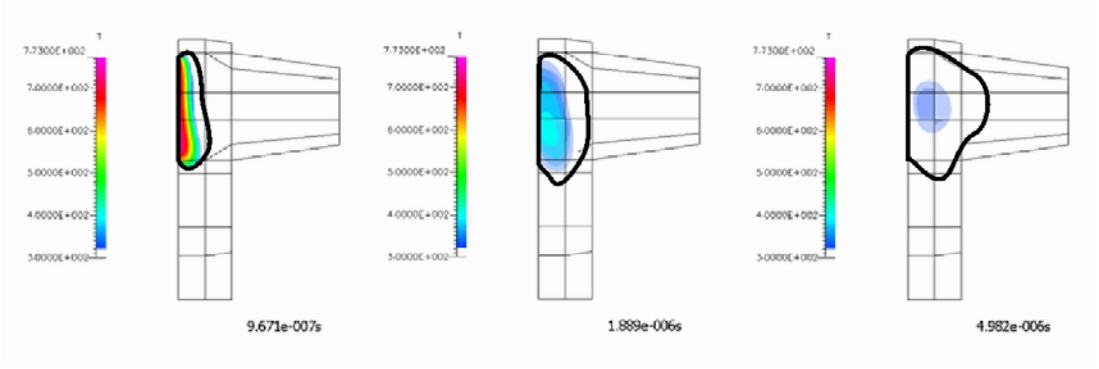

Figure 5.22: *Simulated picture sequence of the temperature distribution inside the vapor bubble which is indicated by the black line.*

In figure 5.23 the simulated temperature progress depending on the distance to the heater surface is displayed. The initial temperature of 773 K is only present directly at the surface. After about 1.5 µs the temperature is below 400 K everywhere. In a distance of 10 µm above the heater surface the temperature achieves only about 350 K.

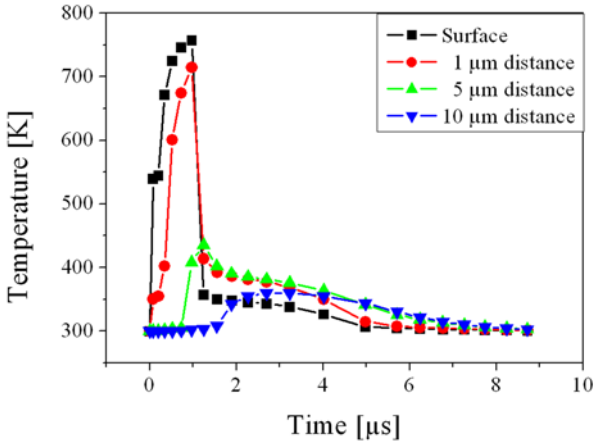

Figure 5.23: *Simulated temperature progress depending on the distance to the heater surface.*

5.5 Influence of Specific Design Parameters

After the validation of the simulation model further simulations have been performed to optimize the printhead by varying parameters like geometrical dimensions, heating pulse or ink properties.

5.5.1 Laser Machining and Assembly Tolerances

The knowledge of the allowable mechanical tolerances is very important for the laser machining and the assembly of the printhead. Especially the effect of lateral alignment deviations or differences of chamber height have been studied in detail. The effect of a variation of the nozzle diameter or the draft angle which are both affected by the laser machining process on the droplet volume and velocity are displayed in figure 5.24 and figure 5.25, respectively. In this case the intended design is a slight variation of the 1/3 inch design presented before concerning the chamber height and the design of the supply channels. Due to this the simulated droplet volume of 25.6 pl varies from the above presented 30 pl. With increasing nozzle diameter the droplet volume increases because the fluidic resistance of the nozzle decreases compared to the supply channels. Moreover it leads to a slight decreasing of the droplet velocity. The variation of the draft angle was done by reducing the nozzle outlet diameter at a fixed nozzle inlet diameter. Due to this the fluidic resistance is increased by a larger draft angle which leads to a smaller droplet volume and a higher velocity.

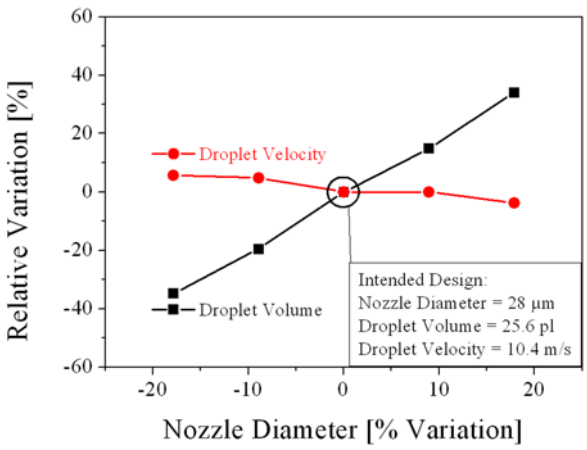

Figure 5.24: *Simulated effect of varying the nozzle diameter on the droplet volume and velocity.*

Furthermore, also the critical pressure $p_{critical}$, the critical time $t_{critical}$ and the critical power $P_{critical}$ for the inkjet printhead as presented in section 5.4.2 are changing with varying nozzle diameter like displayed in figure 5.26. To compare the results of the energetic approach with the effect on droplet volume and velocity out of the CFD simulation depicted in figure 5.24 the nozzle diameter was varied in the same way. With increasing nozzle diameter the critical pressure decreases whereas the critical time increases. However, the critical power is nearly independent on the nozzle

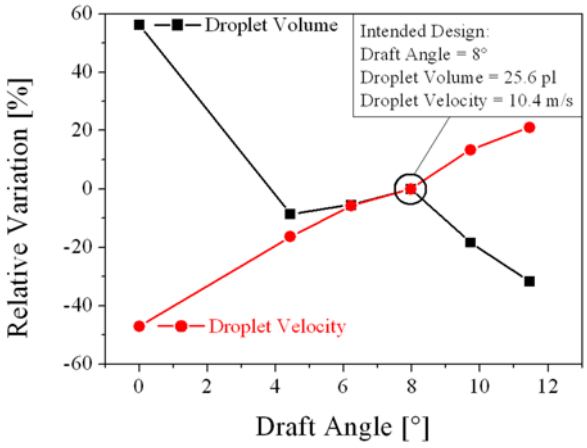

Figure 5.25: *Simulated effect of varying the draft angle on the droplet volume and velocity.*

diameter. Nevertheless, the results of the energetic approach agree quite good with the CFD results because with increasing nozzle diameter, respectively decreasing fluidic resistance, the droplet volume increases whereas the critical pressure decreases. Moreover, varying the nozzle diameter in the range of about ± 20 % leads to a variation of about ± 40 % of the droplet volume as well as of the critical pressure.

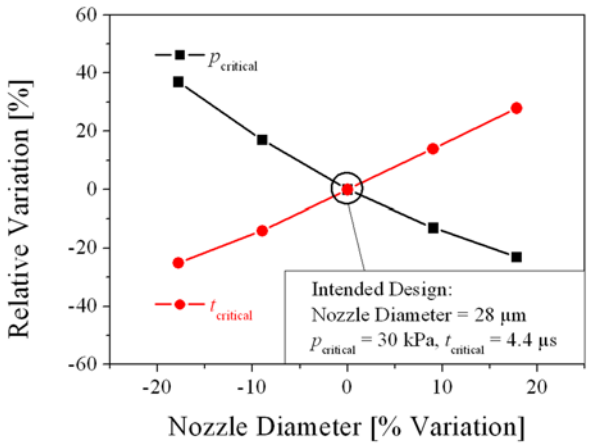

Figure 5.26: *Critical pressure $p_{critical}$ and critical time $t_{critical}$ of the inkjet model calculated using equation (3.20) and (3.24) depending on the nozzle diameter.*

The effect of other variations like a misalignment or an increased height of the adhesive layer on the droplet volume and velocity is summarized in figure 5.27. As mentioned before these results are very useful for determination of allowable tolerances for the assembling and packaging.

Summarizing the figures above it can be stated that a small variation of the nozzle chamber height or even a misalignment of up to 67 % leads to a negligible change of the resulting droplet volume and velocity. Whereas a deviation of the nozzle diameter or its draft angle induces a more significant change of the ejected droplet volume and velocity. In this case a variation of 20 % of the nozzle diameter leads to a variation of

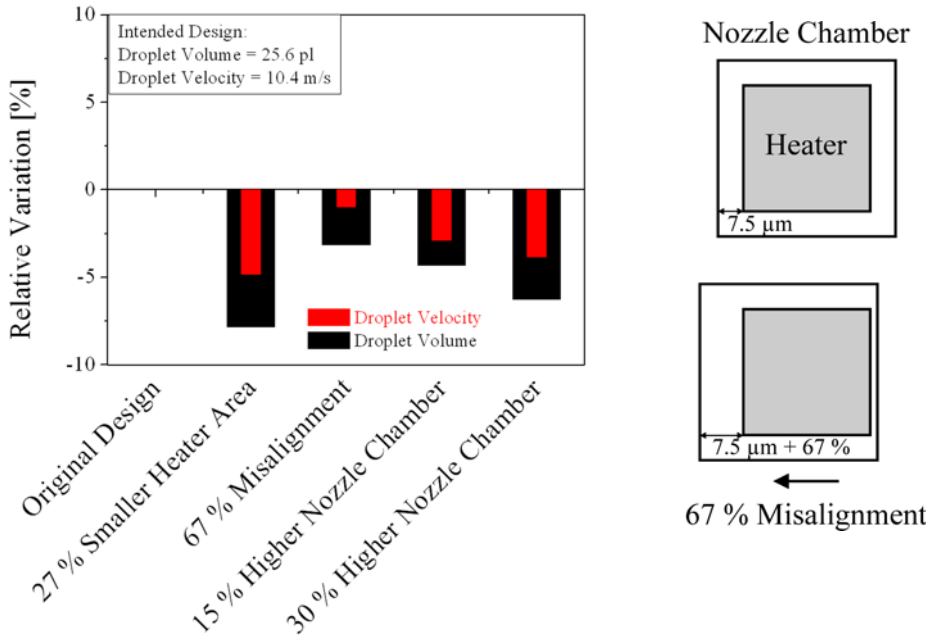

Figure 5.27: *Comparison of simulated droplet volumes and velocities considering different geometrical tolerances. The 67 % misalignment means a misalignment of heater and nozzle chamber of 67 % (= 5 µm) compared to the original distance of them like it is displayed in the schematic drawing.*

the droplet volume of 35 % and a variation of the droplet velocity of 5 %. A variation of 50 % of the nozzle diameter leads to a variation of the droplet volume of 30 % and a variation of the droplet velocity of 20 %.

5.5.2 Ink Properties

It is well known that the ink properties play a major role in determining the print volume (cf. section 3.2.2). Tuning of the ink is the usual method applied to adjust the volume. Varying the ink parameters like density, surface tension or dynamic viscosity leads to a significant change in the droplet volume as displayed in figure 5.28 for the considered Olivetti printhead. The droplet volume can be halved by increasing the density six fold. But reducing the droplet volume by varying ink parameters induces also additional changes in the ejection behavior. The droplet velocity for example is also very sensitive to fluid properties especially to the ink density (cf. figure 5.29). High density ink leads to very low droplet velocities, which is not desirable. Furthermore altering surface tension or viscosity also causes a significant change of the velocity.

Another result of the VOF simulations can be educed by surveying the shape of the ejected droplet and its tail. Tail length and potential satellites are an important criterion for the quality of later printouts. The dependence of the tail length on the different ink properties is illustrated in figure 5.30. The bandwidth of the tail length ranges between very long tails (1000 µm) and very short tails (100 µm). For a very long tail, the tail

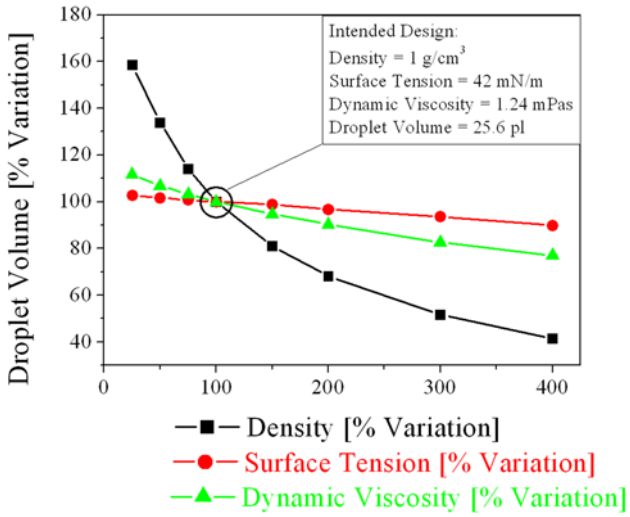

Figure 5.28: *Simulated droplet volume dependence on the density, the surface tension and the dynamic viscosity of the ink, respectively.*

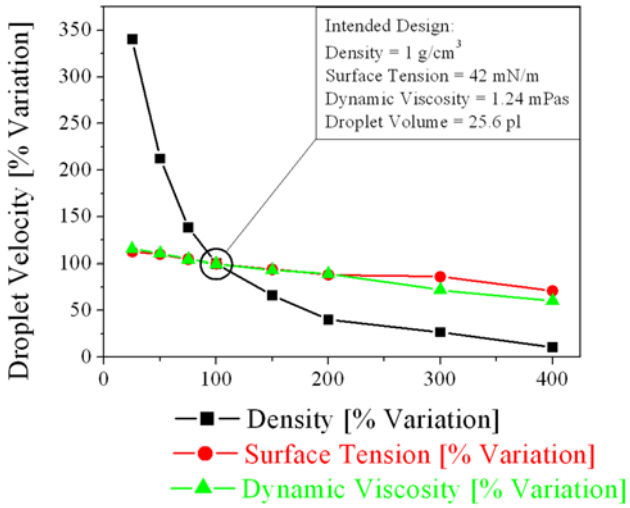

Figure 5.29: *Simulated droplet velocity dependence on the density, the surface tension and the dynamic viscosity of the ink, respectively.*

breaks in some satellites whereas for very short ones the tail contracts with the droplet so that no satellites occur. Beyond increasing the print resolution [166-168] and realizing a monolithic printhead [164,165] preventing satellite droplets is an important part of current research and development activities [169,170].

Admittedly regarding this results one has to keep in mind that the ink properties cannot be tuned independently. In reality density, surface tension and dynamic viscosity are intimately connected. The optimum interaction between printhead geometry and ink parameters has to be found by combining all of the simulation results appropriately.

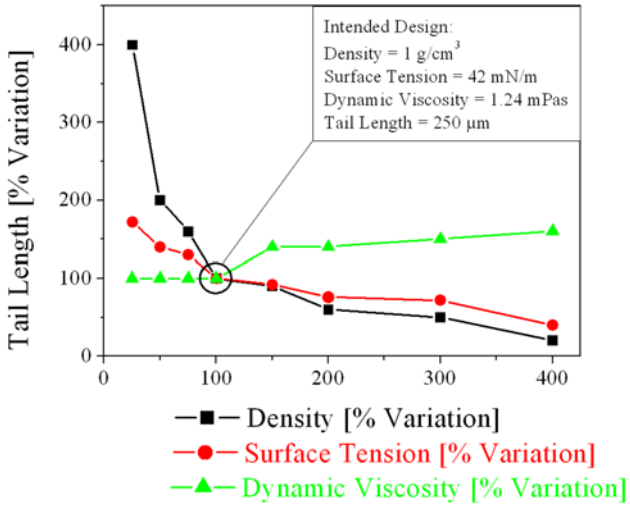

Figure 5.30: *Simulated tail length of the droplet dependence on the density, the surface tension and the dynamic viscosity of the ink, respectively.*

5.6 Optimization Potential

The only serious disadvantage of the studied printhead design is the fact, that the nozzle chamber is not symmetric (cf. figure 5.14). This leads to an asymmetric bubble generation where the bubble touches three walls of the chamber like it is displayed in figure 5.31 a). As a result the trajectory of the ejected droplet is not perfectly parallel to the nozzle (cf. figure 5.31 b) which leads to different impact positions of main droplet and satellite droplets. This leads to an undesired blurring of the picture. These results are also confirmed by experimental measurements of Olivetti I-Jet.

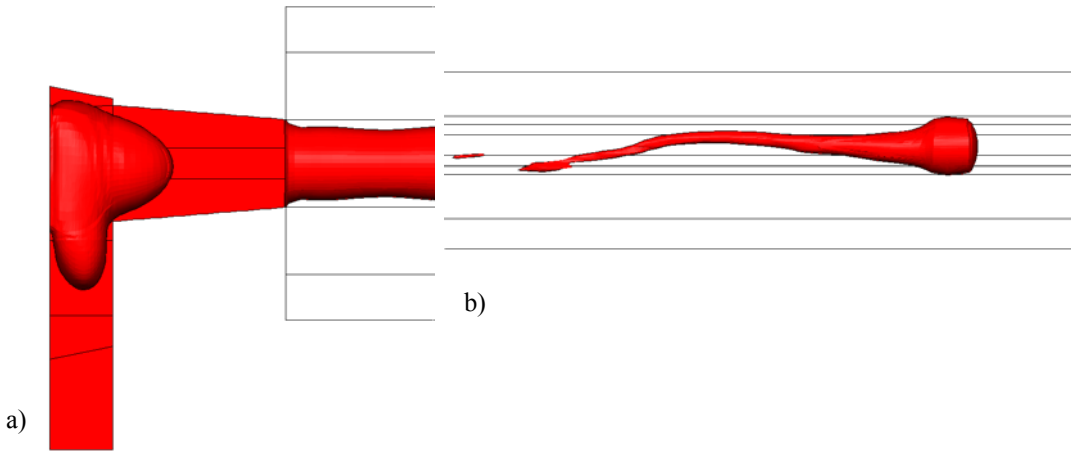

Figure 5.31: *Effect of the asymmetric nozzle chamber of the actual design. a) An asymmetric bubble generation and b) a slantwise trajectory of the ejected droplet.*

This problem can be avoided by using a different geometry of the nozzle chamber where its shape is more symmetrically and the bubble touches two walls of the chamber. In figure 5.32 the schematic top view of such an optimized geometry is displayed. In this case the bubble only touches the upper and the lower walls of the nozzle chamber which should result in a linear droplet ejection. An advantage of the examined design compared to the new proposal is the probably higher maximum frequency due to the optimized supply channel design. This advantage might be lost if the three supply channels are reduced to two like sketched in figure 5.32.

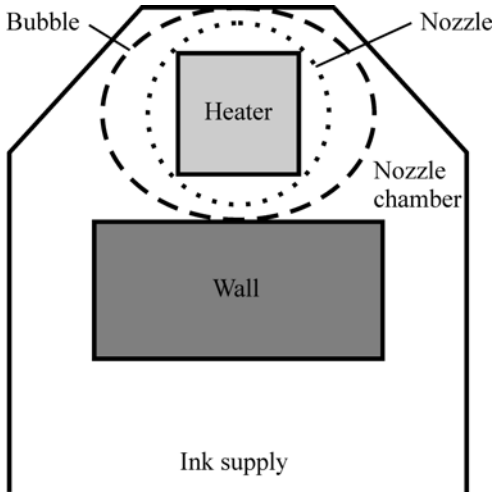

Figure 5.32: *Schematic top view of an improved printhead design concerning the asymmetric bubble generation and droplet ejection.*

6 Alternative Droplet Generators

In this chapter alternative droplet generators are considered. Some of the discussed devices eject jets rather than droplets but in an on-demand mode in contrast to the already discussed continuous jet mode. The individual systems are described considering dosage technology, experimental results, the theoretical or numerical description and a short conclusion. The droplet generators are systematically arranged according to decreasing minimum dosage volume, starting with about 50 nl for the Dispensing Well Plate, followed by fast switching valve systems with about 10 µl to 20 nl, the NanoJet system with about 60 nl to 20 nl, the PipeJet with about 40 nl to 5 nl. Below 1 nl there are the TopSpot with a dosage volume of about 800 pl, TopSpot Vario with 1.5 nl to 200 pl and finally the aerosol atomizer with about 100 fl. The volume range of about 100 pl to 10 pl missing here is covered by the bubble jet printhead presented in the previous chapter.

In figure 6.1 the different droplet ejectors are displayed in a kind of map depending on the ejected volume and the amount of liquids which can be handled in parallel. The number of different liquids handled in parallel is an important property for many life science applications like micro array fabrication or micro well plate technology.

The results presented in the following have been partially achieved by others and are cited to complete the work. The corresponding sections are denoted accordingly.

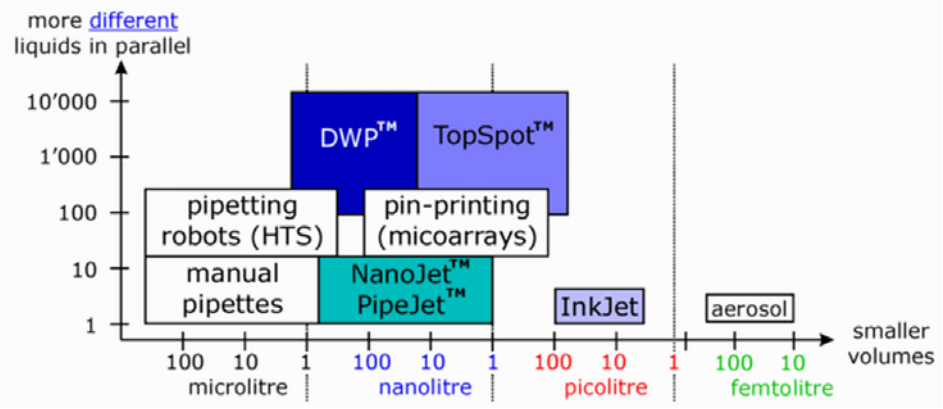

Figure 6.1: *Classification of droplet ejectors depending on the ejected volume and the amount of liquids which can be handled in parallel [172].*

6.1 Dispensing Well Plate (DWP™)

In order to reach ever higher integration densities of small amounts of liquid, a pneumatically actuated fixed volume dispenser, termed Dispensing Well Plate (DWP) has been developed and studied by Zengerle, Koltay, Steger et al. [209-212]. The DWP

is a dispensing system of up to 1536 dispensing units for the massive parallel delivery of liquid volumes in the range of 50 nl. A cheap and simple pneumatic actuation mechanism allows for the simultaneous and contact free delivery of different liquids. The geometrical defined dispensing volume is the main reason for the extraordinary performance of the system, a reproducibility of 2 - 5 % and a homogeneity within individual droplet arrays of 1 - 2 %. One key application for the DWP system within High-Throughput-Screening (HTS) is the rapid compound reformatting by direct addition of nanoliter volumes to an assay. The standard configuration for the DWP is therefore an array of dispensing units where every reservoir of a dispensing unit is connected to one nozzle via a micro channel. The dispensing performance of different liquids is in a certain range independent from liquid properties because the liquid volume is predefined only by the nozzle geometry. Advantages of the DWP system are given by the small dispensing volumes which can be handled accurately and in a highly parallel way and by the possibility of the extremely high integration density up to the 1536 well plate format. The DWP method can be classified as droplet generator with pressure boundary condition according to section 3.3.

6.1.1 DOSAGE TECHNOLOGY

The complete DWP dispensing system is composed of a pneumatic actuation unit driving the microfluidic chip termed DWP as it is displayed in figure 6.2. The DWP-chip itself consists of 24, 96 or 384 independent dispensing units arranged at conventional well plate spacing. Each dispensing unit of the DWP consists of a reservoir, a connection channel and a nozzle chamber like it is displayed in figure 6.3 [212].

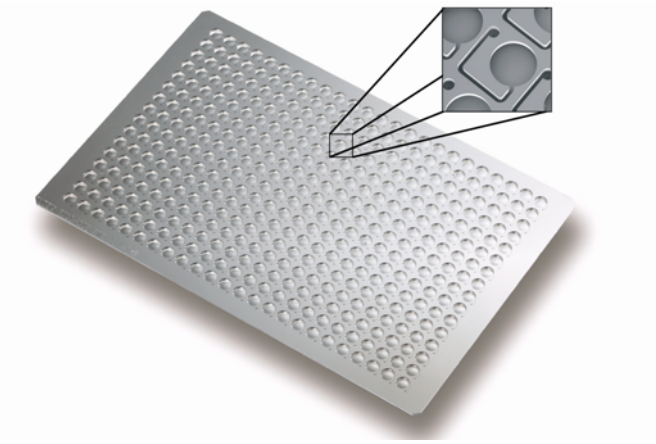

Figure 6.2: *Dispensing Well Plate with 384 dispensing units made by silicon bulk micromachining (pitch of 4.5 mm) [212].*

The reservoirs have a volume of about 6.8 µl and can be filled by conventional pipetting systems. The subsequent dispensing process proceeds like illustrated in figure 6.4. The nozzle chambers are always filled completely via the connection channels from the reservoirs due to capillary forces (figure 6.4 b) - c)). A pressure

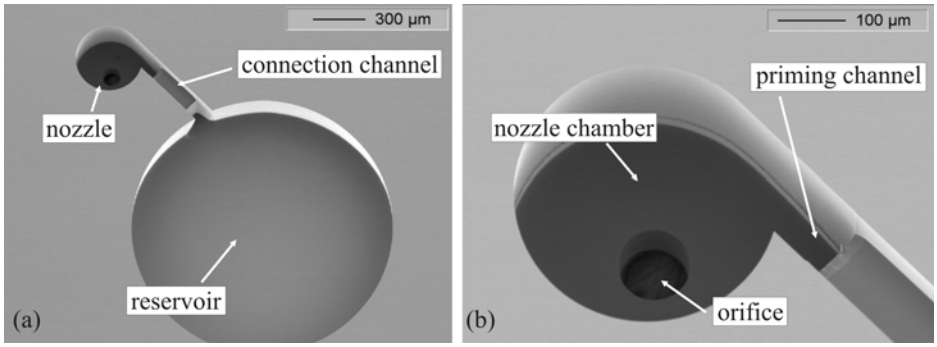

Figure 6.3: *SEM micrograph of a) a single DWP dispensing unit micromachined in silicon b) a close up of the nozzle chamber [212].*

pulse, provided by the actuation mechanism, applied to the whole upper surface of the DWP leads to a driving out of the entire liquid contained in the nozzle chambers (figure 6.4 d) - e)). No pressure driven flow occurs within the connection channel because reservoir and nozzle chamber are on the same pressure level. Thus essentially the volume confined in the nozzle chamber is dispensed. After switching off the driving pressure, the nozzle chambers refill from the reservoirs by capillary forces. Hence, the DWP performs as a fixed volume dispenser where the dosage volume is mainly determined by the geometrical volume of the nozzle chamber. There against, the liquid properties and external parameters like pressure intensity and duration are not affecting the dispensed volume [212].

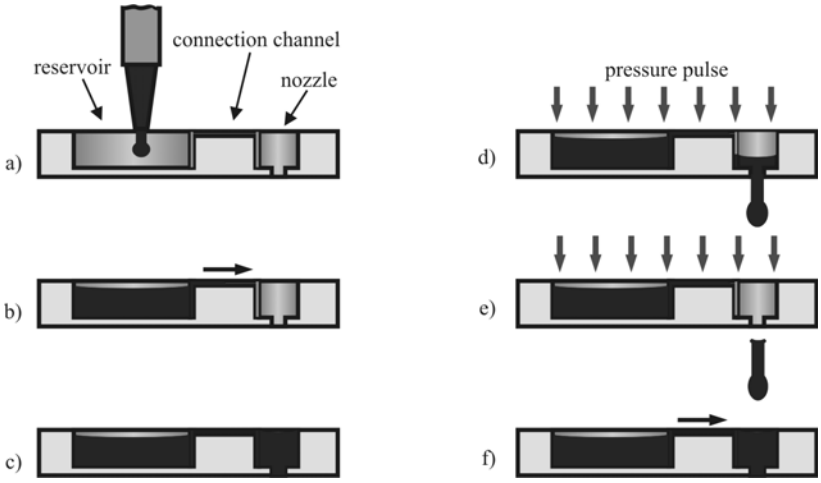

Figure 6.4: *Schematic illustration of the DWP working principle: a) Filling of the DWP b) capillary priming of the nozzle c) DWP ready for dispensing d) actuation of the DWP by pneumatic pressure e) complete depletion of the nozzle chamber during jet ejection f) refilling by capillary forces [212].*

6.1.2 EXPERIMENTAL RESULTS

The experimental examination of the DWP was done by Zengerle, Koltay, Steger et al. [209-212]. The homogeneous and reproducible jet generation is demonstrated by the stroboscopic picture displayed in figure 6.5. An actuation pressure of 20 kPa leads to a jet escape from the 100 µm wide nozzles at a speed of approximately 1.6 m/s and terminates in a spray of liquid after jet tear off. The rest volume is continuously driven out of the nozzle by the following high speed air flow which causes the spray [210].

The presented DWP prototypes have been characterized by gravimetric measurements. The overall dispensed mass was measured with a micro balance according to the procedure presented in section 4.1 leading to a mean dosage volume of about 50 nl to 60 nl per unit. Furthermore, the influence of pressure intensity and pulse duration on the dosage volume was studied. No pressure dependence of the dosage volume has been detected which proves the fixed volume dispensing concept. In figure 6.6 the high reproducibility of the dispensed volume for different actuation parameters and different liquids is displayed. The single measurements correspond to the mean value of dispensers having 24 dispensing channels in parallel. Moreover, excellent CVs of about 1 % can be obtained by the measurements [210]. The used medium was DMSO (ρ = 1100 kg/m^3, η = 2.3 mPas, σ = 44 mN/m).

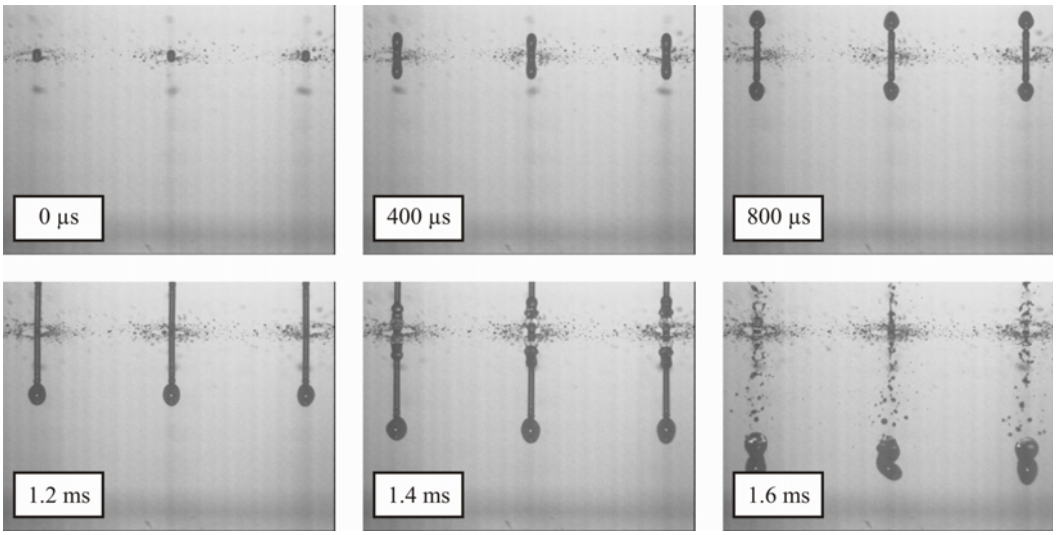

Figure 6.5: *Stroboscopic pictures of the jet ejection from three nozzles of a DWP at successive points in time (dispensed medium: DMSO).*

6.1.3 NUMERICAL DESCRIPTION

The CFD simulations of the dispensing process presented in this section have been carried out using the software package CFD-ACE+ by Zengerle, Koltay, Steger et al. [209-212]. The aim was to study the fluid flow within the system as well as the jet ejection. Because these data contain essential information on the dynamic behavior required for system optimization.

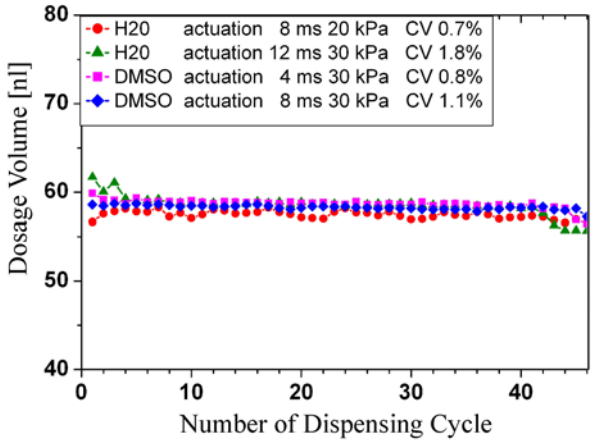

Figure 6.6: *High reproducibility of the dispensed volume for different actuation parameters and different liquids.*

For the CFD simulations a fully three-dimensional model of a single dispensing unit has been set up taking advantage of the symmetry along the connection channel as displayed in figure 6.7 a). The applied boundary conditions are also visualized. The upper surface as well as the distant end of the connection channel have been defined as pressure inlet for the actuation (arrows in figure 6.7 a)). The applied pressure pulse has been determined by experimental findings presented in [210]. The measured pressure is displayed in figure 6.7 b). The pressure history was approximated within the simulations by a straight line like also depicted in figure 6.7 b) [211].

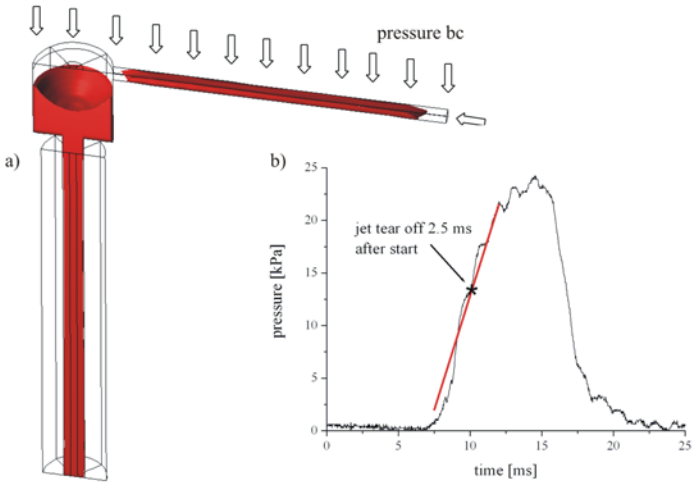

Figure 6.7: *a) Grid model and boundary conditions used for the CFD simulation b) measured pressure history of a DWP prototype device and the applied pressure for the CFD simulation [211].*

In order to validate the CFD model stroboscopic pictures are compared with corresponding pictures of the simulation like it is displayed in figure 6.8. The qualitative agreement between simulation and measurement is good. The ejection

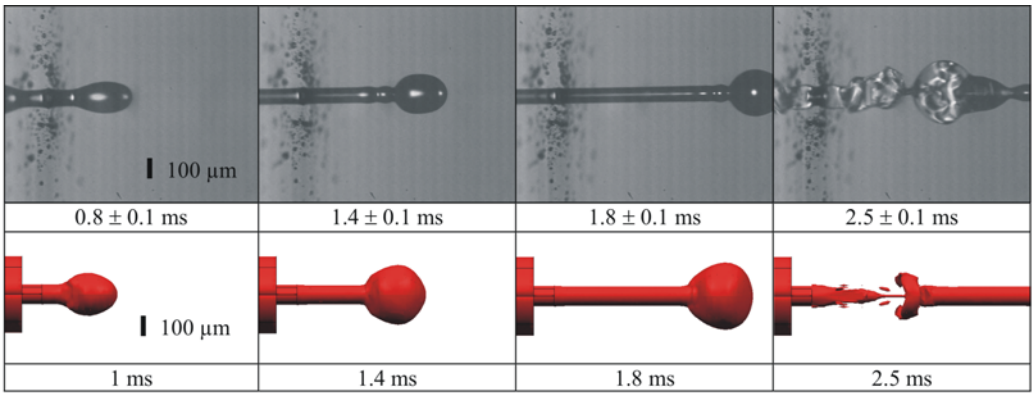

Figure 6.8: *Sequence of the jet ejection obtained from stroboscopic measurements (top) and CFD simulations respectively (bottom). Both picture series are drawn to scale (see scale in the first picture) [211].*

speed as well as the jet shape are correctly reproduced. Minor deviations might be explained by the approximated driving pressure or by slightly deviating material properties [211].

The flow through the connection channel as well as through the nozzle have been extracted out of the simulations as displayed in figure 6.9 a). The volume flow through the nozzle increases linearly after the jet has formed and reaches a plateau after jet tear off which defines the dispensed volume. Hence, the duration of the pressure pulse is not critical regarding the dosage volume. The volume flow through the connection channel during that time is inessential [211]. The pressure intensity influences only the slope of the curve, hence, the jet duration but not the dispensed volume which can be seen in figure 6.9 b). However, the dispensed volume does not achieve the geometrical volume (displayed as dashed line in figure 6.9 b) of the nozzle channel in any case, i.e. a certain fraction of the liquid remains in the nozzle chamber [211]. The ejection process could not be simulated longer than the displayed results because of convergence problems of the simulation due to the spray generation after the jet tear off.

6.1.4 Conclusion

Summarizing the above presented results the mainly influential design parameters for the DWP are the geometrical dimensions of the single dispensing units because the ejected volume is nearly independent on applied pressure value and duration. The total dosage volume contained in the nozzle chamber is defined by its geometrical dimensions and the volume remaining in the nozzle which mainly depends on the shape of the nozzle. The DWP method can be classified as droplet generator with pressure boundary condition according to section 3.3 regarding the droplet generation. However, regarding the application and the dosage accuracy the DWP method can be classified as droplet generator with flow boundary condition according to section 3.3 because of the geometrical defined volume.

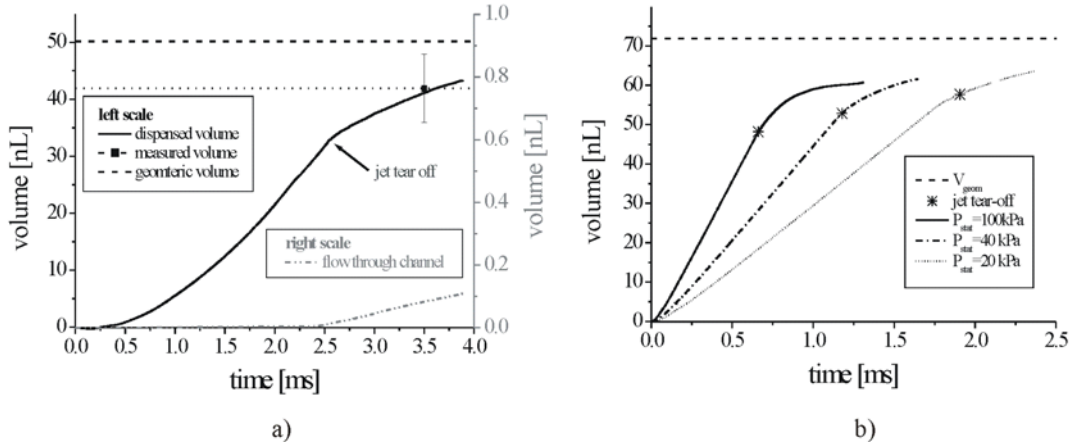

Figure 6.9: *Dispensed volume as a function of time a) as simulated with the geometry displayed in figure 6.7, b) Dispenser driven by various constant pressures.*

The above presented DWP system as described in [209-212] with 100 µm nozzle exhibits a critical pressure of 6.9 kPa, a critical time of 30.0 µs and a critical power of 119 µW according to the model presented in section 3.1.2. The used pressure of at least 20 kPa is above the critical value as well as the used times which are in the range of some milliseconds. Due to this data a jet rather than a single droplet can be expected. This can be confirmed with experimental findings as well as with CFD simulations. The approximated velocity of the jet of 1.6 m/s and the parameters of the used liquid DMSO can be used to calculate the attained Weber number. The resulting Weber number of 6.4 is smaller than the expected 8 or higher. The reason for this could be the approximated velocity of the jet. The velocity inside the nozzle might be higher. Assuming a real velocity of 1.8 m/s inside the nozzle would provide a Weber number of 8.1.

Thus the DWP system is no droplet generator in the sense of chapter 3. It is rather a device where the liquid plug is delivered as a jet, hence a jet-on-demand dispenser according to the definition in section 3.3.5. The required energy is delivered during the comparably long ejection time (2 ms - 3 ms).

6.2 Fast Switching Valve Systems

In this section fast switching valve systems are explained by means of one example. However, many of the droplet generators on the market like from Vermes [143], Delo Industrieklebstoffe [42], NanoJet from microdrop Technologies [144], or Cartesian Dispensing Systems [145] are based on this or a quite similar working principle. Generally fast switching valve systems can be classified as droplet generator with pressure boundary condition according to section 3.3.

6.2.1 Dosage Technology

Most fast switching valve systems are based on a pressurized reservoir and of course a fast switching valve controlled by a piezostack actuator or a solenoid. The valve is usually placed near the nozzle for the droplet ejection to avoid pressure losses downstream. In figure 6.10 a working principle of an exemplary fast switching valve system is displayed. A cylindrical piston actuated by a piezostack can be moved inside a drilling which serves as a guidance and ends in a nozzle at the bottom. This valve can be opened and closed by the actuator and is pressurized from the back side. Moving the piston upwards leads to an opening of the valve and results in a possible liquid ejection due to the overpressure. If the velocity of the piston v_{piston} is sufficiently high during the subsequent closing, additional kinetic energy can be applied to the nozzle.

Mainly there are two possibilities to control or affect the droplet ejection. On the one hand there is the pressure inside the reservoir, and on the other hand the movement of the actuator respectively piston including the stroke and the velocity of the piston and the time during which the valve stays open.

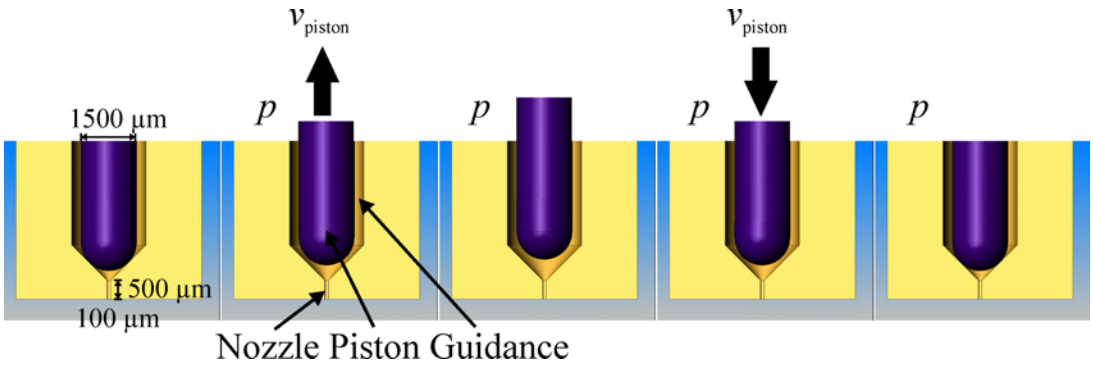

Figure 6.10: *Working principle of a fast switching valve system.*

6.2.2 Experimental Results

For the examination of the fast switching valve system from Vermes [143], stroboscopic pictures as well as gravimetrical measurements were made. Figure 6.11 shows a typical ejection of water recorded with the stroboscopic camera. Depending on the period of time that the valve stays open either a jet, as in this example, or a single droplet can be obtained.

Some gravimetrical measurements showing the reproducibility and the dependence on the piezo stroke are shown in figure 6.12 using water as dispensing medium. The total opening time was fixed to 2 ms and the driving pressure was set to 40 kPa. The total opening time includes the time for opening the valve, the time the valve stays open and the time for closing the valve. The measurements indicate a significant but non-linear dependence of the dispensed volume on the piezo stroke. However, the

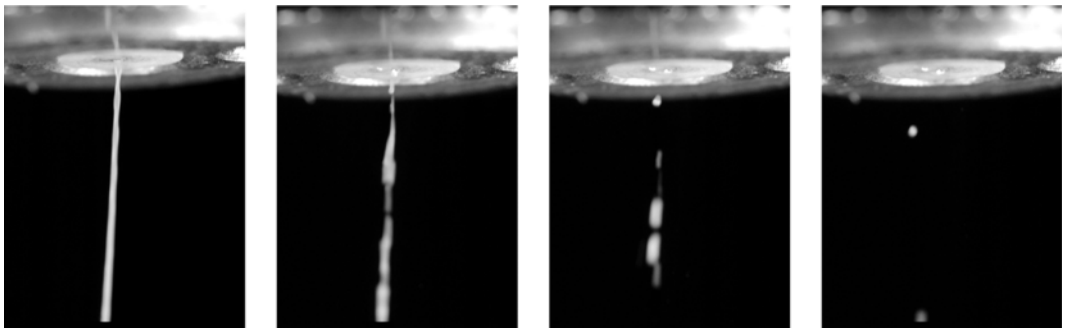

Figure 6.11: *Dispensing of water using the fast switching valve system from Vermes [143].*

different volumes are caused by the longer period of time that the valve stays open because the piezo speed was fixed in these experiments and not by the piezo stroke itself.

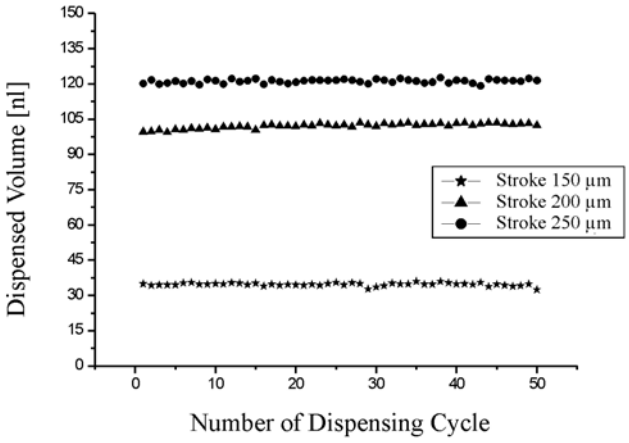

Figure 6.12: *Dispensed volume for different dispensing cycles using various piezo strokes. The used medium was water, the total opening time was fixed to 2 ms and the driving pressure was set to 40 kPa.*

6.2.3 NUMERICAL DESCRIPTION

The simulation of such a valve using a CFD tool is not trivial because of two main problems. First of all, the total closing of the valve cannot be simulated straight forward due to the collapsing grid during the closing near the contact area. The grid elements in this area have to disappear during the closing which is not foreseen in CFD-ACE+ and most other CFD codes. Furthermore, a transient simulation including the movement of the piezo is not compatible with the use of the VOF method for the simulation of the free surface of the ejected liquid in CFD-ACE+.

To overcome these problems a succession of steady state simulations was performed using the AMG solver but without using the VOF method. This was done to determine approximately the mean velocity inside the nozzle as a function of time. The applied two-dimensional axisymmetric model consists of a structured computational grid of about 7,600 cuboid cells where the smallest one has an area of

1.3 x 10^{-17} m^2 and the largest one has an area of 5.9 x 10^{-14} m^2 as it is displayed in figure 6.13. It shows also the applied boundary conditions. At the pressure boundary condition the constant reservoir pressure is applied. A velocity of the wall in *x*-direction is applied to realize the piston movement. Assuming that the velocity of the liquid at the end of the piston is equal to the velocity of the piston itself, this velocity is implemented in each steady state simulation as initial boundary condition at the piston surface. The piston movement is divided into two parts, an opening of the valve with constant velocity up to a certain stroke and the successive closing with the same velocity as it is depicted in figure 6.14. The outlet to the surrounding environment has a constant pressure of 0 Pa. At this outlet the mean velocity is recorded. Finally the model is rotational symmetric around the axis of symmetry. Typically, one complete simulation takes about 2 to 3 hours on a state of the art PC (Pentium P4, 1.8 GHz, 512 MB RAM). The used medium was water with a density of $\rho = 1$ g/cm^3, a surface tension of $\sigma = 72.5$ mN/m and a dynamic viscosity of $\eta = 1$ mPas respectively $\eta = 350$ mPas to mimic a higher viscous liquid.

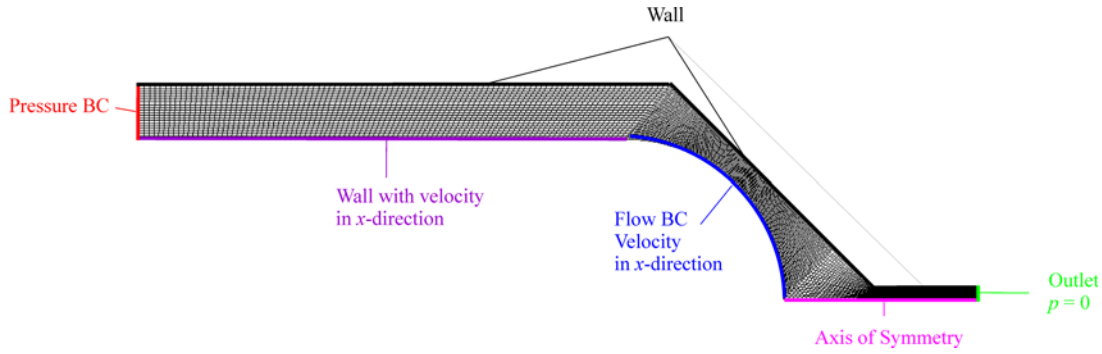

Figure 6.13: *Two-dimensional axisymmetric computational grid of the fast switching valve system and applied boundary conditions for the steady state simulations.*

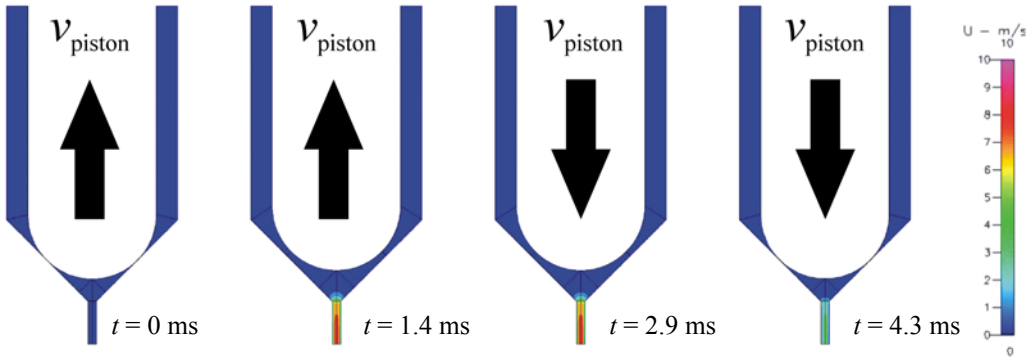

Figure 6.14: *Succession of steady state simulations without using the VOF method to determine the mean velocity inside the nozzle.*

Two examples of the resulting mean velocity inside the nozzle as a function of time are displayed in figure 6.15. Figure 6.15 a) shows the velocity for water as dispensing medium with a piezo stroke of 150 µm, a velocity of the piston of 70 mm/s and a reservoir pressure of 40 kPa. In this case the valve operates as valve duly, because the

velocity is nearly constant during opening and mainly determined by the constant pressure head. Only at the end of the dispensing cycle the velocity increases slightly due to the acceleration of the closing piston. Figure 6.15 b) shows the velocity for a medium with a dynamic viscosity of 350 mPas as dispensing medium with a piezo stroke of 220 µm, a velocity of the piston of 500 mm/s and a reservoir pressure of 300 kPa. In this case the movement of the piston is the crucial actuation and not the reservoir pressure. First the backward movement of the piston leads to a negative velocity followed by a positive velocity after the reversal of the piston movement and finally leads to high velocities at the end of the cycle.

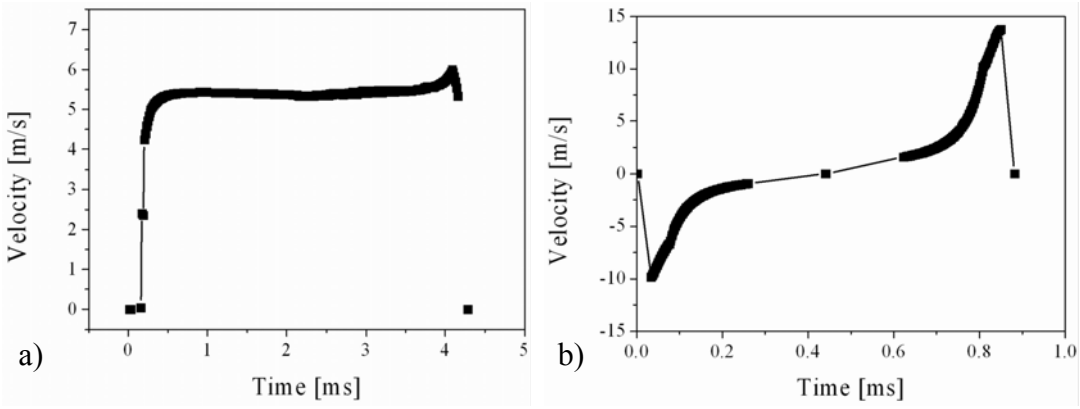

Figure 6.15: *Simulated mean velocity as a function of time for two different system setups.*
a) η *= 1 mPas, piezo stroke = 150 µm,* v_{piston} *= 70 mm/s, p = 40 kPa;*
b) η *= 350 mPas, piezo stroke = 220 µm,* v_{piston} *= 500 mm/s, p = 300 kPa.*

After the calculation of the time dependent velocity at the nozzle outlet, these results can be used as actuation input for VOF simulations of the jet ejection. Therefore, the resulting velocity as a function of time was used as flow boundary condition in a simple two-dimensional model of the nozzle. The axisymmetric model consists of a structured computational grid of about 9,500 cuboid cells as it is displayed in figure 6.16. The VOF method including surface tension and the auto time step function was used with a CFL number of 0.2 (cf. section 2.6.2). The time steps varied in the range of 0.1 µs - 1 µs. The CGS solver and the PLIC surface reconstruction was chosen and the removal of "Flotsam and Jetsam" was activated (cf. section 3.2.4). The volume at the nozzle outlet is called control volume and it is necessary to simulate and visualize the trajectory of the ejected droplet. Figure 6.16 shows also the applied boundary conditions. At the inlet a flow boundary condition was applied using the obtained time dependent velocity out of the previous simulations as mean velocity over the cross section pushing fluid 1 respectively the liquid inside the model. The inner walls are assumed to be full-wetting. The wall surrounding the outside of the nozzle is assumed to be non-wetting. The outlet to the surrounding environment of fluid 0 respectively air has a constant pressure of 0 Pa. Typically, one complete simulation takes about 30 to 50 hours on a state of the art PC (Pentium P4, 1.8 GHz, 512 MB RAM).

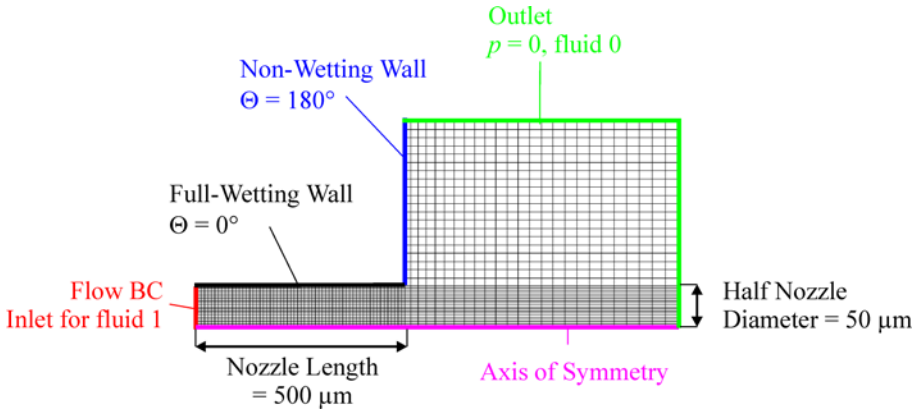

Figure 6.16: *Two-dimensional axisymmetric computational grid of the fast switching valve system and applied boundary conditions for the subsequent transient simulations using the VOF method.*

In figure 6.17 the results of the jet generation simulations are displayed. The boundary condition depicted in figure 6.15 a) leads to a jet ejection whereas the boundary condition depicted in figure 6.15 b) leads to a single droplet ejection. Hence, the two different operation modes of the fast switching valve system are confirmed. This way the performance of the fast switching valve system could be described qualitatively but not quantitatively due to the made approximations.

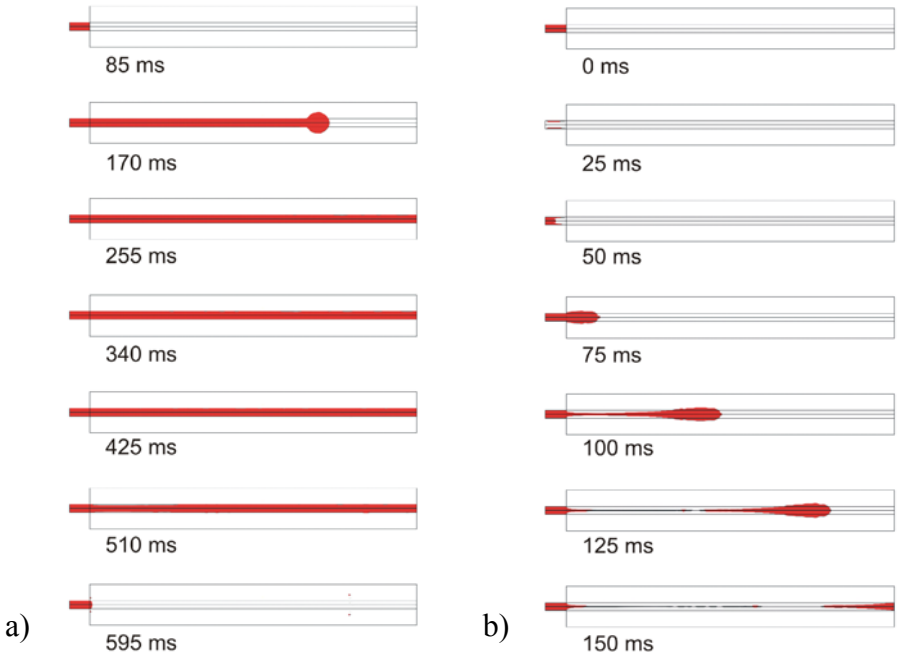

Figure 6.17: *Continuing simulation using the VOF method and the velocity as a function of time obtained by the previous succession of steady state simulations.*
a) η *= 1 mPas, piezo stroke = 150 µm,* v_{piston} *= 7 mm/s, p = 40 kPa;*
b) η *= 350 mPas, piezo stroke = 220 µm,* v_{piston} *= 50 mm/s, p = 300 kPa.*

6.2.4 CONCLUSION

The most influential parameters for fast switching valve systems are the valve stroke, the opening/closing speed and the reservoir pressure. Depending on these, the presented system can be used as jet or droplet generator as it can be seen in figure 6.17. If these principles are distinguished, for the jet generation mode the most influential parameter is the reservoir pressure, whereas for the droplet generation mode the velocity and stroke of the piston are of equal importance. Any fast switching valve system can be classified as droplet generator with pressure boundary condition according to section 3.3 because the pressure is the only accessible parameter. However, if the fast switching valve system performs like described before it can also be considered as dispenser with combined pressure and flow boundary condition according to section 3.3. This is because of the increasing influence of the piston movement on the outlet velocity.

The above presented fast switching valve system indicates a critical pressure of 13.4 kPa, a critical time of 22.6 µs and a critical power of 311 µW for water according to the model presented in section 3.1.2. For the higher viscous liquid (η = 350 mPas) the critical pressure is 5.6 MPa, the critical time is 6.7 µs and the critical power is 435 mW. The used pressure of 40 kPa for water is enough to surpass the critical value and to cause a jet ejection. The opening time of 2 ms is also far above the critical value so that a jet is ejected. The used pressure of 300 kPa for the high viscous liquid is not sufficient to surpass the critical value. In this case the additional energy of the piston movement is needed to enforce a droplet ejection.

The calculated mean velocity inside the nozzle depicted in figure 6.15 can be used to calculate the attained Weber number. The resulting Weber number of 38.7 for water is far above the critical value and thus a jet-on-demand ejection can be obtained. For the second case a much higher critical Weber number has to be considered as threshold due to the higher liquid viscosity (η = 350 mPas). The critical Weber number for the high viscous liquid is calculated to be $We_{\text{critical}} = 135$ using equation (3.2). Nevertheless, the attained Weber number of 270 using the CFD simulation output surpasses this critical value to enforce a droplet breakup.

6.3 NANOJET™

The dispensing technology referred to as NanoJet method developed from HSG-IMIT and IMTEK in the following has proven to be an accurate and robust contact free dispensing method for a wide variety of liquids. The NanoJet technology was developed and studied by Zengerle, Koltay et al. [209,213-215]. The presented accurate and very robust system is able to handle a variety of different liquids having a wide range of different viscosities with an up to now unequalled precision in that volume range. This viscosity independence occurs due to the fact that the dispensed

volume only depends on the displaced volume and the ratio of the fluidic resistance of the inlet and outlet channel. Due to this the system also offers an outstanding tunability. The NanoJet method can be classified as droplet generator with flow boundary condition according to section 3.3.

6.3.1 DOSAGE TECHNOLOGY

The NanoJet is based on a micromachined silicon dosage chip usually realized as a two layer bond of Silicon or Silicon/Pyrex which can be seen in figure 6.18 a). The key features of the dosage chip are an inlet channel for liquid supply, a dosage chamber bounded on one side by a Silicon diaphragm and an outlet channel with nozzle for liquid ejection. The nozzle has a diameter of 80 µm and is 150 µm long.

The NanoJet chip is self-priming only by capillary forces. A fast displacement of the diaphragm evoked by a piezoelectric stack actuator leads to a liquid displacement inside the dosage chamber as depicted in figure 6.18 b). The dynamics of the displacement is an important part of the NanoJet method. A fast displacement is required to create a liquid jet detaching from the nozzle and a slow release of the membrane is needed for the proper refilling of the dosage chip. Typically, the fast downwards movement takes about 2 ms with a velocity of approximately 18 µm/ms [213]. After that the piston remains static for a short time of about 100 µs to ensure the attainment of the new equilibrium. During this time, the fluid flow stops completely and the liquid jet breaks off at the nozzle.

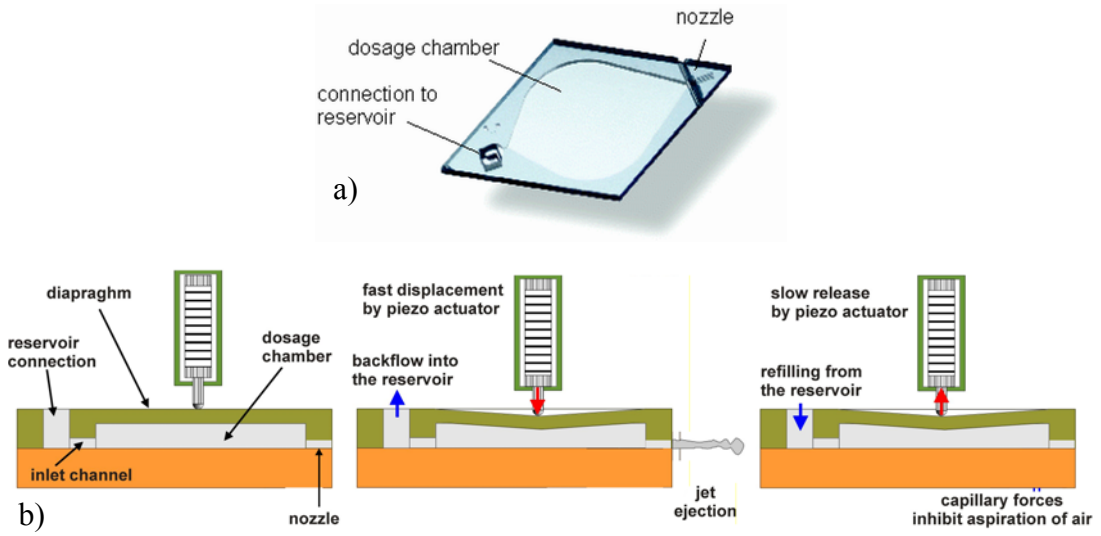

Figure 6.18: *a) Picture of the NanoJet dosage chip, b) Schematic of the NanoJet dosage chip and the working principle [213].*

Like in the case of the bubble jet printhead the initiated flow is not only directed towards the nozzle but also towards the outlet channel, thus back into the reservoir. Hence, the dispensed volume is smaller than the displaced volume inside the dosage chamber.

The refilling of the dosage chip is supported by a slow release of the membrane. This is essential for the proper refilling of the device because the pressure inside the dosage chamber may not exceed the capillary pressure at the nozzle. Otherwise air would be sucked through the nozzle into the dosage chamber and could cause a failure of the whole device.

6.3.2 Experimental Results

Various measurements have been carried out for characterization and proving the reliability of the NanoJet method by Zengerle, Koltay et al. [209,213-215]. First of all, the jet ejection was observed using a stroboscopic camera to check the shape of the jet and the reproducibility of the ejection. In figure 6.19 a picture sequence of an ejection cycle is displayed. Using the experimental data the jet velocity can be estimated to be 5 m/s - 6 m/s following the description given in section 4.2.1.

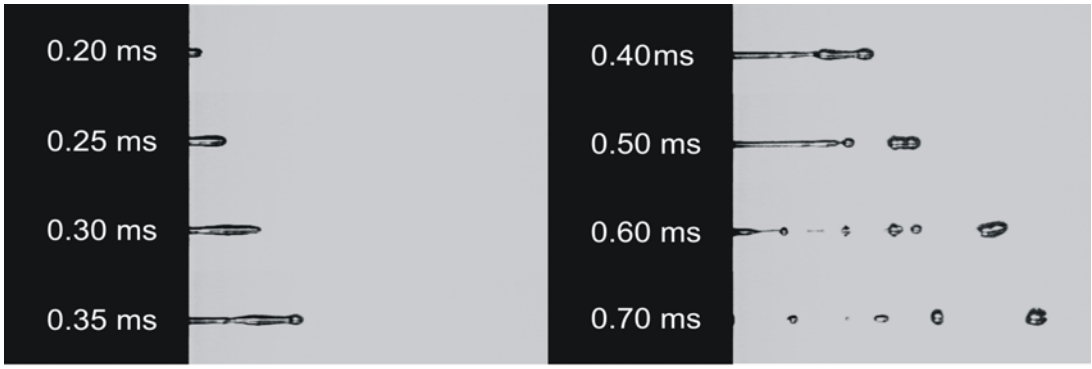

Figure 6.19: *Stroboscopic picture sequence of the jet ejection of a NanoJet chip at different points in time [209].*

Gravimetrical measurements are performed to investigate the reproducibility of the ejected volume as well as the dependency of the dispensed volume on different piston strokes and various media properties. Using the gravimetrical measurement method described in section 4.1 an accuracy of better than 1 µg (corresponding to 1 nl for water) could be achieved. Reproducibility measurements exhibit very low CV values between 3 % and 5 % [213].

Varying the dispensed volume can be done by varying the piston stroke and thereby the displaced volume. However, the maximum dispensable volume for maximum displacement is defined by the layout of the chip. As can be seen from figure 6.20 the dispensed volume indeed scales linearly with the deflection of the diaphragm thus with the displaced volume. Furthermore, figure 6.20 reveals also the effect of the relative

resistance R_n/R_r on the dosage volume, where R_n and R_r represents the fluidic resistance of the nozzle and the reservoir channel, respectively. The lower the relative resistance (i.e. the larger R_r/R_n), the steeper the slope of the volume displacement line and the higher dosage volumes can be reached. This dependency can also be described analytically which is done in section 6.3.3.

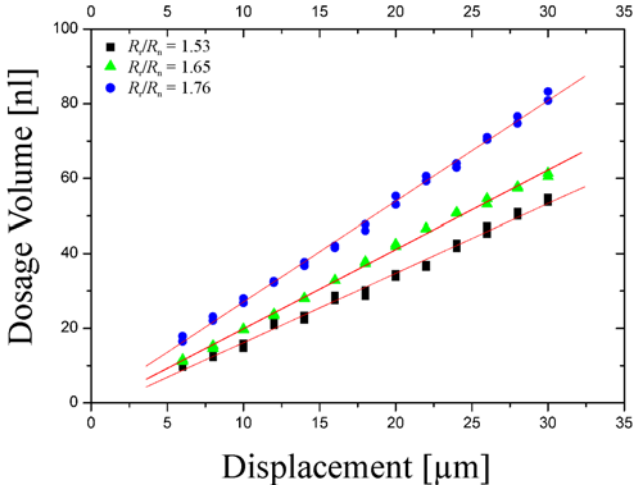

Figure 6.20: *Dependency of the dosage volume on the piezo stack displacement respectively membrane displacement [213].*

The small influence of liquid parameters on the dispensing performance has also been proven experimentally. Liquids with different dynamic viscosities have been dispensed using fixed actuation parameters. The obtained dosage volume remains nearly constant in the region from 1 mPas to 100 mPas as it can be seen in figure 6.21. For higher viscosities the dosage volume decreases significantly which might be attributed to the increasing significance of fluid structure interaction between the fluid in the dosage chamber and the diaphragm. For high viscous fluids the volume change dV/dt is no longer determined by the actuation force alone. But it is significantly influenced by the fluidic resistance of the system and the plate constant of the membrane [213].

6.3.3 Theoretical Description

In order to understand the dynamic behavior and the outstanding performance of the NanoJet dispensing device the dynamics of the dispensing process has been considered in detail by Koltay et al. [211]. Therefore, following system of differential equations has been set up and investigated:

$$\frac{dV}{dt} = \Phi_{v,r} - \Phi_{v,n}, \tag{6.1}$$

$$L_n \cdot \frac{d\Phi_{v,n}}{dt} - p_{cap} + R_n \cdot \Phi_{v,n} = p_r - L_r \cdot \frac{d\Phi_{v,r}}{dt} - R_r \cdot \Phi_{v,r}. \tag{6.2}$$

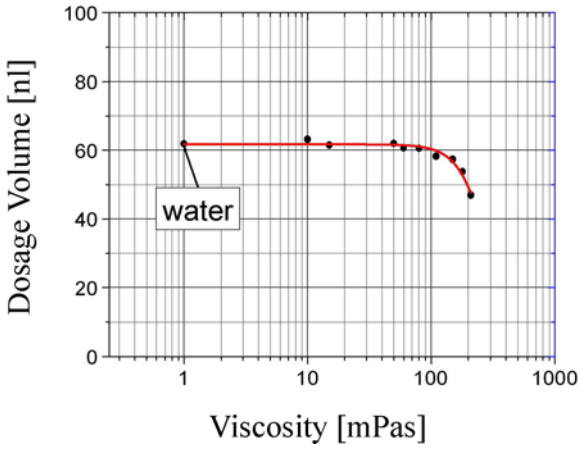

Figure 6.21: *Dependency of the dosage volume on the fluid viscosity [213].*

Where V, the actual volume of the dosage chamber and $\Phi_{v,\,n}$ and $\Phi_{v,\,r}$ the volume flow through the nozzle and into the reservoir, respectively are time dependent. Furthermore L_n and L_r are the fluidic inertances of the outlet and the inlet channel, R_n and R_r are the fluidic resistances of the outlet and the inlet channel, and p_{cap} and p_r are the capillary pressure and the pressure inside the reservoir, respectively, and finally ρ is the density of the liquid. While equation (6.1) simply expresses the mass conservation of an incompressible fluid in the dosage chip, equation (6.2) gives the pressure balance inside the system by summation over the pressure drop due to friction and inertia in the fluid channels.

For small channel dimensions the fluidic resistance causes the dominating effect. The inertances can be neglected, because they have only effects for fast changes like on the microsecond scale (cf. figure 3.24). Thus a simplified expression for the flow through the nozzle can be derived:

$$\Phi_{v,\,n} \approx \frac{p_r + p_{cap}}{R_n + R_r} - \frac{R_r}{R_n + R_r} \cdot \frac{dV}{dt}. \tag{6.3}$$

Herein the first term accounts for the offset induced by the pressure in the reservoir (which is assumed to vanish ($p_r = 0$) in the following) and the capillary pressure. The second term describes the flow through the nozzle in dependence of the fluidic resistances and the volume displacement. Integrating equation (6.3) under the assumption that the capillary pressure vanishes, which is true except for a very short period before the jet generation starts, one arrives at:

$$V_{jet} = \int \Phi_{v,\,n}(t)\, dt \approx \frac{R_r}{R_n + R_r} \cdot \int \frac{dV}{dt}\, dt = \frac{1}{\frac{R_n}{R_r} + 1} \cdot \Delta V. \tag{6.4}$$

Thus the ejected volume is mainly determined by the relative resistance R_n/R_r and scales linearly with the total displacement ΔV. Though the liquid properties like viscosity and density influence essentially the flow resistance of the fluidic channels,

they do not change the ratio of two fluidic resistances, because the media dependent constants cancel each other. Therefore, the dosage volume V_{jet} is not dependent on liquid parameters like density and viscosity by which the very low sensitivity (robustness) of the NanoJet method on these parameters can be explained.

A three-dimensional CFD simulation of the NanoJet chip was investigated in [113], considering the fluid-structure interaction of the fluid and the membrane. However, due to convergence problems using the fluid-structure interaction the simulations provided no reliable results.

6.3.4 CONCLUSION

The design parameters influencing the ejection performance of the NanoJet dispenser are indicated by the previous presented results. The two most important parameters are the piezostack stroke and therewith the volume displacement which linearly affects the ejected volume, and the relative resistance R_n/R_r, the ratio of inlet resistance compared to outlet resistance which determines the apportionment of the generated volume flow. The NanoJet system can be classified as droplet generator with flow boundary condition according to section 3.3 because the flow is strictly controlled by the displaced volume which is controlled by the piezo stack stroke. Due to the strong piezo stack actuator and the high displacement of the actuator in the NanoJet system the resulting volume displacement can be assumed as pressure independent. This means that only negligible coupling is present between volume displacement and generated pressure for a liquid with low to medium viscosity. This is the reason why it is qualified rather for the flow boundary condition class than for the combined pressure and flow boundary condition class. The pressure inside the dosage chamber varies proportional to the liquid viscosity.

The NanoJet system, when operated with water, indicates a critical pressure of 13.4 kPa, a critical time of 16.2 µs and a critical power of 222 µW according to the model presented in section 3.1.2. The estimated velocity of the jet of 5 m/s - 6 m/s can be used to calculate the attained Weber number. The resulting Weber number of 27.6 - 39.7 is far above the critical value. However, for a viscosity of 100 mPas the critical Weber number increases to 31.9. This is the reason for the rapid decrease of the dispensed volume for higher viscosities because for this viscosities the critical Weber number is not surpassed anymore. The typical dosage time of some milliseconds which is longer than the critical time leads to a jet-on-demand ejection. However, when the displaced volume dV approaches 0 and dV/dt is fast enough, the NanoJet system can change in the drop-on-demand mode. It thus might be operated as a piezoelectric inkjet if actuation frequencies are higher than 500 Hz [216]. But in this case the pressure independent behavior gets lost, too.

6.4 PIPEJET™

The PipeJet dispenser is an unrivalled simple, disposable non-contact dispenser for the nanoliter range. In contrast to other known dispensers manufactured by silicon micromachining the new device simply consists of an elastic polymer tube with circular cross section. The PipeJet dispenser combines the good performance of the NanoJet with its robust, cheap and disposable construction [131,132,217]. Media in the viscosity range from 1 mPas to 27 mPas were dispensed successfully. The PipeJet method can be classified as droplet generator with flow boundary condition according to section 3.3.

6.4.1 DOSAGE TECHNOLOGY

The key element of the dispensing technique termed PipeJet™ technology is a commercially available polymer tube clamped between two jaws. The inner diameter of the tube is typically in the range of 200 µm - 500 µm. The rear end of the tube is connected to a reservoir and serves as a supply channel. The front end sticks out of the mount and forms the nozzle for the liquid ejection. By a fast displacement of a piston connected to a piezostack actuator, the tube is squeezed on an active area of approximately 5 mm length displacing the liquid towards both ends of the tube as depicted in figure 6.22. Due to the low fluidic resistance between the actuation area and the nozzle, most of the displaced volume is ejected as free liquid jet. The dosage process is finished by a slow release of the piston leading to the reset of the tube deformation. During this process the tube is refilled by capillary forces allowing the system to be ready for the next dosage event.

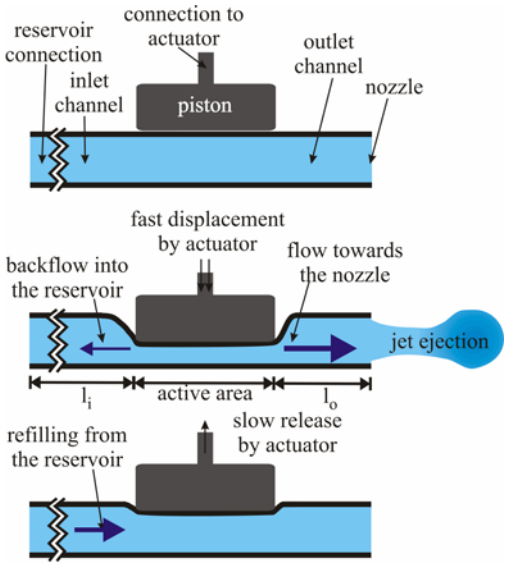

Figure 6.22: *Schematic cross section view and working principle of the PipeJet dispenser [131].*

In principle the PipeJet system is very similar to the previously presented NanoJet system. This is due to the fact that also in this case the dispensed volume can be determined by the volume displacement of the actuation and the ratio of the fluidic resistance towards the reservoir and towards the nozzle. Hence, the theoretical description of the NanoJet system in section 6.3.3 is in principle also valid for the PipeJet system. Thus the dispensed volume can be calculated using equation (6.4). However, the volume displacement of the tube is more complicated compared to the bending of the membrane for the NanoJet system. Due to this the volume displacement cannot be estimated easily, hence, equation (6.4) can only be used for a rough estimation of the ejected volume.

6.4.2 Experimental Results

The working principle sketched in figure 6.22 has been proven by stroboscopic as well as gravimetric measurements. For the experiments a tube with 200 µm inner diameter and a wall thickness of 25 µm was used. At a piezostack displacement of 40 µm and a displacement velocity of 90 µm/ms droplets of approximately 22.5 nl have been obtained. Studying the stroboscopic picture sequence in figure 6.23, the droplet ejection is very stable, no tail or satellite droplets can be observed. Recording a stroboscopic picture sequence results in a fluent video indicating the very high reproducibility comparable to inkjet devices. The CV of the dosage volume of 1.6 % is excellent, the change of the dosage volume is less than 1 % on changes of the hydrostatic pressure acting from the reservoir within about one centimeter, depending on the diameter of the tube used. As confirmed in a long term experiment the performance stays stable over at least 1,000,000,000 cycles [218].

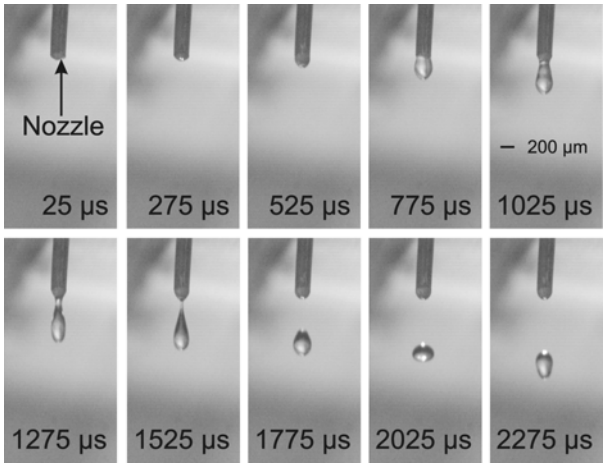

Figure 6.23: *Stroboscopic pictures of an ejection process of the PipeJet dispenser [131].*

One reason for the good performance of the PipeJet dispenser is that there is nearly no material surrounding the nozzle like in other dispenser devices [210,214,219], except the extremely thin wall of the tube of about 20 µm. Thus liquid is securely kept inside the tube because no wetting of the nozzle surroundings can occur which could

lead to pending droplets or spreading of liquid on the nozzle plate. Furthermore, the tube has a nearly perfect circular shape with no edges leading to an optimum jet shape. Different media in the viscosity range from 1 mPas to 27 mPas have been dispensed successfully as can be seen in figure 6.24. With 200 µm tubes, a dosage volume nearly independent on the viscosity up to 20 mPas can be achieved similar to the NanoJet described before. The frequency characteristics show a frequency independent dosage volume up to frequencies of 15 Hz with a very long tube with a diameter of 200 µm. At higher frequencies the significant flow resistance of the tube limits the capillary refill leading to a smaller volume of the single droplet and a constant flow rate [131].

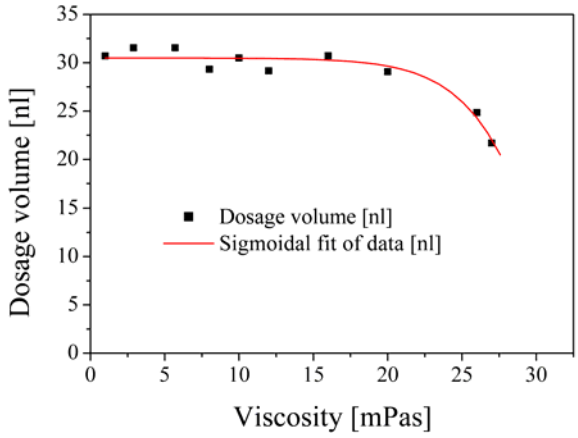

Figure 6.24: *Dosage volume depending on the viscosity at a frequency of 0.1 Hz with 50 µm stroke and different glycerol/water dilutions getting the different viscosities. The tube diameter is 200 µm [131] (calibration ≈ 70 µm).*

To increase the flow rate of the PipeJet shorter tubes with larger inner diameter have been used. Using a 500 µm tube, a dosage volume of about 53 nl was obtained at a piezostack stroke of 30 µm. With this setup flow rates up to 15.7 µl/s have been reached for operating frequencies up to 290 Hz. For a tube of 1000 µm diameter, the maximum obtainable flow rate was found to be 143 µl/s at a droplet volume of 420 nl with a frequency of 340 Hz.

The ejected droplet volume can be defined by varying different parameters like the diameter of the tube, the piston stroke, the dimension and the shape of the active area and finally the fraction of inlet channel length to the nozzle channel length. Increasing the piston stroke, the active area, or the fraction of inlet and nozzle channel length l_i/l_o leads to an increase of the ejected volume. In figure 6.26 the dependency of the dosage volume on the piston stroke is displayed. In the considered configuration there is a linear correlation between the dosage volume and the piezostack stroke. The comparison with simulation results which are also illustrated in figure 6.26 leads to a good agreement with the stroke characteristics [131].

6.4.3 NUMERICAL DESCRIPTION

CFD simulations of the dispensing process have been performed using CFD-ACE+. However, like in section 6.2 the simulations had to be divided into two separate simulations to overcome convergence problems caused by the large tube deformation and the VOF module implemented in CFD-ACE+. Hence, the first simulation approach was a simulation neglecting the free surface respectively not using the VOF method. The movement of the piston was implemented as a moving wall boundary condition in a three-dimensional model of one fourth of the tube utilizing all symmetries like it is displayed in figure 6.25. The model consists of a structured computational grid of about 28,000 cuboid cells where the smallest one has a volume of 1.0×10^{-17} m^3 and the largest one has a volume of 6.4×10^{-15} m^3. A fixed time step of 0.1 µs and the AMG solver were chosen for the simulation. Figure 6.25 shows also the applied boundary conditions. The inner wall of the system is assumed to be full-wetting. Two symmetry boundary conditions complete the tube. Due to the large spatial dimensions of the length of the tube the horizontal grid can not be displayed in this work. The total length of the tube of up to 14 mm (8 mm inlet channel + 5 mm active area + 1 mm nozzle) is discretized with 150 uniformly distributed elements. This means that one element has an edge length of about 100 µm in horizontal direction. A moving boundary condition was applied in the horizontal direction over a length of 5 mm to realize the piston deflection. Both ends of the tube were implemented as pressure boundary conditions (p = 0 Pa). Due to the large deformation of the tube it was not possible to simulate all materials of the dispenser and the resulting fluid-structure interaction (FSI) with the existing simulation tool. Instead of that, only the fluidic part of the tube was simulated using the piston deflection as moving boundary condition. Typically, one complete simulation takes about 60 to 80 hours on a state of the art PC (Pentium P4, 1.8 GHz, 512 MB RAM). The used medium was water with a density of $\rho = 1$ g/cm^3, a surface tension of $\sigma = 72.5$ mN/m and a dynamic viscosity of $\eta = 1$ mPas. This way the linear dependence of the dosage volume on the actuator stroke could be reproduced (cf. figure 6.26). The slightly lower values provided by the simulation compared to the experiment are caused by the short tube of the simulation model compared to the real device. While the measured tube was about 50 mm long the simulated tube had to be limited to 14 mm to avoid convergence problems and unacceptable long computation times. Thus the resistance towards the reservoir R_r was larger in the experiments compared to the simulations, which leads to a higher dosage volume according to equation (6.4).

Simulations worked well up to a stroke of 80 µm which corresponds to 40 % of the tube diameter. A larger displacement was not possible because of convergence problems of the simulation algorithm.

In order to find an optimum of the tubing dimensions different ratios of inlet length l_i to outlet length l_o were simulated as it is displayed in figure 6.27. The dosage volume can be varied from 13 nl ($l_i/l_o = 1$) to 19 nl ($l_i/l_o = 8$) at a stroke of 40 µm. Comparing

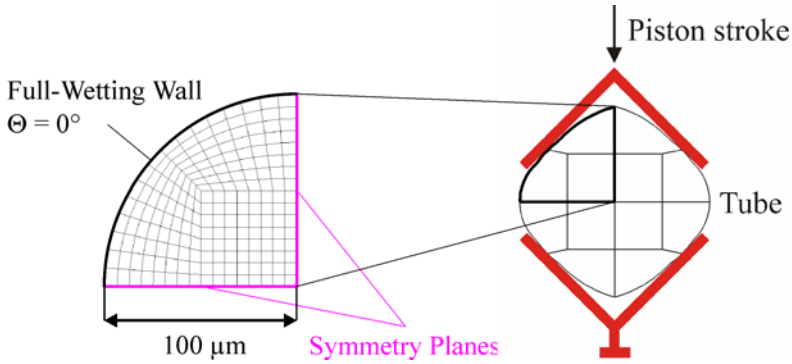

Figure 6.25: *Three-dimensional computational grid, used boundary conditions and applied grid deformation for the simulations of the tube.*

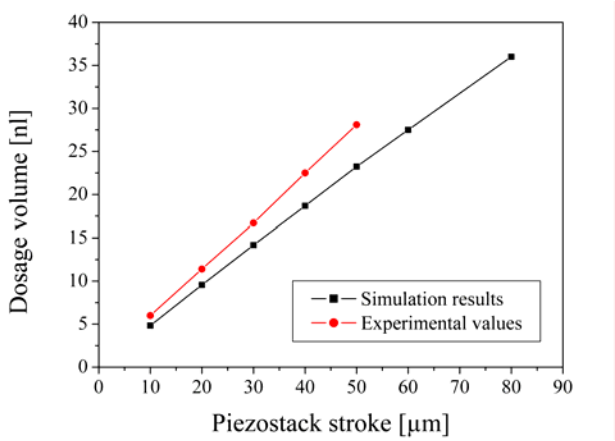

Figure 6.26: *Measured and simulated dosage volume for H_2O depending on the piezostack stroke at a frequency of 0.1 Hz. (l_i/l_o = 8, tube diameter = 200 µm) [131].*

the simulated volume of 19 nl (l_i/l_o = 8) with the gravimetric measured droplet volume of 22.5 nl with the same piezo stroke leads to a deviation of 15 %. This disagreement is supposed to be caused by the fact that the fraction of inlet and outlet channel in the real experimental setup was considerably higher (cf. figure 6.27). For the used experimental setup, the l_i/l_o fraction was estimated to be approximately 100 [131]. However, as mentioned before, this aspect ratio cannot be simulated with CFD because the required grid would cause an unacceptable computation time. Nevertheless, the CFD simulations show a suitable tendency concerning the dependency on the tube aspect ratio which is confirmed by the implemented extrapolation of the simulation data. For a final assessment of the simulation model compared to the experiments the simulations and experiments have to be repeated for identical configurations of the tube lengths.

To have also a qualitative comparison of experimental and calculated droplet shapes further simulations have been performed using the VOF method. They were achieved by substituting the moving boundary condition at the walls of the tube with an equivalent pressure boundary condition where the applied time dependent pressure function was obtained from the previous simulations without the VOF algorithm. Like

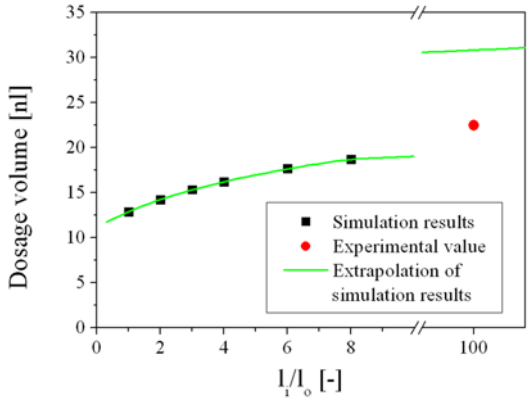

Figure 6.27: *Simulated dosage volume of H_2O depending on l_i/l_o, where l_i and l_o are the length of the inlet and outlet channel respectively compared to the experimental value (40 µm stroke, tube diameter = 200 µm).*

in section 6.2 this procedure was necessary to overcome convergence problems caused by the large tube deformation in combination with the VOF module implemented in CFD-ACE+. First the pressure inside the tube at the moving grid boundary condition (cf. figure 6.25) was recorded with the nozzle defined as outlet. This pressure characteristics was subsequently used as boundary condition for the new simulation without accounting for the tube deformation anymore. The moving grid boundary condition was changed in an inlet where fluid 1 respectively the liquid is pushed inside the system. The computational grid was the same as for the previous simulations (cf. figure 6.25) with an additional control volume at the nozzle outlet to simulate and visualize the trajectory of the ejected droplet. The VOF method including surface tension was used. The time step was fixed to a value of 10 ns. The CGS solver and the PLIC surface reconstruction were chosen and the removal of "Flotsam and Jetsam" was activated (cf. section 3.2.4). The inner walls were assumed to be full-wetting. The wall surrounding the outside of the nozzle was assumed to be non-wetting. The outlet to the surrounding environment of fluid 0 respectively air was set to a constant pressure of 0 Pa. One complete simulation takes about incredible six months on a state of the art PC (Pentium P4, 1.8 GHz, 512 MB RAM). The reason for this was the used fixed time step of only 10 ns which was necessary to overcome convergence problems. A variable time step did not lead to convergence regardless of the CFL number applied.

Compared to the stroboscopic pictures the shape of the ejected droplet depicted in figure 6.28 shows poor agreement. The shape and length of the tail could not be reproduced correctly. Unfortunately, there are also some discrepancies in the time behavior. So the simulation indicates a faster droplet ejection compared to the experiments. Thus the presented CFD model cannot be used for droplet shape optimization. The reason for this might certainly be the applied approximation neglecting the tube deformation and the FSI [131]. Then an elasticity of the tube has to be considered which might explain the observed deviation. Due to an additional

elasticity of the tube a fluidic capacitance (cf. section 2.4.3) should be considered. Neglecting this fluidic capacitance leads to a faster droplet ejection compared to the real device because no "charging" of the fluidic capacitance occurs.

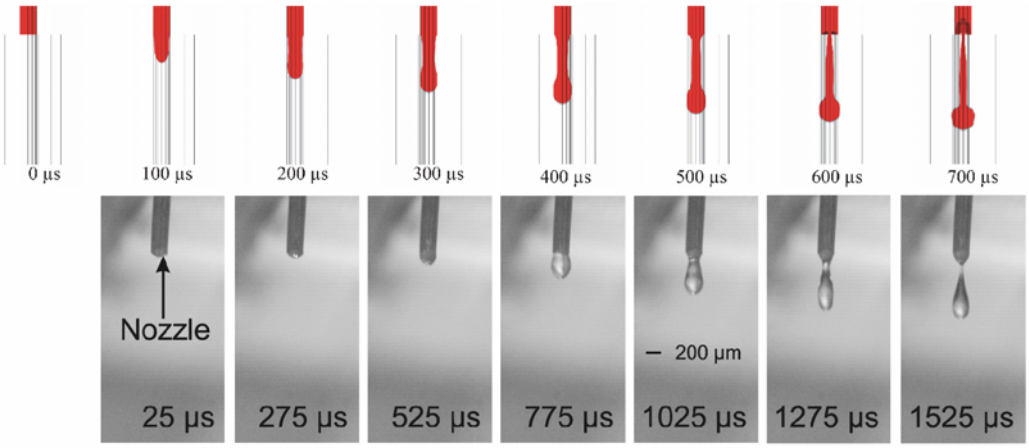

Figure 6.28: *Simulation results of a droplet ejection of H_2O using the VOF method (l_i/l_o = 8, stroke = 40 µm, tube diameter = 200 µm) compared to corresponding stroboscopic pictures.*

6.4.4 CONCLUSION

The amount of delivered fluid by the PipeJet can, on the one hand be defined by the size and position of the piston, the ratio of the fluidic resistances pointing towards the nozzle and the reservoir and by the diameter of the tube used. On the other hand, the volume can be regulated by varying the piston stroke within a given setup. A chamfered active area of the actuator towards the nozzle outlet additionally leads to a flow in this preferred direction and therefore a higher dosage volume. Due to the direct displacement principle the PipeJet system can be classified as droplet generator with flow boundary condition according to section 3.3. The flow is the only accessible parameter controlled by the piezo stack stroke. However, as mentioned before, if the tube shows elastic deformation, a fluidic capacitance has to be considered creating a coupling between the pressure boundary condition and the flow boundary condition. In this case the PipeJet has to be classified in the group of combined actuated systems because than it has an additional pressure component which can not be neglected.

The PipeJet system as studied here exhibits a critical pressure of 6.0 kPa, a critical time of 63.9 µs and a critical power of 395 µW according to the model presented in section 3.1.2. The maximum velocity inside the nozzle which can be extracted out of the CFD simulations is about 2.5 m/s. According to this the attained Weber number is 17.2. A similar critical Weber number of 17.4 occurs for a viscosity of 70 mPas. Therefore the PipeJet system should theoretically demonstrate a nearly constant dispensing volume up to this viscosity. The lower attained limit of about 20 mPas might be attributed to the increasing significance of fluid structure interaction between the fluid and the tube and the resulting decrease of the velocity. The obtained droplet

volume of about 22.5 nl is approximately 5.4 times the volume of a droplet with the diameter of the nozzle. The reason for the larger volume is the longer actuation time. The actuation time can be estimated by taking the piezostack displacement of 40 µm and the displacement velocity of 90 µm/ms to be 444 µs. This is 6.9 times the critical time. Comparing these both ratios indicates a quite good agreement of the device with the analytical model presented in section 3.1.2.

6.5 TOPSPOT®

The TopSpot technology has been developed as a method for the fast mass production of low and medium density microarrays. The system enables highly parallel non-contact printing of different media like oligonucleotides, DNA or protein solutions. It is based on a micromachined printhead which is driven by a separate actuation unit. The printhead formats allow the simultaneous application of 24, 96 and even 384 different probes in one step, respectively. The TopSpot technology was developed and studied by Zengerle, de Heij, Gutmann, Niekrawietz et al. [217,220-228]. The TopSpot method can be classified as droplet generator with pressure boundary condition according to section 3.3.

6.5.1 DOSAGE TECHNOLOGY

The TopSpot technology is based on a dosage chip featuring the basic elements reservoirs, connection channels and nozzles like the DWP in section 6.1. In this case, however, all nozzles are concentrated within a "print window" in the middle of the chip, each one being connected via a capillary channel to a reservoir [209]. Another difference compared to the DWP system is that the TopSpot ejects only a part of the volume contained in the nozzle chamber rather than the entire volume. The TopSpot printhead consists of three layers, pyrex glass, silicon and another pyrex layer. The liquid reservoirs are drilled in the upper pyrex glass wafer as it is displayed in figure 6.29 a). These can be filled manually or by standard liquid handling robots. The glass wafer is bonded to the intermediary silicon wafer by anodic bonding. The reverse side of the silicon wafer is bonded to a thin pyrex glass wafer with an opening for the outlet nozzles as displayed in figure 6.29 b). A further opening in the upper Pyrex forms the actuation chamber as depicted in figure 6.29 a). The actuation of the printhead is done by a piezostack actuator as displayed in figure 6.29 c). The actuator drives a piston into the actuation chamber of the printhead which generates a pressure pulse by the compressed air that affects all nozzles simultaneously. If the pressure pulse amplitude overcomes the critical pressure (cf. section 3.2.4), it overcomes the capillary forces in the nozzles and droplets are accelerated out of them. To achieve a homogenous ejection of the droplets, the outer surface of the nozzle array is coated with a hydrophobic silane [227].

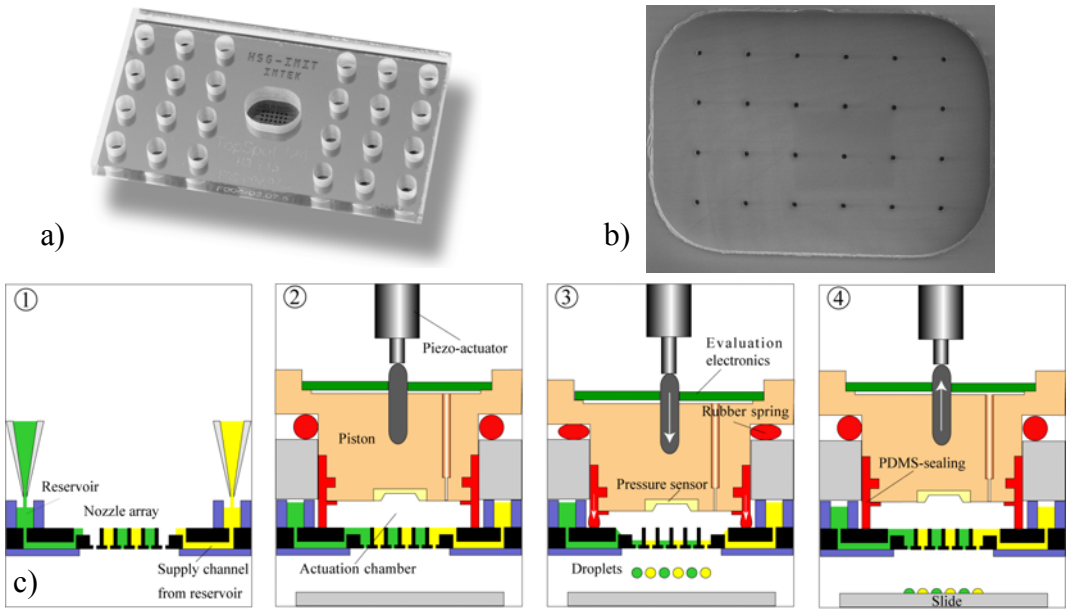

Figure 6.29: *a.) Picture of a TopSpot printhead, b.) SEM picture of the 24 nozzles on the bottom side of the printhead, c.) Working principle of TopSpot. 1. Filling of the printhead reservoirs, 2. Placing a piston into the printhead, 3. Actuation by moving of the piston, 4. Retraction of the piston [226].*

6.5.2 Experimental Results

Using a stroboscopic camera the droplet ejection was studied by Niekrawietz et al. [226] concerning droplet volume, velocity and quality as it is displayed in figure 6.30. Regarding the droplet quality the most important aspect is that the ejected droplet is free of satellite droplets which could falsify the results of the microarray. The reproducibility of the droplet diameter within one single nozzle was better than 1 %, independent of the used printing buffer. Comparison of different single nozzle records of all 24 different nozzles showed a CV better than 1.5 % [226].

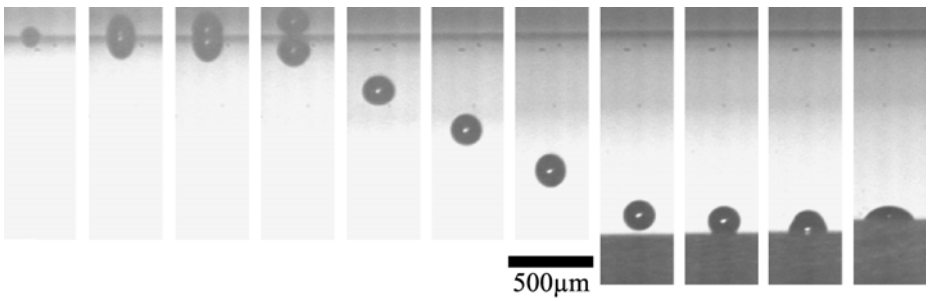

Figure 6.30: *The printing process from the nozzle of the printhead down to the microarray slide. The droplet dispensing process is highly stable and reproducible with all tested printing media [227].*

The pressure conditions for a stable and satellite free droplet dispensing process were investigated as depicted in figure 6.31. For the correlation between printing media and needed printing conditions, the piston movement of the printer device was recorded during printing process using a laser-doppler-vibrometer. The actuation pressure pulse was detected by an integrated pressure sensor in the piston. Hence, the correlation between amplitude, rise time and plateau of the pressure pulse on the one hand and the quality of droplet breakup on the other hand could be analyzed. Based on this the droplet diameter at optimal dispensing conditions was found to be dependent on viscosity and surface tension as well [226].

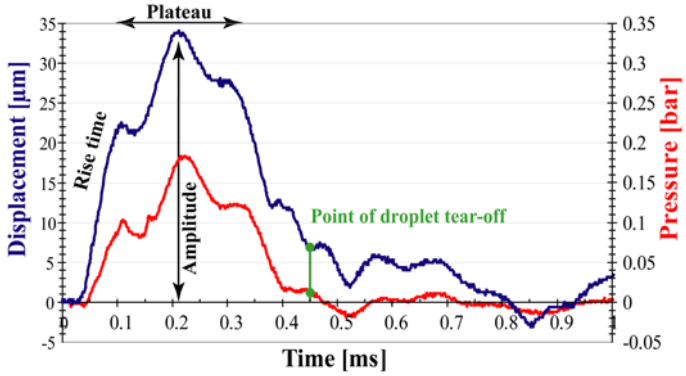

Figure 6.31: *Transient displacement of the piston [blue line] and measured pressure pulse [red line]. The point in time for droplet tear off is indicated by a straight line [226].*

The limited resolution of the used camera and the arrangement of the nozzles on the printhead does not allow the evaluation of all 24 nozzles at the same time. To observe all 24 droplets in one step a typical microarray approach was used by mixing the printing buffer with Cy3-labeled oligonucleotides. Thus the fluorescence signal could be used as a measure of dispensed volume. By using the fluorescence reader the intensity of fluorescence signal of dispensed droplets on the microarray slides could be determined. A CV of 2.1 % for all 24 spots was achieved and demonstrates the homogeneity and the outstanding performance of this technology [226].

6.5.3 Numerical Description

For a more fundamental understanding of the droplet ejection process a fully three-dimensional simulation model was set up by Niekrawietz et al. using the VOF method provided by the simulation package CFD-ACE+ [226]. The measured pressure sensor signal depicted in figure 6.31 was used as inlet pressure boundary condition. A good agreement can be obtained between simulation data and stroboscopic pictures displayed in figure 6.32. The shape of the droplet and point of the droplet tear off fit very well. The deviations for the droplet volume and droplet velocity were less than 5 % [226]. This simulation model was extensively validated and provides excellent qualitative as well as quantitative results compared to experimental findings.

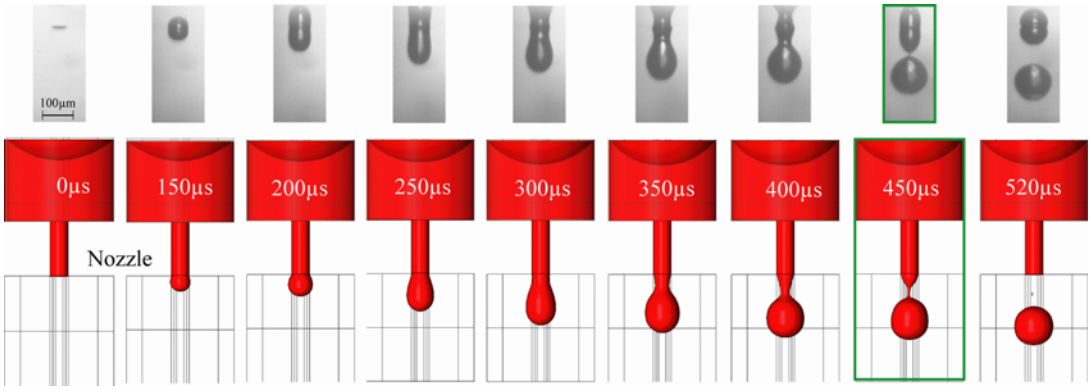

Figure 6.32: *3D simulation of the droplet ejection of one nozzle and corresponding stroboscopic pictures [226].*

The knowledge of the best geometry dimensions of the nozzles provides design rules allowing to expand the media property range for microarray production and reducing the dispensing droplet volume. A reduction of the nozzle length from 150 µm to 50 µm, for example, leads to a 20 % lower pressure pulse and only a 5 % lower droplet volume as depicted in figure 6.33. That means that the dispensing process is very stable and moderately dependent of the nozzle length [226].

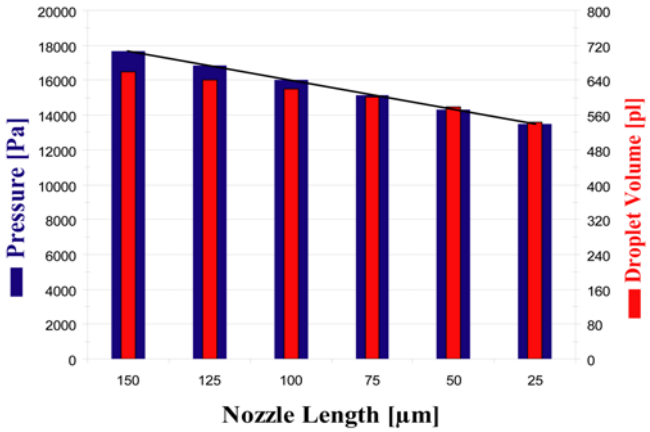

Figure 6.33: *The pressure conditions of the simulation were adjusted for a stable and satellite free droplet dispensing process and the single droplet volume resulting from different nozzle lengths of the printhead were measured (based on CFD simulations) [226].*

6.5.4 Conclusion

As it could be seen in the previous sections the main parameter affecting the droplet generation using the TopSpot is the pressure and its temporal progress inside the actuation chamber. Due to this the most important aspect is to overcome the critical pressure inside the actuation chamber to achieve a droplet ejection. Though the droplet volume is moderately dependent on the pressure pulse, it is mainly determined by the

geometrical dimensions of the nozzle. The TopSpot system can be classified as droplet generator with pressure boundary condition according to section 3.3 because a pressure is generated by the compression of the air inside the actuation chamber.

The TopSpot system indicates a critical pressure of 25.4 kPa, a critical time of 8.0 µs and a critical power of 208 µW according to the model presented in section 3.1.2. However, the experimentally required pressure of 18 kPa (cf. figure 6.33) does not exceed this critical pressure. Hence, no droplet ejection should occur according to the model presented in section 3.1.2. Nevertheless, in reality a droplet formation can be observed which requires a closer examination of the analytical model, when applied to the TopSpot system: The reason for the discrepancy between model and experiment is the big difference of the droplet diameter assumed in the model and the real droplet diameter obtained in the experiment. The real droplet diameter of about 108 µm is about twice the assumed droplet diameter of 50 µm, which shows, that the assumptions of the analytical model are not fulfilled for the TopSpot system. However, if the experimentally observed droplet diameter of 108 µm is inserted in the model presented in section 3.1.2 the critical pressure decreases to 17.3 kPa which comes closed to the experimental value of 18 kPa. This fact is illustrated in figure 6.34. Thus, if one assumes the experimentally observed droplet diameter, the critical value is indeed marginally surpassed in the experiments. This can be interpreted as indication for the fact that the TopSpot system is operated at its limit.

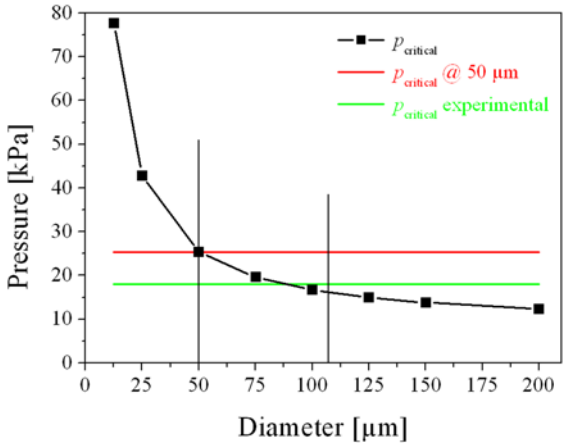

Figure 6.34: *Critical pressure depending on the droplet diameter. The critical pressure obtained by the analytical model with an assumed droplet diameter of 50 µm is indicated as red line. The experimentally determined necessary pressure is indicated as green line. The vertical lines show the assumed droplet diameter of 50 µm and the experimentally obtained droplet diameter of 108 µm.*

Though the assumption of a droplet diameter equalling the nozzle size of the analytical model is not holding in this case, nevertheless the critical pressure calculated with the experimentally observed droplet size (diameter of 108 µm) is quite consistent with the experimentally determined pressure inside the actuation chamber. Therefore the energetic approach presented in section 3.1.2 can still be successfully applied, but

the effective droplet size has to be taken into account. The obtained droplet volume of about 650 pl is approximately 10 times the volume of a droplet with the diameter of the nozzle. The reason for the larger volume is the longer actuation time. The actuation time can be estimated by taking the pressure measurements depicted in figure 6.31. The actuation time can be estimated to be 200 µs - 300 µs which is 25 - 37.5 times the critical time.

The question now arises why the droplets produced with the TopSpot method are generally larger than for typical drop-on-demand devices considered so far. The reason for this is that the critical pressure calculated on basis of the nozzle diameter is never surpassed in the TopSpot system. Therefore a pending droplet is issued from the nozzle. This is not the case for the other drop-on-demand devices discussed so far, where the critical pressure is surpassed before a pending droplet can be generated. This is the main difference between the TopSpot system, the model presented in section 3.1.2 and typical drop-on-demand devices.

The reason for the TopSpot system still being able to create free flying droplets consists in the fact, that during the dispensing event indeed enough energy is supplied to create a free droplet (though not having the size of the nozzle, but considerably larger). The following numbers obtained from a full CFD simulation can serve to motivate the process of droplet breakup:

The mean velocity inside the nozzle extracted out of the CFD simulation is about 2.1 m/s at max. According to this the attained Weber number is 6.6 for a droplet diameter of 108 µm corresponding to the ejected droplet volume of 650 pl. This value is below the critical value of 12 for a drop-on-demand mode and also slightly below the critical value of 8 for the jet ejection with subsequent Rayleigh breakup. This would theoretically prohibit a droplet breakup because the kinetic energy E_{kinetic} of the droplet is smaller than its surface tension energy E_{surface} (cf. section 2.3.2), even for the real 108 µm sized droplet. This reasoning is based on the assumption that at some point in time the liquid velocity is high enough to result in a kinetic energy which overcomes the surface energy. This is the typical drop-on-demand condition. However, strictly speaking it is sufficient that the total energy supplied during the complete dispensing process indeed overcomes the surface energy of the effective droplet. Therefore, strictly speaking, the energy balance has to be considered during the whole dispensing event to assess wether a droplet can be created or not. To create a droplet the total inserted mechanical work W_{pressure} has to surpass at least the surface energy E_{surface} and all possibly occurring friction losses. Thus the necessary condition for a droplet breakup is that the supplied energy overcomes the friction losses and the surface energy of an ejected droplet. To illustrate this the effective energy $E_{\text{effective}}$ at the nozzle outlet extracted out of the CFD simulation is plotted in figure 6.35 versus the time as black line. The effective energy $E_{\text{effective}}$ at the nozzle provided by the actuation can be extracted from the simulation by integrating the time dependent pressure at the nozzle times the displaced volume, determined from the flow rate through the nozzle, over time until droplet breakup. Since the energy directly at the

nozzle outlet is taken, all friction losses are already considered and the effective energy $E_{effective}$ available for droplet formation is taken into account. The effective energy $E_{effective}$ at the nozzle increases until a maximum total energy of 2.9 nJ is reached. Additionally the required surface energy $E_{surface}$ of a given droplet is plotted in figure 6.35 as red line. For the calculation of this curve the diameter of a possibly occurring droplet has to be estimated. For the sake of simplicity the totally displaced volume is assumed to form a spherical droplet. Using this assumption the surface energy $E_{surface}$ at every time step can be calculated straight forward from the flow through the nozzle. Comparing the effective energy $E_{effective}$ and the required surface energy $E_{surface}$ in figure 6.35 yields that the effective energy overcomes the required energy only after 350 µs. Hence, no droplet breakup is possible before that point in time. The corresponding displaced volume respectively the equivalent droplet size at this time results in a droplet diameter of about 106 µm. This means that no droplet smaller than 106 µm can be ejected using the present setup because the available effective energy $E_{effective}$ is not overcoming the surface energy $E_{surface}$ of the corresponding droplet before. Thus it becomes clear, that in the TopSpot system the droplet breakup cannot occur for droplets of the size of the nozzle (50 µm). The total supplied energy is not sufficient to provide the surface energy of a droplet of that size.

The droplet diameter of 106 µm deduced with the energetic approach agrees very good with the experimental observed droplet diameter of 108 µm. However, the point in time of the droplet breakup differentiates. The energetic approach predicts a droplet breakup at about 350 µs whereas experimental findings show a droplet breakup after 450 µs. Nevertheless these results are not contradictorily. Indeed the effective energy surpasses the required energy at 350 µs but this does not mean that the droplet breaks up at this time. It takes some more time until the droplet detaches totally from the nozzle and the breakup takes place. Conclusively the results of the energetic approach are consistent with experimental findings as well as CFD simulations.

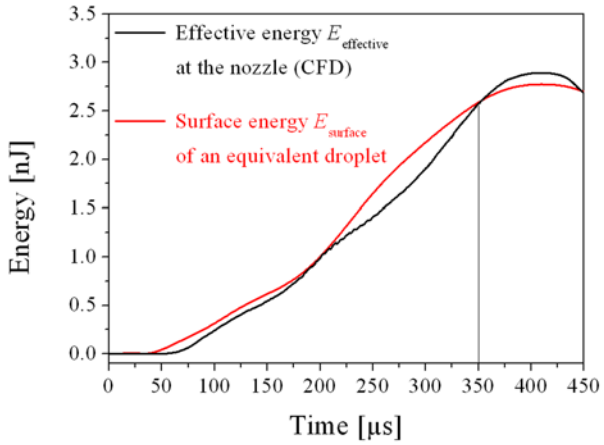

Figure 6.35: *Supplied energy at the nozzle extracted out of the CFD simulation versus the time (black line) and the required surface energy of a given droplet (red line). The vertical line indicates the time when the supplied energy surpasses the required surface energy. At this time a droplet breakup can be anticipated.*

Considering the surface energy of a given droplet as a function of its diameter results in the curve depicted in figure 6.36. Comparing this with the totally supplied energy $E_{supplied}$ of 7.7 nJ which is extracted out of the CFD simulation, indicates that only droplets with lower surface energy than this value can be ejected. Thus at maximum, droplets with a diameter of 180 µm could be created. Additionally taking into account that no droplet smaller than the nozzle size of 50 µm can be ejected leads to the patterned area where droplets potentially could be ejected. However, this area is even smaller because additional friction losses have to be considered. Hence the effective energy of 2.9 nJ instead of the supplied energy has to be considered when comparing it with the surface energy of the droplet. Due to this the blue patterned area in figure 6.36 has to be subtracted from the area where droplets potentially could be ejected. Moreover taking the result of the previously made energetic analysis into account that no droplet smaller than 106 µm can be ejected, the range of a possibly occurring droplet reduces further. Thus the range from 50 µm to 106 µm, the green patterned area in figure 6.36 has also to be subtracted. The small remaining operating range with an effective energy overcoming the surface energy and laying within the given constraints is marked in red. In this range of 106 µm < $D_{droplet}$ < 114 µm a droplet ejection could take place. This result is consistent with the experimental observed droplet diameter of 108 µm and the fact that the TopSpot system is operated at its limit. Small changes in the supplied energy easily could cause a total failure of the system.

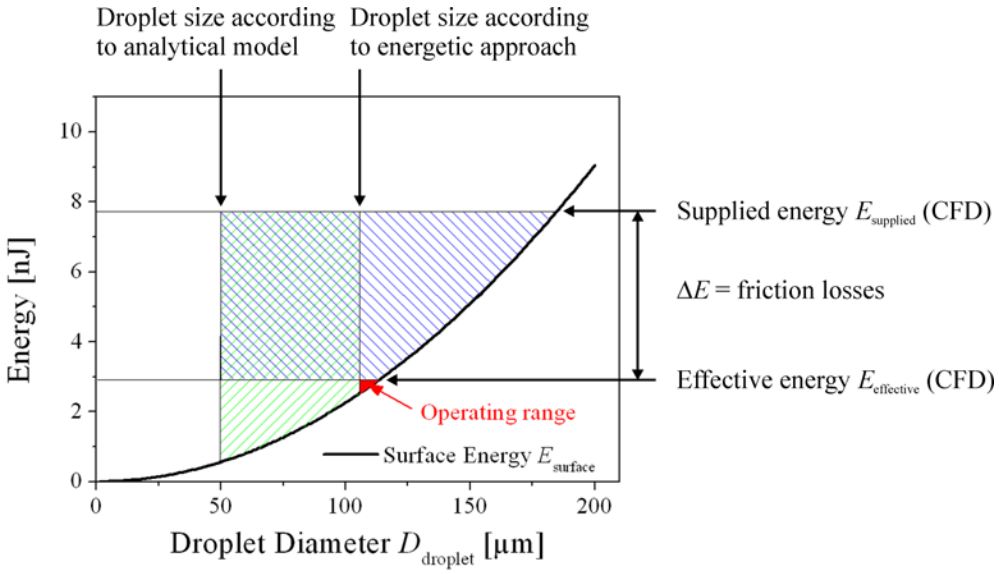

Figure 6.36: *Surface energy of a given droplet as a function of its diameter (black line). The supplied and the effective energy are plotted as horizontal lines. The droplet diameter according to the analytical model and according to the energetic approach are plotted as vertical lines. The remaining operating range of the TopSpot system is plotted in red.*

As mentioned in section 3.1.1 there is a necessary condition and a sufficient condition for the droplet ejection. Due to this there are two regimes of droplet formation. In the first regime the kinetic energy of the droplet indeed overcomes the

surface energy ($E_{kinetic} > E_{surface}$) and a droplet must be created (sufficient condition). In the second regime $E_{kinetic} < E_{surface}$ and a droplet is not necessarily ejected. A successful breakup occurs only if in addition $E_{effective} > E_{surface}$. This leads to the following conclusions:

- $E_{effective} > E_{surface}$ and $E_{kinetic} > E_{surface}$
  This is the mainly occurring droplet ejection regime. In this case the Weber number is a valid criterion for the droplet ejection. The droplet diameter is in the range of the nozzle diameter. The droplet ejection is robust and the droplets usually exhibit a satisfactorily high velocity. This is the favorable droplet ejection regime. In this case the analytical model presented in section 3.1.2 is valid to deduce critical parameters for the droplet ejection.

- $E_{effective} > E_{surface}$ and $E_{kinetic} < E_{surface}$
  If the kinetic energy does not surpass the surface energy a droplet ejection is only possible if the critical pressure is surpassed sufficiently long to provide the necessary energy to build the droplet surface. The droplet breakup takes place not until the effective energy overcomes the surface energy of the ejected droplet. If the energy is provided slowly the droplet size can increase slowly until the provided energy suffices to enforce a droplet breakup. In this case the ejected droplet can be much larger in size than the nozzle. In this case the analytical model presented in section 3.1.2 is not valid anymore and CFD simulations should be used to determine the required operating parameters.

6.6 TopSpot Vario

In the TopSpot Vario technology, which is an advancement of the TopSpot technology, the compressible air is replaced by an incompressible but deformable medium (e.g. rubber or elastomer) by which direct volume displacement is achieved. The TopSpot Vario technology was developed and studied by Steinert et al. [219,229-234]. This is the reason why the TopSpot Vario method can be classified as droplet generator with flow boundary condition according to section 3.3.

6.6.1 Dosage Technology

In the TopSpot Vario, compared to the standard TopSpot discussed in the previous section, an elastomer replaces the air in the actuation chamber of the printhead. This way actuation is changed from compressible pneumatic actuation to direct liquid displacement. All other components remain the same. Figure 6.37 shows a cross section of the printhead, a photograph and its working principle. During actuation, a piezostack actuator moves a piston, placed onto the elastomer. This causes an elastomer deformation into the nozzles. Hence, liquid is displaced resulting in a

parallel droplet ejection out of all 24 nozzles. Droplet velocity and volume can be tuned by speed and amplitude of the piezo actuator. In general the piezo movement can be divided into three time intervals. It starts with piezo deflection to the desired stroke at constant speed, followed by an interval with constant piezo stroke before it contracts back to the starting position [231].

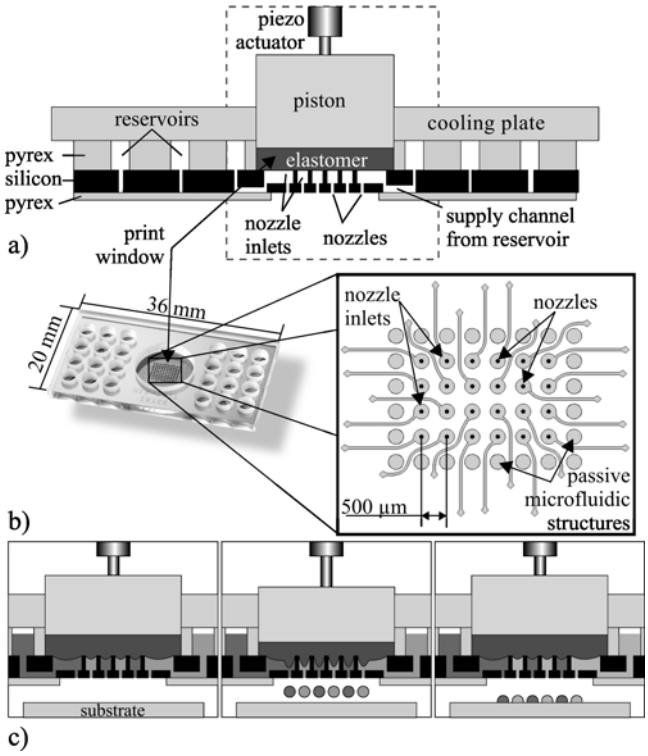

Figure 6.37: *The TopSpot Vario dispenser a) cross section of printhead with an inserted elastomer and piston b) photograph of a 24 channel printhead and an enlargement of its actuation area c) actuation: left: printhead filling and elastomer placement; middle: printing based on direct liquid displacement; right: nozzle refilling [231].*

6.6.2 EXPERIMENTAL RESULTS

The experimental results presented in the following were obtained by Steinert et al. [219,229-234]. The droplet ejection of one specific nozzle was recorded with a stroboscopic camera for measuring droplet volume and speed [231]. In figure 6.38 the ejected droplet volume as function of the piston stroke is displayed which results in a linear dependency with a slope of one, e.g. doubling the piezo stroke doubles the ejected volume. However, the piezo speed has to be adjusted for the different piezo strokes to get a stable droplet ejection [234]. From the direct coupling of the piston movement and the droplet ejection, it is also expected that the ejection speed is directly proportional to the piston speed. The droplet speed depending on the piezo speed at a constant piezo stroke of 4.8 µm is shown in figure 6.39 leading again to a linear relationship between piezo and droplet speed. The slope of the curve is two, e.g. doubling the piezo speed quadruples the droplet speed. But the piezo speed can not be

varied arbitrary if a stable and satellite-free droplet is wanted. For this case the optimum piezo speed is marked in figure 6.39. However, the variation of the piezo speed leads to no significant changes of the droplet volume [234]. All this supports the classification of the technology as dispenser with flow boundary condition.

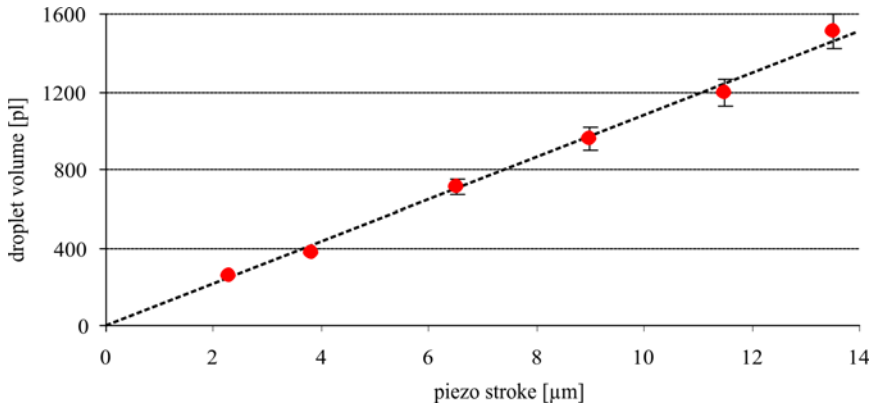

Figure 6.38: *The ejected droplet volume versus piezo stroke [234].*

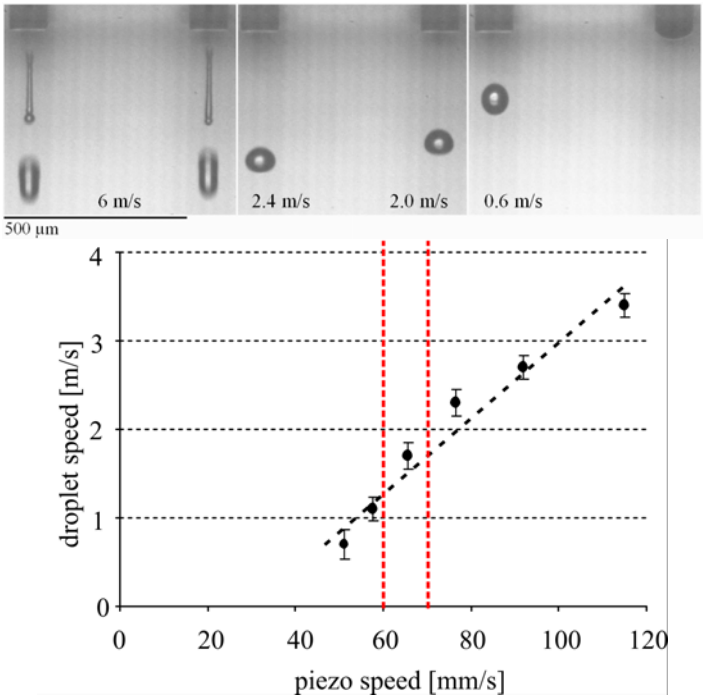

Figure 6.39: *Influence of the piezo speed on the droplet speed at a constant piezo stroke of 4.8 µm. The vertical dashed lines mark the piezo speed range for a stable droplet ejection [234].*

Furthermore, the dependency of droplet volume on the used nozzle diameter was examined using printheads equipped with nozzles with diameters in the range of 35 µm to 60 µm. The results are displayed in figure 6.40 for two different piezo strokes of 3 µm and 9 µm, respectively. Also in this case a linear relation between nozzle diameter and droplet volume was found [234].

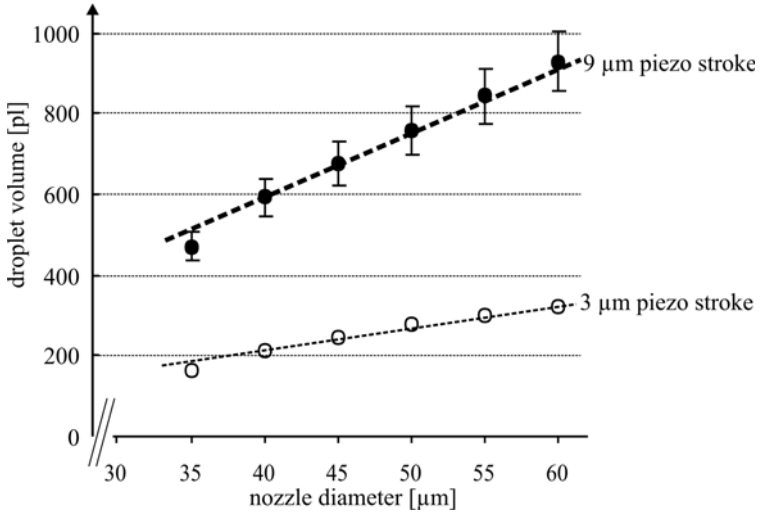

Figure 6.40: *Measured droplet volume depending on the nozzle diameter for two different piezo strokes of 3 µm and 9 µm, respectively [234].*

With increasing viscosity the minimum piezo stroke has to be increased at constant maximum piezo speed to achieve a stable droplet ejection. While stable operation started at a piezo stroke of 2.3 µm using water as printing solution, a minimum piezo stroke of 7 µm was necessary for stable dispensing of a liquid with a viscosity of 11 mPas [234]. With increasing viscosity at a constant piezo stroke of 13 µm the piezo speed has to be increased to enable a successful droplet breakup. For lower viscous media the piezo speed has to be decreased for stable operation (no satellite droplets) and larger droplet volumes were observed as depicted in figure 6.41. A decrease from 1670 pl down to 600 pl was obtained if viscosity was increased from 1 mPas to 11 mPas [234].

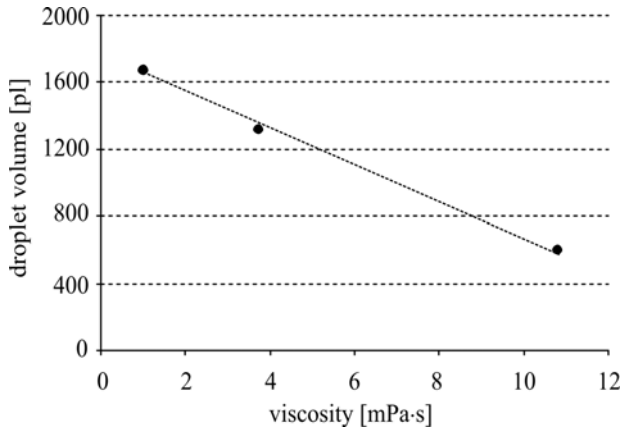

Figure 6.41: *Measured droplet volume versus liquid viscosity at a constant piezo stroke of 13 µm [234].*

6.6.3 NUMERICAL DESCRIPTION

The CFD simulations were realized using CFD-ACE+ by Litterst et al. [235]. The actuation of a single nozzle was attained using a moving boundary condition as approximation of the elastomer entering the nozzle chamber. In contrast to the ellipsoid shape of the entering elastomer the used boundary condition performs a straight moving of the back wall of the simulation model. The movement of the wall was assumed to be equal to the measured piezo stack movement corresponding to a certain piezo stroke and speed [235].

In figure 6.42 the dependence of the droplet volume on the piezo stroke at a constant piezo speed of 130 mm/s is displayed. Despite the fact that the absolute values deviate from the measured values in figure 6.38, the tendency and the slope of the line is correctly reproduced. The differences might be explained by the made approximations concerning the moving grid boundary condition.

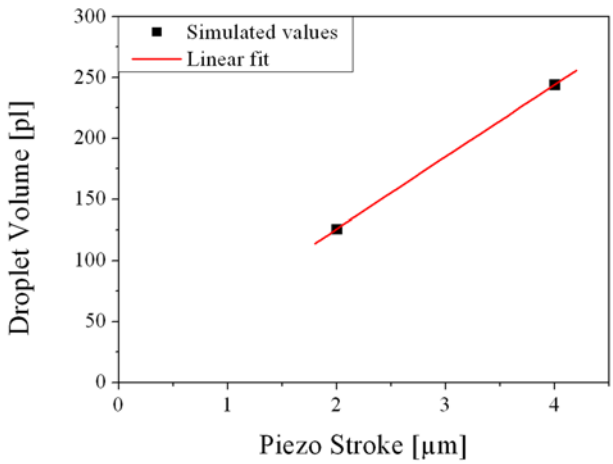

Figure 6.42: *Simulated dependence of the droplet volume on the piezo stroke at a constant piezo speed of 130 mm/s [235].*

Figure 6.43 shows the dependence of the droplet velocity on the piezo speed at a constant piezo stroke of 4 µm. Again the absolute values are varying from the experimental values depicted in figure 6.39. But also in this case the slope of the linear fit agrees well with the experiments depicted in figure 6.39.

6.6.4 CONCLUSION

Concerning the TopSpot Vario technology the most relevant parameters are the piezo stroke and the piezo speed. The piezo stroke affects significantly the droplet volume as well as the droplet speed whereas the piezo speed has to be adjusted appropriately to guaranty a stable droplet ejection. This means that the displaced volume due to the elastomer is the controlling parameter. The piezo speed influences the droplet velocity but not the droplet volume. Certainly the media parameters, mainly the viscosity, have

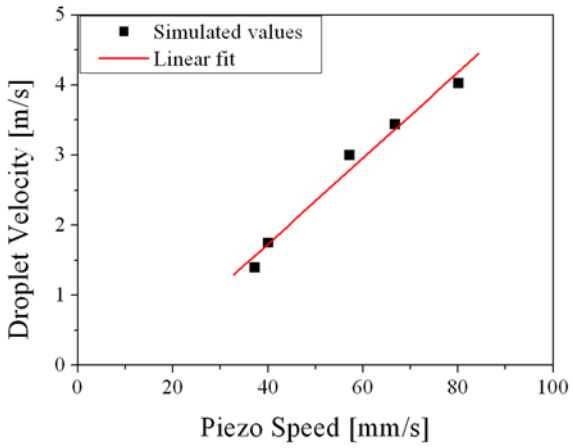

Figure 6.43: *Simulated dependence of droplet velocity on the piezo speed at constant piezo stroke of 4 µm [235].*

an influence on the performance of the TopSpot Vario. The TopSpot Vario system can be classified as droplet generator with flow boundary condition according to section 3.3 because the elastomer displaces a fixed volume inside the nozzle chambers.

Due to the same spatial dimensions the TopSpot Vario system indicates the same critical values like the TopSpot system: a critical pressure of 25.4 kPa, a critical time of 8.0 µs and a critical power of 208 µW according to the model presented in section 3.1.2. The maximum velocity inside the nozzle cannot be determined directly. Using the fact that the droplets ejected with the TopSpot Vario are nearly twice as fast as the droplets ejected with the TopSpot at same spatial dimensions, leads to the assumption that the velocity inside the nozzle is twice the velocity obtained with the TopSpot system. This would lead to a velocity of about 4.2 m/s. According to this the attained Weber number would be 12.1. This is in accordance with the theoretical description and proves a classical drop-on-demand mode for the TopSpot Vario.

6.7 Aerosol Atomizer

Varying from all other presented applications the studied aerosol atomizer from Pfeiffer [36] and MicroFlow [37] shows very low droplet volumes of about 50 fl to 500 fl at a very high frequency of 50 kHz to 500 kHz. Nevertheless, due to the huge amount of nozzles of 500 to over 2000 and the high frequency the maximum obtainable flow rate can be in the range of 20 µl/s. Because of the complicated actuation principle the aerosol atomizer can be classified as droplet generator with combined pressure and flow boundary condition according to section 3.3. Moreover, additional acoustic effects cannot be excluded totally.

6.7.1 DOSAGE TECHNOLOGY

The dosage technology of the aerosol atomizer is based on an actuation chamber capsuled by a silicon chip containing the nozzles on the one side and a membrane with attached piezo disc actuator on the other side as it can be seen in figure 6.44 schematically. The total setup is surrounded by a plastic housing with integrated fluidic supply channels. By stimulating the membrane via the piezo disc actuator with 50 kHz to 500 kHz a droplet generation can be observed. The bending membrane leads to a volume displacement as well as to a pressure generation inside the actuation chamber. Hence, a droplet ejection can be obtained depending on the piezo stroke and frequency. However, the piezo stroke cannot be regarded as simple displacement of the membrane because at such high frequencies the membrane bends in higher modes as it can be seen in figure 6.45. This figure shows the measured displacement of the membrane at several kilohertz where the maximum stroke is < 1 µm and the total integrated volume displacement of the membrane is in the range of 1 pl to 2 pl.

The silicon chip is divided into several cavities to guaranty the mechanical stiffness, each containing various nozzles. The nozzles are manufactured using dry etching methods.

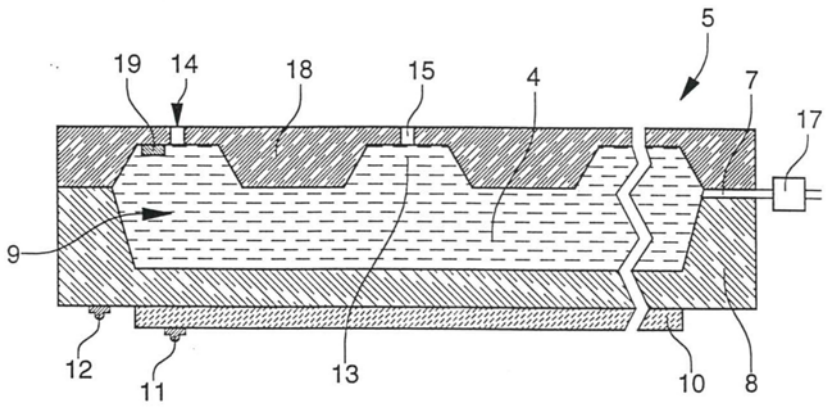

Figure 6.44: *Schematic of the construction of the studied aerosol atomizer [36,37].*

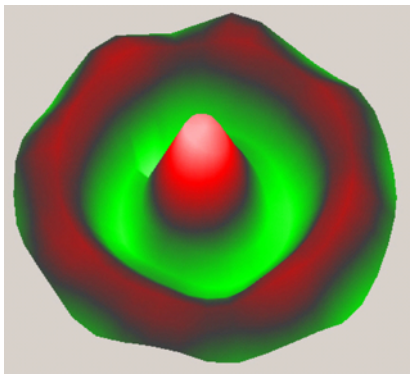

Figure 6.45: *Bending of the actuated membrane at several kilohertz measured with a laser interferometer [36,37].*

6.7.2 Experimental Results

Also in this case optical measurements as well as measurements for the determination of the droplet volume were performed. However, to visualize and evaluate these numerous small droplets it is necessary to find alternative measurement methods. The optical measurements were performed by LaVision [159] using a high-speed camera as described in section 4.2.2. With this method two different variants of the droplet breakup could be observed. On the one hand it occurs a jet ejection with successive Rayleigh droplet breakup as depicted in figure 6.46 a), and on the other hand it occurs a drop-on-demand breakup as depicted in figure 6.46 b), depending on the system design.

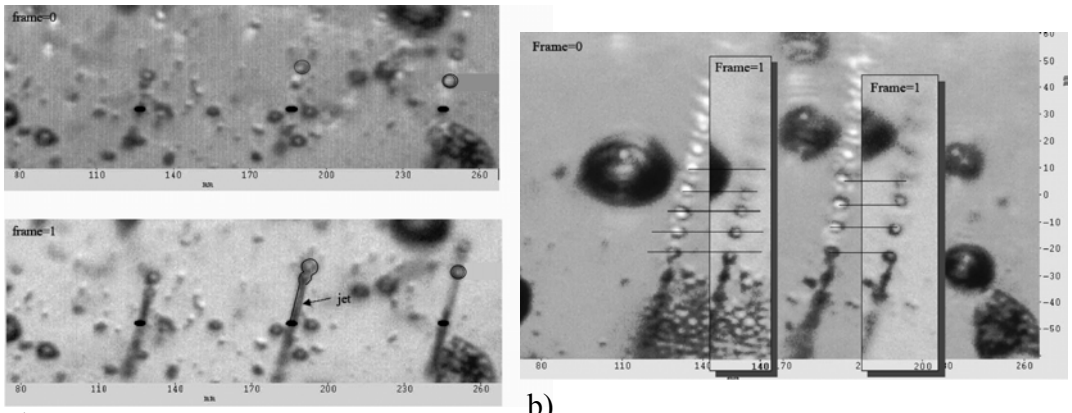

Figure 6.46: *High-speed pictures of the both occurring droplet ejection modes of the aerosol atomizer. a) Jet ejection with successive Rayleigh breakup. b) Drop-on-demand breakup [159].*

6.7.3 Numerical Description

Due to the high complexity of the system, the high actuation frequency and the strong interaction between membrane and fluid, it is not possible to realize a CFD simulation of the entire system. Hence, it was necessary to investigate the atomizer considering some simplifications or approximations.

In this case the CFD tool was only capable to simulate the capillary filling of the entire device and to simulate the droplet ejection out of a single nozzle. For this, only the required pressure could be stated to get either the Rayleigh or the drop-on-demand breakup both obtained by experimental findings. The outcome of these simulations can be summarized that a constant pressure with a slightly superimposed disturbance preferable leads to a jet ejection with subsequent Rayleigh breakup whereas a small constant pressure with an evident pressure fluctuation preferable leads to a drop-on-demand breakup. In both cases the critical Weber number of 8 for the Rayleigh breakup and 12 for the drop-on-demand breakup has to be surpassed.

Furthermore, a network model was set up to simulate the entire fluidic system including the supply channels to the reservoir, the nozzles and an actuating flow boundary condition computed by the measured volume displacement depicted in figure 6.45. Therefore, a network model similar to the one presented in section 3.2.4 (cf. figure 3.28) was enlarged to be able to simulate the entire system including all nozzles and the supply channels but neglecting any free surface effects. A sketch of the final network model is displayed in figure 6.47. The supply channel is realized by a fluidic resistance and inertance. There against, the nozzle side is realized as described in section 3.2.4.

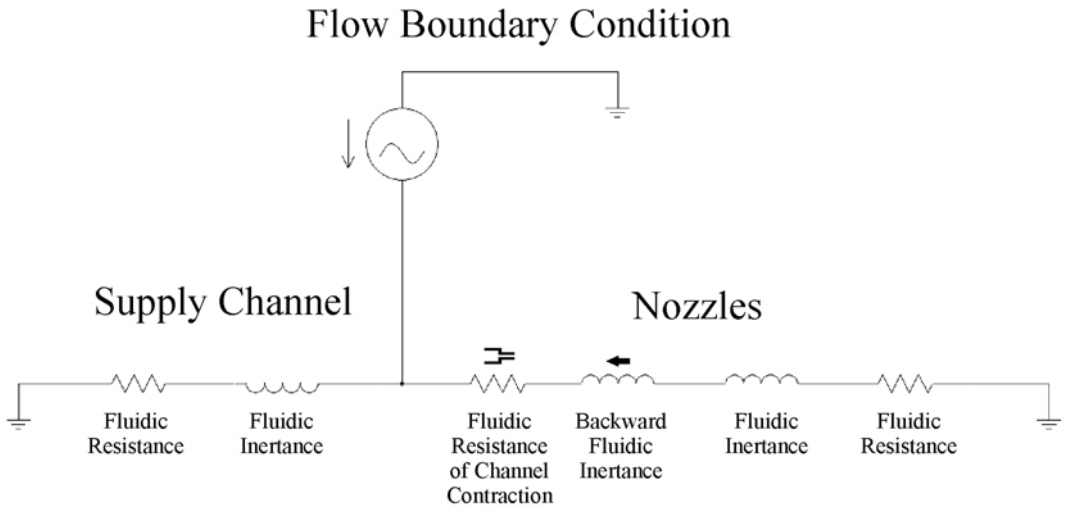

Figure 6.47: *Network model for the entire aerosol atomizer.*

Using this model it was possible to investigate the aerosol atomizer concerning cutting-off frequency, generated pressure, preferred flow direction and dependence on the amount of nozzles. This way the experimental behavior could be confirmed qualitatively. Investigating the frequency dependence, as depicted in figure 6.48, the damping and the phase shift of the both directions at different frequencies can be observed. At low frequencies the damping of the supply channel is nearly zero whereas the damping of the nozzles is about -10 dB. Between 100 Hz and 300 kHz is a kind of transition regime and at higher frequencies the damping of the supply channel is about -50 dB whereas the damping of the nozzles is zero. Hence, the system is "open" towards the nozzle direction at higher frequencies.

Investigating the pressure at the point of intersection, i.e. the actuation chamber and the volume flow towards the both ends of the system, as depicted in figure 6.49, a possible overpressure and the preferred flow direction can be observed. The break-in of the pressure is due to the turnaround of the flow direction and the resulting activation of the backward fluidic inertance. Also the pressure intensity seems to be very high compared to the results obtained from the CFD simulations.

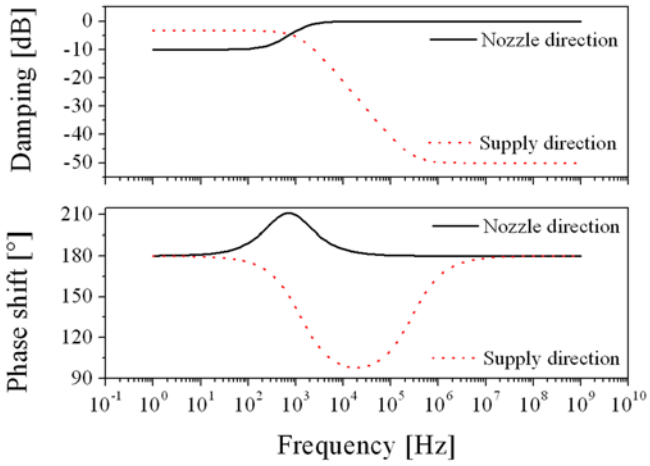

Figure 6.48: *Dependence of the damping and the phase shift on the actuation frequency.*

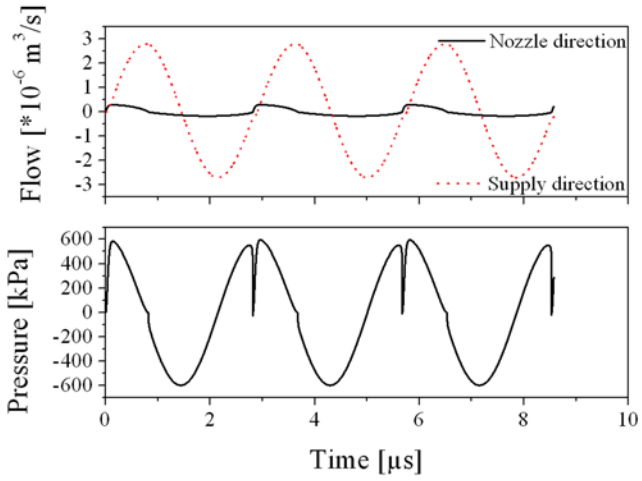

Figure 6.49: *Pressure and flow as a function of time for the supply channel and the nozzles, respectively.*

6.7.4 CONCLUSION

The main parameter influencing the performance of the aerosol atomizer is the piezo disc stroke and the resulting volume displacement as well as the generated pressure. Due to this it is possible to generate a sufficient volume flow and pressure inside the actuation chamber to enable a droplet ejection, either by Rayleigh or drop-on-demand breakup. The total number of nozzles affect the maximum achievable flow rate of the system. However, it is still not clear which parameter is responsible for the variation of the droplet diameter respectively droplet volume. The aerosol atomizer can be classified as droplet generator with combined pressure and flow boundary condition according to section 3.3 because of the strong coupling between membrane and flow. Furthermore, acoustic effects cannot be ruled out, such that there might be a combined pressure and flow boundary condition plus an acoustic boundary condition.

The aerosol atomizer indicates a critical pressure of 197 kPa, a critical time of 0.3 µs and a critical power of 26 µW according to the model presented in section 3.1.2. The maximum velocity inside the nozzle which can be extracted out of the CFD simulations varies depending on the operation mode. According to this the attained Weber numbers range from 10.0 to 17.4.

6.8 Summary of the Relevant Affecting Parameters

In this section the bubble jet presented in chapter 5 and all droplet generators presented in this chapter are conclusively compared. All droplet generators are totally different concerning actuation mechanism, attained droplet volume and performance. The droplet or jet volumes are in the range of 100 fl to 50 nl. All actuation principles presented in section 3.3 except of the purely acoustic actuation are demonstrated by means of various droplet generators. The DWP, the fast switching valve systems and the TopSpot are representatives of an applied pressure boundary condition. The NanoJet, the PipeJet and the TopSpot Vario are representatives of an applied flow boundary condition. Finally, the bubble jet and the aerosol atomizer are representatives of an applied combined pressure and flow boundary condition. The obtained droplet volume and velocity are influenced by different parameters depending on the droplet generator as discussed before.

In general only the pressure pulse and liquid properties are influencing the droplet volume if a pressure boundary condition is used. If a flow boundary condition is used only the piezo movement defining the volume displacement is influencing the droplet volume. Depending on the technology liquid properties can be considered to be of minor importance or negligible in many cases. An applied combined pressure and flow boundary condition cannot be influenced easily concerning droplet volume. The coupling typically prevents an easy description on a clear relation between actuation and dosage volume.

The studied boundary conditions, the parameters affecting the droplet volume and the parameters affecting the droplet velocity are summarized in table 6.1. Due to this also general design rules can be proposed to design a proper droplet generator for different kind of applications or requirements. This approach is detailed in chapter 7.

Table 6.1: *Comparison of all presented droplet generators concerning actuation boundary condition and important control parameters.*

	Boundary condition	**Parameters affecting the droplet volume**	**Parameters affecting the droplet velocity**
Bubble jet	Combined pressure and flow boundary condition	Heating power, heating duration, liquid properties	Heating power, heating duration, liquid properties
DWP	Pressure boundary condition	Geometrical dimensions, (liquid properties)	Pressure head, liquid properties
Fast switching valve systems	Pressure boundary condition	Piezo stroke, piezo velocity, reservoir pressure, liquid properties	Piezo velocity, reservoir pressure, liquid properties
NanoJet	Flow boundary condition	Piezo stroke, relative resistance, (liquid properties)	Piezo stroke, piezo velocity, liquid properties
PipeJet	Flow boundary condition	Tube diameter, piezo stroke, relative resistance, (liquid properties)	Piezo stroke, piezo velocity, liquid properties
TopSpot	Pressure boundary condition	Geometrical dimensions, liquid properties	Pressure pulse, liquid properties
TopSpot Vario	Flow boundary condition	Piezo stroke, liquid properties	Piezo velocity, liquid properties
Aerosol atomizer	Combined pressure and flow boundary condition (acoustic boundary condition?)	Number of nozzles (?), liquid properties	Piezo frequency, number of nozzles (?), liquid properties

For all presented droplet generators the critical pressure, the critical time and the critical power were calculated according to the model presented in section 3.1.2. The attained data could mostly be confirmed closely using experimental findings or simulation outputs. In one special case (TopSpot dispenser) droplet breakup is even observed below the critical parameters. This observation is explained by the fact, that the necessary condition for droplet breakup in fact is different from the conditions given by the critical parameters of the model. However, the droplet ejection could successfully explained by an energetic approach.

Furthermore, also the present Weber numbers could be calculated using the velocities provided either by the CFD simulations or by estimations out of experimental results. Also concerning the Weber numbers all droplet generators exceed the corresponding critical Weber numbers. However, again the TopSpot system is the only exception. The Weber number for the TopSpot system only achieves a value of 6.6 which is below the critical value for a drop-on-demand breakup.

7 GUIDELINES FOR SYSTEMATIC DESIGN OF DROPLET GENERATORS

The purpose of this chapter is to provide guidelines for the systematic design of droplet generators based on the presented results and the attained experiences. Due to the fact that the quest for a suitable droplet generator strongly depends on the main requirement of the system, it is distinguished between three important main requirements along which the guidelines are developed. These three main requirements are the media variability, the degree of parallelism and the volume variability. First of all the definition of the applied criteria are stated and general design rules are presented which should be followed and which are valid for all kind of droplet generators. After that specific design rules are recommended for the three different main requirements. Based on this a decision tree can be established for different priority successions of the single criteria. Therein the classification of droplet generators concerning applied actuation boundary condition, introduced in section 3.3, is used to choose the appropriate droplet generator. In the last section of this chapter a decision tree is presented as example.

7.1 DEFINITION OF APPLIED CRITERIA

In the following the different criteria for possible decision trees are defined. These criteria are the media variability, the degree of parallelism and the volume variability. These are the main criteria to distinguish between droplet generators or to design new ones for a specific application. However, the single criteria can further be divided as it is shown in the following.

7.1.1 MEDIA VARIABILITY

The media variability is the objective with highest priority if a droplet generator is to be used with a variety of many different liquids or even in different applications. This is a minor problem if the used liquids have similar properties. But if the use of a broad media range is desired the applied droplet generator should exhibit a low sensitivity to the liquid properties, or in other words: a good media variability. However, it can be distinguished between two kinds of media variable droplet generators. Droplet generators which exhibit a performance independent of the liquid properties. This means that the same defined volume can be ejected for a set of actuation parameters, regardless which liquid is used as long as the liquid properties are within the specific range. And droplet generators which exhibit a performance adjustable to the liquid

properties. This means that for every liquid the dispensing parameters might have to be adjusted, but droplet generation will be achievable for a large class of liquids. However, this second class of droplet generators is equivalent to droplet generators which exhibit a controllable variable dosage volume which are treated in section 7.1.3. Due to this volume variability, the ejected volume can be adjusted to different liquid properties.

In general a desirable system concerning media variability consists of a droplet generation mechanism where the droplet volume depends on geometrical parameters only. Otherwise, if an adjustable droplet generator is acceptable, the system has to be adapted to the new liquid either by using a calibration or by trial and error. In the best case a calibration curve is established beforehand based on a set of different liquid properties. Using this, the droplet generator can easily be adapted to new liquids.

7.1.2 PARALLELISM

If the parallelism is the main requirement, which is for example the case in high throughput screening (HTS) applications, all single channel droplet ejectors fall short. HTS methods allow the testing of several 100,000 chemicals per day which are used in many domains of life sciences as well as in pharmaceutical and chemical sciences. However, alike or even more important is the number of different liquids which can be handled in parallel. This is the case if the nozzles are partially or even totally fed by separate reservoirs. For example the DWP system (cf. section 6.1) can handle up to 384 different liquids simultaneously whereas an inkjet printhead (cf. section 5.1) indeed has up to 300 nozzles but can handle only one liquid.

Considering the parallelism of a droplet ejection two different kinds of droplet generators have to be distinguished:

- Simultaneous parallel droplet ejection.
- Consecutive droplet ejection.

For a parallel ejection of many droplets the actuation is preferably done simultaneously for all nozzles to reduce the required time for the ejection. Usually also the system setup is simpler if only one actuation unit is used. In contrast to this, there are also systems where the nozzles can be actuated separately like in inkjet applications. In this case the droplets are ejected in serial which makes this method much slower compared to the simultaneous ejection. Moreover, due to the single actuation units the system setup is mostly more complex and more expensive than a simultaneous parallel droplet ejector.

7.1.3 VOLUME VARIABILITY

A controllable variable volume is important in many applications. If the volume variability is a desired feature than it is important that the ejected volume can easily be adjusted preferably by a linear relation between actuation signal and droplet volume. A volume variability should be attainable by only varying the actuation parameters rather than by changing the whole setup. This volume variability is not obvious because it depends on the applied actuation principle whether the volume is adjustable or not.

7.2 GENERAL DESIGN RULES

Besides the specific design rules which are necessary to attain one of the previously defined criteria there are also general design rules which should be followed in any case. These are important to guaranty a stable, reproducible and precise droplet ejection. Hence, the general design rules are the fundamentals for every device. Thereafter the specific design rules are discussed to optimize a single droplet generator concerning one criterion for a selected application.

First of all the precision of a droplet generator has to be ensured in any case. However, therefore firstly it has to be considered what is meant by "precision". One can distinguish between accuracy and precision of the droplet volume like defined below. Additionally the quality of droplet placement or spot position, again divided into accuracy and precision, can be considered as additional measure.

- The accuracy of the droplet volume is the closeness of a measured volume to the true volume as specified by the volume setting of the droplet generator, also known as "mean error".
- The precision of the droplet volume is the closeness of agreement among the individual measurements, also known as "standard deviation", "reproducibility" and "repeatability".
- Both terms can be expressed using the "coefficient of variation" (CV) which is defined as relative standard deviation in %.
- The placement accuracy is defined in the same manner as the volume accuracy attributing to the placement position.
- The placement precision is defined in the same manner as the volume precision attributing to the placement position.

To guaranty all these kinds of precision and additionally a stable and reproducible droplet ejection some prerequisites have to be ensured. These are mainly based on the fabrication quality and the actuation control. In the following some general design rules are summarized.

7.2.1 Fabrication Quality

Obviously, the fabrication quality of a droplet generator is of outstanding importance. A good quality of the nozzle edges are important to guaranty a reproducible droplet formation. Any disruption of the edge leads to a vitiation of the droplet formation. On the one hand this can influence the droplet volume as well as the droplet trajectory. On the other hand, and this is more serious, this can lead to a non reproducibility of the droplet formation because the disruption can interfere non constantly. Furthermore, also the residuary spatial dimensions have to exhibit tolerances as small as possible. This is due to the fact that not only the reproducibility of one device has to be ensured but also a low device to device variation. Moreover, also devices with the same construction style should indicate a performance as similar as possible (cf. section 3.2.1). Finally also the surfaces play an important role for the droplet formation (cf. section 3.2.3). Due to this also the reproducible adjustment of the surface properties has to be done very carefully.

7.2.2 Actuator Control

Besides the fabrication quality the reproducibility is also influenced by the boundary condition applied for driving the system. This is mainly influenced by the control of the actuation respectively the actuator. In general it can be stated that a good volume accuracy and precision can be maintained if the actuation is well controllable (cf. section 3.2.4) and reproducible. Hence, not only the actuator itself has to exhibit a reproducible response on the provided input signal, but also the electric input signal itself has to exhibit a stable and reproducible pattern.

Moreover, a strong actuator is recommended because due to this the interaction between actuator and the liquid inside the system can be minimized. This interaction or coupling is usually disadvantageous because the performance of the droplet ejector cannot be controlled easily (cf. section 3.3). Furthermore, the mechanical/fluidic setup should be solid and well designed. Any mechanical resonance, fluidic capacitances or similar might influence and deteriorate the reproducibility of the dosage volume.

7.3 Specific Design Rules

The specific design rules presented in the following provide guidance to achieve the performance criteria introduced in section 7.1. The design rules are arranged according to the presented criteria. In order to distinguish between different methods to realize an

appropriate droplet generator the classification of the various actuation boundary conditions introduced in section 3.3 is applied. The corresponding actuation principles are marked with different priorities according to their suitability to achieve a specific performance criterion. The actuation principles are abbreviated corresponding to section 3.3, pressure boundary condition (P_{BC}), flow boundary condition (Φ_{BC}), mixed boundary condition ($Mixed_{BC}$) and acoustic actuation (Ac_{BC}). Three priorities are introduced to judge the suitability of the actuation principle to achieve a specific performance criterion. The following commendations can be allocated to the single actuation principles.

- Very advisable (++)
- Advisable (+)
- Not recommended (-)

7.3.1 Media Variability

As mentioned in section 7.1.1 the media variability can be considered in two different ways. Due to this also the specific design rules have to be divided corresponding to this. However, as also mentioned before, droplet generators which exhibit a performance adjustable to the liquid properties are equivalent to droplet generators which exhibit a controllable variable dosage volume. Due to this these systems are treated in section 7.3.3. The Droplet generators which exhibit a performance independent of the liquid properties are discussed in this section.

The best media variability can be obtained using a droplet generation mechanism where the droplet volume depends on geometrical parameters only. Thereby the droplet volume depends only on the size of the nozzle and nozzle chamber. Hence, the droplet volume is completely independent on the liquid properties. Such systems commonly are actuated with a pressure boundary condition like the DWP system (cf. section 6.1) which is the best example for these class because in the DWP system the droplet volume depends on geometrical parameters only. Due to this an applied pressure boundary condition is categorized as very advisable for the media variability (P_{BC}(++)). However, if the droplet volume is not defined by geometrical parameters only, a pressure boundary condition is not recommended. This is due to the fact that the ejected volume strongly depends on the liquid viscosity using a pressure boundary condition via the coupling over the Navier-Stokes equation (P_{BC}(-), if not geometrical defined). But also mixed boundary condition systems like the new bubble jet printhead concept of Canon [193,194] make use of the geometrical defined droplet volume. This leads to an advisable classification because the performance is not as good as pressure driven systems ($Mixed_{BC}$(+)). Moreover, also the NanoJet system (cf. section 6.3), which is a system with flow boundary condition, exhibits a performance independent on the liquid viscosity in a certain range. Due to this also the flow boundary condition is categorized as advisable (Φ_{BC}(+)). However, no droplet generator with acoustic

actuation with geometrical defined droplet volume is known. This is the reason why the acoustic actuation is classified as not recommended ($Ac_{BC}(-)$). Conclusively the following commendations are allocated to the single actuation principles:
$P_{BC}(++)$, $Mixed_{BC}(+)$, $\Phi_{BC}(+)$ and $Ac_{BC}(-)$, ($P_{BC}(-)$, if not geometrical defined).

7.3.2 PARALLELISM

As mentioned in section 7.1.2 the degree of parallelism can be considered in two different ways, whether the droplets have to be ejected simultaneously or not. Due to this also the specific design rules have to be divided corresponding to this. The main difference of the simultaneous parallel and the consecutive droplet ejection concerning used design is the size of the actuator. A simultaneous parallel droplet generator can use one big and strong actuator. Advantage is that a strong actuator like a pressure or a flow actuator can always enforce a droplet ejection. There against, a consecutive droplet generator usually use many single small and weak actuators. Advantage is that every nozzle can be addressed separately. Disadvantage is that usually only weak actuators like mixed or acoustic actuators are used to realize the integration of many nozzles in parallel.

SIMULTANEOUS PARALLEL DROPLET EJECTION

For a simultaneous parallel ejection of several droplets it is advantageous to use a pressure boundary condition as explained in section 3.3.1 because this actuation can easily be applied to several nozzles. Within a pressure chamber a constant pressure can be applied to many nozzles simultaneously because the pressure does not depend on the position. Examples are the DWP system (cf. section 6.1) or the TopSpot system (cf. section 6.5). Both have a common pressure chamber for all nozzles. Due to this an applied pressure boundary condition is categorized as very advisable for the simultaneous parallel droplet ejection ($P_{BC}(++)$). There against, systems driven by a flow boundary condition, mixed boundary condition or acoustic actuation have often the drawback that every nozzle has to be actuated separately like in inkjet applications, which make them more complex and more expensive. With these actuation principles usually no common actuation is possible in a way that the droplet ejection is stable and reproducible. However, the TopSpot Vario technology (cf. section 6.6) is an exception because all nozzles are actuated by a corporate deformation of the elastomer inside the nozzle chambers. Due to this an applied flow boundary condition is categorized as advisable for the simultaneous parallel droplet ejection ($\Phi_{BC}(+)$). Moreover, there are also systems with a common mixed boundary condition like the aerosol atomizer (cf. section 6.7). However, such a mixed actuation principle is not easy to control to guaranty a stable and reproducible droplet generation out of every nozzle. Due to this also the mixed boundary condition is categorized as restricted advisable ($Mixed_{BC}(+)$). Finally, there are no known systems using an acoustic actuation principle for a simultaneous parallel droplet ejection. This is the reason why the acoustic actuation is

classified as not recommended (Ac_{BC}(-)). Conclusively the following commendations are allocated to the single actuation principles:
P_{BC}(++), Φ_{BC}(+), $Mixed_{BC}$(+) and Ac_{BC}(-).

CONSECUTIVE DROPLET EJECTION

A consecutive droplet ejection used to have a high degree of parallelism require a high dispensing frequency to compensate the drawback of the serial droplet ejection. The best examples for this class are the bubble jet printheads (cf. chapter 5) [2-5] and the piezoelectric printhead systems [6-10,144,148,154] because they combine a high print frequency with a high amount of nozzles in one row. Therefore the mixed boundary condition and the acoustic actuation can be used for a consecutive droplet ejection with a high degree of parallelism. As mentioned before mixed and acoustic actuators are more easy to integrate because of their usual smaller construction. However, concerning the parallelism the serial droplet ejection is a disadvantage which leads to a reduction in the categorization. Due to this an applied mixed boundary condition as well as an acoustic actuation are categorized as advisable for the parallel droplet ejection ($Mixed_{BC}$(+), Ac_{BC}(+)). Pressure and flow driven systems are relatively slow compared to the previous discussed systems because they have to be actuated in serial like the fast switching valve systems (cf. section 6.2) [143-145] or the TTP Labtech system [146]. A further disadvantage of pressure or flow driven systems is the usual bigger setup which leads to a bigger device and larger nozzle spacings. Due to this an applied pressure as well as flow boundary condition are categorized as not recommended for the parallel droplet ejection (P_{BC}(-), Φ_{BC}(-)). Conclusively the following commendations are allocated to the single actuation principles:
$Mixed_{BC}$(+), Ac_{BC}(+), P_{BC}(-) and Φ_{BC}(-).

7.3.3 VOLUME VARIABILITY

A good volume variability can only be attained by a controllable actuation method like a flow boundary condition according to section 3.3.2 because in this case the ejected volume directly depends on the created volume displacement. Examples are the NanoJet (cf. section 6.3), the PipeJet (cf. section 6.4), the TopSpot Vario system (cf. section 6.6) and the TTP Labtech system [146]. Due to this an applied flow boundary condition is categorized as very advisable for the volume variability (Φ_{BC}(++)). However, also pressure driven fast switching valve systems (cf. section 6.2) [143-145] can also be arranged in this class because therewith the ejected volume can easily be tuned by the opening time of the valve. Hence, also pressure actuated systems can be adjusted concerning the droplet volume in a certain range. This leads to an advisable classification because the performance is not as good as in flow driven systems (P_{BC}(+)). The same is true for all kind of systems based on the piezoelectric inkjet technology and thus on acoustic effects [6-10,144,148,154]. They exhibit also good volume variability in a certain range but they are very sensitive to media changes. Due to this also the flow boundary condition is categorized as

advisable ($Ac_{BC}(+)$). In all of these systems the ejected volume can be adjusted easily to different kinds of liquid. Droplet generators with a mixed boundary condition like bubble jet printheads usually do not have a good volume variability because the displaced volume can not be controlled by the actuation. This is the reason why the mixed actuation is classified as not recommended ($Mixed_{BC}(-)$). Conclusively the following commendations are allocated to the single actuation principles:
$\Phi_{BC}(++)$, $P_{BC}(+)$, $Ac_{BC}(+)$ and $Mixed_{BC}(-)$.

As mentioned before, droplet generators which exhibit a controllable variable dosage volume also exhibit a good media variability.

7.4 SUMMARY

In the previous section the single performance criteria were appraised concerning the applicable actuation boundary condition. In this summary in contrast the presented reflection should be reversed. Here the actuation boundary conditions are summarized concerning the provided beneficial features. Furthermore, an exemplary guideline is presented in order to demonstrate the procedure to design a droplet generator according to the given design rules.

Using a droplet generator with pressure boundary condition typically provides a good media variability in combination with a geometrically defined volume. Applied to an adjustable droplet generator a pressure boundary condition will lead to a low media variability because the flow depends strongly on the viscosity. The simultaneous parallel droplet ejection is also very advantageously using the pressure boundary condition because it can be applied easily to all nozzles at a time. However, the parallel ejection using a consecutive droplet ejection is not recommended because of the much slower attainable frequencies and the much bigger system setup. Finally the volume variability can also be accomplished in a certain range using a pressure actuation.

A droplet generator with flow boundary condition provides a remarkable volume variability and thus the possibility to build a droplet generator adjustable to media properties. Furthermore, droplet generator with flow boundary condition provided by a strong actuator also exhibits a media variability in a certain range. The degree of parallelism depends on the method. If a simultaneous parallel ejection is desired the flow actuation is advisable although it is not easy to realize. But if the consecutive method is desired the flow actuation is not recommended because of the much slower attainable frequencies and the much bigger system setup.

A droplet generator with mixed boundary condition can be used to attain a fixed volume dispenser to guaranty the media variability. A droplet generator with mixed boundary condition is also capable to achieve a parallel droplet ejection using a simultaneous as well as a consecutive method. However, biggest disadvantage of the mixed boundary condition is the lack of volume variability.

A droplet generator with acoustic actuation is not recommended for a fixed volume device. Furthermore, also a simultaneous parallel acoustic actuation is not possible. But a parallel acoustic actuation using a consecutive droplet ejection is beneficial. The volume variability is given in a certain range by an acoustic actuation.

Considering the presented results an existing droplet generator can be chosen or a new one can be designed. Therefore priorities have to be assigned to the mentioned criteria to get the importance of the criteria. Assuming, for example, that the volume variability is the most important feature, a valence of the factor 2 can be assigned. If the degree of parallelism and the media variability have a lower priority a valence of the factor 1 can be assigned. Due to the volume variability the fixed volume dispenser falls out. Assuming that a single actuation is wanted the consecutive droplet ejection has to be considered. Comparing now the number of pluses and minuses the best actuation principle can be chosen. Then the flow boundary condition attains four pluses, the acoustic actuation two pluses and the pressure boundary condition and the mixed boundary condition obtain zero. Hence, the flow boundary condition is the recommended actuation principle for this example. This procedure can also be applied to other scenarios.

8 REFERENCES

[1] J. Ducrée and R. Zengerle, *FlowMap - Microfluidics Roadmap for the Life Sciences*, Books on Demand GmbH, Norderstedt, Germany, 2004.

[2] Hewlett Packard, http://www.hp.com, 2005.

[3] Canon Inc., http://www.canon.com, 2005.

[4] Olivetti I-Jet, http://www.olivettii-jet.it, 2004.

[5] Lexmark International, Inc., http://www.lexmark.com, 2005.

[6] Seiko Epson Corporation, http://www.epson.com, 2005.

[7] Xaar, http://www.xaar.co.uk, 2005.

[8] Spectra Printing Division, Dimatix, Inc., http://www.diamtix.com, http://www.spectra-inc.com, 2005.

[9] Xerox Corporation, http://www.xerox.com, 2005.

[10] TallyGenicom, http://www.tallygenicom.de, 2005.

[11] M. Garbero, M. Vanni and G. Baldi, "CFD Modelling of a Spray Deposition Process of Paint", *Macromolecular Symposia*, vol. 187, pp. 719-729, 2002.

[12] tesa AG, http://www.tesa.de, 2005.

[13] Pattex, Henkel KGaA, http://www.pattex.de, 2005.

[14] Kontakt Chemie, CRC Industries GmbH, http://www.kontaktchemie.dk, 2005.

[15] Caramba Chemie GmbH & Co. KG, http://www.caramba.de, 2005.

[16] Agilent Technologies, http://www.agilent.com, 2005.

[17] microfluidic ChipShop GmbH, http://www.microfluidic-chipshop.com, 2005.

[18] Protensive Ltd., http://www.protensive.com, 2005.

[19] Hiden Isochema Ltd., http://www.hidenisochema.com, 2005.

[20] Micronit Microfluidics BV, http://www.micronit.com, 2005.

[21] J. H. Lee, "Microactuation by Continuous Electrowetting and Electrowetting: Theory, Fabrication, and Demonstration", PhD thesis, University of California, 2000.

[22] V. Srinivasan, V. K. Pamula and R. B. Fair, "An integrated digital microfluidic lab-on-a-chip for clinical diagnostics on human physiological fluids", *Lab on a Chip*, vol. 4, pp. 310-315, 2004.

[23] O. D. Velev, B. G. Prevo and K. H. Bhatt, "On-chip manipulation of free droplets", *Nature*, vol. 426, pp. 515-516, 2003.

[24] A. Wixforth, C. Strobl, C. Gauer, A. Toegl, J. Scriba and Z. von Guttenberg, "Acoustic manipulation of small droplets", *Analytical and Bioanalytical Chemistry*, vol. 379, pp. 982-991, 2004.

[25] Advalytix AG, http://www.advalytix.com, 2005.

[26] T. Okamoto, T. Suzuki and N. Yamamoto, "Microarray fabrication with covalent attachment of DNA using Bubble Jet technology", *Nature Biotechnology*, vol. 18, no. 4, pp. 438-441, 2000.

[27] T. Goldmann and J. S. Gonzalez, "DNA-printing: utilization of a standard inkjet printer for the transfer of nucleic acids to solid supports", *Journal of Biochemical and Biophysical Methods*, vol. 42, no. 3, pp. 105-110, 2000.

[28] T. Phou and A. M. Gué, "A Microarray Ejectors for In-situ Oligonucleotide Synthesis on DNA Chips", *Proceedings of the Micromechanics Europe Workshop, MME*, Sinaia, Romania, 2002, pp. 149-152.

[29] L. R. Allain, M. Askari, D. L. Stokes and T. Vo-Dinh, "Microarray sampling-platform fabrication using bubble-jet technology for a biochip system", *Fresenius Journal of Analytical Chemistry*, vol. 371, no. 2, pp. 146-150, 2001.

[30] F. Takagi, R. Kurosawa, D. Sawaki, S. Kamisuki, M. Takai, K. Ishihara and M. Atobe, "Pico Liter Dispenser with 128 Independent Nozzles For High Throughput Biochip Fabrication", *Proceedings of IEEE International Conference on Micro Electro Mechanical Systems, MEMS*, Maastricht, The Netherlands, 2004, pp. 276-279.

[31] P. Cooley, D. Wallace and B. Antohe, "Applications of Ink-Jet Printing Technology to BioMEMS and Microfluidic Systems", *SPIE Conference on Microfluidics and BioMEMS Proceedings*, San Francisco, USA, 2001, pp. 177-188.

[32] A. Kuoni, M. Boillat and N. F. de Rooij, "A Modular High Density Multi-Channel Dispenser for Micro-Array Printing", *Proceedings of IEEE Transducers*, Boston, USA, 2003, pp. 372-375.

[33] A. Kuoni, M. Boillat and N. F. de Rooij, "A Highly Parallel Piezoelectric Printing Device for Micro-Array Technology", *Proceedings of IEEE International Conference on Micro Electro Mechanical Systems, MEMS*, Maastricht, The Netherlands, 2004, pp. 466-469.

[34] O. Resina-Pelfort, J. Comas-Riu and J. Vives-Rego, "Effects of Deflected Droplet Electrostatic Cell Sorting on the Viability and Exoproteolytic Activity of Bacterial Cultures and Marine Bacterioplankton", *Systematic and Applied Microbiology*, vol. 24, pp. 31-36, 2001.

[35] Böhringer Ingelheim microParts, http://www.microparts.de, 2005.

[36] Ing. Erich Pfeiffer GmbH, http://www.pfeiffer.de, 2005.

[37] Microflow Engineering SA, http://www.microflow.ch, 2005.

[38] W. Wehl, J. Wild and B. Lemmermeyer, "A drop-on-demand metal jet printer for wafer bumping", *Proceedings of 14th European Microelectronics and Packaging Conference & Exhibition*, Friedrichshafen, Germany, 2003.

[39] W. Wehl and J. Wild, *Druckkopf zum Ausspritzen eines heißen flüssigen Mediums und Verfahren zur Herstellung einer metallisches Lot umfassenden Verbindungsstelle*, German Patent DE 19931110 A1, 1999.

[40] D. B. Wallace and D. J. Hayes, "Solder Jet Technology Update", *The International Journal of Microcircuits and Electronic Packaging*, vol. 21, no. 1, 1998.

[41] MicroFab Technologies, Inc., http://www.microfab.com, 2005.

[42] DELO Industrieklebstoffe GmbH & Co. KG, http://www.delo.de, 2005.

[43] R. Bennet, C. Edwards, J. Lee, K. Silz, "Precision Industrial Ink Jet Printing Technology for Full Color PLED Display and TFT-LCD Manufacturing", *International Display Manufacturing Conference*, 2003.

[44] M. Grove, D. Hayes, R. Cox and D. Wallace, "Color Flat Panel Manufacturing Using Ink Jet Technology", *Display Works*, 1999.

[45] D. J. Hayes, W. R. Cox and M. E. Grove, "Low-Cost Display Assembly and Interconnect Using Ink-Jet Printing Technology", *Display Works*, 1999.

[46] T. R. Hebner, C. C. Wu, D. Marcy, M. H. Lu and J. C. Sturm, "Ink-jet printing of doped polymers for organic light emitting devices", *Applied Physics Letters*, vol. 72, no. 5, pp. 519-521, 1998.

[47] F. X. Tanner, "Liquid Jet Atomization and Droplet Breakup Modeling of Non-Evaporating Diesel Fuel Sprays", *SAE Transactions: Journal of Engines*, vol. 106, no. 3, pp. 127-140, 1998.

[48] Y.-K. Lee, U.-C. Yi and F. G. Tseng, "Fuel Injection by a Thermal Microinjector", *Proceedings of IEEE International Conference on Micro Electro Mechanical Systems, MEMS*, Nashville, USA, 1999, pp. 419-425.

[49] R. Schmehl, G. Klose, G. Maier and S. Wittig, "Efficient Numerical Calculation of Evaporating Sprays in Combustion Chamber Flows", *Gas Turbine Engine Combustion, Emissions and Alternative Fuels (AGARD-RTO-MP-14)*, 1999, pp. 51-1 - 51-14.

[50] R. Schmehl, G. Maier and S. Wittig, "CFD Analysis of Fuel Atomization, Secondary Droplet Breakup and Spray Dispersion in the Premix Duct of a LPP Combustor", *Eighth International Conference on Liquid Atomization and Spray Systems*, Pasadena, USA, 2000.

[51] N. Reis, C. Ainsley and B. Derby, "Ink-jet delivery of particle suspensions by piezoelectric droplet ejectors", *Journal of Applied Physics*, vol. 97, no. 9, 2005.

[52] R. Ohigashi and K. Tsuchiya, "Micro Capillaries Array Head for Direct Drawing of Fine Patterns", *Proceedings of IEEE International Conference on Micro Electro Mechanical Systems, MEMS*, Interlaken, Switzerland, 2001, pp. 389-392.

[53] H. Fan, Y. Lu, A. Stump, S. T. Reed, T. Baer, R. Schunk, V. Perez-Luna, G. P. López and C. J. Brinker, "Rapid Prototyping of Patterned Functional Nanostructures", *Nature*, vol. 405, pp. 56-60, 2000.

[54] J. Chung, S. K. C. P. Grigoropoulos, N. R. Bieri, C. Dockendorf and D. Poulikakos, "Damage-Free Low Temperature Pulsed Laser Printing of Gold Nanoinks On Polymers", *Journal of Heat Transfer*, vol. 127, pp. 724-732, 2005.

[55] PMDM Precision Motors Deutsche Minebea GmbH, http://www.pmdm.de, 2005.

[56] F. R. S. Lord Rayleigh, "On the Instability of Jets", *Proceedings of the London mathematical society*, vol. 10, no. 4, pp. 4-13, 1878.

[57] H. C. Lee, "Drop Formation in A Liquid Jet", *IBM Journal of Research and Development*, vol. 18, no. 4, pp. 364-369, 1974.

[58] J. Eggers, "Theory of Drop Formation", *Physics of Fluids*, vol. 7, no. 5, pp. 941-953, 1995.

[59] J. Eggers and and T. F. Dupont, "Drop Formation in A One-Dimensional Approximation of the Navier-Stokes Equation", *Journal of Fluid Mechanics*, vol. 262, pp. 205-221, 1994.

[60] J. Eggers, "Nonlinear dynamics and breakup of free-surface flows", *Reviews of Modern Physics*, vol. 69, no. 3, 1997.

[61] J. Eggers, "Tropfenbildung", *Phys. Bl.*, vol. 53, pp. 431-434, 1997.

[62] E. D. Wilkes, S. D. Phillips and O. A. Basaran, "Computational and experimental analysis of dynamics of drop formation", *Physics of Fluids*, vol. 11, no. 12, pp. 3577-3598, 1999.

[63] R. Zengerle and M. Richter, "Simulation of microfluid systems", *Journal of Micromechanics and Microengineering*, vol. 4, no. 4, pp. 192-204, 1994.

[64] M. Sesterhenn, J. Mellmann, M. Lohr, B. Stierle, T. Strobelt and H. Sandmaier, "Simulation of (Self-) Priming in Capillary Systems Using Lumped Models", *Proceedings of International Conference on Modeling and Simulation of Microsystems, MSM*, Cambridge, USA, 1999, pp. 537-541.

[65] P. Koltay, C. Moosmann, C. Litterst, W. Streule and R. Zengerle, "Simulation of a Micro Dispenser Using Lumped Models", *Proceedings of International Conference on Modeling and Simulation of Microsystems, MSM*, Puerto Rico, 2002, pp. 112-115.

[66] A. Olsson, G. Stemme and E. Stemme, "A numerical design study of the valveless diffuser pump using a lumped-mass model", *Journal of Micromechanics and Microengineering*, vol. 9, no. 1, pp. 34-44, 1999.

[67] C. Litterst, W. Streule, R. Zengerle and P. Koltay, "Simulation Toolkit for Micro-Fluidic Pumps Using Lumped Models", *Technical Proceedings of the NSTI Nanotechnology Conference and Trade Show*, Anaheim, USA, 2005, pp. 736-739.

[68] R. Scheicher, "Kompaktmodell zur Systemsimulation eines Tropfenerzeugers mit Piezobiegewandlern", PhD thesis, TU München, 2004.

[69] Saber (Synopsis Inc.), http://www.synopsys.com, 2005.

[70] PSpice (OrCAD, Cadence Design Systems Inc.), http://www.orcad.com, 2005.

[71] J.-T. Yeh, "Simulation and Industrial Applications of Inkjet", *Proceedings of the 7th National Computational Fluid Dynamics Conference*, Kenting, USA, 2000.

[72] J.-T. Yeh, "A VOF-FEM and Coupled Inkjet Simulation", *Proceedings of ASME FEDSM*, New Orleans, USA, 2001, pp. 1-5.

[73] H. Wijshoff, "Free surface flow and acousto-elastic interaction in piezo inkjet", *Technical Proceedings of the NSTI Nanotechnology Conference and Trade Show*, Boston, Massachusetts, USA, 2004, pp. 215-218.

[74] CFD-ACE+, ESI CFD, Inc., http://esi-group.com, http://www.cfdrc.com, 2004.

[75] Flow3D, Flow Science, Inc., http://www.flow3d.com, 2005.

[76] Fluent Inc., http://www.fluent.com, 2005.

[77] CFX, ANSYS, Inc., http://www.ansys.com/products/cfx.asp, 2005.

[78] Comet, ICCM, Institute of Computational Continuum Mechanics GmbH, http://www.iccm.de, 2005.

[79] STAR-CD, CD-adapco, http://www.cd-adapco.com, 2005.

[80] N.-T. Nguyen, *Mikrofluidik - Entwurf, Herstellung und Charakterisierung*, B.G. Teubner Verlag, 2004.

[81] N.-T. Nguyen, S. T. Wereley, *Fundamentals and Applications of Microfluidics*, Norwood: Artech House, 2002.

[82] M. Moseler and U. Landman, "Formation, Stability, and Breakup of Nanojets", *Science*, vol. 289, no. 1165, 2000.

[83] K. Shibata, S. Koshizuka and Y. Oka, "Numerical analysis of jet breakup behavior using particle method", *Journal of Nuclear Science and Technology*, vol. 41, no. 7, pp. 715-722, 2004.

[84] I. Pivkin and G.E. Karniadakis, "A New Method to Impose No-Slip Boundary Conditions in Dissipative Particles", *Journal of Computational Physics*, vol. 207, no. 2, pp. 114-128, 2005.

[85] E. G. Flekkøy and P. V. Coveney, "From Molecular Dynamics to Dissipative Particle Dynamics", *Physical Review Letters*, vol. 83, no. 9, pp. 1775-1778, 1999.

[86] H. Sigloch, *Technische Fluidmechanik*, 3 ed., Düsseldorf: VDI Verlag, 1996.

[87] S. Middleman, *Modeling Axisymmetric Flows*, 1 ed., San Diego: Academic Press, 1995.

[88] J. Ducrée, *Scriptum to Microfluidics*, WS 2005/2006, IMTEK at Albert Ludwigs University in Freiburg / Germany.

[89] H. K. Versteeg and M. Malalasekera, *An Introduction to Computational Fluid Dynamics, The Finite Volume Method*, Prentice Hall, 1996.

[90] H. M. Schädel, *Fluidische Bauelemente und Netzwerke*, Wiesbaden: Vieweg, 1979.

[91] W. Bohl, *Technische Strömungslehre*, 10 ed., Würzburg: Vogel-Verlag, 1994.

[92] H. Oertel jr., *Prandtl-Führer durch die Strömunglehre*, 10 ed., Braunschweig / Wiesbaden: Friedr. Vieweg & Sohn Verlagsgesellschaft, 2001.

[93] E. Truckenbrodt, *Grundlagen und elementare Strömungsvorgänge dichtebeständiger Fluide*, 1 ed., Berlin: Springer Verlag, 1995.

[94] E. Truckenbrodt, *Elementare Strömungsvorgänge dichteveränderlicher Fluide sowie Potentialströmungen und Grenzschichtströmungen*, 4 ed., Berlin: Springer Verlag, 1998.

[95] I. N. Bronstein, K. A. Semendjajew, G. Musiol, H. Mühlig, *Taschenbuch der Mathematik*, 4 ed., Frankfurt am Main, Thun: Verlag Harri Deutsch, 1999.

[96] C. Litterst, "The Channel-In-Channel (CHIC) principle - A study on bubble management in microfluidic systems", Diploma thesis, IMTEK - Institute of Microsystem Technologies, University of Freiburg, 2003.

[97] E. Buckingham, "On Physically Similar Systems; Illustrations of the Use of Dimensional Equations", *Physical Review*, vol. 4, pp. 345-376, 1914.

[98] Dubbel, Beitz, Küttner, *Taschenbuch für den Maschinenbau*, 19 ed., Springer Verlag, 1997.

[99] H. Liu, *Science and Engineering of Droplets: Fundamentals and Applications*, Norwich, New York, USA: Noyes Publications / William Andrew Publishing, LLC, 1981.

[100] E. R. Lee, *Microdrop Generation*, 1 ed., Boca Raton: CRC Press, 2002.

[101] A. Frohn and N. Roth, *Dynamics of Droplets*, 1 ed., Berlin / Heidelberg: Springer Verlag, 2000.

[102] C. Weber, "Zum Zerfall eines Flüssigkeitsstrahles", *Zeitschrift für angewandte Mathematik und Mechanik*, vol. 11, no. 2, pp. 136-154, 1931.

[103] A. Haenlein, "Über den Zerfall eines Flüssigkeitsstrahles", *Forschung auf dem Gebiete des Ingenieurwesens*, vol. 2, no. 4, pp. 139-149, 1931.

[104] J. E. Fromm, "Numerical-Calculation of the Fluid-Dynamics of Drop-On-Demand Jets", *IBM Journal of Research and Development*, vol. 28, no. 3, pp. 322-333, 1984.

[105] M. Pilch and C. A. Erdman, "Use of Breakup Time Data and Velocity History Data to Predict the Maximum Size of Stable Fragments for Acceleration-Induced Breakup of A Liquid-Drop", *International Journal of Multiphase Flow*, vol. 13, no. 6, pp. 741-757, 1987.

[106] G. O. Thomas, "The aerodynamic breakup of ligaments", *Atomization and Sprays*, vol. 13, no. 1, pp. 117-129, 2003.

[107] A. Tarnogrodzki, "Theoretical Prediction of the Critical Weber Number", *International Journal of Multiphase Flow*, vol. 19, no. 2, pp. 329-336, 1993.

[108] W. von Ohnesorge, "Die Bildung von Tropfen an Düsen und die Auflösung flüssiger Strahlen", *Zeitschrift für angewandte Mathematik und Mechanik*, vol. 16, no. 6, pp. 355-358, 1936.

[109] H. Kuchling, *Taschenbuch der Physik*, 16 ed., Fachbuchverlag Leipzig, 1996.

[110] J. D. Anderson, *Computational Fluid Dynamics*, 1st Edition, McGraw-Hill Science/Engineering/Math, 1995.

[111] R. W. Johnson, *The Handbook of Fluid Dynamics*, Heidelberg: Springer Verlag, 1998.

[112] Wikipedia, http://de.wikipedia.org, 2005.

[113] J. Hansen-Schmidt, "Computational Fluid Dynamic (CFD) Simulation of NanoJet Dispenser", Diploma thesis, IMTEK - Institute of Microsystem Technologies, University of Freiburg, 2002.

[114] J. G. Korvink, *Scriptum to Microsystem Simulation I*, WS 1999/2000, IMTEK at Albert Ludwigs University in Freiburg/Germany.

[115] S. Y. Saad, "Iterative Methods For Sparse Linear Systems", *PWS Publishing Company*, Boston, 1996.

[116] C. W. Hirt, B. D. Nichols and N. C. Romero, "SOLA - A Numerical Solution Algorithm for Transient Fluid Flows", *Los Alamos National Laboratory Report*, LA-5852, 1975.

[117] B. D. Nichols, C. W. Hirt and R. S. Hotchkiss, "SOLA-VOF: A Solution Algorithm for Transient Fluid Flow with Multiple Free Boundaries", *Los Alamos National Laboratory Report*, LA-8355, 1980.

[118] C. W. Hirt and B. D. Nichols, "Volume of Fluid (VOF) Method for the Dynamics of Free Boundaries", *Journal of Computational Physics*, vol. 39, no. 1, pp. 201-225, 1981.

[119] J. E. Pilliod and E. G. Puckett, "Second-order accurate volume-of-fluid algorithms for tracking material interfaces", *Journal of Computational Physics*, vol. 199, no. 2, pp. 465-502, 2004.

[120] M. V. Annaland, N. G. Deen and J. A. M. Kuipers, "Numerical simulation of gas bubbles behaviour using a three-dimensional volume of fluid method", *Chemical Engineering Science*, vol. 60, no. 11, pp. 2999-3011, 2005.

[121] D. Lorstad and L. Fuchs, "High-order surface tension VOF-model for 3D bubble flows with high density ratio", *Journal of Computational Physics*, vol. 200, no. 1, pp. 153-176, 2004.

[122] CFD-ACE+, User Manual, ESI CFD, Inc., 2004.

[123] W. F. Noh and P. R. Woodward, "SLIC (simple line inteface method)", *Lecture Notes in Physics*, vol. 59, pp. 330-340, 1976.

[124] W. J. Rider and D. B. Kothe, "Reconstructing Volume Tracking", *Los Alamos National Laboratory, Technical Report* LA-UR-96-2375, 1997.

[125] D. B. Kothe, W. J. Rider, S. J. Mosso, J. S. Brock, "Volume Tracking of Interfaces Having Surface Tension in Two and Three Dimensions", *AIAA Paper*, 96-0859, 1996.

[126] D. B. Kothe and W. J. Rider, "Comments on Modeling Interfacial Flows with Volume-of-Fluid Methods", *Los Alamos National Laboratory, Technical Report* LA-UR-94-3384, 1995.

[127] A. R. Hanson, E. G. Domich and H. S. Adams, "Shock tube investigation of the breakup of drops by air blasts", *Physics of Fluids*, vol. 6, pp. 1070-1080, 1963.

[128] S. P. Lin and R. D. Reitz, "Drop and Spray Formation from a Liquid Jet", *Annual Review of Fluid Mechanics*, vol. 30, pp. 85-105, 1998.

[129] L. Hentschel, "Berührungslose Dosierung durch strahlbildende Verfahren", *Seminar Mikrodosiersysteme*, München, Germany, 2003, pp. 35-38.

[130] H. Kuchling, *Taschenbuch der Physik*, 16 ed., Leipzig: Fachbuchverlag Leipzig, 1996.

[131] W. Streule, T. Lindemann, G. Birkle, R. Zengerle and P. Koltay, "PipeJet: A Simple Disposable Dispenser for the Nano- and Microliter Range", *Journal of the Association for Laboratory Automation*, vol. 9, no. 5, pp. 300-306, 2004.

[132] T. Lindemann, W. Streule, G. Birkle, R. Zengerle and P. Koltay, "PipeJet™ - A Simple Disposable Dispenser for the Nanoliter Range", *Proceedings of Actuator*, Bremen, Germany, 2004, pp. 224-227.

[133] Q. Liu and M. Orme, "On precision droplet-based net-form manufacturing technology", *Proceedings of the Institution of Mechanical Engineers Part B-Journal of Engineering Manufacture*, vol. 215, no. 10, pp. 1333-1355, 2001.

[134] T. Funada, D. D. Joseph and S. Yamashita, "Stability of a liquid jet into incompressible gases and liquids", *International Journal of Multiphase Flow*, vol. 30, no. 11, pp. 1279-1310, 2004.

[135] J. H. Hilbing and S. D. Heister, "Droplet size control in liquid jet breakup", *Physics of Fluids*, vol. 8, no. 6, pp. 1574-1581, 1996.

[136] S. P. Lin, M. Hudman and J. N. Chen, "Absolute and Convective Instability of a Liquid Jet", *Proceedings of the Fourth Microgravity Fluid Physics & Transport Phenomena Conference*, Cleveland, USA, 1998, pp. 534-538.

[137] E. P. Furlani, C. N. Delametter, J. M. Chwalek and D. Trauernicht, "Surface Tension Induced Instability of Viscous Liquid Jets", *Technical Proceeding of the Fourth International Conference on Modeling and Simulation of Microsystems*, Montreux, Switzerland, 2001, pp. 186-189.

[138] R. P. Grant and S. Middleman, "Newtonian Jet Stability", *AIChE Journal*, vol. 12, no. 4, pp. 669-678, 1966.

[139] J. D. J. S. Samuel, R. Steger, G. Birkle, R. Zengerle, P. Koltay and J. Rühe, "Modification of Micronozzle Surfaces Using Fluorinated Polymeric Nanofilms for Enhanced Dispensing of Polar and Nonpolar Fluids", *Analytical Chemistry*, vol. 77, no. 19, pp. 6469-6474, 2005.

[140] S. Breisch, B. de Heij, M. Löhr and M. Stelzle, "Selective chemical surface modification of fluidic microsystems and characterization studies", *Journal of Micromechanics and Microengineering*, vol. 14, pp. 497-505, 2004.

[141] A. U. Chen and O. A. Basaran, "A new method for significantly reducing drop radius without reducing nozzle radius in drop-on-demand drop production", *Physics of Fluids*, vol. 14, no. 1, pp. L1-L4, 2002.

[142] W. Wehl, "Akustik und Fluidmechanik in Kanälen und Düsen von Tintenschreibwerken", PhD thesis, Technische Universität München, 1984.

[143] Vermes Technik GmbH & Co. KG, http://www.vermes.de, 2005.

[144] microdrop Technologies GmbH, http://www.microdrop.de, 2005.

[145] Cartesian™ Dispensing Systems, http://www.cartesiantech.com, 2005.

[146] TTP LabTech Ltd, http://www.ttplabtech.com, 2005.

[147] GeSiM Gesellschaft für Silizium-Mikrosysteme mbH, http://www.gesim.de, 2005.

[148] Tecan Trading AG, http://www.tecan.com, 2005.

[149] S. Zoltan, *Pulsed Droplet Ejecting System*, US Patent US 3683212, 1972.

[150] S. Zoltan, *Printing Head for Ink Jet Printer*, US Patent US 4641155, 1987.

[151] S. A. Elrod, B. T. Khuri-Yakub and C. F. Quate, *Acoustic Lens Arrays for Ink Printing*, US Patent US 4751530, 1988.

[152] B. Hadimioglu, S. A. Elrod, D. L. Steinmetz, M. Lim, J. C. Zesch, B. T. Khuri-Yakub, E. G. Rawson and C. F. Quate, "Acoustic Ink Printing", *Proceedings of IEEE Ultrasonics Symposium*, Tucson, USA, 1992, pp. 929-935.

[153] B. B. Hadimioglu, C. F. Quate and B. T. Khuri-Yakub, *Liquid Surface Control with an Applied Pressure Signal in Acoustic Ink Printing*, US Patent US 5229793, 1993.

[154] Labcyte Inc., http://www.labcyte.com, 2005.

[155] W. Streule, "Sensoric Concepts for the NanoJet Dispensing Device", Diploma thesis, IMTEK - Institute of Microsystem Technologies, University of Freiburg, 2003.

[156] Sartorius AG, http://www.sartorius.com, 2005.

[157] S. Gracki, "Characterisation of a nanolitre dispenser based on PipeJet™ Technology", Diploma thesis, IMTEK - Institute of Microsystem Technologies, University of Freiburg, 2004.

[158] VISIT Video-Stroboskop Innovations-Technik GmbH & Co KG, http://www.visit-gmbh.de, 2005.

[159] LaVision GmbH, http://www.lavision.de, 2005.

[160] Copley Scientific Ltd., http://www.copleyscientific.co.uk, 2005.

[161] Malvern Instruments Ltd., http://www.malvern.co.uk, 2005.

[162] J. L. Vaught, F. L. Cloutier, D. K. Donald, J. D. Meyer, C. A. Tacklind and H. H. Taub, *Thermal Ink Jet Printer*, US Patent 4490728, 1984.

[163] H. P. Le, "Progress and trends in ink-jet printing technology", *Journal of Imaging Science and Technology*, vol. 42, no. 1, pp. 49-62, 1998.

[164] S. S. Baek, H. T. Lim, H. Song, Y. S. Kim, K. D. Bae, C. H. Cho, C. S. Lee, J. W. Shin, S. J. Shin, K. Kuk and Y. S. Oh, "T-Jet: A Novel Thermal Inkjet Printhead with Monolithically Fabricated Nozzle Plate on SOI Wafer", *Proceedings of IEEE Transducers*, Boston, USA, 2003, pp. 472-475.

[165] Y.-J. Chuang, F. G. Tseng and W.-K. Lin, "A Thermal Droplet Generator with Monolithic Photopolymer Nozzle Plate", *Proceedings of IEEE Transducers*, Boston, USA, 2003, pp. 476-479.

[166] M. Murata, M. Kataoka, R. Nayve, A. Fukugawa, Y. Ueda, T. Mihara, M. Fujii and T. Iwamori, "High resolution long array thermal ink jet printhead with on-chip LSI heater plate and micromachined Si channel plate", *IEICE Transactions on Electronics*, vol. E84C, no. 12, pp. 1792-1800, 2001.

[167] R. Nayve, M. Fujii, A. Fukugawa and M. Murata, "High Resolution Long Array Thermal Ink Jet Printhead Fabricated by Anisotropic Wet Etching and Deep Si RIE", *Proceedings of IEEE International Conference on Micro Electro Mechanical Systems, MEMS*, Kyoto, Japan, 2003, pp. 456-461.

[168] R. Nayve, M. Fujii, A. Fukugawa, T. Takeuchi, M. Murata, Y. Yamada and M. Koyanagi, "High-resolution long-array thermal ink jet printhead fabricated by anisotropic wet etching and deep Si RIE", *Journal of Microelectromechanical Systems*, vol. 13, no. 5, pp. 814-821, 2004.

[169] F. G. Tseng, C. J. Kim and C. M. Ho, "A high-resolution high-frequency monolithic top-shooting microinjector free of satellite drops - Part I: Concept, design and model", *Journal of Microelectromechanical Systems*, vol. 11, no. 5, pp. 427-436, 2002.

[170] F. G. Tseng, C. J. Kim and C. M. Ho, "A high-resolution high-frequency monolithic top-shooting microinjector free of satellite drops - Part II: Fabrication, implementation and characterization", *Journal of Microelectromechanical Systems*, vol. 11, no. 5, pp. 437-447, 2002.

[171] HSG-IMIT, http://www.hsg-imit.de, 2005.

[172] IMTEK, Institute of Microsystems Technology, Laboratory for MEMS Applications, University of Freiburg, http://www.imtek.de, 2005.

[173] W. Wehl, "Tintendrucktechnologie - Paradigma und Motor der Mikrosystemtechnik Teil 1: Stand der Tintendrucktechnologie - Zwang zur Mikrosystemtechnik", *F&M Feinwerktechnik & Messtechnik*, vol. 103, no. 6, pp. 318-324, 1995.

[174] W. Wehl, "Tintendrucktechnologie - Paradigma und Motor der Mikrosystemtechnik Teil 2: Entwicklung eines Mikrosystem-Tintendruckkopfes in Deutschland", *F&M Feinwerktechnik & Messtechnik*, vol. 103, no. 9, pp. 486-491, 1995.

[175] S. W. Lee, H. C. Kim, K. Kuk and Y. S. Oh, "A monolithic inkjet print head: DomeJet", *Sensors and Actuators A-Physical*, vol. 95, no. 2-3, pp. 114-119, 2002.

[176] C. Rembe, S. aus der Wiesche and E. P. Hofer, "Thermal ink jet dynamics: modeling, simulation and testing", *Microelectronics Reliability*, vol. 40, no. 3, pp. 525-532, 2000.

[177] C. Rembe, S. aus der Wiesche and E. P. Hofer, "Dynamics in a Thermal Ink Jet A Model for Identification and Simulation", *Technical Proceedings of the International Conference on Modeling and Simulation of Microsystems, MSM*, 1999, pp. 550-553.

[178] S. aus der Wiesche, C. Rembe and E. P. Hofer, "Boiling of superheated liquids near the spinodal: I General theory", *Heat and Mass Transfer*, vol. 35, no. 1, pp. 25-31, 1999.

[179] S. aus der Wiesche, C. Rembe and E. P. Hofer, "Boiling of superheated liquids near the spinodal: II Application", *Heat and Mass Transfer*, vol. 35, no. 2, pp. 143-147, 1999.

[180] S. aus der Wiesche, C. Rembe, C. Maier and E. P. Hofer, "Dynamics in Microfluidic Systems with Microheaters", *Technical Proceedings of the International Conference on Modeling and Simulation of Microsystems, MSM*, 1999, pp. 510-513.

[181] Z. Zhao, S. Glod and D. Poulikakos, "Pressure and power generation during explosive vaporization on a thin-film microheater", *International Journal of Heat and Mass Transfer*, vol. 43, no. 2, pp. 281-296, 2000.

[182] C. G. Cooney and B. C. Towe, "A thermopneumatic dispensing micropump", *Sensors and Actuators A-Physical*, vol. 116, no. 3, pp. 519-524, 2004.

[183] J.-H. Tsai and L. Lin, "A thermal-bubble-actuated micronozzle-diffuser pump", *Journal of Microelectromechanical Systems*, vol. 11, no. 6, pp. 665-671, 2003.

[184] P. Deng, Y.-K. Lee and P. Cheng, "Design and Characterization of a Micro Single Bubble Actuator", *Proceedings of IEEE Transducers*, Boston, USA, 2003, pp. 647-650.

[185] X. Geng, H. Yuan, H. N. Oguz and A. Prosperetti, "Bubble-based micropump for electrically conducting liquids", *Journal of Micromechanics and Microengineering*, vol. 11, no. 3, pp. 270-276, 2001.

[186] T. K. Jun and C.-J. Kim, "Valveless pumping using traversing vapor bubbles in microchannels", *Journal of Applied Physics*, vol. 83, no. 11, pp. 5658-5664, 1998.

[187] T. K. Jun and C.-J. Kim, "Microscale Pumping with Traversing Bubbles in Microchannels", *Technical Digest Solid-State Sensor and Actuator Workshop*, Hilton Head Island, USA, 1996, pp. 144-147.

[188] R. Conta and A. Scardovi, *Printhead with Multiple Ink Feeding Channels*, Patent WO 0147715 A1, 2001.

[189] T. Lizotte, O. Ohar and S. C. Waters, "Excimer lasers drill inkjet nozzles", *Laser Focus World*, vol. 38, no. 5, pp. 165-168, 2002.

[190] Lambda Physik AG, http://www.lambdaphysik.com, 2005.

[191] Finetech GmbH & Co KG, http://www.finetech.de, 2004.

[192] Polytec GmbH, http://www.polytec.com, 2004.

[193] A. Asai, *Liquid Jet Method, Recording Head using the Method and Recording Apparatus using the Method*, US Patent US 5218376, 1993.

[194] M. Kaneko and H. Matsuda, "New Bubble Jet Print Head for Photo-Quality Printing", *Proceedings of NIP15, International Conference on Digital Printing Technologies*, Orlando, USA, 1999, pp. 44-47.

[195] R. R. Allen, J. D. Meyer and W. R. Knight, "Thermodynamics and Hydrodynamics of Thermal Ink Jets", *Hewlett-Packard Journal*, vol. 36, no. 5, pp. 21-27, 1985.

[196] J. D. Beasley, "Model for Fluid Ejection and Refill in an Impulse Drive Jet", *Photographic Science and Engineering*, vol. 21, no. 2, pp. 78-82, 1977.

[197] N. V. Deshpande, "Significance of inertance and resistance in fluidics of thermal ink-jet transducers", *Journal of Imaging Science and Technology*, vol. 40, no. 5, pp. 396-400, 1996.

[198] A. Asai, T. Hara and I. Endo, "One-Dimensional Model of Bubble-Growth and Liquid Flow in Bubble Jet Printers", *Japanese Journal of Applied Physics Part 1 - Regular Papers Short Notes & Review Papers*, vol. 26, no. 10, pp. 1794-1801, 1987.

[199] A. Asai, S. Hirasawa and I. Endo, "Bubble Generation Mechanism in the Bubble Jet Recording Process", *Journal of Imaging Technology*, vol. 14, no. 5, pp. 120-124, 1988.

[200] A. Asai, "Application of the Nucleation Theory to the Design of Bubble Jet Printers", *Japanese Journal of Applied Physics Part 1 - Regular Papers Short Notes & Review Papers*, vol. 28, no. 5, pp. 909-915, 1989.

[201] A. Asai, "Bubble Dynamics in Boiling Under High Heat-Flux Pulse Heating", *Journal of Heat Transfer - Transactions of the ASME*, vol. 113, no. 4, pp. 973-979, 1991.

[202] A. Asai, "3-Dimensional Calculation of Bubble-Growth and Drop Ejection in a Bubble Jet Printer", *Journal of Fluids Engineering - Transactions of the ASME*, vol. 114, no. 4, pp. 638-641, 1992.

[203] T. Lindemann, D. Sassano, A. Bellone, R. Zengerle and P. Koltay, "Three-Dimensional CFD-Simulation of a Thermal Bubble Jet Printhead", *Technical Proceedings of the NSTI Nanotechnology Conference and Trade Show*, Boston, Massachusetts, USA, 2004, pp. 227-230.

[204] T. Lindemann, H. Ashauer, T. Goettsche, H. Sandmaier, Y. Yu, R.-P. Peters, D. Sassano, A. Bellone, A. Scardovi, R. Zengerle and P. Koltay, "Thermal Bubble Jet Printhead with Integrated Nozzle Plate", *Proceedings of NIP20, International Conference on Digital Printing Technologies*, Salt Lake City, Utah, USA, 2004, pp. 834-839.

[205] T. Lindemann, H. Ashauer, T. Goettsche, H. Sandmaier, Y. Yu, R.-P. Peters, D. Sassano, A. Bellone, R. Zengerle and P. Koltay, "Bubble Jet Printhead with Integrated Polyimide Nozzle Plate", *Proceedings of 18th IEEE International Conference on Micro Electro Mechanical Systems, MEMS*, Miami Beach, Florida, USA, 2005, pp. 560-563.

[206] R. L. Lide, *Handbook of Chemistry and Physics*, 82 ed., Boca Raton, USA: CRC Press, 2001.

[207] H. Stöcker, *Taschenbuch der Physik*, 3 ed., Thun und Frankfurt am Main, Germany: Verlag Harri Deutsch, 1998.

[208] P. H. Chen, W. C. Chen and S. H. Chang, "Bubble growth and ink ejection process of a thermal ink jet printhead", *International Journal of Mechanical Sciences*, vol. 39, no. 6, pp. 683-695, 1997.

[209] P. Koltay, J. Ducree and R. Zengerle, "Nanoliter & picoliter liquid handling", pp. 151-171, in R. E. Oosterbroek and A. van den Berg, *Lab-on-a-Chip, Miniaturized Systems for (Bio)Chemical Analysis and Synthesis*, 1 ed., Amsterdam, The Netherlands: Elsevier B. V., 2003.

[210] P. Koltay, R. Steger, B. Bohl and R. Zengerle, "The Dispensing Well Plate: A novel nanodispenser for the multi parallel delivery of liquids (DWP Part I)", *Sensors and Actuators A-Physical*, vol. 116, no. 3, pp. 483-491, 2004.

[211] P. Koltay, J. Kalix and R. Zengerle, "Theoretical Evaluation of the Dispensing Well Plate method (DWP Part II)", *Sensors and Actuators A-Physical*, vol. 116, no. 3, pp. 472-483, 2004.

[212] R. Steger, B. Bohl, R. Zengerle and P. Koltay, "The Dispensing Well Plate: A Novel Device for Nanoliter Liquid Handling in Ultra High-Throughput Screening", *Journal of the Association for Laboratory Automation*, vol. 9, no. 5, pp. 291-299, 2004.

[213] P. Koltay, G. Birkle, R. Steger, H. Kuhn, M. Mayer, H. Sandmaier and R. Zengerle, "Highly parallel and accurate nanoliter dispenser for High-Throughput-Synthesis of chemical compounds", *Proceedings of International MEMS Workshop, I-MEMS*, Singapore, 2001, pp. 115-124.

[214] R. Steger, P. Koltay, G. Birkle, T. Strobelt, H. Sandmaier and R. Zengerle, "A Two-Dimensional Array of Piezostack Actuated Nanoliter Dispensers", *Proceedings of Actuator*, Bremen, Germnay, 2002, pp. 537-541.

[215] R. Zengerle, M. Freygang, M. Stehr, S. Messner, M. Ashauer, R. Roßberg, *Mikrodosiervorrichtung und Verfahren zum Betreiben derselben*, German Patent DE 19706513, 1997.

[216] G. Birkle, IMTEK, University of Freiburg, personal communication, 2005.

[217] BioFluidix GmbH, http://www.biofluidix.com, 2005.

[218] W. Streule, IMTEK, University of Freiburg, personal communication, 2005.

[219] B. de Heij, C. P. Steinert, H. Sandmaier and R. Zengerle, "A Tunable and Highly Parallel Picoliter-Dispenser Based on Direct Liquid Displacement", *Proceedings of 15th IEEE International Conference on Micro Electro Mechanical Systems, MEMS*, Las Vegas, USA, 2002, pp. 706-709.

[220] J. Ducrée, H. Gruhler, N. Hey, M. Mueller, S. Békési, M. Freygang, H. Sandmaier and R. Zengerle, "TopSpot - A New Method for the Fabrication of Microarrays", *Proceedings of the 13th IEEE International Conference on Micro Electro Mechanical Systems, MEMS*, Mizyazaki, Japan, 2000, pp. 317-322.

[221] B. de Heij, S. Békési, M. Loehr, G. Kattinger, H. Sandmaier and R. Zengerle, "A 96 Channel Printhead for Production of Microarrays", *Proceedings of International MEMS Workshop, I-MEMS*, Singapore, 2001, pp. 125-131.

[222] B. de Heij, M. Daub, O. Gutmann, R. Niekrawietz, H. Sandmaier and R. Zengerle, "Highly parallel dispensing of chemical and biological reagents", *Anal. Bioanal. Chem.*, vol. 378, no. 1, pp. 119-122, 2004.

[223] O. Gutmann, R. Kuehlewein, S. Reinbold, R. Niekrawietz, C. P. Steinert, B. de Heij, R. Zengerle and M. Daub, "A highly parallel nanoliter dispenser for microarray fabrication", *Biomed. Microdevices*, vol. 6, no. 2, pp. 131-137, 2004.

[224] O. Gutmann, R. Niekrawietz, R. Kuehlewein, C. P. Steinert, S. Reinbold, B. de Heij, M. Daub and R. Zengerle, "Non-contact production of oligonucleotide microarrays using the highly integrated TopSpot nanoliter dispenser", *Analyst*, vol. 129, no. 9, pp. 835-840, 2004.

[225] O. Gutmann, R. Niekrawietz, R. Kuehlewein, C. P. Steinert, B. de Heij, R. Zengerle and M. Daub, "Impact of medium properties on droplet release in a highly parallel nanoliter dispenser", *Sensors and Actuators A-Physical,* vol. 116, no. 2, pp. 187-194, 2004.

[226] R. Niekrawietz, W. Honstein, O. Gutmann, B. de Heij, M. Daub and R. Zengerle, "Integrated Process Control for Highly Parallel and Contact-Free Microarray Printing", *Proceedings of the 18th IEEE International Conference on Micro Electro Mechanical Systems, MEMS*, Miami, USA, 2005, pp. 738-741.

[227] O. Gutmann, R. Kuehlewein, S. Reinbold, R. Niekrawietz, C. P. Steinert, B. de Heij, R. Zengerle and M. Daub, "Fast and reliable protein microarray production by a new drop-in-drop technique", *Lab on a Chip*, vol. 5, no. 6, pp. 675-681, 2005.

[228] R. Niekrawietz, "TopSpot: Highly Integrated Printheads of a Pneumatic Non-Contact Dispenser", PhD thesis, Institute of Microsystem Technology (IMTEK), Laboratory for MEMS Applications, University of Freiburg, Germany, to be published in 2006.

[229] B. de Heij, C. P. Steinert, H. Sandmaier and R. Zengerle, "A tuneable and highly-parallel picolitre-dispenser based on direct liquid displacement", *Sensors and Actuators A-Physical*, vol. 103, no. 1-2, pp. 88-92, 2003.

[230] C. P. Steinert, I. Goutier, O. Gutmann, H. Sandmaier, S. Messner, M. Daub, B. de Heij and R. Zengerle, "An Improved 24 Channel Picoliter Dispenser Based on Direct Liquid Displacement", *Proceedings of IEEE International Conference on Solid-State Sensors, Actuators and Microsystems*, Boston, USA, 2003, pp. 376-379.

[231] C. P. Steinert, I. Goutier, O. Gutmann, H. Sandmaier, M. Daub, B. de Heij and R. Zengerle, "A highly parallel picoliter dispenser with an integrated, novel capillary channel structure", *Sensors and Actuators A-Physical*, vol. 116, no. 1, pp. 171-177, 2004.

[232] C. P. Steinert, H. Sandmaier, M. Daub, B. de Heij and R. Zengerle, "Bubble-Free Priming of Blind Channels", *Proceedings of the 17th IEEE International Conference on Micro Electro Mechanical Systems, MEMS*, Maastricht, The Netherlands, 2004, pp. 224-228.

[233] C. P. Steinert, N. Schmitt, E. Deier, M. Daub, B. de Heij and R. Zengerle, "A Novel Fabrication Method for Hybrid, Microfluidic Devices", *Proceedings of the 18th IEEE International Conference on Micro Electro Mechanical Systems, MEMS*, Miami, USA, 2005, pp. 552-555.

[234] C. P. Steinert, "TopSpot Vario: A Novel Microarrayer System for Highly Parallel Picoliter Dispensing", PhD thesis, IMTEK - Institute of Microsystem Technologies, University of Freiburg, 2005.

[235] C. Litterst, "Praktikumsbericht", IMTEK - Institute of Microsystem Technologies, University of Freiburg, 2002.

[236] LaVision GmbH, http://www.LaVision.de, 2005.

9 NOMENCLATURE

Symbol	Description [Unity]
A	Area [m^2]
$A_{channel}$	Cross section area of a channel [m^2]
$A_{droplet}$	Surface of a spherical droplet [m^2]
A_{nozzle}	Cross section area of a nozzle [m^2]
a	Acceleration [m/s^2] or aspect ratio [-]
α	Contraction number [-] or link factor [-]
$C_{geometry}$	Geometry factor [-]
C_{hd}	Fluidic capacitance [N m]
D	Diameter [m]
$D_{channel}$	Diameter of a channel [m]
$D_{droplet}$	Droplet diameter [m]
D_{nozzle}	Diameter of a nozzle [m]
E	Energy [J]
$E_{effective}$	Effective energy at the nozzle [J]
$E_{friction}$	Energy loss due to friction [J]
$E_{kinetic}$	Kinetic energy [J]
$E_{surface}$	Surface tension energy [J]
$E_{viscous}$	Frictional energy [J]
e	Inner energy [J]
F	Force [N] or volume fraction [-]
f	Frequency [Hz]
f_{body}	Body force [N]
f_{max}	Maximum frequency [Hz]
f_{opt}	Optimum frequeny [Hz]
Φ_m	Mass flow [kg/s]
Φ_v	Volume flow [m^3/s]
$\Phi_{v,\ critical}$	Critical volume flow [m^3/s]
$\Phi_{v,\ n}$	Volume flow through the nozzle [m^3/s]
$\Phi_{v,\ r}$	Volume flow through the reservoir channel [m^3/s]
$\Phi_{v,\ th}$	Theoretical volume flow [m^3/s]
ϕ	Volume-specific quantity [-]

Symbol	Description [Unity]
g	Normal earth acceleration [m/s^2]
Γ	Diffusion coefficient [-]
η	Dynamic viscosity [Pa s]
I_{el}	Electric current [A]
ϑ	Curvature angle [°]
φ	Velocity coefficient [-]
K	Constant for inlet resistance [-]
k	Thermal conductivity [W m^{-1} K^{-1}]
κ	Compressibility [Pa]
$L_{breakup}$	Breakup length of a Rayleigh droplet breakup [m]
L_{hd}	Fluidic Inertance [kg/m^4]
L_{inlet}	Entering length [m]
L_n	Fluidic Inertance of the nozzle [kg/m^4]
L_r	Fluidic Inertance of the reservoir channel [kg/m^4]
l	Length [m]
l_i	Inlet length [m]
l_o	Outlet length [m]
λ	Wave length [m]
λ_{opt}	Optimum wave length [m]
m	Mass [kg]
m_M	Molecular weight [kg]
μ	Outflow number [-]
n	Normal force [N]
On	Ohnesorge number [-]
$P_{critical}$	Critical power [W]
$P_{droplet}$	Droplet diameter in pixels [-]
P_{nozzle}	Nozzle diameter in pixels [-]
p	Pressure [Pa]
p_{atm}	Atmospheric pressure (= 100 kPa) [Pa]
p_{cap}	Capillary pressure [Pa]
$p_{critical}$	Critical pressure [Pa]
p_{dyn}	Dynamic pressure [Pa]
p_r	Pressure inside the reservoir [Pa]
p_{stat}	Static pressure [Pa]
p_v	Vapor pressure [Pa]
π	Number Pi [-]

Symbol	Description [Unity]
Q_{vap}	Heat of vaporization [J/kg]
θ	Angle in a cylindrical coordinate system [°]
Θ	Contact Angle [°]
R	Gas constant (= 8.3148 J mol^{-1} K^{-1}) [J mol^{-1} K^{-1}]
R	Radius [m]
$R_{contraction}$	Fluidic resistance due to contraction [kg s^{-1} m^{-4}]
R_{el}	Electric resistance [Ω]
$R_{expansion}$	Fluidic resistance due to expansion [kg s^{-1} m^{-4}]
R_{hd}	Fluidic resistance [kg s^{-1} m^{-4}]
$R_{hd, mod}$	Modified fluidic resistance due to entering effects [kg s^{-1} m^{-4}]
R_n	Fluidic resistance of the nozzle [kg s^{-1} m^{-4}]
$R_{outflow}$	Fluidic resistance due to the outflow of a nozzle [kg s^{-1} m^{-4}]
R_r	Fluidic resistance of the reservoir channel [kg s^{-1} m^{-4}]
r	Radius [m]
Re	Reynolds number [-]
$Re_{critical}$	Critical Reynolds number [-]
ρ	Liquid density [kg/m^3]
S	Source term [-]
s	Measure of length [m]
σ	Surface tension [N/m]
T	Temperature [K]
T_{amb}	Ambient temperature [K]
T_b	Boiling temperature [K]
T_v	Vapor temperature [K]
t	Time [s]
t_0	Time constant [s]
$t_{critical}$	Critical time [s]
t_{on}	Duration of a rectangular pressure pulse [s]
τ	Tangential force [N]
U_{el}	Electrical voltage [V]
υ	Kinematic viscosity [m^2/s]
V	Volume [m^3]
$V_{droplet}$	Droplet volume [m^3]
V_{jet}	Jet volume [m^3]
V_{nozzle}	Volume of a droplet with a diameter equal to the nozzle diameter [m^3]
v	Velocity [m/s]

Symbol	Description [Unity]
$v_{channel}$	Velocity in a channel [m/s]
$v_{critical}$	Critical velocity [m/s]
$v_{droplet}$	Droplet velocity [m/s]
v_{piston}	Piston velocity [m/s]
v_{θ}	Angle velocity [m/s]
v_{r}	Velocity in radial direction [m/s]
v_{x}	Velocity in *x*-direction [m/s]
v_{y}	Velocity in *y*-direction [m/s]
v_{z}	Velocity in *z*-direction [m/s]
$W_{pressure}$	Mechanical work generated by an external pressure [J]
We	Weber number [-]
$We_{critical}$	Critical Weber number [-]
x	Cartesian coordinate in *x*-direction [m]
y	Cartesian coordinate in *y*-direction [m]
z	Cartesian coordinate in *z*-direction [m]
ζ	Resistance number for contraction resistance [-]

ACKNOWLEDGEMENTS

I wish to express my gratitude to Prof. Dr. Roland Zengerle for giving me the exciting possibility to perform this thesis at his Laboratory for MEMS Applications.

Many thanks to Prof. Dr. Jan G. Korvink for the kind acceptance to co-referee this thesis.

I want to thank also Dr. Peter Koltay for being my tutor, for always being available for my questions and supporting me whenever any problems occurred.

Many thanks to Melanie and Ulrike the helpful spirit of the department.

I also want to express my gratitude to Claudio Cupelli and Remigius Niekrawietz for being more than just room mates for me.

I also want to thank Wolfgang Streule the rescuer for all computer and network problems, Christian Litterst for the easy-going discussions about CFD-ACE+ and Thomas Glatzel for directing me to the leader in the Reference Manager.

Many thanks to Gerhard Birkle for answering any laboratory related questions.

Many thanks to my volleyball colleagues providing me a counterbalance to the everyday work.

Certainly I want to thank the entire staff of the Laboratory for MEMS Applications for the friendly atmosphere

For reading the manuscript of my thesis at different stages and giving me a lot of helpful suggestions, improvements and corrections, I would like to thank Prof. Dr. Roland Zengerle, Dr. Peter Koltay, Claudio Cupelli, Thomas Glatzel, Christian Litterst and Remigius Niekrawietz. Especially Dr. Peter Koltay and Claudio Cupelli supported me notably in the final period writing this thesis.

I thank my family for supporting and encouraging me throughout my personal and professional life.

Last but not least I want to thank my girl friend Anne Huber for all her love and support throughout the last years and her patience in the last months in particular.